PERGAMON

Progress in Quantum Electronics 27 (2003) 59–210

Progress in Quantum Electronics

www.elsevier.com/locate/pquantelec

Review

Infrared detectors: status and trends

Antoni Rogalski*

Institute of Applied Physics, Military University of Technology, 49 00-908 Warsaw, 2 Kaliskiego Street, Warsaw 49-00-908, Poland

Abstract

At present efforts in infrared detector research are directed towards improving the performance of single element devices, large electronically scanned arrays and higher operating temperature. Another important aim is to make IR detectors cheaper and more convenient to use. All these aspects are discussed in this paper.

Investigations of the performance of infrared thermal detectors as compared to photon detectors are presented. Due to fundamental different types of noise, these two classes of detectors have different dependencies of detectivities on wavelength and temperature. Next, an overview of focal plane array architecture is given with emphasise on monolithic and hybrid structures. The objective of the next sections is to present the status of different types of detectors: HgCdTe photodiodes, Schottky-barrier photoemissive devices, silicon and germanium detectors, InSb photodiodes, alternative to HgCdTe III–V and II–VI ternary alloy detectors, monolithic lead chalcogenide photodiodes, quantum well and quantum dot infrared photodetectors.

Final part of the paper is devoted to uncooled two-dimensional arrays of thermal detectors. Three most important detection mechanisms, namely, resistive bolometer, pyroelectric detectors and termopile are considered. The development of outstanding technical achievements in uncooled thermal imaging is also presented.
© 2003 Elsevier Science Ltd. All rights reserved.

Contents

1. Introduction 61
2. Historical aspects of modern infrared technology 62
3. Classification of infrared detectors 65

*Tel./fax: +48-22-685-9109.
E-mail address: rogan@wat.waw.pl (A. Rogalski).

0079-6727/03/$ - see front matter © 2003 Elsevier Science Ltd. All rights reserved.
PII: S0079-6727(02)00024-1

4. General theory of photon detectors 68

5. General theory of thermal detectors 75

6. Comparison of fundamental limits of photon and thermal detectors . 79

7. Focal plane arrays 80
7.1. FPA architectures 81
7.2. CCD and CMOS architectures 86
7.3. Passive and active pixel sensors 91
7.4. Focal plane array performance 92

8. Photon detectors 95
8.1. HgCdTe photodiodes 97
8.1.1. Frontside illuminated photodiodes 99
8.1.2. Backside illuminated photodiodes 101
8.1.3. Fundamental limitation to HgCdTe photodiode performance 103
8.1.4. Non-fundamental sources of dark current of HgCdTe photodiodes 112
8.1.5. Avalanche photodiodes 115
8.1.6. Non-equilibrium photodiodes 116
8.2. Photoemissive detectors 117
8.2.1. Schottky-barrier photoemissive detectors 118
8.2.2. Novel internal photoemissive detectors 123
8.3. Extrinsic silicon and germanium detectors 124
8.3.1. Silicon and germanium photoconductive detectors . . 125
8.3.2. Blocked impurity band devices 127
8.4. InSb photodiodes 129
8.5. InGaAs photodiodes 131
8.6. InAsSb photodiodes 134
8.7. Hg-based alternatives to HgCdTe 135
8.7.1. HgZnTe detectors 136
8.7.2. HgMnTe detectors 136
8.8. Lead chalcogenide photodiodes 137
8.9. Quantum wells and superlattice detectors 141
8.9.1. GaAs/AlGaAs QWIPs 142
8.9.2. InAs/InGaSb strained layer superlattice detectors . . . 148
8.10. QWIP versus HgCdTe in LWIR spectral region 152
8.10.1. Quantum efficiency 152
8.10.2. Dark current and R_oA product 153
8.10.3. Detectivity 155
8.10.4. Noise equivalent difference temperature 157
8.10.5. Cost 161
8.10.6. Reliability 162
8.10.7. Summary 163
8.11. Quantum dot infrared photodetectors 164
8.12. Dual-band detectors 167
8.12.1. Dual-band HgCdTe 169
8.12.2. Dual-band QWIPs 171

9. Thermal detectors 174
9.1. Micromachined silicon bolometers 175
9.2. Pyroelectric detectors 181
9.3. Thermoelectric arrays 186
9.4. Novel sensors 187
9.5. Status and trends of uncooled arrays 190

10. Conclusions 191

References 193

1. Introduction

Looking back over the past 1000 years we notice that infrared (IR) radiation itself was unknown until 202 years ago when Herschel's experiment with thermometer was first reported. He built a crude monochromator that used a thermometer as a detector so that he could measure the distribution of energy in sunlight. In April 1800 he wrote: [1]

> "Thermometer No. 1 rose 7 degrees in 10 minutes by an exposure to the full red coloured rays. I drew back the stand....... thermometer No. 1 rose, in 16 minutes, 8 3/8 degrees when its centre was 1/2 inch out of the visible rays."

The early history of IR was reviewed about 40 years ago in two well-known monographs [2,3]. The most important steps in development of IR detectors are the following:

- in 1921 Seebeck discovered the thermoelectric effect and soon thereafter demonstrated the first thermocouple,
- in 1829 Nobili constructed the first thermopile by connecting a number of thermocouples in series [4].
- in 1833 Melloni modified design of thermocouple and used bismuth and antimony for it design [5].

Langley's bolometer appeared in 1880 [6]. Langley used two thin ribbons of platinum foil, connected so as to form two arms of a Wheatstone bridge. Langley continued to develop his bolometer for the next 20 years (400 times more sensitive than his first efforts). His latest bolometer could detect the heat from a cow at a distance of quarter of mile. Thus, at the beginning the development of IR detectors was connected with thermal detectors.

The photon detectors were developed in XX century. The first IR photoconductor was developed by Case in 1917 [7]. In 1933, Kutzscher at the University of Berlin, discovered that lead sulphide (from natural galena found in Sardinia) was photoconductive and had response to about 3 μm [8].

Many materials have been investigated in the IR field. Observing a history of the development of the IR detector technology, a simple theorem, after Norton [9], can

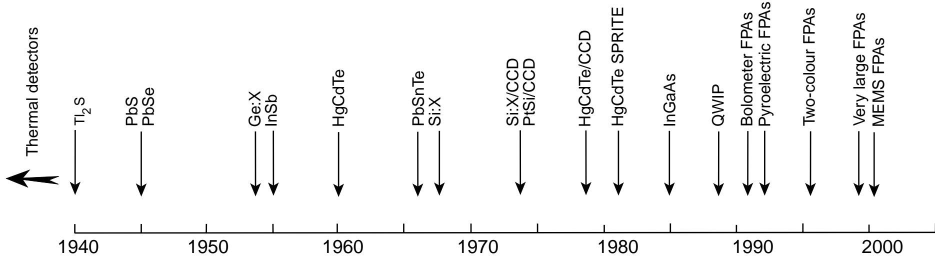

Fig. 1. History of the development of infrared detectors.

be stated: *All physical phenomena in the range of about 0.1–1 eV can be proposed for IR detectors.* Among these effects are: thermoelectric power (thermocouples), change in electrical conductivity (bolometers), gas expansion (Golay cell), pyroelectricity (pyroelectric detectors), photon drag, Josephson effect (Josephson junctions, SQUIDs), internal emission (PtSi Schottky barriers), fundamental absorption (intrinsic photodetectors), impurity absorption (extrinsic photodetectors), low dimensional solids [superlattice (SL) and quantum well (QW) detectors], different type of phase transitions, etc.

Fig. 1 gives approximate dates of significant development efforts for the materials mentioned. The years during World War II saw the origins of modern IR detector technology. Photon IR technology combined with semiconductor material science, photolithography technology developed for integrated circuits, and the impetus of Cold War military preparedness have propelled extraordinary advances in IR capabilities in just a fraction of the last century [10].

2. Historical aspects of modern infrared technology

During the 1950s IR detectors were built using single-element-cooled lead salt detectors, primarily for anti-air-missile seekers. Usually lead salt detectors were polycrystalline and were produced by vacuum evaporation and chemical deposition from a solution, followed by a post-growth sensitisation process [8]. The first extrinsic photoconductive detectors were reported in the early 1950s. Since the techniques for controlled impurity introduction became available for germanium at an earlier date, the first high performance extrinsic detectors were based on germanium. Extrinsic photoconductive response from copper, zinc and gold impurity levels in germanium gave rise to devices using in the 8- to 14-μm long wavelength IR (LWIR) spectral window and beyond to the 14- to 30- m very long wavelength IR (VLWIR) region. Extrinsic photoconductors were widely used at wavelengths beyond 10 μm prior to the development of the intrinsic detectors. They must be operated at lower temperatures to achieve performance similar to that of intrinsic detectors, and a sacrifice in quantum efficiency is required to avoid thick detectors. Although Si has several advantages over Ge (namely, a lower dielectric constant giving shorter dielectric relaxation time and lower capacitance, higher

dopant solubility and larger photoionization cross section for higher quantum efficiency, and lower refractive index for lower reflectance), these were not sufficient to warrant the necessary development efforts needed to bring it to the level of the, by then, highly developed Ge detectors. After being dormant for about ten years, extrinsic Si was reconsidered after the invention of charge-coupled devices (CCDs) by Boyle and Smith [11]. In 1973, Shepherd and Yang [12] proposed the metal-silicide/silicon Schottky-barrier detectors. For the first time it became possible to have much more sophisticated readout schemes—both detection and readout could be implemented on one common silicon chip.

At the same time, rapid advances were being made in narrow bandgap semiconductors that would later prove useful in extending wavelength capabilities and improving sensitivity. The first such material was InSb, a member of the newly discovered III–V compound semiconductor family. The end of the 1950s and the beginning of the 1960s saw the introduction of narrow gap semiconductor alloys in III–V ($InAs_{1-x}Sb_x$), IV–VI ($Pb_{1-x}Sn_xTe$), and II–VI ($Hg_{1-x}Cd_xTe$) material systems. These alloys allowed the bandgap of the semiconductor and hence the spectral response of the detector to be custom tailored for specific applications. In 1959, research by Lawson and co-workers [13] triggered development of variable bandgap $Hg_{1-x}Cd_xTe$ (HgCdTe) alloys, providing an unprecedented degree of freedom in infrared detector design. This first paper reported both photoconductive and photovoltaic response at the wavelength extending out to 12 μm. Soon thereafter, working under a U.S. Air Force contract with the objective of devising an 8–12-μm background-limited semiconductor IR detector that would operate at temperatures as high as 77 K, the group lead by Kruse at the Honeywell Corporate Research Center in Hopkins, Minnesota developed a modified Bridgman crystal growth technique for HgCdTe. They soon reported both photoconductive and photovoltaic detection in rudimentary HgCdTe devices [14].

The fundamental properties of narrow-gap semiconductors (high optical absorption coefficient, high electron mobility and low thermal generation rate), together with the capability for bandgap engineering, make these alloy systems almost ideal for a wide range of IR detectors. The difficulties in growing HgCdTe material, significantly due to the high vapour pressure of Hg, encouraged the development of alternative detector technologies over the past forty years. One of these was PbSnTe, which was vigorously pursued in parallel with HgCdTe in the late 1960 s, and early 1970 s [15–17]. PbSnTe was comparatively easy to grow and good quality LWIR photodiodes were readily demonstrated. However, in the late of 1970 s two factors led to the abandonment of PbSnTe detector work: high dielectric constant and large temperature coefficient of expansion (TCE) mismatch with Si. Scanned IR imaging systems of the 1970 s required relatively fast response times so that the scanned image is not smeared in the scan direction. With the trend today towards staring arrays, this consideration might be less important than it was when first generation systems were being designed. The second drawback, large TCE, can lead to failure of the indium bonds in hybrid structure (between silicon readout and the detector array) after repeated thermal cycling from room temperature to the cryogenic temperature of operation.

The material technology development was and continues to be primarily for military applications. In the United State, the Vietnam War caused the military services to initiate the development of IR systems that could provide imagery arising from the thermal emission of terrain vehicles, buildings, and people. Exactly, HgCdTe has inspired the development of the three "generations" of detector devices. The first generation, linear arrays of photoconductive detectors, has been produced in large quantities and is in widespread use today. The second generation, two-dimensional (2-D) arrays of photovoltaic detectors are now in high-rate production. Third generation devices, defined here to encompass the more exotic device structure embodied in two-colour detectors and hyperspectral arrays, and are now in demonstration programs.

A negative aspect of support by defence agencies has been the associated secrecy requirements that inhibit meaningful collaborations among research teams on a national and especially on an international level. In addition, the primary focus has been on focal plane array (FPA) demonstration and much less on establishing the knowledge base. Nevertheless, significant progress has been made over four decades. At present, HgCdTe is the most widely used variable gap semiconductor for IR photodetectors. Over the years it has successfully fought off major challenges from extrinsic silicon and lead-tin telluride devices, but despite that it has more competitors today than ever before. These include Schottky barriers on silicon, SiGe heterojunctions, AlGaAs multiple quantum wells, GaInSb strain layer superlattices, high temperature superconductors and especially two types of thermal detectors: pyroelectric detectors and silicon bolometers. It is interesting, however, that none of these competitors can compete in terms of fundamental properties. They may promise to be more manufacturable, but never to provide higher performance or, with the exception of thermal detectors, to operate at higher or even comparable temperatures.

It must not be inferred from the preceding outline that work on thermal detectors has not also been actively pursued. Indeed, some interesting and important developments have taken place along this line. In 1947, for example, Golay constructed an improved pneumatic infrared detector [18]. The thermistor bolometer, originally developed by Bell Telephone Laboratories, has found widespread use in detecting radiation from low temperature sources [19]. The superconducting effect has been used to make extremely sensitive bolometers.

Thermal detectors have also been used for infrared imaging. Evaporographs and absorption edge image converters were among the first non-scanned IR imagers. Originally an evaporograph was employed in which the radiation was focused onto a blackened membrane coated with a thin film of oil [20]. The differential rate of evaporation of the oil was proportional to radiation intensity. The film was then illuminated with visible light to produce an interference pattern corresponding to the thermal picture. The second thermal imaging device was the absorption edge image converter [21]. Operation of the device was based upon utilising the temperature dependence of the absorption edge of semiconductor. The performance of both imaging devices was poor because of the very long time constant and the poor spatial resolution. Despite numerous research initiatives and the attractions of ambient

temperature operation and low cost potential, thermal detector technology has enjoyed limited success in competition with cooled photon detectors for thermal imaging applications. A notable exception is the pyroelectric vidicon (PEV) [22], that is widely used by firefighting and emergency service organisations. The pyroelectric vidicon tube can be considered analogously to the visible television camera tube except that the photoconductive target is replaced by a pyroelectric detector and germanium faceplate. Compact, rugged PEV imagers have been offered for military applications but suffer the disadvantage of low tube life and fragility, particularly the reticulated vidicon tubes required for enhanced spatial resolution.

The second revolution in thermal imaging is underway now. The development of uncooled IR arrays capable to imaging scenes at room temperature has been an outstanding technical achievement. Much of the technology was developed under classified military contracts in the United States, so the public release of this information in 1992 surprised many in the worldwide IR community. There has been an implicit assumption that only cryogenic photon detectors operating in the 8–12-μm atmospheric window had the necessary sensitivity to image room-temperature objects. Although thermal detectors have been little used in scanned imagers because of their slow response, they are currently of considerable interest for 2-D electronically addressed arrays where the bandwidth is low and the ability of thermal devices to integrate over a frame time is an advantage [23–29]. Much recent research has focused on both hybrid and monolithic uncooled arrays and has yield significant improvements in the detectivity of both bolometric and pyroelectric detector arrays. Honeywell has licensed bolometer technology to several companies for the development and production of uncooled FPAs for commercial and military systems. At present, the compact 320×240 microbolometer cameras are produced by Raytheon, Boeing, and Lockheed-Martin in the United States. The U.S. government allowed these manufactures to sell their devices to foreign countries, but not to divulge manufacturing technologies. In recent years, several countries, including the United Kingdom, Japan, Korea, and France have picked up the ball, determined to develop their own uncooled imaging systems. As a result, although the U.S. has a significant lead, some of the most exciting and promising developments for low-cost uncooled IR systems may come from non-U.S. companies, e.g., microbolometr FPAs with series p–n junction elaborated by Mitsubishi Electric. This approach is unique, based on an all-silicon version of microbolometer.

3. Classification of infrared detectors

Spectral detectivity curves for a number of commercially available IR detectors are shown in Fig. 2. Interest has centred mainly on the wavelengths of the two atmospheric windows 3–5 μm [middle wavelength IR (MWIR)] and 8–14 μm (LWIR region) (atmospheric transmission is the highest in these bands and the emissivity maximum of the objects at $T \approx 300\,\mathrm{K}$ is at the wavelength $\lambda \approx 10\,\mu\mathrm{m}$), though in recent years there has been increasing interest in longer wavelengths stimulated by space applications.

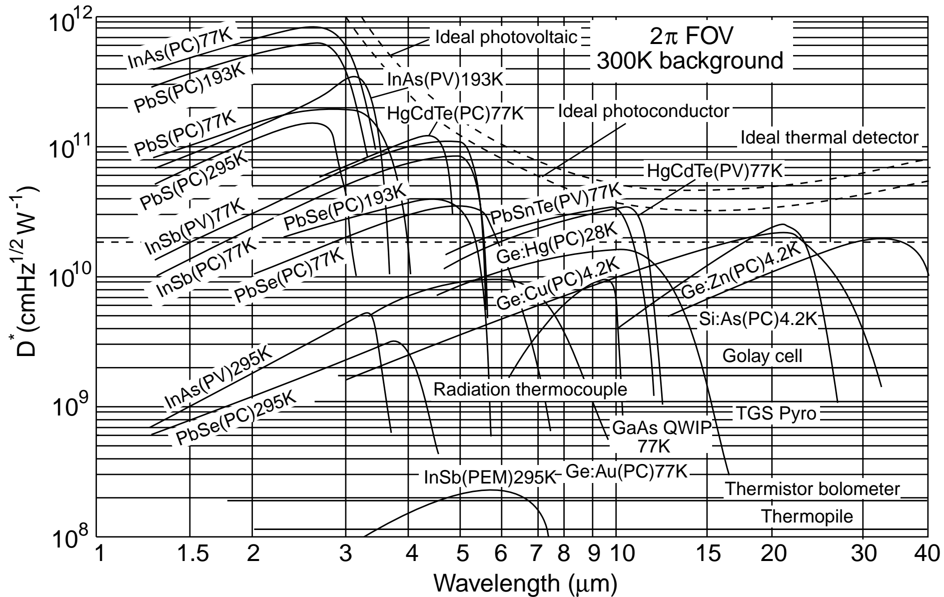

Fig. 2. Comparison of the D^* of various commercially available infrared detectors when operated at the indicated temperature. Chopping frequency is 1000 Hz for all detectors except the thermopile (10 Hz), thermocouple (10 Hz), thermistor bolometer (10 Hz), Golay cell (10 Hz) and pyroelectric detector (10 Hz). Each detector is assumed to view a hemispherical surrounding at a temperature of 300 K. Theoretical curves for the background-limited D^* (dashed lines) for ideal photovoltaic and photoconductive detectors and thermal detectors are also shown. PC—photoconductive detector, PV—photovoltaic detector, and PEM—photoelectromagnetic detector.

Progress in IR detector technology is connected with semiconductor IR detectors, which are included in the class of photon detectors. In this class of detectors the radiation is absorbed within the material by interaction with electrons either bound to lattice atoms or to impurity atoms or with free electrons. The observed electrical output signal results from the changed electronic energy distribution. The photon detectors show a selective wavelength dependence of response per unit incident radiation power. They exhibit both perfect signal-to-noise performance and a very fast response. But to achieve this, the photon detectors require cryogenic cooling. Photon detectors having long-wavelength limits above about 3 μm are generally cooled. This is necessary to prevent the thermal generation of charge carriers. The thermal transitions compete with the optical ones, making non-cooled devices very noisy. Cooling requirements are the main obstacle to the more widespread use of IR systems based on semiconductor photodetectors making them bulky, heavy, expensive and inconvenient to use.

Depending on the nature of the interaction, the class of photon detectors is further sub-divided into different types as shown in Table 1. The most important are: intrinsic detectors, extrinsic detectors, photoemissive (metal silicide Schottky barriers) detectors, and quantum well detectors. Depending on how the electric or

Table 1
Comparison of infrared detectors

Detector type			Advantages	Disadvantages
Thermal (thermopile, bolometers, pyroelectric)			Light, rugged, reliable, and low cost Room temperature operation	Low detectivity at high frequency Slow response (ms order)
Photon	Intrinsic	IV–VI (PbS, PbSe, PbSnTe)	Easier to prepare More stable materials	Very high thermal expansion coefficient Large permittivity
		II–VI (HgCdTe)	Easy bandgap tailoring Well developed theory & exp. Multicolour detectors	Non-uniformity over large area High cost in growth and processing Surface instability
		III–V (InGaAs, InAs, InSb, InAsSb)	Good material & dopants Advanced technology Possible monolithic integration	Heteroepitaxy with large lattice mismatch Long wavelength cutoff limited to 7 μm (at 77 K)
	Extrinsic (Si:Ga, Si:As, Ge:Cu, Ge:Hg)		Very long wavelength operation Relatively simple technology	High thermal generation Extremely low temperature operation
	Free carriers (PtSi, Pt_2Si, IrSi)		Low-cost, high yields Large & close packed 2-D arrays	Low quantum efficiency Low temperature operation
	Quantum wells	Type I (GaAs/AlGaAs, InGaAs/AlGaAs)	Matured material growth Good uniformity over large area Multicolour detectors	High thermal generation Complicated design and growth
		Type II (InAs/InGaSb, InAs/InAsSb)	Low Auger recombination rate Easy wavelength control	Complicated design and growth Sensitive to the interfaces
	Quantum dots	InAs/GaAs, InGaAs/InGaP, Ge/Si	Normal incidence of light Low thermal generation	Complicated design and growth

magnetic fields are developed, there are various modes such as photoconductive, photovoltaic, photoelectromagnetic (PEM), and photoemissive ones. Each material system can be used for different modes of operation.

The second class of IR detectors is composed of thermal detectors. In a thermal detector, the incident radiation is absorbed to change the material temperature, and the resultant change in some physical property is used to generate an electrical output. The detector is suspended on lags which are connected to the heat sink. The signal does not depend upon the photonic nature of the incident radiation. Thus, thermal effects are generally wavelength independent; the signal depends upon the radiant power (or its rate of change) but not upon its spectral content. This assumes that the mechanism responsible for the absorption of the radiation is itself wavelength independent (see Fig. 2), which is not strictly true in most instances. Attention is directed toward three approaches which have found the greatest utility in infrared technology, namely, bolometers, pyroelectric and thermoelectric effects. In pyroelectric detectors a change in the internal electrical polarisation is measured, whereas in the case of thermistor bolometers a change in the electrical resistance is measured. In contrast to photon detectors, thermal detectors typically operate at room temperature. They are usually characterised by modest sensitivity and slow response (because heating and cooling of a detector element is a relatively slow process), but they are cheap and easy to use. They have found widespread use in low cost applications, which do not require high performance and speed. Being unselective, they are frequently used in IR spectrometers.

Up till the 1990s, thermal detectors have been considerably less exploited in commercial and military systems in comparison with photon detectors. The reason for this disparity is that thermal detectors are popularly believed to be rather slow and insensitive in comparison with photon detectors. As a result, the worldwide effort to develop thermal detectors was extremely small relative to that of photon detectors. In the last decade, however, it has been shown that extremely good imagery can be obtained from large thermal detector arrays operating uncooled at TV frame rates. The speed of thermal detectors is quite adequate for non-scanned imagers with 2-D detectors. The moderate sensitivity of thermal detectors can be compensated by a large number of elements in 2-D electronically scanned arrays. With large arrays of thermal detectors the best values of NEDT, below 0.05 K, could be reached because effective noise bandwidths less than 100 Hz can be achieved.

4. General theory of photon detectors

The photodetector is a slab of homogeneous semiconductor with the actual "electrical" area, A_e, that is coupled to a beam of infrared radiation by its optical area, A_o (Fig. 3). Usually, the optical and electrical areas of the device are the same or close. The use of optical concentrators can increase the A_o/A_e ratio.

The current responsivity of the photodetector is determined by the quantum efficiency, η, and by the photoelectric gain, g. The quantum efficiency value describes how well the detector is coupled to the radiation to be detected. It is usually defined

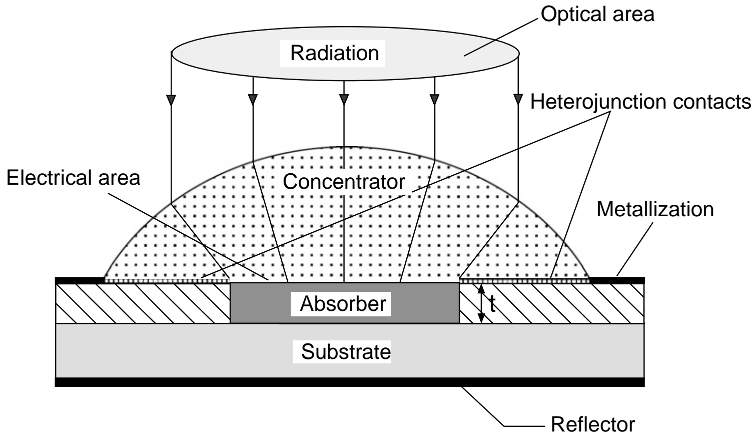

Fig. 3. Model of a photodetector.

as the number of electron–hole pairs generated per incident photon. The idea of photoconductive gain, g, was put forth by Rose [30] as a simplifying concept for the understanding of photoconductive phenomena and is now widely used in the field. The photoelectric gain is the number of carriers passing contacts per one generated pair. This value shows how well the generated electron–hole pairs are used to generate the current response of a photodetector. Both values are assumed here as constant over the volume of the device.

The spectral current responsivity is equal to

$$R_i = \frac{\lambda\eta}{hc} qg, \tag{1}$$

where λ is the wavelength, h is Planck's constant, c is the light velocity, and q is the electron charge. Assuming that the current gains for photocurrent and noise current are the same, the current noise due to generation and recombination processes is [30]

$$I_n^2 = 2(G + R)A_e t \Delta f q^2 g^2, \tag{2}$$

where G and R are the generation and recombination rates, Δf is the frequency band and t is the thickness of the detector.

Detectivity D^* is the main parameter characterizing normalized signal to noise performance of detectors and can be defined as

$$D^* = \frac{R_i (A_o \Delta f)^{1/2}}{I_n}. \tag{3}$$

According to Eqs. (1)–(3) [31]

$$D^* = \frac{\lambda}{hc}\left(\frac{A_o}{A_e}\right)^{1/2} \eta [2(G + R)t]^{-1/2}. \tag{4}$$

For a given wavelength and operating temperature, the highest performance can be obtained by maximising $\eta/[t(G + R)]^{1/2}$ which corresponds to the condition of the

highest ratio of the sheet optical generation to the square root of sheet thermal generation-recombination. This means that high quantum efficiency must be obtained with a thin device. For a given wavelength and operating temperature the performance can be optimised by reducing the total number of generation and recombination acts, which is $(G+R)(A_e t)$.

In further considerations we put that $A_o/A_e = 1$. Assuming a single pass of the radiation and negligible frontside and backside reflection coefficients, the quantum efficiency and detectivity are

$$\eta = 1 - \exp(-\alpha t), \tag{5}$$

$$D^* = \frac{\lambda}{hc}(1 - e^{-\alpha t})[2(G+R)t]^{-1/2}, \tag{6}$$

where α is the absorption coefficient.

The highest detectivity can be obtained for $t = 1.26/\alpha$ for which $(1—e^{\alpha t})t^{-1/2}$ achieves a maximum value of $0.62\alpha^{1/2}$. This thickness is the best compromise between the requirements of high quantum efficiency and low thermal generation. In this optimum case $\eta = 0.716$ and detectivity is equal to [31]

$$D^* = 0.45\frac{\lambda}{hc}\left(\frac{\alpha}{G+R}\right)^{1/2}. \tag{7}$$

To achieve a high performance, the thermal generation must be suppressed to possible the lowest level. This is usually done with cryogenic cooling of the detector. For practical purposes, the ideal situation occurs when the thermal generation is reduced below the optical generation.

At equilibrium the generation and recombination rates are equal, and we have

$$D^* = 0.31\frac{\lambda}{hc}\left(\frac{\alpha}{G}\right)^{1/2}. \tag{8}$$

Considerations carried out in Ref. [31] indicate, that for a double pass of radiation the detectivity of an optimised photodetector, lead to the following expression

$$D^* = 0.31\frac{\lambda}{hc}k\left(\frac{\alpha}{G}\right)^{1/2}, \tag{9}$$

where $1 \leqslant k \leqslant 2$ is dependent on the contribution of recombination and backside reflection.

The ratio of absorption coefficient to the thermal generation rate, α/G_{th}, is the fundamental figure of merit of any material for infrared photodetectors, which directly determines the detectivity limits of the devices. Any potential material should be compared on this basis.

Fig. 4 shows the measured intrinsic absorption coefficients for various narrow gap photodetector materials. The absorption coefficient and corresponding penetration depth vary among the different materials. It is well known that the absorption curve for direct transitions between parabolic bands at photon energy greater than energy gap, E_g, obeys a square-root law

$$\alpha(h\nu) = \beta(h\nu - E_g)^{1/2}, \tag{10}$$

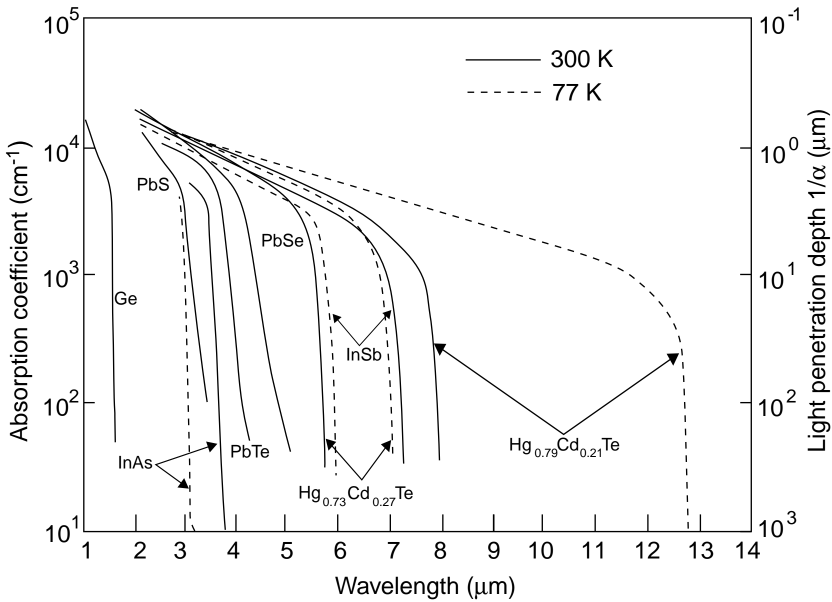

Fig. 4. Absorption coefficient for various photodetector materials in spectral range of 1–14 μm.

where β is a constant. As can be readily seen in Fig. 4, in MWIR spectral region, the absorption edge value changes between $2\times10^3\,\text{cm}^{-1}$ and $3\times10^3\,\text{cm}^{-1}$; in LWIR region is about $10^3\,\text{cm}^{-1}$.

Since α is a strong function of the wavelength, for a given semiconductor the wavelength range in which appreciate photocurrent can be generated is limited. Near the material's band gap, there is tremendous variation causing a three orders of magnitude variation in absorption. In the region of the material's maximum usable wavelength, the absorption efficiency drops dramatically. For wavelengths longer than cut-off wavelength, the values of α are too small to give appreciable absorption.

Fig. 5 shows the infrared absorption spectra for different *n*-doped, 50 period $GaAs/Al_xGa_{1-x}As$ QWIP structures measured at room temperatures using a 45° multipass waveguide geometry. The spectra of the bound-to-bound continuum (B–C) QWIP (samples A, B, and C) are much broader than the bound-to-bound (B–B) (sample E) or bound-to-quasibound (B–QB) QWIP (sample F). Correspondingly, the value of the absorption coefficient for the B–C QWIP is significantly lower than that of the B–B QWIP, due to conservation of oscillator strength. The values of the absorption coefficient at 77 K, peak wavelength λ_p, cutoff wavelength λ_c (long wavelength for which α drops to half-α_p), and spectral width $\Delta\lambda$ (full width at half-α_p) are given in Table 2. It appears, that the low-temperature absorption coefficient $\alpha_p(77\,\text{K})\approx1.3\alpha_p(300\,\text{K})$ and $\alpha_p(\Delta\lambda/\lambda)/N_D$ is a constant (N_D is the well's doping) [32]. Typical value of absorption coefficient in 77 K in LWIR region is between 600 and $800\,\text{cm}^{-1}$. Comparing Figs. 4 and 5 we can notice that the absorption coefficients for direct band-to-band absorption is higher than that for intersubband transitions.

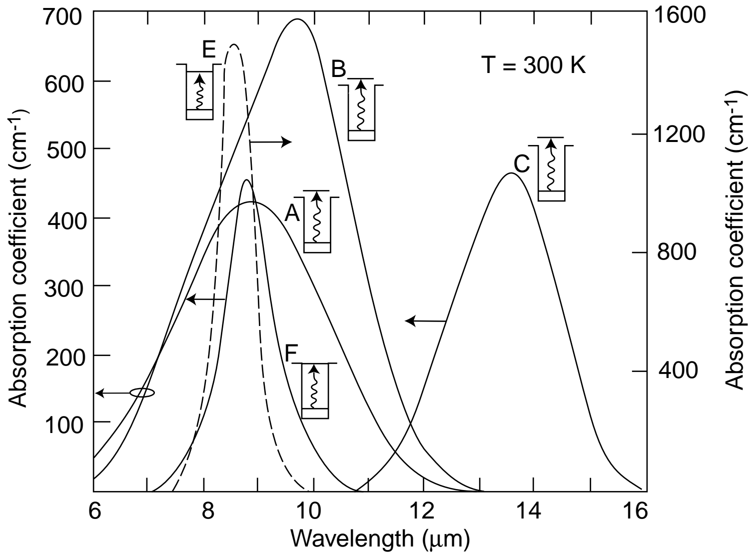

Fig. 5. Absorption coefficient spectra measured at $T = 300\,\mathrm{K}$ for different QWIP samples described in Table 2 after [32].

Table 2
Structure parameters for different n-doped, 50 period $Al_xGa_{1-x}As$ QWIP structures (after Ref. [32])

Sample	Well width (Å)	Barrier width (Å)	Composition x	Doping density (10^{18} cm^{-3})	Inter-subband transition	λ_p (µm)	λ_c (µm)	$\Delta\lambda$ (µm)	$\Delta\lambda/\lambda$ (%)	α_p (77 K) (cm^{-1})	η_a (77 K) (%)
A	40	500	0.26	1.0	B–C	9.0	10.3	3.0	33	410	13
B	40	500	0.25	1.6	B–C	9.7	10.9	2.9	30	670	19
C	60	500	0.15	0.5	B–C	13.5	14.5	2.1	16	450	14
E	50	500	0.26	0.42	B–B	8.6	9.0	0.75	9	1820	20
F	45	500	0.30	0.5	B–QB	7.75	8.15	0.85	11	875	14

The α/G_{th} ratio versus temperature for different types of tunable materials with hypothetical energy gap equal to 0.25 eV ($\lambda = 5\,\mu m$) and 0.124 eV ($\lambda = 10\,\mu m$) is shown in Figs. 6 and 7. It is apparent that HgCdTe is by far the most efficient detector of IR radiation; it is characterized by high absorption coefficient and relatively low thermal generation rate. We can also notice that QWIP is better material than extrinsic silicon. The above two figures are completed by Fig. 8, where the α/G_{th} ratio in dependence on wavelength is presented for different materials at 77 K.

An optimised photodetector should consist of [33]

- lightly doped active (base) region, which acts as an absorber of IR radiation. Its band gap E_g, doping and geometry should be selected,

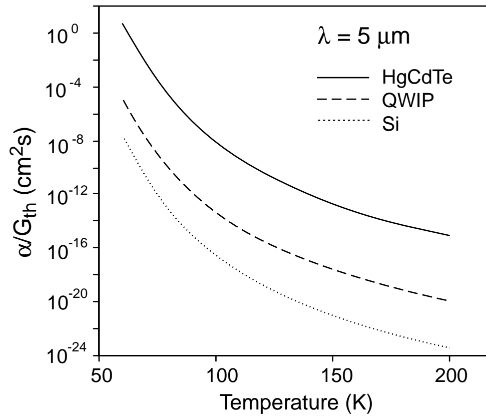

Fig. 6. α/G_{th} ratio versus temperature for MWIR ($\lambda_c = 5\,\mu$m) photon detectors.

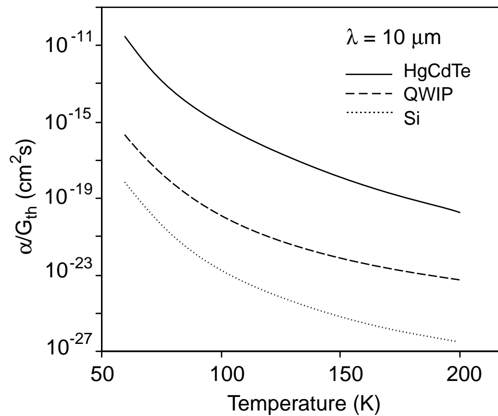

Fig. 7. α/G_{th} ratio versus temperature for LWIR ($\lambda_c = 10\,\mu$m) photon detectors.

- electric contacts to the base region, which sense optically generated charge carriers, should not contribute to the dark current of the device,
- surfaces of the absorber regions that must be insulated from the ambient by a material which also does not contribute to the generation of carriers; in addition, the carriers, which are optically generated in absorber, should be kept away from surfaces, where recombination can reduce the quantum efficiency, backside mirror for double pass of IR radiation.

The above conditions can be fulfilled using heterojunctions like N^+–p–p^+ and P^+–n–n^+ with heavily doped contact regions (symbol "+" denotes strong doping, capital letter—wider gap). Homojunction devices (like n–p, n^+–p, p^+–n) suffer from surface problems; excess thermal generation results in increased dark current and recombination, which reduces photocurrent.

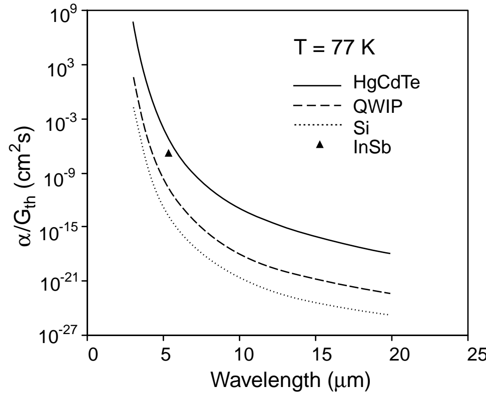

Fig. 8. α/G_{th} ratio versus cutoff wavelength for different types of photon detectors operated at 77 K.

To achieve a high performance, the thermal generation must be suppressed to possible the lowest level. This is usually done with cryogenic cooling of the detector. For practical purposes, the ideal situation occurs when the thermal generation is reduced below the optical generation. The requirements for thermal generation rate can be highly reduced in heterodyne systems, in which optical excitation by the local oscillator can dominate the generation, even for high thermal generation.

The total generation rate is a sum of the optical and thermal generation (Fig. 8)

$$G = G_{th} + G_{op}. \tag{10'}$$

The optical generation may be due to the signal or background radiation. For infrared detectors, usually background radiation is higher compared to the signal radiation. If the thermal generation is reduced much below the background level, the performance of the device is determined by the background radiation (BLIP conditions for Background Limited Infrared Photodetector). This condition can be described as

$$\frac{\eta \Phi_B \tau}{t} > n_{th}, \tag{11}$$

where n_{th} is the density of thermal carriers at the temperature T, and τ is the carrier lifetime, and Φ_B is the total background photon flux density (unit cm^{-2} s^{-1}) reaching the detector. Re-arranging we have for the BLIP requirements

$$G_{op} = \frac{\eta \Phi_B}{t} > \frac{n_{th}}{\tau} = G_{th}, \tag{12}$$

i.e. the photon generation rate per unit volume needs to be greater than the thermal generation rate per unit volume. The carriers can be either majority or minority in nature.

The direct bandgap semiconductor photodiode is a minority carrier device and in thermal equilibrium

$$n_{\min} = \frac{n_i^2}{n_{\text{maj}}}, \tag{13}$$

where n_i is the intrinsic carrier concentration, and n_{maj} is the majority carrier concentration. The ultimate limit on carrier lifetime in a direct gap semiconductor is given by band-to-band recombination, by either radiative or Auger processes. Humphreys inticated [34] that van Roosbroeck and Shockley theory of radiative recombination underestimates the radiative lifetime due to noiseless photon re-absorption. As a result, Auger recombination is the dominant process in narrow gap semiconductors like e.g., HgCdTe ternary alloy.

The extrinsic semiconductor photoconductor is strictly a majority carrier device.

The background limited detectivity, or so-called "photovoltaic" BLIP detectivity, is given by [35,36]

$$D^*_{\text{BLIP}} = \frac{\lambda}{hc}\left(\frac{\eta}{2\Phi_B}\right)^{1/2}. \tag{14}$$

D^*_{BLIP} for photoconductors is $\sqrt{2}$ times lower that for photodiodes. This is attributable to the recombination process in photoconductors, which is uncorrelated with the generation process, which contributes to the detector noise. The background photon flux density received by the detector depends on its angular field of view (FOV) of the background and on its ability to respond to the wavelengths contained in this source. Plots of D^*_{BLIP} as a function of wavelength for $T_{\text{BLIP}} = 300\,\text{K}$ and for full 2π FOV are shown in Fig. 2.

BLIP temperature is defined that the device is operating at a temperature at which the dark current equals the background photocurrent, given a FOV, and a background temperature. In Fig. 9, plots of the calculated temperature required for background limited operation in 30° FOV are shown as a function of cutoff wavelength. We can see that the operating temperature of "bulk" intrinsic IR detectors (HgCdTe and PbSnTe) is higher than for other types of photon detectors. HgCdTe detectors with background limited performance operate with thermoelectric coolers in the MWIR range, instead the LWIR detectors ($8 \leqslant \lambda_c \leqslant 12\,\mu\text{m}$) operate at $\approx 100\,\text{K}$. HgCdTe photodiodes exhibit higher operating temperature compared to extrinsic detectors, silicide Schottky barriers and QWIPs. However, the cooling requirements for QWIPs with cutoff wavelengths below $10\,\mu\text{m}$ are less stringent in comparison with extrinsic detectors and Schottky barrier devices.

5. General theory of thermal detectors

Thermal detectors operate on a simple principle, that when heated by incoming IR radiation their temperature increases and the temperature changes are measured by any temperature-dependent mechanism, such as thermoelectric voltage, resistance, pyroelectric voltage. The simplest representation of the thermal detector is shown in

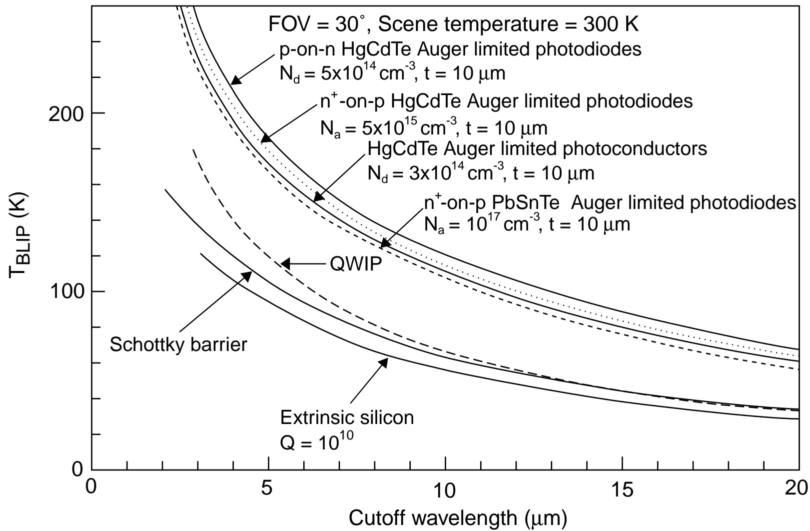

Fig. 9. Estimation of the temperature required for background limited operation of different types of photon detectors. In the calculations FOV = 30° and $T_B = 300$ K are assumed (after Ref. [37]).

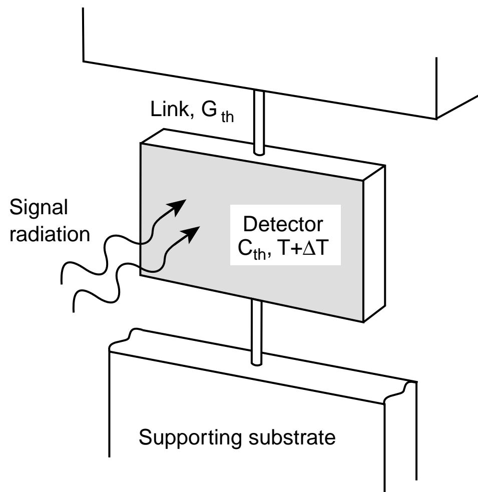

Fig. 10. Thermal detector mounted via lags to heat sink.

Fig. 10. The detector is represented by the thermal capacitance C_{th} coupled via the thermal conductance G_{th} to a heat sink at the constant temperature T. In the absence of a radiation input, the average temperature of the detector will be also T, although it will exhibit a fluctuation about this value. When a radiation input is received by the detector, the rise in temperature is found by solving the heat balance equation.

Assuming the radiant power to be a periodic function, the change in temperature of any thermal detector due to incident radiative flux is [35,38]

$$\Delta T = \frac{\varepsilon \Phi_o}{(G_{th}^2 + \omega^2 C_{th}^2)^{1/2}}. \tag{15}$$

Eq. (15) illustrates several features of thermal detector. Clearly it is advantageous to make ΔT as large as possible. To do this, the thermal capacity of the detector (C_{th}) and its thermal coupling to its surroundings (G_{th}) must be as small as possible. The interaction of the thermal detector with the incident radiation should be optimised while reducing, as far as possible, all other thermal contacts with its surroundings. This means that a small detector mass and fine connecting wires to the heat sink are desirable.

A characteristic thermal response time for the detector can therefore be defined as

$$\tau_{th} = \frac{C_{th}}{G_{th}} = C_{th} R_{th}, \tag{16}$$

where $R_{th} = 1/G_{th}$ is the thermal resistance.

Typical value of thermal time constant is in the millisecond range. This is much longer than the typical time of a photon detector. There is a trade-off between sensitivity, ΔT, and frequency response. If one wants a high sensitivity, then a low frequency response is forced upon the detector.

For further discussion we introduce the coefficient $K = \Delta V/\Delta T$, which reflects how good the temperature changes translates into the electrical output voltage of detector.

The voltage responsivity, R_v, of the detector is the ratio of the output signal voltage ΔV to the input radiation power and is given by

$$R_v = \frac{K \varepsilon R_{th}}{(1 + \omega^2 \tau_{th}^2)^{1/2}}. \tag{17}$$

In order to determine the detectivity of the detector, it is necessary to define a noise mechanism. One major noise is Johnson noise. Two other fundamental noise sources are important for assessing the ultimate performance of a detector: thermal fluctuation noise and background fluctuation noise.

Thermal fluctuation noise arises from temperature fluctuations in the detector. These fluctuations are caused by heat conductance variations between the detector and the surrounding substrate with which the detector element is in thermal contact.

The spectral noise voltage due to temperature fluctuations is [35,38]

$$V_{th}^2 = \frac{4kT^2 \Delta f}{1 + \omega^2 \tau_{th}^2} K^2 R_{th}. \tag{18}$$

A third noise source is background noise that results from radiative heat exchange between the detector at the temperature T_d and the surrounding environment at the temperature T_b that is being observed. It is the ultimate limit of a detector's

performance capability and is given for a 2π FOV by [35,38]

$$V_b^2 = \frac{8k\varepsilon\sigma A(T_d^2 + T_b^2)}{1 + \omega^2\tau_{th}^2} K^2 R_{th}^2, \tag{19}$$

where σ is the Stefan-Boltzmann constant.

The fundamental limit to the sensitivity of any thermal detector is set by temperature fluctuation noise, i.e., random fluctuations in the temperature of the detector element due to fluctuations in the radiant power exchange between the detector and its surroundings. Under this condition at low frequencies ($\omega \ll 1/\tau_{th}$) results

$$D_{th}^* = \left(\frac{\varepsilon^2 A}{4kT_d^2 G_{th}}\right)^{1/2}. \tag{20}$$

It is assumed here that ε is independent of wavelength, so that the spectral D_λ^* and blackbody $D^*(T)$ values are identical.

If radiant power exchange is the dominant heat exchange mechanism, then G is the first derivative with respect to temperature of the Stefan-Boltzmann function. In that case, known as the background fluctuation noise limit, we have

$$D_b^* = \left[\frac{\varepsilon}{8k\sigma(T_d^5 + T_b^5)}\right]^{1/2}. \tag{21}$$

Note that D_b^* is independent of A, as is to be expected.

Eqs. (20) and (21) assume that background radiation falls upon the detector from all directions when the detector and background temperature are equal, and from the forward hemisphere only when the detector is at cryogenic temperatures. The highest possible D^* to be expected for a thermal detector operated at room temperature and viewing a backgrounds at room temperature is $1.98 \times 10^{10}\,\mathrm{cmHz^{1/2}W^{-1}}$. Even if the detector or background, not both, were cooled to absolute zero, the detectivity would improve only by the square root of two. This is basic limitation of all thermal detectors. The background noise limited photon detectors have higher detectivities as a result of their limited spectral responses.

The performance achieved by any real detector will be inferior to that predicted by Eq. (21). The degradation of performance will arise from:

- encapsulation of detector (reflection and absorption losses at the window),
- effects of excess thermal conductance (influence of electrical contacts, conduction through the supports, influence of any gas—conduction and convection),
- additional noise sources.

Typical values of detectivities of thermal detectors at 10 Hz change in the range between 10^8 and $10^9\,\mathrm{cmHz^{1/2}W^{-1}}$.

6. Comparison of fundamental limits of photon and thermal detectors

The temperature dependence of the fundamental limits of D^* of photon and thermal detectors for different levels of background are shown in Figs. 11 and 12.

It results from Fig. 11 that in LWIR spectral range, the performance of intrinsic IR detectors (HgCdTe photodiodes) is higher than for other types of photon detectors. HgCdTe photodiodes with background limited performance operate at temperature below ≈ 80 K. HgCdTe is characterized by high optical absorption coefficient and quantum efficiency and relatively low thermal generation rate compared to extrinsic detectors and QWIPs. The extrinsic photon detectors require more cooling than intrinsic photon detectors having the same long wavelength limit.

The theoretical detectivity value for the thermal detectors is much less temperature dependent than for the photon detectors. At temperatures below 50 K and zero background, LWIR thermal detectors are characterized by D^* values lower that those of LWIR photon detectors. However, at temperatures above 60 K, the limits favour the thermal detectors. At room temperature, the performance of thermal detectors is much better than LWIR photon detectors. The above relations are modified by influence of background, what is shown in Fig. 11 for a background of 10^{17} photons cm^{-2} s^{-1}. It is interesting to notice, that the theoretical curves of D^* for photon and thermal detectors show similar fundamental limits at low temperatures.

Similar considerations have been carried out for VLWIR detectors operated in the 14–50 μm spectral range. The calculation results are presented in Fig. 12. Detectors operating within this range are cryogenic Si and Ge extrinsic photoconductors and cryogenic thermal detectors, usually bolometers. Nevertheless, in Fig. 12, theoretical prediction for intrinsic detectors (HgCdTe photodiodes) is also included. Fig. 12 shows that the theoretical performance limit of VLWIR thermal detectors at zero

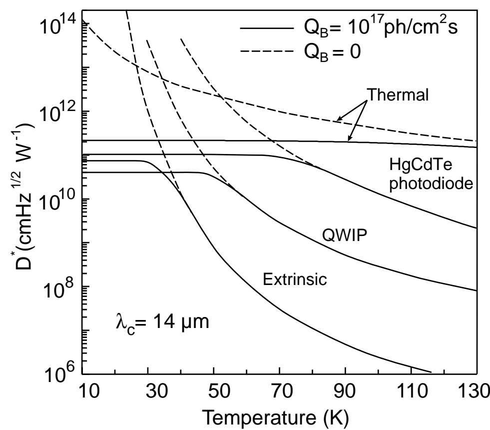

Fig. 11. Theoretical performance limits of LWIR photon and thermal detectors at wavelength 14 μm, zero background and background of 10^{17} photons cm^{-2} s^{-1}, as a function of detector temperature (after Ref. [39]).

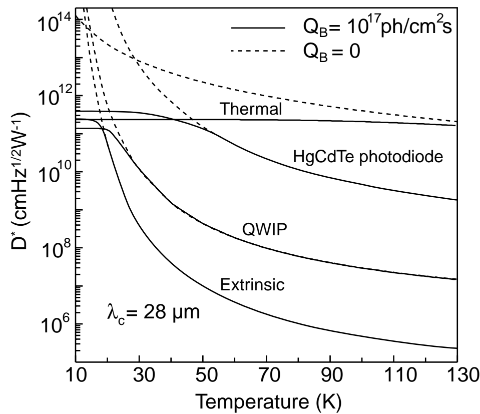

Fig. 12. Theoretical performance limits of VLWIR photon and thermal detectors at wavelength 28 μm, zero background and background of 10^{17} photons cm^{-2} s^{-1}, as a function of detector temperature (after Ref. [39]).

and high backgrounds in wide range of temperature equals or exceeds that of photon detectors.

The comparison of both types of detectors indicates that theoretical performance limits for thermal detectors are more favourable as wavelength of operation moves from the LWIR to the VLWIR. It is due to influence of fundamental different types of noise (generation-recombination noise in photon detectors and temperature fluctuation noise in thermal detectors), these two classes of detectors have different dependencies of detectivities on wavelength and temperature. The photon detectors are favoured at long wavelength infrared and lower operating temperatures. The thermal detectors are favoured at very long wavelength spectral range. The temperature requirements to attain background fluctuation noise performance in general favour thermal detectors at the higher cryogenic temperatures and photon detectors at the lower cryogenic temperatures.

7. Focal plane arrays

There are many important military and civilian applications of IR FPAs, which are frequently called "dual technology applications." Lately, one should point out the growing utilisation of IR technologies in the civilian sphere at the expense of new materials and technologies and also the noticeable price decrease in these high cost technologies. Demands to use these technologies are quickly growing due to their effective applications, e.g., in global monitoring of environmental pollution and climate changes, long time prognoses of agriculture crop yield, chemical process monitoring, Fourier transform IR spectroscopy, IR astronomy, car driving, IR imaging in medical diagnostics, and others. Traditionally, IR technologies are connected with controlling functions and night vision problems with earlier applications connected simply with detection of IR radiation, and later by forming

IR images form temperature and emissivity differences (systems for recognition and surveillance, tank sight systems, anti-tank missiles, air–air missiles).

7.1. FPA architectures

Two families of multielement detectors can be considered; one used for scanning systems and the other used for staring systems. The simplest scanning linear FPA consists of a row of detectors [Fig. 13(a)]. An image is generated by scanning the scene across the strip using, as a rule, a mechanical scanner. At standard video frame rates, at each pixel (detector) a short integration time has been applied and the total charges are accommodated. A staring array is a 2-D array of detector pixels [Fig. 4(b)] which are scanned electronically. These types of arrays can provide enhanced sensitivity and gain in camera weight.

The scanning system, which does not include multiplexing functions in the focal plane, belongs to the first generation systems. A typical example of this kind of detector is a linear photoconductive array (PbS, PbSe, HgCdTe) in which an electrical contact for each element of a multielement array is brought off the cryogenically-cooled focal plane to the outside, where there is one electronic channel at ambient temperature for each detector element. The US common module HgCdTe arrays employ 60, 120 or 180 photoconductive elements depending on the application.

The second generation systems (full-framing systems), which are at present being developed, have at least three orders of magnitude more elements ($>10^6$) on the focal plane than first generation systems and the detectors elements are configured in a 2-D array. These staring arrays are scanned electronically by circuits integrated

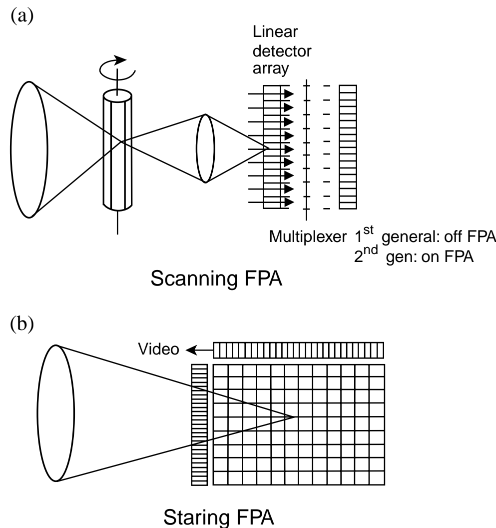

Fig. 13. (a) Scanning focal plane array and (b) staring focal plane array.

with the arrays. These readout integrated circuits (ROICs) include, e.g., pixel deselecting, antiblooming on each pixel, subframe imaging, output preamplifiers, and some other functions.

Intermediary systems are also fabricated with multiplexed scanned photodetector linear arrays in use and with, as a rule, time delay and integration (TDI) functions. Typical examples of these systems are HgCdTe multilinear 288×4 arrays fabricated by Sofradir both for 3–5-μm and 8–10.5-μm bands with signal processing in the focal plane (photocurrent integration, skimming, partitioning, TDI function, output preamplification and some others).

A number of architectures are used in the development of IR FPAs [40]. In general, they may be classified as hybrid and monolithic, but these distinctions are often not as important as proponents and critics state them to be. The central design questions involve performance advantages versus ultimate producibility. Each application may favour a different approach depending on the technical requirements, projected costs and schedule.

Hybrid FPAs detectors and multiplexers are fabricated on different substrates and mated with each other by flip-chip bonding or loophole interconnection (Fig. 14). First demonstration in the mid-1970s, indium bump bonding of readout electronics provides for multiplexing the signals from thousands pixels onto a few output lines, greatly simplifying the interface between the vacuum-enclosed cryogenic sensor and the system electronics. Two hybridization approaches are in use today. In one approach, indium bumps are formed on both the detector array and the ROIC chip. The array and the ROIC are aligned and force is applied to cause the indium bumps to cold-weld together. In the other approach, indium bumps are formed only on the ROIC; the detector array is brought into alignment and proximity with the ROIC, the temperature is raised to cause the indium to melt, and contact is made by reflow. Today, millions of pixels are connected to millions of amplifiers/integrators in the unit cells of readout circuits. In this case we can optimise the detector material and multiplexer independently. Other advantages of the hybrid FPAs are near 100% fill factors and increased signal-processing area on the multiplexer chip.

The detector array can be illuminated from either the frontside (with the photons passing through the transparent silicon multiplexer) or backside (with photons passing through the transparent detector array substrate). In general, the latter approach is most advantageous, as the multiplexer will typically have areas of metallizations and other opaque regions, which can reduce the effective optical area of the structure. In HgCdTe hybrid FPAs, photovoltaic detectors are formed on thin HgCdTe epitaxial layers on transparent CdTe or CdZnTe substrates. For HgCdTe flip-chip hybrid technology, the maximum chip size is of the order of 10-mm^2. To overcome this problem, PACE (producible alternative to CdTe for epitaxy) technology is being developed with sapphire or silicon as the substrate of HgCdTe detectors. A SWIR 1024×1024 element HgCdTe hybrid FPA was developed using the PACE technology [41]. When using opaque materials, substrates must be thinned to 10–20 μm to obtain sufficient quantum efficiencies and reduce crosstalk. In the “indirect” backside illuminated configuration both the detector array and the silicon ROIC chip are bump mounted side-by-side onto a common circuit board. The

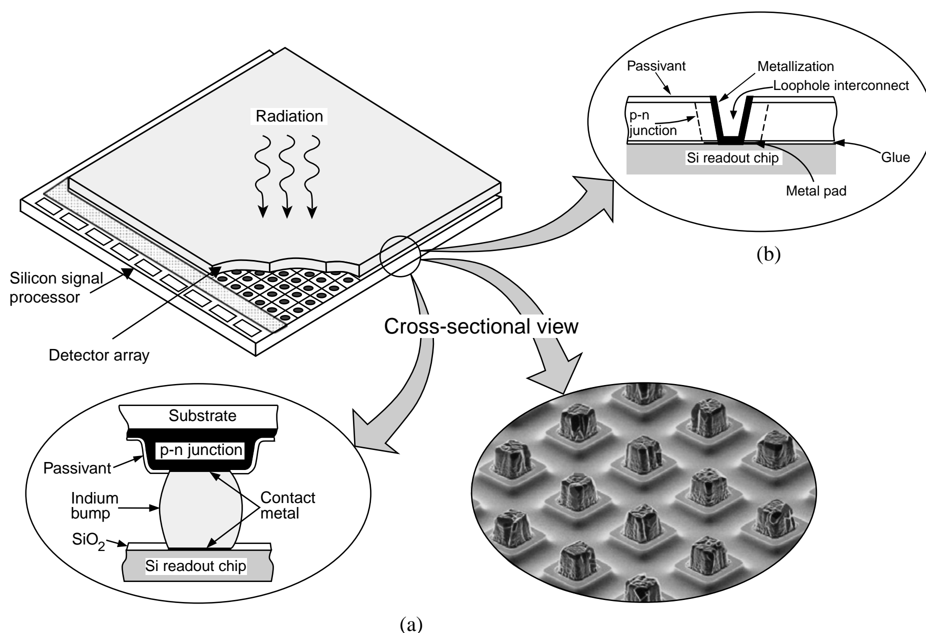

Fig. 14. Hybrid IR FPA with independently optimised signal detection and readout: (a) indium bump technique, (b) loophole technique.

"indirect" configuration allows the unit cell area in the silicon ROIC to be larger than the detector area and is usually used for small scanning FPAs, where stray capacitance is not an issue.

In the loophole interconnection, the detector and the multiplexer chips are glued together to form a single chip before detector fabrication [42]. The photovoltaic detector is formed by ion implantation and loopholes are drilled by ion-milling and electrical interconnection between each detector and its corresponding input circuit is made through a small hole formed in each detector. The junctions are connected down to the silicon circuit by cutting the fine, few μm in diameter holes through the junctions by ion milling, and then backfilling the holes with metallization. The thermal expansion mismatch problem is approached by using about 10-μm thick p-type HgCdTe, bonded rigidly to the silicon so that strain is taken up elastically. This makes the devices mechanically and electrically very robust with contact obscuration typically less than 10%. The disadvantages include the necessity of mechanical thinning of the HgCdTe, which may lead to damage that may affect photodiode performance and the necessity of devising clever low-temperature techniques for junction formation and passivation because of the presence of the epoxy (e.g., the ion milling process to form the *n*-type regions is done at room temperature). A similar type of hybrid technology called VIMS (vertically integrated metal–insulator–semiconductor) was reported by DRS Infrared Technologies (former Texas Instruments).

In the monolithic approach, some of the multiplexing is done in the detector material itself rather than in an external readout circuit. The basic element of a monolithic array is a metal–insulator–semiconductor (MIS) structure as shown in Fig. 15(c). Used as part of a charge transfer device, a MIS capacitor detects and integrates the IR-generated photocurrent. Although most IR imaging applications tend to require high charge handling capabilities in the unit cells, an MIS capacitor fabricated in a narrow-gap semiconductor material (e.g., HgCdTe and InSb) has a limited charge capacity because of its low background potential as well as more severe problems involving noise, tunnelling effects and charge trapping when shifting charge through the narrow bandgap CCD to accomplish the readout function. Because of the non-equilibrium operation of the MIS detector, much larger electric fields are set up in the depletion region than in the p–n junction, resulting in

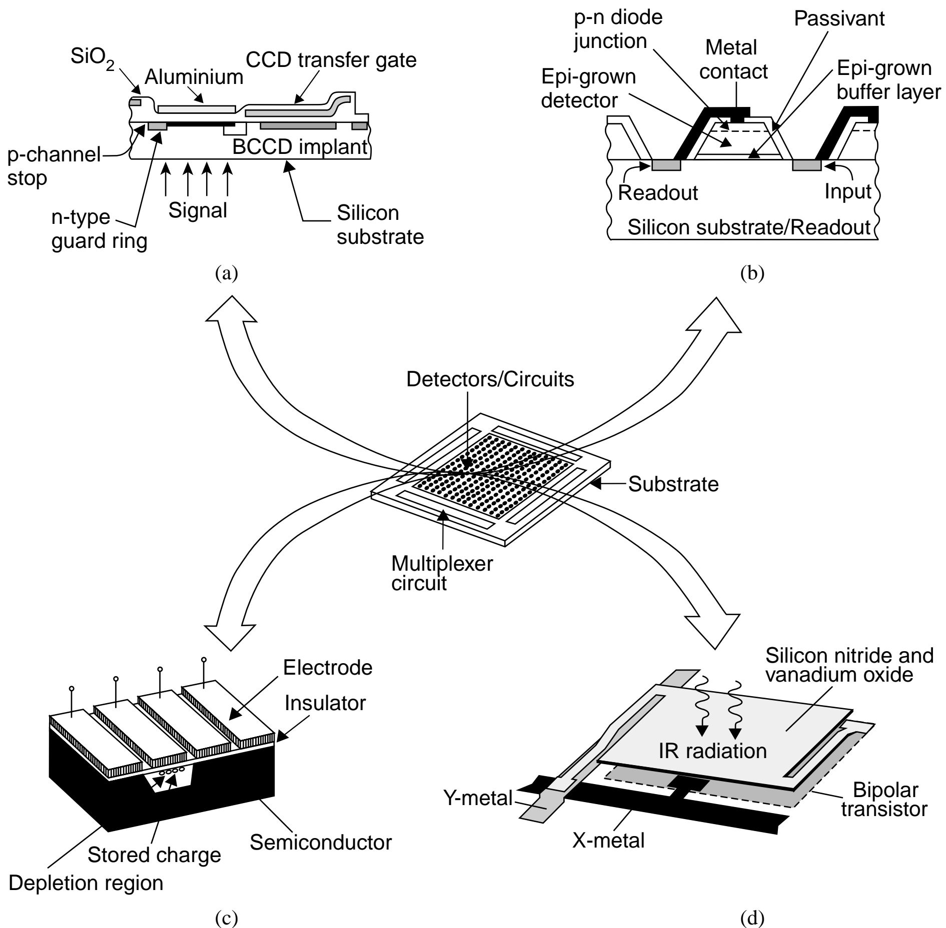

Fig. 15. Monolithic IR FPAs: (a) all-silicon; (b) heteroepitaxy-on-silicon; (c) non-silicon (e.g., HgCdTe CCD); (d) microbolometer.

defect-related tunnelling current that is orders of magnitude larger than the fundamental dark current. The MIS detector required much higher material quality than p–n junction detectors, which still has not been achieved. For this reason, all development of HgCdTe MIS detector was abandoned around 1987. So, although efforts have been made to develop monolithic FPAs using narrow-gap semiconductors, silicon based FPA technology with Schottky-barrier detectors is the only technology, which has matured to a level of practical use. An example of a fully monolithic silicon unit cell design is shown in Fig. 15(a). Several PtSi Schottky barrier FPAs with full TV resolution have been commercially available, and a 1040×1040 element array was reported [43]. As the production of Schottky-barrier FPAs is fully compatible with silicon VLSI technology, this technology offers the cost-effective and producible FPA.

Thermal detectors, which are relative newcomers, are narrowing the gap with photon detectors with respect to numbers of detectors per chip. IR FPAs have nominally the same growth rate as dynamic random access memory (RAM) integrated circuits (ICs) (which have had a doubling rate of approximately 18 months; it is a consequence of Moore's Law, which predicts the ability to double transistor integration on each IC about every 18 months) but lag behind in size by about 5–10 years. ROICs are somewhat analogous to dynamic RAM—only readouts, requiring a minimum of three transistors per pixel compared to one per memory cell. Readouts are also analogous in terms of an emphasis on low noise inputs and generally maximum charge storage capacity. Over the last decade, dramatic improvements in detector and readout technology have resulted in a 200-fold increase in the size of the largest FPAs. Consequently, whereas various 64×64 FPAs were available in the early 1980s, several vendors are now producing monolithic FPAs in TV-compatible 1040×1040 formats. Fig. 16 illustrates the trend in array size over the past 25 years and some projections of what will evolve in the coming decade. Rockwell has developed the world's largest HgCdTe short wavelength IR (SWIR) FPA for astronomy and low background applications [45]. The format of the device is a hybrid 2048×2048 with a unit cell size of 18-μm × 18-μm. Table 3 contains a description of representative IR FPAs that are commercially available as standard products and/or catalogue items from the major manufactures.

Since the IR wavelengths are of the order of micrometers, pixel sizes ultimately will not be driven bellow about 5 μm. Hybrid technology has only demonstrated pixel sizes as small as 17–18 μm. To fit into the present die silicon size order of 20 mm, a 2048×2048 array would have to have pixels smaller than 10 μm. A significant impediment to large array size progression is the field size of silicon foundry mask aligners. Very large readouts will have to be built with field stitching, where only a quadrant of the device is printed with each mask step [45]. Fortunately, the step accuracy is so good that this approach should be successful.

The development of IR FPAs using IC techniques together with development of new material growth techniques and microelectronic innovations began about 20 years ago. The combination of the last two techniques gives many new possibilities for IR systems with increased sensitivity and spatial resolution. Moreover, a number

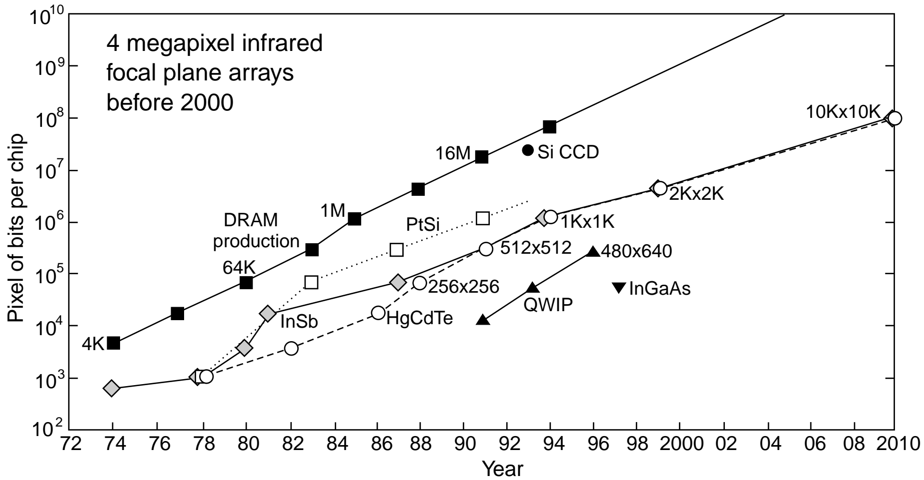

Fig. 16. Increase in array format size over the past 25 years and projections for the coming decade. PtSi, InSb and HgCdTe have been following the pace of dynamic RAM, offset by about a decade. QWIP detectors have been recently reported in sizes as large as 640×480 pixels (after Ref. [44]).

of other important advantages are accrued in terms of simplicity, reliability and reduced costs. Ten years ago, high quality single element detectors often were priced over \$2000, but now some current IR FPA production costs are less than \$0.1 per detector, and even greater reductions are expected in the near future. As the commercial market for uncooled imagers expand, the cost of commercial systems will inevitably decrease. At present, the cost of 320×240, $50 \times 50\,\mu m^2$, bolometer arrays for thermal imagers is \$15 000–20 000.

Two generic types of silicon addressing circuits have been developed: CCDs and complementary metal-oxide-semiconductor (CMOS) switches. CCD technology is used for not very large scale arrays and their technology is more complicated compared to the CMOS production line.

7.2. CCD and CMOS architectures

CCD technology is very mature with respect to fabrication yield and attainment of near-theoretical sensitivity. Fig. 17 shows the schematic circuit for a typical CCD imager. The photogenerated carriers are first integrated in the well formed by a photogate and subsequently transferred to slow and fast CCD shift registers. Then, the charge is converted to a voltage at a sense node usually formed by a floating diffusion typically having about 12 fF capacitance [46]. Both the photovoltage and floating diffusion's reset voltage are serially read to suppress and sense the node's reset noise and the output buffer's 1/f noise via off-chip correlated double sampling (CDS). The dominant sources of read noise after CDS include the wideband noise of the output amplifier and excess noise of the video electronics. Both are minimised by minimising the sense node capacitance and thereby maximising the conversion gain.

Table 3
Representative IR FPAs offered by some major manufactures

Manufacturer/web site	Size/architecture	Pixel size (μm)	Detector material	Spectral range (μm)	Oper. temp. (K)	$D^*(\lambda_p)$ ($cmHz^{1/2}/W$)/ NETD (mK)
Raytheon/www.raytheon.com	256×256/H	30×30	InSb	1–5.5	10–77	
	1024×1024/H	27×27	InSb	0.6–5.0	35	
	320×240/H	50×50	Si:As BIB	2–28	4–10	
	128×128/H	40×40	HgCdTe	9–11	80	
	256×256/H	30×30	HgCdTe	8.5–11	77–100	
	320×240/M	48×48	VO_x(bolometer)	8–14	300	50
	328×245/H	35×35	Pyro (BST)	8–14	300	>50
Rockwell/Boeing/www.boeing.com www.rsc.rockwell.com	256×256/H	40×40	HgCdTe	>15	77	
	640×480/H	27×27	HgCdTe	>10	77	
	225×256/H	40×40	HgCdTe	1–4.6	120	>10
	640×480/H	27×27	HgCdTe	1–4.6	120	>25
	2048×2048/H	18×18	HgCdTe	1–2.5	95–120	$>1\times10^{14}$
	320×240/M	48×48	VO_x(bolometer)	8–14	300	50
Mitsubishi/www.mitsubishi-imaging.com	256×256/M	52×40	PtSi	3–5	77	0.036
	512×512/M	26×20	PtSi	3–5	77	0.033
	1024×1024/M	17×17	PtSi	3–5	77	0.10
BAE Systems	256×256/H	30×30	HgCdTe	1–10	80	
	432×432/H		HgCdTe	1–5	80	
	640×480/M	28×28	VO_x(bolometer)	8–14	≈300	60
Sofradir/infrared.sofradir.com	128×128/H	50×50	HgCdTe	7.7–10	80	1.1×10^{11}/10
	128×128/H	50×50	HgCdTe	3.7–4.8	90	4.3×10^{11}/7
	128×128/H	50×50	HgCdTe	2.5–4.2	195	7.5×10^{11}/36
	320×240/H	30×30	HgCdTe	3.7–4.8	120	1.0×10^{12}/8
	320×240/M	45×45	Amorphous Si(bolometer)	8–14	–20 to 60°C	80

Table 3 (*continued*)

Manufacturer/web site	Size/architecture	Pixel size (μm)	Detector material	Spectral range (μm)	Oper. temp. (K)	$D^*(\lambda_p)$ ($cmHz^{1/2}/W$)/ NETD (mK)
Sarnoff/www.sarnoff.com	320 × 244/M	23 × 32	PtSi	1–5	77	
	640 × 480/M	24 × 24	PtSi	1–5	77	
Eastman-Kodak/www.kodak.com	486 × 640/M	25 × 25	PtSi	1–5	77	
Marconi/www.gec-marconi.com/infra-red/	128 × 128/H	50 × 50	HgCdTe	8–12	77	
	384 × 288/H	30 × 30	HgCdTe	3–5	80	15
	256 × 128/H	56 × 56	Pyro (PST)	8–14	≈300	90
	384 × 288/H	40 × 40	Pyro (PST)	8–14	≈300	130
AEG/www.aeg.com/e_produkte.htm	256 × 256/M	24 × 24	PtSi	3–5	77	75
	486 × 640/M	24 × 24	PtSi	3–5	77	70
	256 × 256/H	40 × 40	HgCdTe	8–10	80	20
	640 × 512/H	24 × 24	HgCdTe	3–5	80	20
	256 × 256/H	40 × 40	QWIP	8–10	60	10
	640 × 512/H	24 × 24	QWIP	8–10	60	20
JPL/www.jpl.nasa.gow	128 × 128/H	50 × 50	QWP	15 (λ_c)	45	30
	256 × 256/H	38 × 38	QWIP	9 (λ_c)	70	40
	640 × 486/H	18 × 18	QWIP	9 (λ_c)	70	36
Sensors Unlimited/www.sensorsinc.com	128 × 128/H	60 × 60	InGaAs	0.9–1.7	300	$>10^{13}$
	320 × 240/H	40 × 40	InGaAs	0.9–1.7	300	$>10^{12}$

H—hybrid, M—monolithic.

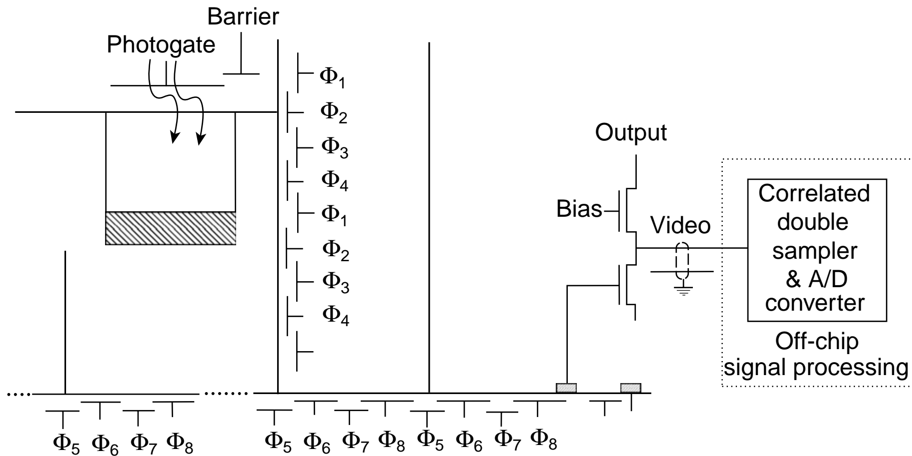

Fig. 17. Architecture of typical CCD imager (after Ref. [46]).

To minimise the capacitance various schemes are used, e.g., double stage amplifiers and alternative sense node implementation.

An attractive alternative to the CCD readout is coordinative addressing with CMOS switches. Hybrid IR FPAs have used CMOS readouts since ~1985 for low-noise readout of photo-generated signals. A typical CMOS multiplexer architecture (see Fig. 18) consists of fast (column) and slow (row) shift registers at the edges of the active area, and pixels are addressed one by one through the selection of a slow register, while the fast register scans through a column, and so on. Each photodiode is connected in parallel to a storage capacitor located in the unit cell. A column of diodes and storage capacitors is selected one at a time by a digital horizontal scan register and a row bus is selected by the vertical scan register. Therefore, each pixel can be individually addressed.

CMOS multiplexers are the best choice to perform the integration and signal processing for 2-D arrays. The advantages of CMOS are that existing foundries, which fabricate application specific integrated circuits, can be readily used by adapting their design rules. Design rules of 0.25 μm are in production with pre-production runs of 0.18 μm design rules. As a result of such fine design rules, more functionality has been put into the unit cells of IR and visible multiplexers and smaller unit cells, leading to large array sizes. Fig. 19 shows the timelines for minimum circuit features and the resulting CCD, IR FPA and CMOS visible imager sizes with respect to imaging pixels. Along the horizontal axis is also a scale depicting the general availability of various MOS and CMOS processes. The ongoing migration to even finer lithographies will thus enable the rapid development of CMOS-based imagers having even higher resolution, better image quality, higher levels of integration and lower overall imaging system cost than CCD-based solutions. At present, CMOS with minimum features of $\leqslant$0.5 μm is also enabling monolithic visible CMOS imagers, because the denser photolithography allows low-noise signal extraction and high performance detection with the optical fill

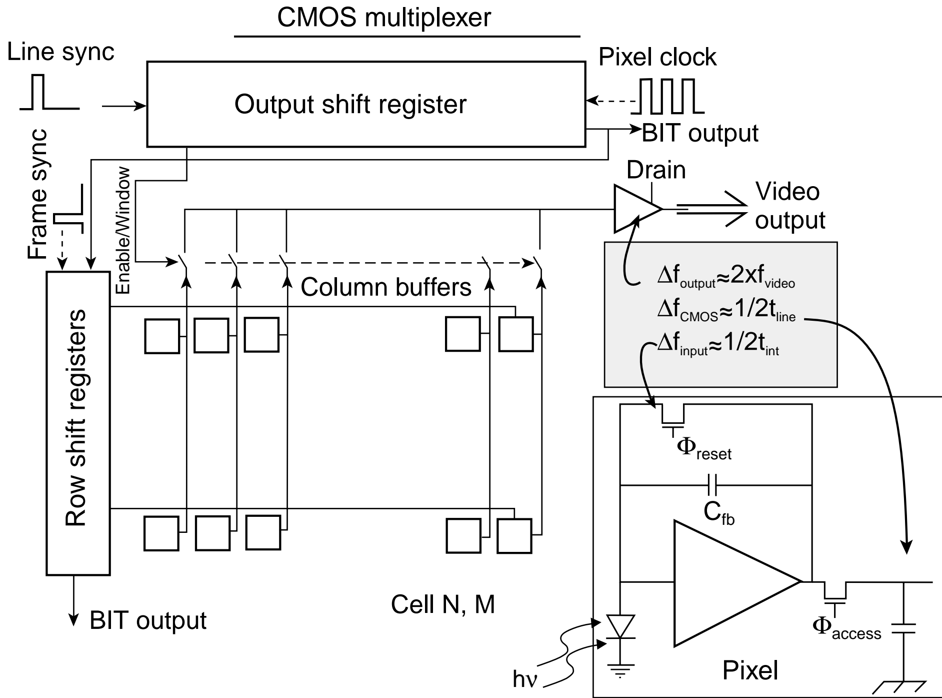

Fig. 18. CMOS multiplexing readout with CTIA detector interface (after Ref. [47]).

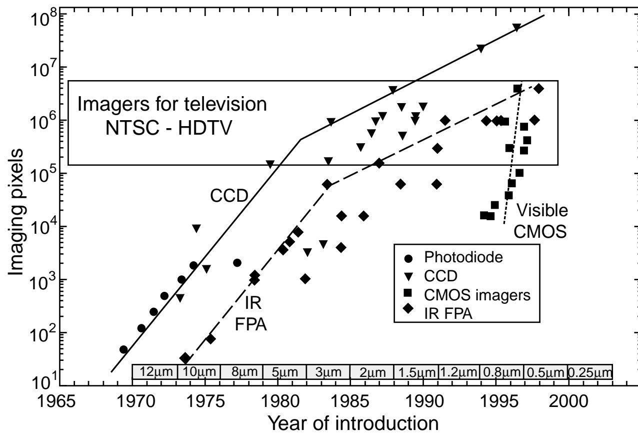

Fig. 19. Chronology of imager pixel count (CCD, IR FPA and CMOS). The timeline design rules are shown at the bottom (after Ref. [46]).

factor within each pixel [47]. The silicon wafer production infrastructure which has put personal computers into many homes is now enabling CMOS-based imaging in consumer products such as video and digital still cameras.

In comparison with CCDs, the MOS multiplexers exhibit important advantages due to high circuit density, fewer drive voltages, fewer clocks, much lower voltages and packing density compatible with many more special functions. The minimum theoretical read noise of a CCD is limited in large imagers by the output amplifier's thermal noise after CDS is applied in off-chip support circuits. The alternative CMOS paradigm offers lower temporal noise because the relevant noise bandwidth is fundamentally several orders of magnitude smaller and better matches the signal bandwidth. While CCD sensitivity is constrained by the limited design space involving the sense node and the output buffer, CMOS sensitivity is limited only by the desired dynamic range and operating voltage. CMOS-based imagers also offer practical advantages with respect to on-chip integration of camera functions including command and control electronics, digitisation and image processing. CMOS is now suitable also for TDI-type multiplexers because of the availability from foundries of design rules lower than 1.0 μm, more uniform electrical characteristics and lower noise figures.

7.3. Passive and active pixel sensors

CMOS-based imagers for both IR and visible applications use active or passive pixels [46–50] as shown, in simplified form, in Fig. 20. In comparison with passive pixel sensors (PPSs), active pixel sensors (APSs) apart from read functions exploit some form of amplification at each pixel. PPSs have simple pixels consisting of as few as two components (a photodiode and a MOSFET switch). As a result, circuit overhead is low and the optical collection efficiency [fill factor (FF)] is high even for monolithic devices. A large optical FF of up to 80% maximises signal selection and minimises fabrication cost by obviating the need for microlenses. Microlenses, typically used in CCD and CMOS APS imagers for visible application, concentrate the incoming light into the photosensitive region when they are accurately deposited over each pixel (see Fig. 21). When the FF is low and microlenses are not used, the light falling elsewhere is either lost or, in some cases, creates artifacts in the imagery by generating electrical currents in the active circuitry.

APSs incorporate transistors in each pixel to convert the photo-generated charge to a voltage, amplify the signal voltage and reduce noise. Adding these components,

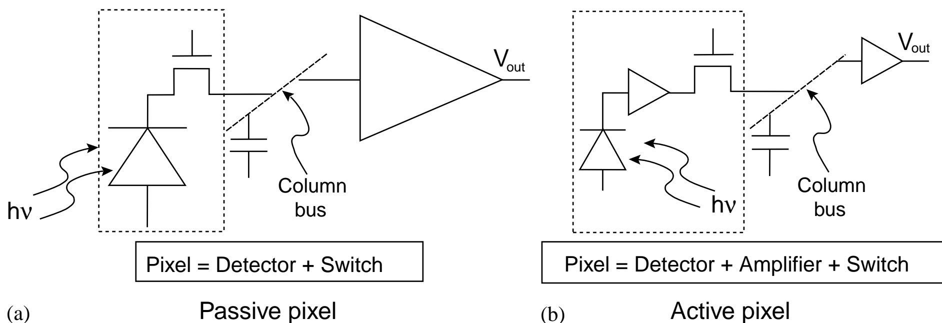

Fig. 20. Passive and active pixel sensors (after Ref. [47]).

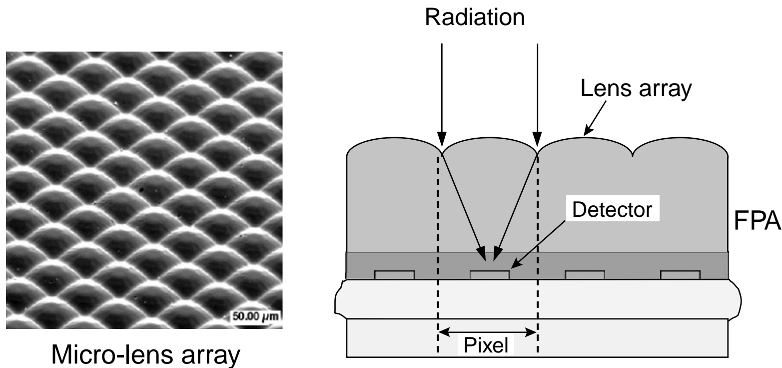

Fig. 21. Micrograph and cross-sectional drawing of microlensed hybrid FPA (after Ref. [47]).

however, reduces the FF of monolithic imagers to about 30–50% in 0.5-μm processes at a 5–6-μm pixel pitch or in 0.25-μm processes at a 3.3–4.0-μm pixel pitch [47].

In hybrid HgCdTe FPAs, various detector interface circuits are used to appropriately condition the signal. Specifically optimised input circuits are typically required for strategic and tactical applications. For tactical applications, where the backgrounds are high and detector resistances are moderate, direct injection (DI) is a commonly used input circuit [51]. The goal is to fit as large a capacitor as possible into the unit cell, particularly for high tactical applications where signal-to-noise ratios can be obtained through longer integration times. This circuit is widely used for simplicity; however, it requires a high impedance detector interface and is not generally used for low backgrounds due to injection efficiency issues. Many times the strategic applications have low backgrounds and require low noise multiplexers interfaced to high resistance detectors. A commonly used input circuit for strategic applications is the capacitative transimpedance amplification (CTIA) input circuit [51].

Besides the DI and CTIA inputs mentioned above, we can distinguish other multiplexers; the most important are: source follower per detector (SFD), electronically scanned buffered direct injection (ESBDI), buffered direct injection (BDI), and MOSFET load gate modulation (BGM) input circuits. These schemes are described in many papers, e.g., Refs. [46–54].

The CMOS switched readouts have been used for long >1024 elements, 30 μm element size linear, and various (64×64, 128×128, 256×256, 480×640, 1024×1024, and 2048×2048) 2-D arrays. Rockwell has successfully demonstrated nearly 40 multiplexer designs since switching over from CCD readouts a decade ago [55].

7.4. Focal plane array performance

For FPAs the relevant figure of merit is the noise equivalent temperature difference (NEDT), the temperature change of a scene required to produce a signal equal to the rms noise.

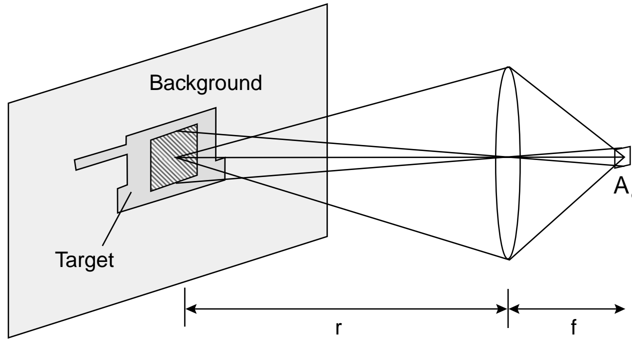

Fig. 22. Thermal imager system configuration.

The configuration of the basic thermal-imager system is shown in Fig. 22. The spectral photon incidence for a full hemispheric surround is

$$Q = \int_{\lambda_1}^{\lambda_2} \tau(\lambda) Q(T, \lambda)\, d\lambda \tag{22}$$

if a zero-emissivity bandpass filter having in-band transmission, $\tau(\lambda)$, the cut-on wavelength λ_1, and the cutoff wavelength λ_2 is used (zero emissivity is practically obtained by cooling the spectral filter to a temperature where its self-radiation is negligible).

The photon flux density incident on detector focal plane arrays is

$$Q_B = \frac{1}{1 + 4(f/\#)^2} Q, \tag{23}$$

where $f/\#$ is the ratio of the focal length to the diameter of the limiting aperture or lens. Under these conditions the background-induced photocurrent in any photon detector of area A_d is

$$I_{ph} = \frac{qA_d}{1 + 4(f/\#)^2} \int_{\lambda_1}^{\lambda_2} \tau(\lambda)\eta(\lambda) Q(T, \lambda)\, d\lambda, \tag{24}$$

where $\eta(\lambda)$ is a spectral response per photon (quantum efficiency) and $\tau(\lambda)$ is an optics (filter) transmission spectrum.

The thermal contrast is one of the important parameters for IR imaging devices. It is the ratio of the derivative of spectral photon incidence to the spectral photon incidence

$$C = \frac{\partial Q / \partial T}{Q}. \tag{25}$$

Fig. 23 is a plot of C for several MWIR subbands and the 8–12 μm LWIR spectral band. We can notice, that contrast in the MWIR bands at 300 K is 3.5–4% compared to 1.6% for the LWIR band.

Noise equivalent difference temperature of a detector represents the temperature change, for incident radiation, that gives an output signal equal to the rms noise

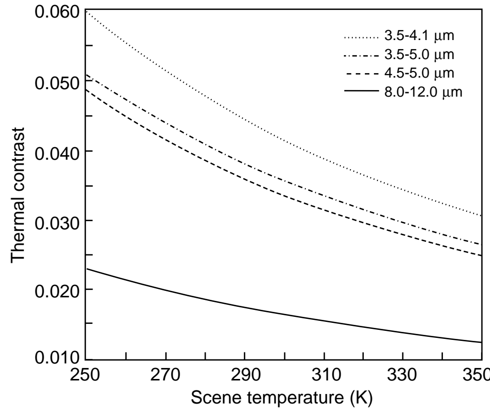

Fig. 23. Spectral photon contrast in the MWIR and LWIR (after Ref. [53]).

level. While normally thought of as a system parameter, detector NEDT and system NEDT are the same except for system losses. NEDT is defined

$$\mathrm{NEDT} = \frac{V_n(\partial T/\partial Q)}{(\partial V_s/\partial Q)} = V_n \frac{\Delta T}{\Delta V_s}, \tag{26}$$

where V_n is the rms noise and ΔV_s is the signal measured for the temperature difference ΔT. It can be shown that [53]

$$\mathrm{NEDT} = \left(\tau C \eta_{\mathrm{BLIP}} \sqrt{N_w}\right)^{-1}, \tag{27}$$

where N_w is the number of photogenerated carriers integrated for one integration time, t_{int}

$$N_w = \eta A_d t_{int} Q_B. \tag{28}$$

Percentage of BLIP, η_{BLIP}, is simply the ratio of photon noise to composite FPA noise

$$\eta_{\mathrm{BLIP}} = \left(\frac{N_{\mathrm{photon}}^2}{N_{\mathrm{photon}}^2 + N_{\mathrm{FPA}}2}\right)^{1/2}. \tag{29}$$

It results from the above formulas that the charge handling capacity of the readout, the integration time linked to the frame time, and dark current of the sensitive material become the major issues of IR FPAs. The NEDT is inversely proportional to the square root of the integrated charge and therefore the greater the charge, the higher the performance.

It must be noted the distinction between integration time and FPA's frame time. At high backgrounds it is often impossible to handle the large amount of carriers generated over frame time compatible with standard video rates. Off-FPA frame integration can be used to attain a level of sensor sensitivity that is commensurate with the detector-limited D^* and not the charge-handling-limited D^*.

It is of interest to compare the performance of uncooled photon and thermal detectors in the MWIR ($\lambda = 5\,\mu m$) and LWIR ($\lambda = 10\,\mu m$) spectral range. In this comparison we are followed after the paper recently published by Kinch [56]. Fig. 24 compares theoretical NEDT of detectors operated at 290 K for $f/1$ optics and a 1 mil pixel size. Parameters typical for micromachined resonant cavity bolometers are assumed in calculations. As a photon detector N^+-π-P^+ HgCdTe photodiode is chosen, first proposed by Ashley and Elliott [57]. π designates an intrinsic region containing a p-type background dopant equals 5×10^{14} cm^{-3} with carrier lifetime limited by Auger 7 process. It is also assumed that the detector node capacity can store the integrated charge due to detector dark current.

Fig. 24 shows that the ultimate performance of the uncooled HgCdTe photon detectors is far superior to the thermal detectors at wide frame rates and spectral bands. Also any other tunable bandgap alloy, such as type II InAs/GaInSb superlattices, could be worth-while with regard to the development of an uncooled photon detector technology [58,59]. The ultimate performance of HgCdTe photodiodes with optimally doped base region are comparable with that of InAs/InGaSb strain layer superlattices in the temperature range between 300 and 77 K [60].

Comparing both curves of Fig. 24 for thermal detectors we can see, that for long integration times in the LWIR region excellent performance is achieved, with NEDT values below 10 mK for frame rates of 30 Hz. However, for snapshot systems with integration time below 2 ms, the available NEDT is above 100 mK even at LWIR region. For MWIR band the thermal detector has obvious performance limitations at any frame rate.

8. Photon detectors

The increased sensitivity, resolution in system complexity of FPAs offer significant advantages in military as well as civilian applications in thermal imaging, guidance, reconnaissance, surveillance, ranging and communication systems. From fundamental considerations HgCdTe is the most important semiconductor alloy system for IR detectors in the spectral range between 1 and 25 μm. HgCdTe detectors as the intrinsic photon detectors absorb the IR radiation across the fundamental energy gap and are characterized by high optical absorption coefficient and quantum efficiency and relatively low thermal generation rate compared to extrinsic detectors, silicide Schottky barriers and QWIPs. The operating temperature for intrinsic detectors is, therefore, higher than for other types of photon detectors. The attributes of HgCdTe translate to flexibility and the capability to produce short wavelength infrared (SWIR), MWIR and LWIR detectors. HgCdTe has, however, serious technological problems in mass production, which result from a weak Hg–Te bond. The basic problems are: health hazard due to the highly toxic compounds, high mercury vapour pressure over melts, the Hg–Cd–Te phase diagram shape resulting in serious difficulties in repeatable growth of uniform-composition bulk crystals and epitaxial layers. Uniformity and yield are still issues. The majority of these problems

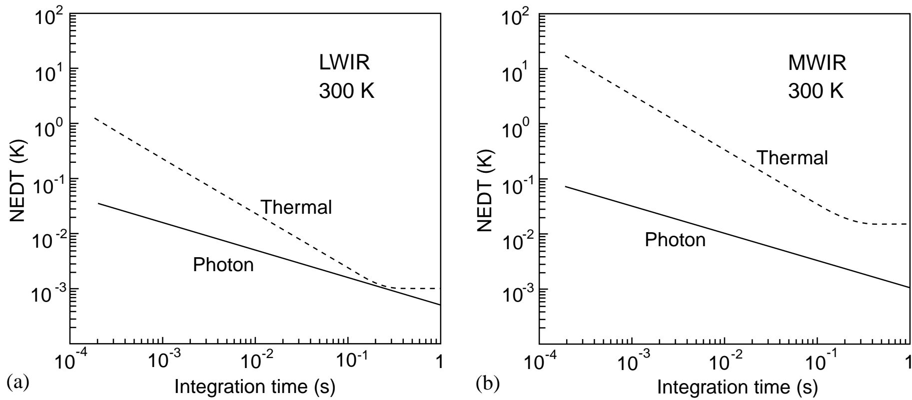

Fig. 24. Theoretical NEDT comparison of uncooled thermal and HgCdTe uncooled photon LWIR (a) and MWIR (b) detectors (after Ref. [56]).

have been successfully overcome. However, in spite of the achievements in material and device quality, difficulties still exist due to lattice, surface, and interface instabilities, which can lead to large variation in stoichiometry and transport properties as a result of treatments as diverse as oxidation, mechanical damage, and reaction with metals. The difficulties with this material have made it desirable to examine other material systems to determine whether performance can be improved. However,

- None of the new materials offers fundamental advantages over HgCdTe. While α/G figure of merit (see Section 4) of various narrow gap semiconductors seems to be very close to that of HgCdTe, the free carrier detectors, extrinsic and quantum well superlattice devices have several order of magnitude smaller α/G.
- HgCdTe exhibits extreme flexibility, it can be tailored for optimised detection at any region of IR spectrum, dual and multicolour devices can be easily constructed.
- Present development of IR photodetectors has been dominated by complex band gap heterostructures. Among various variable band gap semiconductor alloys, HgCdTe is the only material covering the whole IR spectral range having nearly the same lattice parameter. The difference of lattice parameter between CdTe ($E_g = 1.5$ eV) and $Hg_{0.8}Cd_{0.2}Te$ ($E_g = 0.1$ eV) is $\approx 0.2\%$ (see Fig. 25). Replacing small fraction of Cd with Zn or Te with Se can compensate the residual lattice mismatch. The independence of lattice parameter on composition is a major advantage of HgCdTe over any other materials.

Epitaxy is the preferable technique to obtain device-quality materials. Among the various epitaxial techniques, liquid phase epitaxy (LPE) is the most mature method for production of both first- and second-generation tactical detectors. LPE growth must be carried out at relatively high growth temperature with adherent interdiffusion and resulting graded interfaces. Recent efforts are aimed mostly at low growth temperature techniques: metalorganic chemical vapour deposition

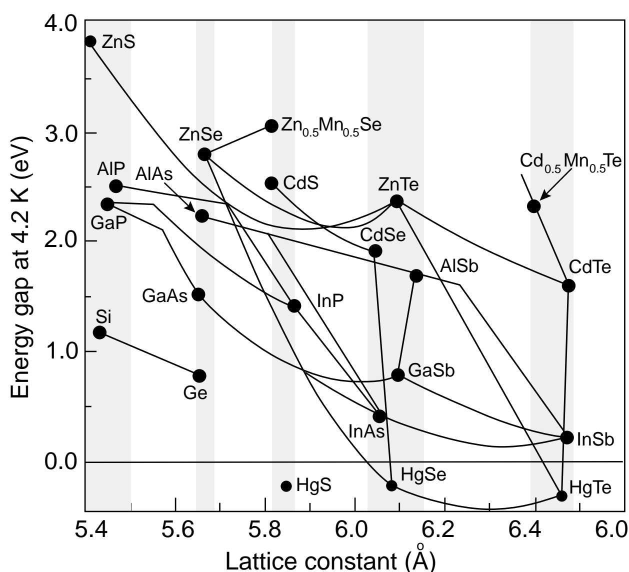

Fig. 25. A plot of the low temperature energy bandgaps of a number of semiconductors with the diamond and zinc-blende structure versus their lattice constants. The shaded regions highlight several families of semiconductors with similar lattice constants. $Cd_{0.96}Zn_{0.04}Te$ is a good match for a wide range of MWIR to LWIR HgCdTe alloys.

(MOCVD) and molecular beam epitaxy (MBE). At this time, MBE has become the dominant vapour-phase growth method for HgCdTe. Although the quality of MBE material is not yet on a par with LPE, it made tremendous progress in the past decade to the point where a variety of high-background device formats have been successfully demonstrated using this growth technique. Key to this success was ability to dope layers, both p- and n-type, and reduction of etch pit densities to below $10^7/cm^2$.

8.1. HgCdTe photodiodes

Different HgCdTe photodiode architectures have been fabricated that are compatible with backside and frontside illuminated hybrid FPA technology. Cross section views of these various architectures are shown in Figs. 26 and 27. The most important architectures are also included in Table 4, which summarises the applications of HgCdTe photodiode designs by the major FPA manufactures today.

Table 4 contains description of representative HgCdTe FPAs that are commercially available and described on web sides of the major HgCdTe manufactures. The LWIR FPAs usually operate at 77 K and are near the BLIP limit for higher background fluxes. The MWIR FPAs operate at temperatures above 77 K, and they are often thermoelectrically cooled. Their temperature operation depends on the design of the ROIC. Standard products for SWIR may be operated

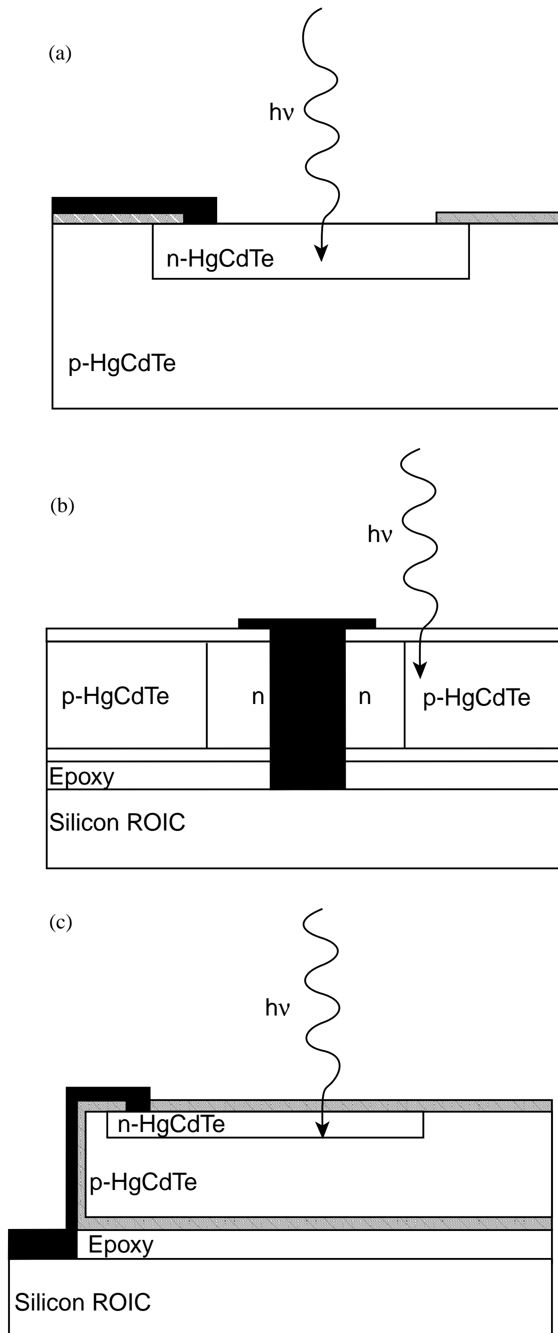

Fig. 26. Frontside illuminated HgCdTe photodiode architectures: (a) planar Hg-diffused n-on-p homojunction, (b) n–p "loophole" homojunction, and (c) n-on-p vertically integrated photodiode (VIP).

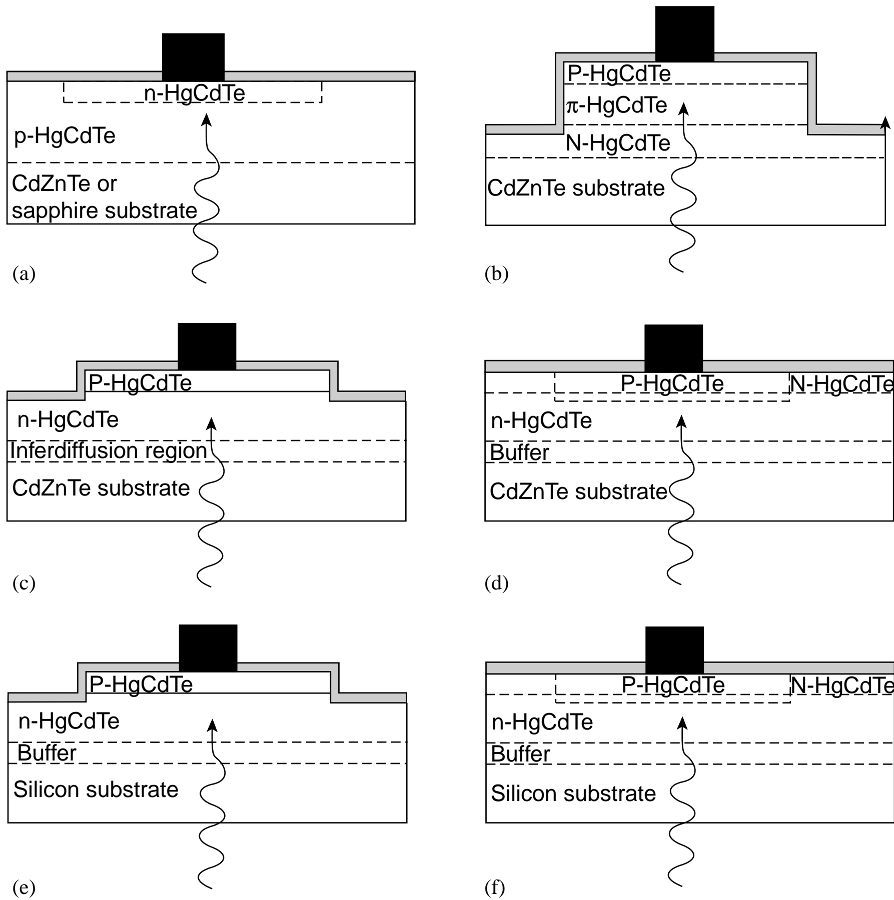

Fig. 27. Backside illuminated HgCdTe photodiode architectures: (a) planar ion implanted n^+–n^-–p homojunction, (b) P–π–N non-equilibrium photodiode, (c) backside illuminated mesa P-on-n heterojunction, (d) backside illuminated arsenic-implanted P-n-N planar buried junction heterostructure, (e) backside illuminated mesa P-on-n heterojunction on silicon substrate, (f) backside illuminated arsenic-implanted P–n–N planar buried junction heterostructure on silicon substrate.

at room temperature. Table 4 does not contain complete list of products, but it illustrates the range of HgCdTe FPAs wavelengths, formats, unit cell size, and describes the FPA performance (D^* and NEDT) that can be considered as commercially available.

8.1.1. Frontside illuminated photodiodes

The frontside illuminated n-on-p homojunction [see Fig. 26(a)] was the first HgCdTe device structure pioneered by Societe Anonyme de Telecommunications (SAT) [62]. Hg in-diffusion into vacancy doped HgCdTe has been the most widely used for very fast photodiodes [63]. Hg is diffused through openings formed in an

Table 4
HgCdTe photodiode architectures used for hybrid FPAs (after Ref. [61])

Configuration	Junction formation	Company
n-on-p VIP	Ion implantation forms n-on-p diode in p-type HgCdTe, grown by Te-solution LPE on CdZnTe and epoxied to silicon ROIC wafer; over the edge contact	DRS infrared technologies (formerly Texas Instruments)
n–p loophole	Ion beam milling forms n-type islands in p-type Hg-vacancy-doped layer grown by Te-solution LPE on CdZnTe, and epoxied onto silicon ROIC wafer; cylindrical lateral collection diodes	BAE Systems Ltd (formerly GEC-Marconi Infrared (GMIRL))
n^+-on-p planar	Ion implant into acceptor-doped p-type LPE film grown by Te-solution slider	Sofradir (Societe Francaise de Detecteurs Infrarouge)
n^+–n^-–p planar homojunctions	Boron implant into Hg-vacancy p-type, grown by Hg-solution tipper on 3" dia. sapphire with MOCVD CdTe buffer; ZnS passivation	Rockwell/Boeing
P-on-n mesa	1. Two-layer LPE on CdZnTe: Base: Te-solution slider, indium-doped Cap: Hg-solution dipper, arsenic-doped 2. MOCVD in situ on CdZnTe Iodine-doped base, arsenic-doped cap	IR Imaging Systems, Sanders—A Lockheed Martin Company (LMIRIS)
P-on-n mesa	1. Two-layer LPE on CdZnTe or Si: Base: Hg-solution dipper, indium-doped Cap: Hg-solution dipper, arsenic-doped 2. MBE in situ on CdZnTe or Si Indium-doped base, arsenic-doped cap	Raytheon Infrared Center of Excellence (RIRCoE, formerly SBRC) and Hughes Research Laboratories (HRLs)
P-on-n planar buried heterostructure	Arsenic implant into indium-doped N–n or N–n–N film grown by MBE on CdZnTe	Rockwell/Boeing

insulator layer, lowering the Hg vacancy concentration below that of the donors, which are either intentionally introduced dopants or residual impurities. For this device structures, the first use of an interdiffused CdTe layer for heterostructure passivation was reported [64].

Conversion of vacancy doped p-type HgCdTe to n-type during low-energy ion milling became another important technique of junction fabrication [see Fig. 26(b)]. GEC-Marconi Infrared Laboratories uses 25–30-μm thick LPE layer (grown from Te-rich solution) epoxied to a silicon CMOS ROIC [65]. A small hole, 5-μm in diameter, is created by ion milling. Just as in the case of ion implanted n-on-p junction, the n-type region is formed when Hg atoms are liberated during the milling process. The Hg atoms diffuse laterally, annihilating Hg vacancy acceptors and uncovering residual and intentional donors. The detector processing incorporates a metalization of small holes which connect one side of the junction to the input circuit node directly beneath. In this device geometry, photocarriers are collected by lateral diffusion. The R_oA products are generally lower than those achieved in junctions

with extrinsically doped absorber layer, due to short lifetime in the vacancy-doped p-type material.

Technology of the front-illuminated n-on-p vertically integrated photodiode (VIP) used by DRS [66] is similar to the lateral "loophole" technology [see Fig. 26(c)]. The VIP process employs planar, ion implanted n on p junction in HgCdTe which is epoxied to a silicon CMOS ROIC. A via hole is etched, and an over-the-edge contact metalization connects each junction area with an input node in the silicon ROIC below.

8.1.2. Backside illuminated photodiodes

The first architecture used for hybrid HgCdTe FPAs was backside illuminated planar ion implanted n^+–n^-–p homojunction [see Fig. 27(a)]. The based p-type absorber layer was grown by LPE onto an IR-transparent substrate such as CdTe, CdZnTe or sapphire. During implantation process, interstitial Hg atoms are liberated, diffused inward, annihilating Hg vacancies and forming an n^--region beneath the n^+-implanted layer [67]. In non-doped HgCdTe, the acceptors are the Hg vacancies and short lifetime in p-type region and suppressed R_0A values are observed. Factor of ten higher R_0A values (655 $\Omega\,cm^2$ at 77 K, $\lambda_c = 10\,\mu m$) for this structure was attributed to higher lifetime in the acceptor-doped p-type absorber layer, but there was no explanation for how longer lifetime was achieved [68]. The theoretically predicted Auger-limited value of R_0A product, equal to 680 $\Omega\,cm^2$, is nearly identical to the experimental value [69].

To reducing the detector cooling requirements, British workers have proposed non-equilibrium photodiode structures which employ both minority carrier exclusion and minority carrier extraction to suppress the Auger generation [57,70]. This type of device, the P–π–N structure (the capital letter denotes a region of wider band gap) is shown in Fig. 27(b). The low doped p-type absorber layer is sandwiched between wider-gap n- and p-type layers. The π-type layer is electrically neutral; only a narrow depletion region occurs at the π–n interface. This junction is operated in reverse bias producing extraction of minority carriers. The other, isotype junction is excluding to minority carriers preventing their injection into the π layer. Under these conditions, the electron concentration is negligible and hole concentration is lowered to the extrinsic acceptor concentration. The thermal generation rates due to the Auger 1 and 7 mechanisms are reduced substantially. The non-equilibrium devices have been realised in different configuration, and more recently in sophisticated five-layer films grown in situ by MOCVD with cut-off wavelengths ranging between 7.5 and 10.5 μm at room temperature [71]. However, the Auger suppression devices suffer from large $1/f$ noise and hence the improvement in the detectivity resulting from the reduced leakage currents can only be realised at high frequencies.

Next four device structures shown in Figs. 27(c)–(f), are based on P-on-n heterostructures. The backside illuminated mesa P-on-n heterojunction [see Fig. 27(d)] has became the most widely used junction architecture for bump-mounted hybrid FPAs. In this so-called double-layer heterojunction (DLHJ) structure, about 10-μm thick absorber layer is doped with indium at $1\times10^{15}\,cm^{-3}$

or less, and is grown either by horizontal-slider LPE from Te-rich solution or by vertical-dipper LPE from Hg-rich solution. The p-type cap layer with wider band gap energy ($\Delta x \approx 0.04$) is doped with arsenic around $(1–4) \times 10^{17}\,cm^{-3}$ and is grown by vertical-dipper LPE from Hg-rich solution. Several factors favoured the n-type absorber over the p-type absorber. n-type HgCdTe at low carrier concentrations is easier to control and passivate, and is comparatively free of the Schockley–Read defects that limited the lifetime of p-type material.

The small gradients in HgCdTe absorber layer cause small gradients in energy band gap, which, for backside illuminated LPE photodiodes, have the beneficial effect of setting up an effective electric field that provides drift-associated collection of photogenerated carriers. Also a thin (2–4 μm) interdiffused layer between the n-type absorber and the substrate causes that carriers are repelled away from the interface, thereby preventing recombination at the defects present at this interface. The critical parameters—composition difference across the heterojunction (Δx), composition gradient, placement of the P–n junction relative to the composition junction, and base dopant concentration (N_d)—are technology-specific to each material growth process and they are discussed in detail by Reine [61]. Barriers are more troublesome for very LWIR photodiodes because the rate of compositional interdiffusion increases with decreasing x-value [72].

The unique feature of the structure shown in Fig. 27(d), the backside illuminated arsenic-implanted P–n–N planar buried heterostructure, is that the junction is buried beneath the top wide-bandgap n-type layer. The junction intersects the surface in wider-bandgap HgCdTe, thereby reducing the generation rates for any surface defects and prevents carrier recombination at this interface. The arsenic doped p-type region must extend sufficiently deep into narrow-bandgap absorber layer to effectively collect photocarriers. The P–n–N device structures are fabricated using low-temperature in situ growth and bandgap engineering provided by MBE onto a CdZnTe substrate, instead the junction are formed by arsenic implantation. To active As as an acceptor, it must occupy a Te side in the lattice. Full As activation is achieved for annealing temperature of 300°C or higher. According to Ref. [73], the sample underwent two consecutive annealings, at about 430°C (to diffuse the arsenic into the base layer) for approximately 10 min and the other at 250°C (to annihilate Hg vacancies formed in the HgCdTe lattice during growth and diffusion of arsenic). The electrical junction is positioned near the metallurgical interface and it is wise to place the junction in the small band gap layer to avoid deleterious effects on the quantum efficiency and dark currents. At present, most laboratories use CdTe or CdZnTe (deposited by MBE, MOCVD, sputtering and e-beam evaporation) for photodiode passivation [74].

Near lattice matched CdZnTe substrates severe drawbacks such as lack of large area, high production cost, and more importantly, the difference of thermal expansion coefficient in CdZnTe substrates and silicon readout integrated circuits as well as interest in large area based IR FPAs (1024 × 1024 and larger), have resulted in CdZnTe substrate application limitations. The use of Si substrates is very attractive in IR FPA technology not only because it is less expensive and available in large area wafers but also because in an FPA structure, the coupling of the Si

substrates with Si readout circuitry allows the fabrication of very large arrays exhibiting long-term thermal cycle reliability.

Despite the large lattice mismatch ($\approx 19\%$) between CdTe and Si, MBE has been successfully used for the heteroepitaxial growth of CdTe on Si. Since 1989, Santa Barbara Research Center has successfully utilised "infinite-melt" vertical LPE technology from Hg-rich solution to grow high-quality epitaxial HgCdTe on the Si-based alternative substrates for the fabrication of p-on-n DLHJ detectors for high-performance MWIR FPAs [75]. During the past several years, progress has been made in the growth of MBE and MOCVD CdTe on silicon substrates as well as MBE- and MOCVD–HgCdTe growth on these alternative substrates. Different procedures have been used to fabricate composite substrates. de Lyon et al. [76] have fabricated buffer layer structures consisting of a 1 μm thick layer of ZnTe followed by 8 μm thick CdTe grown at a rate of 1.0 μm/h at Si(1 1 2) substrate temperature of 270°C. More complex procedure has been used by Wijewarnasuriya et al. [77]. Following special chemical treatment and predeposition of few $SiTe_2$ monolayers (created by exposing the surface to Te flux), a thin ZnTe layer was grown at 220°C followed by 10 min annealing under CdTe and Te flux at 380°C. Finally, CdTe(2 1 1)B layer was grown at the temperature of 300°C. Using optimised growth condition for Si(2 1 1)B substrates, CdTe(2 1 1)B layers with EPD of 10^5–$10^6\,cm^{-2}$ range could be obtained.

The last two HgCdTe photodiode architectures shown in Fig. 27 (e and f) can be fabricated using silicon substrates.

8.1.3. Fundamental limitation to HgCdTe photodiode performance

It results from consideration carried out previously, that we can distinguish two fundamental HgCdTe photodiode architectures based on p-type absorber layer (simple n^+-on-p homojunction) and n-type absorber layer (P-on-n heterojunction). Necessity of using heterojunction in the case of n-type absorber layer is theoretically evidenced in Ref. [69]. Fig. 28 shows the schematic band profiles of the unbiased homo- and heterojunction photodiodes. To avoid contribution of the tunnelling current, the doping concentration in the base region below $10^{16}\,cm^{-3}$ is required. In both photodiodes, the lightly doped narrow gap absorbing region ["base" of the photodiode: p(n)-type carrier concentration of about $5\times10^{15}\,cm^{-3}$ ($5\times10^{14}\,cm^{-3}$)] determines the dark current and photocurrent. The base p-type layers (or n-type layers) are sandwiched between CdZnTe substrate and high-doped (in n^+-on-p structures) or wider-gap (in P-on-n structure) regions. Due to backside illumination (through CdZnTe substrate) and internal electric fields (which are "blocking" for minority carriers), influence of surface recombinations on the photodiodes performance is eliminated. The influence of surface recombination can be also prevented by the use of suitable passivation. Both optical and thermal generations are suppressed in the n^+-region due to the Burstein–Moss effect and in the P-region due to wide gap. Since the base region determines largely the properties of the device, it should be carefully optimised.

The thickness of the base region should be optimised for near unity quantum efficiency and a low dark current. This is achieved with a base thickness slightly

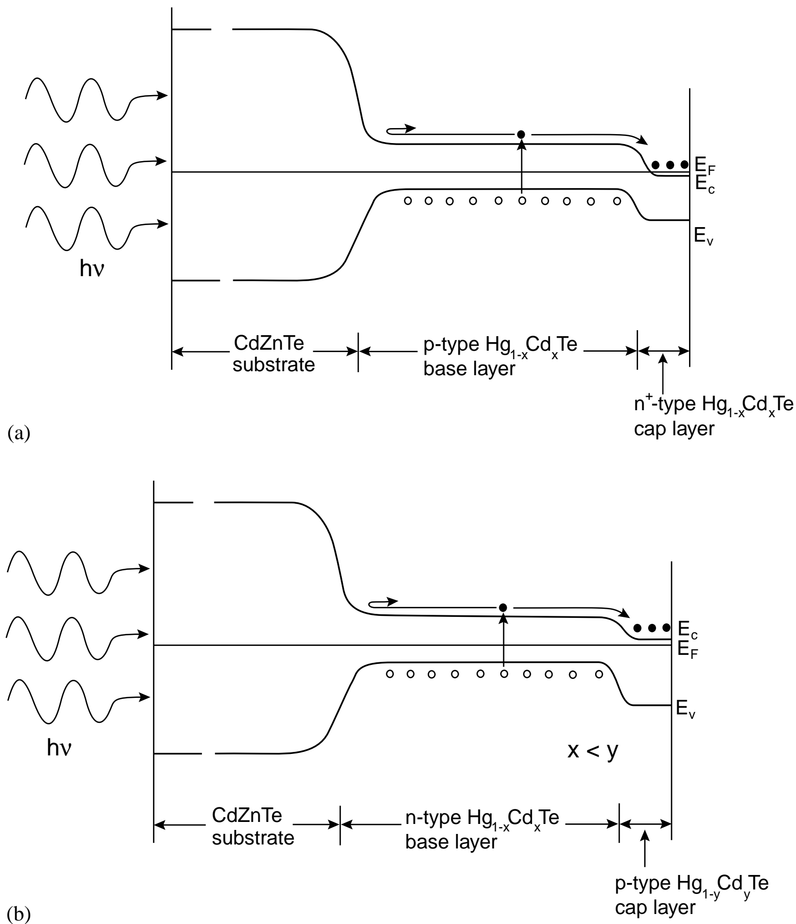

Fig. 28. Schematic band diagrams of n^+-on-p homojunction (a) and P-on-n heterojunction photodiodes (b).

higher than the inverse absorption coefficient for single pass devices: $t = 1/\alpha$ (which is $\approx 10\,\mu$m) or half of the $1/\alpha$ for double pass devices (devices supplied with a retroreflector). Low doping is beneficial for a low thermal generation and a high quantum efficiency. Since the diffusion length in absorbing region is typically longer than its thickness, any carriers generated in the base region can be collected giving rise to the photocurrent.

Assuming that the Auger mechanisms impose fundamental limitations to the HgCdTe photodiode performance and that the saturation dark current, I_s, is only due to thermal generation in the base layer and that its thickness is low compared to the diffusion length,

$$I_s = GtqA, \tag{30}$$

where G is the generation rate in the base layer and A is the detector area. Then the zero bias resistance–area product is

$$R_oA = \frac{kT}{q^2Gt}. \quad (31)$$

Taking into account the Auger 7 mechanism in extrinsic p-type region of n^+-on-p photodiode, we receive

$$R_oA = \frac{2kT\tau_{A7}^i}{q^2N_at}, \quad (32)$$

and the same equation for P-on-n photodiode

$$R_oA = \frac{2kT\tau_{A1}^i}{q^2N_dt}, \quad (33)$$

where N_a and N_d are the acceptor and donor concentrations in the base regions, respectively.

As Eqs. (32) and (33) show, the R_0A product can be decreased by reduction of the thickness of the base layer. Since $\gamma = \tau_{A7}^i T_{A1}^i > 1$, a higher R_oA value can be achieved in p-type base devices compared to that of n-type devices of the same doping level. Detailed analysis shows that the absolute maximum of R_oA is achievable with base layer doping producing $p = \gamma^{1/2}n_i$, which corresponds to the minimum of thermal generation. The required p-type doping is difficult to achieve in practice for low temperature photodiodes (the control of hole concentration below 5×10^{15} cm^{-3} level is difficult) and the p-type material suffers from some non-fundamental limitations; such as: contacts, surface and Shockley–Read processes. These are the reasons why the low temperature detectors are typically produced from the lightly doped n-type materials.

Long wavelength infrared photodiodes. The dependence of the base region diffusion limited R_oA product on the long wavelength cut-off for n^+–p HgCdTe photodiodes at temperatures $\leqslant$77 K is shown in Fig. 29. At 77 K the experimental results show a greater spread, probably due to additional currents in the junctions. p-type base material is characterised by relatively high trap concentration, which dominates the excess carrier lifetime by the Shockley–Read–Hall recombination mechanism. Its influence depends on technological limits. At operating temperatures below 77 K, two other distinct mechanisms dominate the dark current: trap-assisted tunnelling and band-to-band tunnelling. Multistep recombination via defects plus variations in local electrical parameters are probably the reason we do not observe the expected strong band to band gap effect on devices as evidenced in the 77 K data for the best photodiodes, where the currents are diffusion limited. However, the quality of p-type material has considerably improved by acceptor doping [68]. The R_oA improvement of one order of magnitude (in the range between 400 to 650 Ω cm^2 at 77 K for a 10 μm cut-off wavelength detector) has been observed.

The dependence of the base region diffusion limited R_oA product on the long wavelength cut-off for P-on-n LWIR HgCdTe photodiodes at different temperatures is shown in Fig. 30. This figure also includes the experimental data reported by many

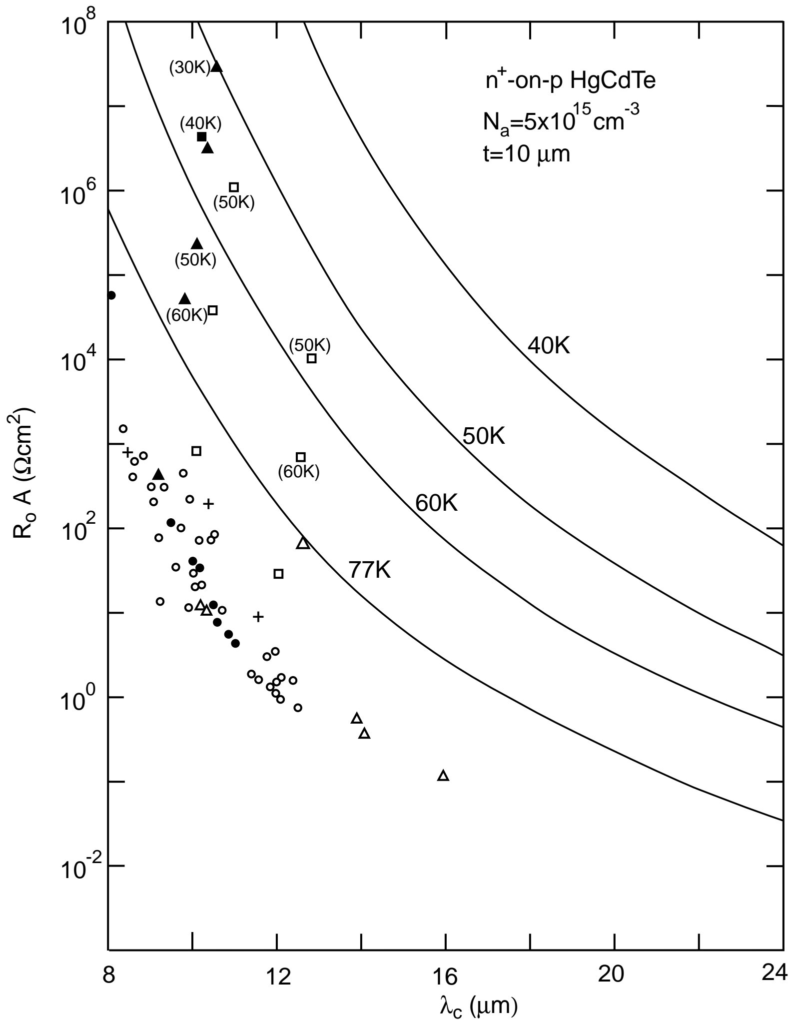

Fig. 29. Dependence of the R_0A product on the long wavelength cut-off for LWIR n^+-on-p HgCdTe photodiodes at temperatures $\leqslant 77\,K$. The solid lines are calculated assuming that the performance of photodiodes are due to thermal generation governed by the Auger mechanism in the base p-type region of photodiodes with $t = 10\,\mu m$ and $N_a = 5 \times 10^{15}\,cm^{-3}$. The experimental values are taken from different papers (after Ref. [69]).

authors for DLHJ P-on-n structures. The wider bandgap cap layer contributes a negligible amount of thermally generated diffusion current compared with that from an n-type absorber layer at 77 K, and the upper experimental data are situated about a half of an order below ultimate theoretical predictions. With a lowering of the operation temperature of photodiodes, the discrepancy between the theoretical

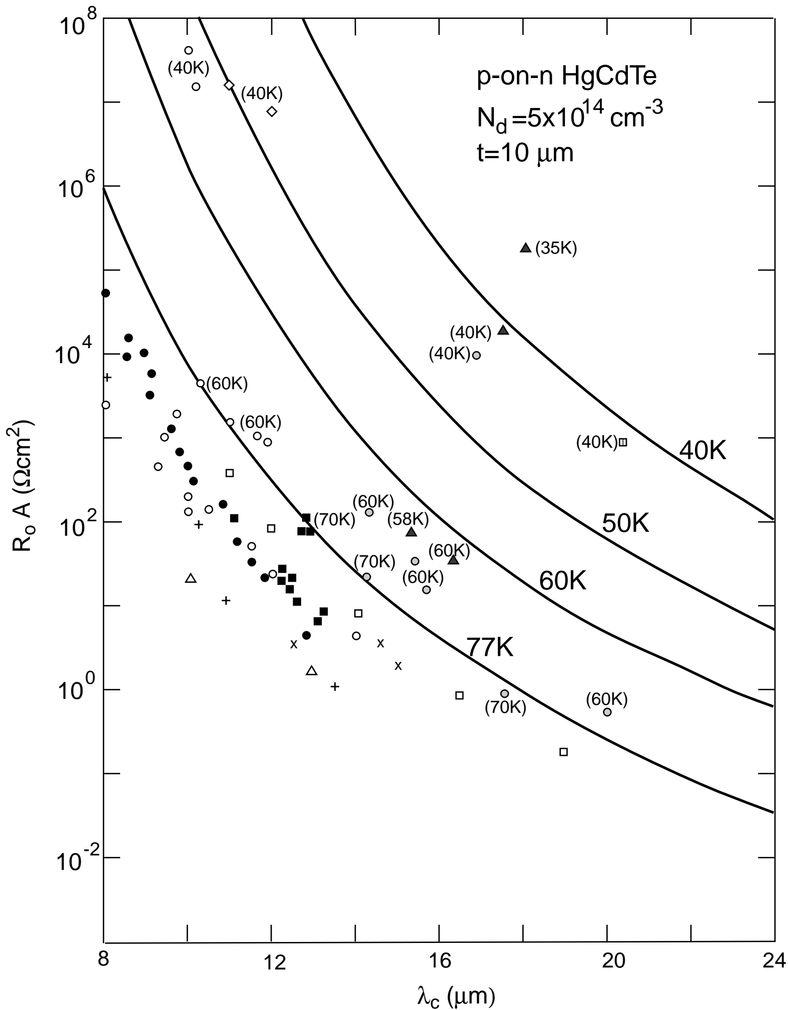

Fig. 30. Dependence of the R_0A product on the long wavelength cut-off for LWIR P-on-n HgCdTe photodiodes at temperatures $\leqslant 77\,\mathrm{K}$. The solid lines are calculated assuming that the performance of photodiodes are due to thermal generation governed by the Auger mechanism in the base n-type region of photodiodes with $t = 10\,\mu\mathrm{m}$ and $N_\mathrm{d} = 5 \times 10^{14}\,\mathrm{cm}^{-3}$. The experimental values are taken from different papers (after Ref. [78]).

curves and experimental data increases, which is due to additional currents in the junctions (such as tunnelling current or surface leakage current) that are not considered. Photodiodes with lower performance usually contain metallurgical defects such as dislocation clusters and loops, pin holes, striations, Te inclusions, and heavy terracing. It should be noticed that the upper experimental data in very long wavelength range (above 14 µm) at lower temperature (40 K) coincides very well with

theoretical predictions. The best devices continued to be diffusion-current limited by Auger mechanism at zero bias to 35 K. At 40 K, the measured R_oA is $2 \times 10^4\,\Omega\mathrm{cm}^2$ and the measured cut-off wavelength is 17.6 μm. At 35 K, R_oA is $2 \times 10^5\,\Omega\mathrm{cm}^2$ at the cut-off wavelength 18.1 μm. Also the performance of photodiodes with cut-off wavelengths of 20.3 μm at 40 K is diffusion limited and R_oA products for the diodes reach values in the $10^3\,\Omega\mathrm{cm}^2$ range. There are the highest reported values at these long cut-offs wavelengths for any HgCdTe device.

Comparing Figs. 29 and 30 we can see that for assumed doping concentrations in the base region of photodiodes ($N_a = 5 \times 10^{15}\,\mathrm{cm}^{-3}$ for n^+–p structure and $N_d = 5 \times 10^{14}\,\mathrm{cm}^{-3}$ for P–n structure) and for a given cut-off wavelength, the theoretical values of R_0A product for P-on-n photodiodes in temperature range below 77 K are a little greater than for n-on-p photodiodes. Instead, 200–300 K LWIR devices exhibit the same R_0A values since the base layer materials becomes intrinsic in both cases. It should be noted that more heavy p-type doping is necessary for the best photodiode performance at high temperature operation [79].

Fig. 31 compares the results of LWIR arrays fabricated on MBE-grown CdZnTe/Si and MOCVD-grown CdZnTe/GaAs/Si with a historical trendlines of arrays fabricated on bulk CdZnTe. Each data point represents the array average R_oA product measured at $f/2$ FOV (300 K) background at temperature of 78 K. LWIR $Hg_{0.77}Cd_{0.23}Te$ DLHJ were grown by vertical LPE from infinite melt Hg-rich solutions. The n-type base layer was doped with indium and the wider-bandgap layer was doped with arsenic. The two continuous curves shown in Fig. 31 were calculated to indicate diffusion-limited behaviour and they are only shown as a guide to the eye. We can see that there is no significant difference between arrays fabricated on either CdZnTe/Si or CdZnTe/GaAs/Si and the results on these Si-substrates are

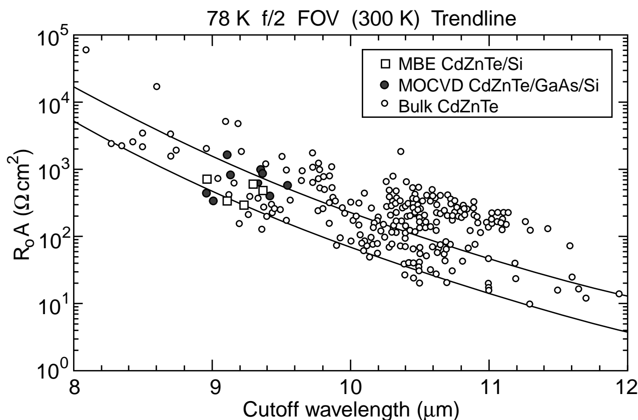

Fig. 31. Comparison of the results of LWIR HgCdTe arrays fabricated on MBE-grown CdZnTe/Si and MOCVD-grown CdZnTe/GaAs/Si with a historical trendlines of arrays fabricated on bulk CdZnTe. Each data point represents the array average R_oA product measured at $f/2$ FOV (300 K) background at a temperature of 78 K (after Ref. [80]).

comparable with results on bulk CdZnTe substrates at 78 K. To improve reverse-bias characteristics at 78 K and improve detector performance at lower temperatures in comparison with bulk CdZnTe substrates, a further reduction in the dislocation density for HgCdTe-grown on Si-based substrates is needed.

Middle wavelength infrared photodiodes. MWIR HgCdTe photodiodes were the first to be developed, and many mature technologies have been used to demonstrate FPAs [81–84]. Rockwell has developed the capability for fabricating large MWIR HgCdTe FPAs by epitaxially growing HgCdTe on sapphire (PACE-1 process). In his process a CdTe layer is grown via MOCVD on the sapphire, and next HgCdTe is grown on the CdTe buffer via LPE. The junctions are formed by boron ion implantation and thermal annealing. Planar and mesa junctions are used, depending on the FPA specifications, and they are passivated with a ZnS or CdTe film. The detector array is backside illuminated through the sapphire substrate, which transmits to 6.5 μm for a 7-mil thickness. PACE-1 process currently provides intrinsic detector arrays with BLIP performance and satisfactory yield.

The sapphire substrate offers several attributes. Its thermal coefficient of expansion matches well to the alumina chip carrier, thereby greatly improving large hybrid reliability. The large substrate also reduces detector cost by increasing throughput, enabling batch processing and reducing breakage. The 3 in wafers, currently in production, enable populating each wafer with either five 18.5-μm pixel 1024×1024 arrays (in addition to four 40 μm 256×256 arrays), eight 27 μm 640×480 arrays, or twenty one 256×256 arrays. Table 5 lists the performance of the PACE-1 256×256, 640×480, and 1024×1024 FPAs [82,85,86]. The hybrid HgCdTe 256×256 FPAs offer TV-type resolution with ≈ 10 mK sensitivity at operating temperatures $\leqslant 130$ K. For 640×480 FPAs, NEDT of 0.015 K has been

Table 5
PACE-1 HgCdTe FPA specifications (after Refs. [86])

Parameters	TCM2000	TCM6000	HAWAII
Format	256×256	640×480	1024×1024
Detector cutoff wavelength (μm)	4.6	4.6	2.5
Operating temperature (K)	120	120	<120
Cell pitch (μm)	40	27	18.5
Chip package (optional) (LLCC)	68 Pin	84 Pin	84 Pin
Typical usable dynamic range (10^3)	>10	>5	1
MWIR NETD@ $\Phi_b = 1 \times 10^{14}$ photons cm^{-2} s^{-1} (mK)	< 10	< 25	
Responsivity nonuniformity (Max:Min)	< 1.4:1	< 1.6:1	10%
Pixel operability (%)	>99	>98	>98
Outputs	1(2)	4	4
Maximum data rate per output (MHz)	>10	>10	>0.8
Minimum D^* @ $\Phi_b = 1 \times 10^{14}$ photons cm^{-2}s^{-1} (10^{11} cmHz$^{1/2}$ W^{-1})	>8	>5	1000 (5×10^9ph cm^{-2} s^{-1})

measured, which means that the sensitivity is higher than it has been typically reported for the currently available PtSi 640×480 FPA technology.

Since 1989, SBRC has successfully utilised "infinite-melt" vertical LPE technology from Hg-rich solution to grow high-quality epitaxial HgCdTe on the Si-based alternative substrates for the fabrication of p-on-n DLHJ detectors for high-performance MWIR FPAs. Tung et al. [75] reported large, up to 480×640, MWIR FPAs, grown on Si-based alternative substrates.

Fig. 32 compares the R_oA product for two PACE MWIR HgCdTe layers with cut-off wavelengths at 78 K of 5.11 and 4.65 μm, respectively, versus temperature. Also compared is the theoretical R_oA performance for 5-μm p-on-n HgCdTe photodiode; this level is readily achieved with MBE MWIR DLHJ HgCdTe/CdZnTe material [83]. The using a buried planar heterostructure produces devices whose performance is less critical of passivation as compared to conventional mesa technology because the junction interface is buried. The planar p-on-n photodiodes are formed by selective pocket diffusion of arsenic (a p-type dopant), which is deposited by ion implantation on the wide bandgap cap layer.

The MBE-grown devices on Si and CdZnTe appear to be identical [84]. Fig. 33 presents a comprehensive comparison of the performance of MWIR P-on-n HgCdTe photodiodes on CdZnTe and Si substrates for cut-off wavelengths ranging from 3.5 to 5 μm. The various data points are median values for mini-arrays included in test structures for each processed wafer. The devices with highest performance are processed from MBE-grown epilayers on bulk CdZnTe substrates. The shorter cut-off devices (with $\lambda_c \approx 3$ μm) are diffusion-limited down to at least 125 K. The devices with longer cut-off wavelength (with $\lambda_c \approx 5$ μm) appear to be diffusion-limited down to approximately 110 K. Below this temperature the experimental data obscure the probable onset of generation-recombination and/or tunnelling current limitations.

Short wavelength infrared photodiodes. Considerable progress in HgCdTe SWIR hybrid FPAs has been achieved in the last decade. At the beginning, the detector arrays were fabricated using a n^+ boron implanted process on p-type HgCdTe layers grown by LPE on CdTe or CdZnTe substrates [81]. Next, the PACE-1 process was adopted to fabricate large, 2.5-μm 1024×1024 FPAs (HAWAII) for IR astronomy [85,86]. Recently, DLPH p-on-n photodiodes in MBE HgCdTe on CdZnTe substrates have been elaborated by As-ion implantation and the p-dopant activation by an open-tube Hg anneal [87].

The highest detector performance is achieved by growing the layers on lattice-matched substrates, such as CdZnTe (their properties are the least affected by threading dislocations). Adding In during growth provided donor doping nominally 1.5×10^{15} cm^{-3} with a majority carrier mobility of ≈ 8000 cm^2/V s at 77 K. The MBE DLHJ HgCdTe/CdZnTe photodiodes are made using a buried planar heterostructure. Typical active layer thickness is ≈ 3.5 μm and cap layer thickness is ≈ 0.4 μm [87]. The highest quality SWIR HgCdTe photodiodes have performance in agreement with the radiative limit. It appears however, that due to photon recycling, an order of magnitude enhancements in the radiative lifetimes over those obtained from the standard van Roosbroeck and Shockley expression is observed in materials

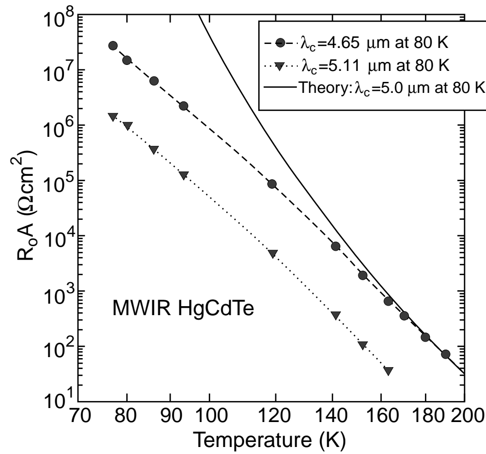

Fig. 32. R_0A product versus temperature for MWIR HgCdTe photodiodes (after Ref. [83]).

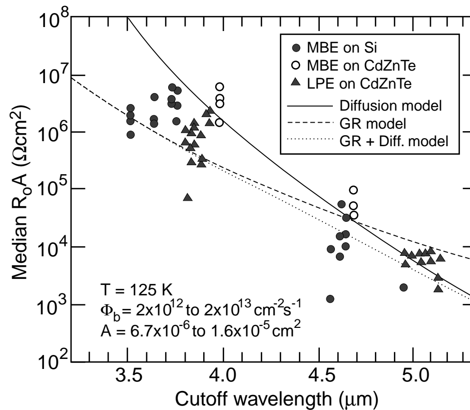

Fig. 33. Comparison of 125 K detector performance for MWIR HgCdTe photodiodes grown on Si and CdZnTe by MBE and photodiodes grown on CdZnTe by LPE. Each data point represents an array-median R_0A product measured at 125 K (after Ref. [84]).

like $In_{0.53}Ga_{0.47}As$ lattice-matched to InP substrates [88]. The same situation can be observed in HgCdTe ternary alloys [89,90]. Consequence of enhancement in the radiative lifetime leads to higher ultimate performance of photodiodes. Assuming the same situation for SWIR HgCdTe photodiodes, Rogalski and Ciupa have reconsidered the ultimate performance of P-on-n HgCdTe photodiodes and compared theoretical predictions with attainable experimental data, what is shown in Fig. 34. We can see, that SWIR HgCdTe photodiodes have good performance over a wider range of wavelengths. It is due to lattice match of active base

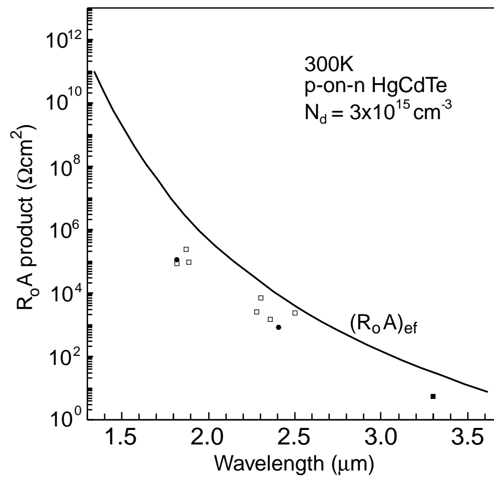

Fig. 34. The dependence of effective R_oA product on the long wavelength cutoff for SWIR HgCdTe photodiodes at room temperature. The calculations are performed assuming that the performance of photodiodes is due to fundamental generation-recombination processes in the base p-type region of photodiodes with $t = 5\,\mu m$ and $N_d = 3 \times 10^{15}\,cm^{-3}$. The experimental values are taken from different papers (after Ref. [88]).

photodiode layers with CdZnTe substrate and consequently negligible influence of induced defects at interface on photodiode leakage current.

Fig. 35 shows the detectivity as a function of temperature for HgCdTe FPAs at various cut-off wavelengths and operating background. In nearly all cases the performance is characterised by background-limited performance, transitioning to detector-limited performance as the temperature is increased.

8.1.4. Non-fundamental sources of dark current of HgCdTe photodiodes

Many additional excess mechanisms are involved in determining the dark current of HgCdTe photodiode [71,91]. Apart from the fundamental band-to-band generation in the base region, additional contributions may arise from non-fundamental sources due to the base and cap layer, depletion region and surface. As the photodiode operating temperature is lowered, the thermal dark current mechanisms become weaker and allow other mechanisms to prevail. In practice, the non-fundamental sources dominate the dark current of the present HgCdTe photodiodes, with the exception of specific cases of near room temperature devices and highest quality 77 K LWIR and 200 K MWIR devices. The main leakage mechanisms of HgCdTe photodiodes are: generation in the depletion region, interband tunnelling, trap-assisted tunnelling, and impact ionisation. Some of them are caused by structural defects in the p–n junction. These mechanisms receive much attention now, particularly because they determine ultimately the array uniformity, yield and cost for some applications, particularly those with lower operating temperatures.

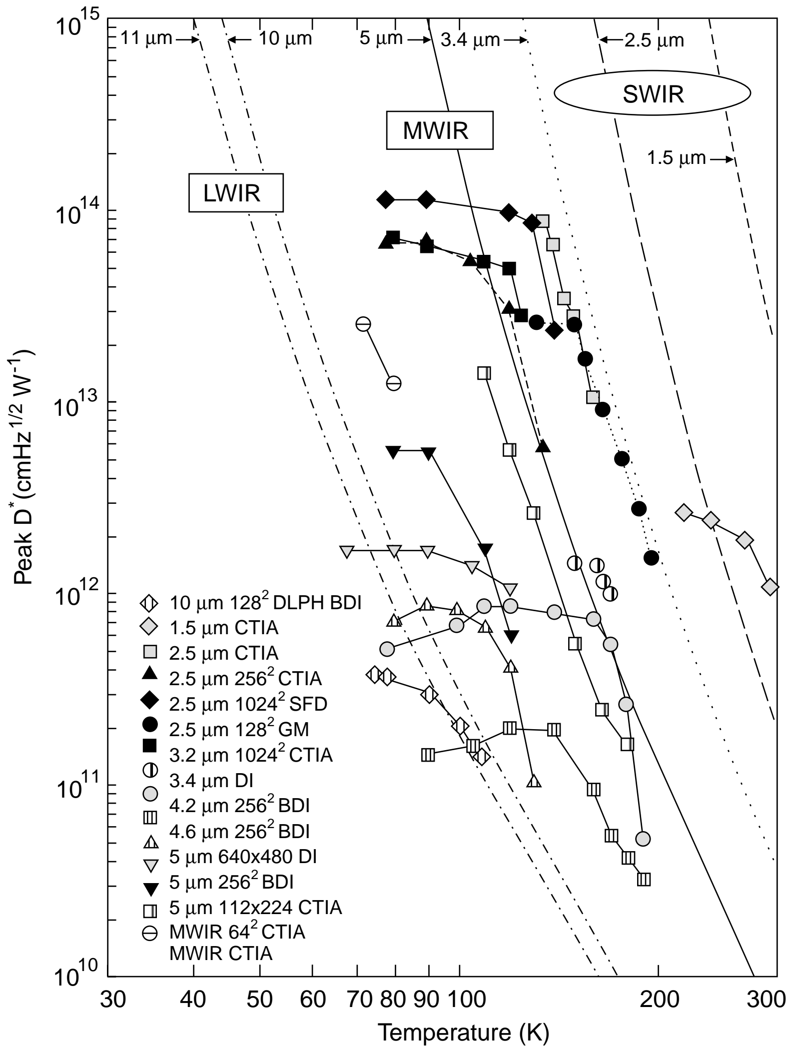

Fig. 35. Detectivity of HgCdTe FPAs versus temperature (after Ref. [83]).

Many authors have successfully modelled the key reverse bias leakage mechanism in LWIR HgCdTe photodiodes at $\leqslant 77$ K in terms of trap-assisted tunnelling [91]. The role played by traps in the depletion region is very complicated. Nemirovsky et al. [92] have shown that, for gold doped material, the observed temperature and voltage behaviour of the current–voltage characteristic fits a trap-assisted tunnelling model below 100 K, and at biases over –80 mV. DeWames et al. [93] have shown that a model based on a thermal-tunnel process can explain the bias-dependent behaviour of reverse current in long wavelength diodes. Also Nemirovsky et al. [94] have

explained the observed properties of their n^+–p junctions by a thermal trap-assisted tunnelling process, modelled for the special case of the trap residing at the Fermi level.

Dislocations are known to increase dark current and $1/f$ noise current. The reverse bias characteristics of HgCdTe diodes depend strongly on the density of dislocations intercepting the junction. Johnson et al. [95] showed that for large dislocations density the R_0A product decreases as the square of the dislocation density; the onset of the square dependence occurs at progressively lower dislocation densities as the temperature decreases, what is shown in Fig. 36. At 77 K, R_oA begins to decrease at an etch-pit density (EPD) of approximately $10^6\,cm^{-2}$, while at 40 K, R_oA is immediately affected by the presence of one or more dislocations in a diode. The scatter in the R_oA data at large EPD may be associated with the presence of an increased number of pairs of "interacting" dislocations being present in some of those diodes; these pairs are more effective in reducing the R_oA than individual dislocations. The dependence of the detector R_oA product on dislocation density is explained by a phenomenological model based on the conductances of individual and interacting dislocations which shunt the p–n junction. Spectral response and quantum efficiency is only weakly affected. Instead, the $1/f$ noise current was found to increase approximately linearly with dislocation density.

For low-background applications, the HgCdTe photodiodes operate at 40 K. The R_oA product distribution for P-on-n DLHJ devices at this temperature spans a wide range of several orders of magnitude. Chen et al. [96] carried out a detailed analysis of the wide distribution of the R_o values. Fig. 37 shows the cumulative distribution functions of R_o values at 40 K from devices with a cut-off wavelength between 9.4 and 10.5 μm. It is clear that while some devices exhibit a fair operability with R_o values spanning only two orders of magnitude, other devices show a poor operability

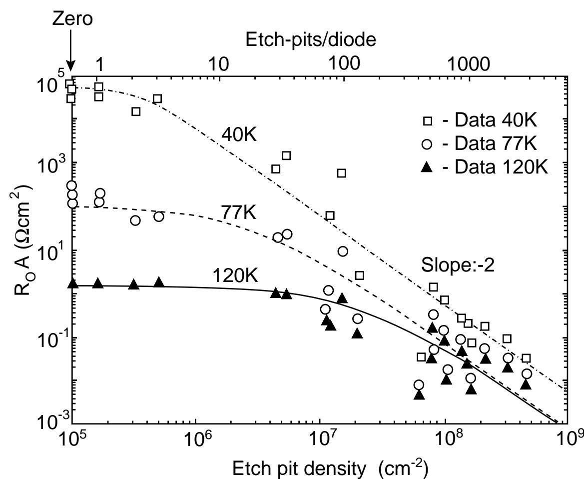

Fig. 36. R_oA product versus EPD, showing fit of model to data for 9.5-μm array (at 78 K), measured at 120, 77, and 40 K at zero FOV (after Ref. [95]).

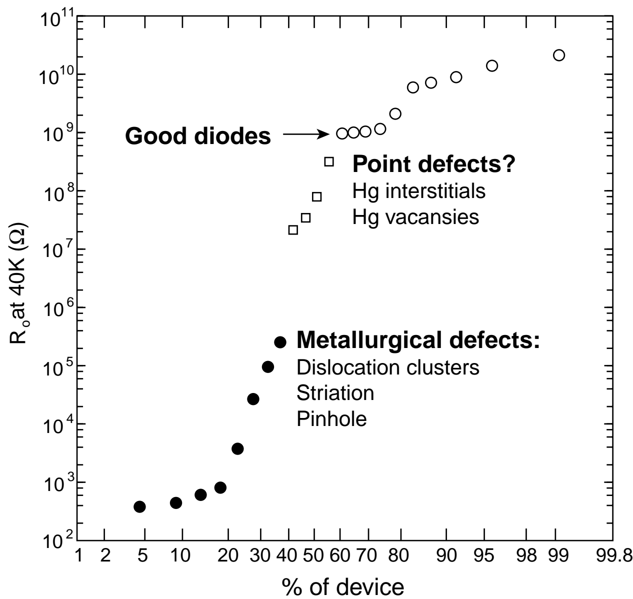

Fig. 37. Detailed analysis separates the cumulative distribution function of R_oA values of LWIR p-on-n HgCdTe photodiodes (fabricated by LPE) into three regions: good diodes, diodes affected by point defects, and diodes affected by metallurgical defects (after Ref. [96]).

with R_o values spanning more than 5–6 orders of magnitude. Lower performance, with R_o values below 7×10^6 at 40 K, usually contained gross metallurgical defects such as dislocation clusters and loops, pin holes, striations, Te inclusions, and heavy terracing. However, diodes with R_o values between 7×10^6 and $1\times10^9\,\Omega$ at 40 K contained no visible defects (Hg interstitials and vacancies). Dislocations, twins and subgrain boundaries in LWIR n^+–p HgCdTe photodiodes primarily produce bias dependent dark current, while Te precipitation and associated dislocation multiplication produces bias dependent noise [97].

8.1.5. Avalanche photodiodes

HgCdTe is an attractive material for room-temperature avalanche photodiodes (APDs) operate at 1.3–1.6 μm wavelengths for fibre optical communication applications, advanced laser rangefinders and 3D-imaging radars operating at eye-safe wavelengths near 1.5 μm. The resonant enhancement occurs when the spin-orbit splitting energy in the valence band is equal to the fundamental energy gap ($E_g = \Delta_0$). This has the beneficial effect, first pointed out by Verie et al. [98], of making the electron and hole impact ionisation rates quite different, which is highly desirable for low-noise avalanche photodiodes. The band structure of HgCdTe gives k-values if 0.1 or less—a highly favourable ratio of hole to electron multiplication during avalanche conditions, resulting in very little noise gain. These properties give HgCdTe APDs a figure of merit better than InGaAs APDs.

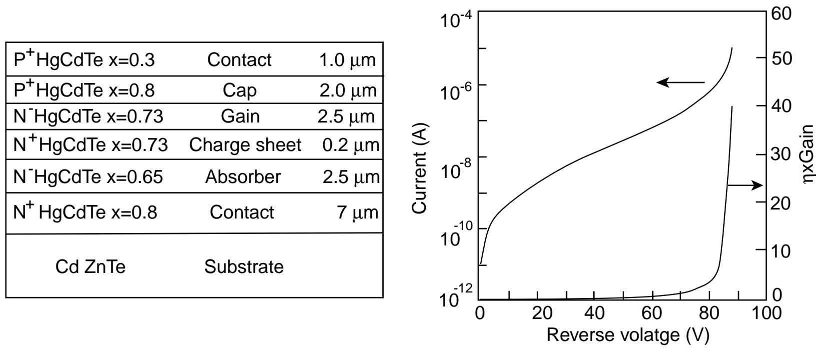

Fig. 38. Cross section of the back-illuminated six-layer HgCdTe SAM-APD grown in situ by MBE (left) and reverse bias $I-V$ data and $\eta \times$ Gain product (right). The cut-off wavelength is 1.6 μm (after Ref. [101]).

Avalanche HgCdTe structures have been built and demonstrated for detection at 1.06, 1.3 and 1.55 μm. Initial demonstrations utilized ion implantation and LPE grown [91]. At present MBE grown is chiefly used [99–101]. Fig. 38 illustrates back-illuminated multilayer separate-absorption-and-multiplication avalanche photodiode (SAM-APD) grown in situ by MBE and their reverse-bias $I-V$ curve for a device with area of 2.54×10^{-5} cm^2, and data for the $\eta \times$ Gain product. Avalanche gain in the range of 30–40 were demonstrated at reverse-bias voltages of 80–90 V in 25-element mini-arrays. The HgCdTe composition value of $x = 0.73$ in the gain layer was chosen to make $E_g = \Delta_0$, which the authors experimentally determined to be 0.928 eV.

Table 6 summarizes the properties and performance for a variety of APD sizes from 50 to 300 μm diameter measured at 1.55 μm. Single elements together with both linear and 2D arrays of these devices are currently being demonstrated in advanced applications.

8.1.6. Non-equilibrium photodiodes

The HgCdTe heterostructure device supplied by GEC-Marconi Infrared Limited are intended for operation at temperatures $\geqslant$145 K. Typical parameters for the LW devices would be $x = 0.184$ in the active π region, $x = 0.35$ in the P^+ region and $x = 0.23$ in the N^+ region. The structures were grown using MOCVD. The π and P^+ regions were doped with arsenic to typical levels of 7×10^{15} and 1×10^{17} cm^{-3}, respectively, and the N^+ region was doped with iodine to a concentration of 3×10^{17} cm^{-3}. Diodes were defined by etching circular trenches to produce 64 element linear arrays with common contact to the P^+ region at each end. These "slotted" mesa devices were passivated with 0.3-μm thick ZnS and metalised with Cr/Au. Finally, the electrical contact to the mesas was achieved by indium bump bonding the array onto a gold lead-out pattern on a sapphire carrier.

The heterostructure devices exhibit diffusion limited behaviour with R_oA product typically 10 times that obtained from simple p–n homojunction diodes. Below 140 K

Table 6
Properties and performance of a variety of HgCdTe APDs ranging in size from 50–300 μm diameter (after Ref. [99])

Diameter (μm)	Bias (V)	Responsivity (A/W)	$\eta \times G$	Noise (pA/$\sqrt{}$Hz)	Total dark (nA)	NEP (nW)	Capacitance (pF)
50	77.7	13.1	10.6	1.9	66	0.92	0.2
100	72.9	12.4	9.9	1.4	120	0.72	0.3
200	76.9	12.8	10.2	3.6	580	1.8	0.8
300	68.9	12.5	10	3	810	1.6	1.6

the resistance becomes independent of temperature due to a surface shunting effect. Fig. 39 shows the variation of R_0A product with wavelength at 145 K. The solid line is calculated assuming that the leakage currents are generated by Auger process in the central π region of the device. The experimental results are slightly below this line because of Shockley-Read processes or surface recombination.

The Auger suppression devices suffer from large $1/f$ noise and hence the improvement in the detectivity resulting from the reduced leakage currents can only be realized at high frequencies. However, this is not a problem for heterodyne systems which employ intermediate frequencies above 40 MHz. A thermoelectrically cooled device operated at 260 K has been studied as a heterodyne detector [103]. The noise equivalent power (NEP) of the receiver has been estimated to be 2×10^{-19} WHz^{-1} for frequencies above the $1/f$ knee ($\approx$15 MHz) and a frequency response above 100 MHz should be possible by reducing the series resistance.

Recently, a new insight into source of $1/f$ noise of non-equilibrium HgCdTe photodiodes has been presented by Jóźwikowski et al. [104]. It is predicted that low-frequency noise is due to the fluctuations of current density caused by mobility fluctuations assisted by electric field.

8.2. Photoemissive detectors

In 1973, Shepherd and Yang of Rome Air Development Center proposed the concept of silicide Schottky-barrier detector FPAs as much more reproducible alternative to HgCdTe FPAs for IR thermal imaging [105]. For the first time it became possible to have much more sophisticated readout schemes—both detection and readout could be implemented in one common silicon chip. Since then, the development of the Schottky-barrier technology progressed continuously and currently offers large IR image sensor formats. These trends in IR FPA development show that the IR community today prefers more producible technologies with higher uniformity to the technology based on the narrow gap semiconductors, which still have serious material problems. Such attributes as: monolithic construction, uniformity in responsivity and signal to noise (the performance of an IR system ultimately depends on the ability to compensate the nonuniformity of an FPA using external electronics and a variety of temperature references), and absence of

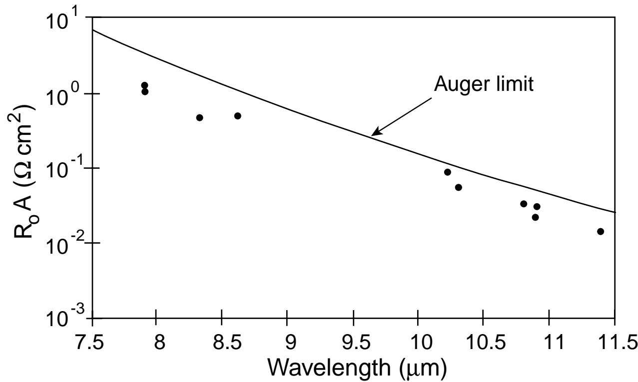

Fig. 39. Variation of R_0A with wavelength for P–π–N HgCdTe heterostructure device at 145 K. The solid line is calculated for an ideal, diffusion limited diode (after Ref. [102]).

discernible $1/f$ noise; make Schottky-barrier devices a formidable contender to the main-stream infrared systems and applications [106–112].

8.2.1. Schottky-barrier photoemissive detectors

The most popular Schottky-barrier detector is the PtSi detector, which can be used for the detection in the 3–5 μm spectral range (see Fig. 40). Radiation is transmitted through the p-type silicon and is absorbed in the metal PtSi (not in the semiconductor—see Fig. 41), producing hot holes which are then emitted over the potential barrier into the silicon, leaving the silicide charged negatively. This fundamental difference in detection mechanism underlies the unique properties of Schottky sensors, including their exceptional spatial uniformity and their modified Fowler spectral response. Negative charge of silicide is transferred to a CCD by the direct charge injection method.

The photoyield (electrons/photons) for the process is given by the modified Fowler equation as [106]

$$Y = \frac{1.24C_1(1-\lambda/\lambda_c)^2}{\lambda}, \tag{34}$$

where the cutoff wavelength λ_c in μm is $1.24/\phi_{ms}$ and ϕ_{ms} is the barrier height in eV. C_1 is an emission coefficient that is dependent upon the physical and geometric parameters of the Schottky electrode. Values of λ_c and C_1 as high as 6 μm and $0.5(\mathrm{eV})^{-1}$, respectively, have been obtained in PtSi–Si [106]. Schottky photoemission is independent of such factors as semiconductor doping, minority carrier lifetime, and alloy composition, and, as a result of this, has spatial uniformity characteristics that are far superior to those of other detector technologies. Uniformity is only limited by the geometric definition of the detectors. The effective quantum efficiency in the 3–5 μm atmospheric window is very low, of the order of 1%, but useful sensitivity is obtained by means of near full frame integration in area arrays.

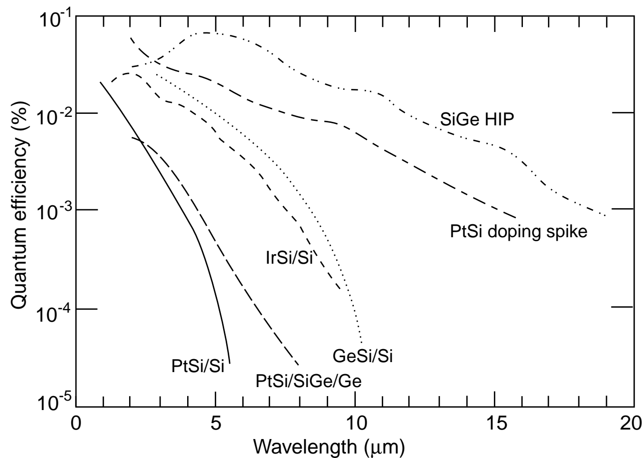

Fig. 40. Comparison of various infrared detectors based on internal photoemission for PtSi, IrSi, PtSi/SiGe, PtSi doping spike, and SiGe/Si HIP (after Ref. [112]).

The fundamental source of dark current in the devices is thermionic emission of holes over the potential barrier and it's magnitude is given by Richardson's equation [113]. The cooling requirements of photoemissive detectors are comparable to the extrinsic devices, and while an extension of the technology to the long wavelength band is possible using IrSi (see Fig. 40) this will require cooling below 77 K [114].

The Schottky-barrier detector is typically operated in backside illumination mode. The quantum efficiency has been improved by thinning PtSi film. The thinning is effective down to the PtSi thickness of 2 nm [108]. Another means of improving responsivity is implementation of an "optical cavity." The optical cavity structure consists of the metal reflector and the dielectric film between the reflector and metal electrode of the Schottky-barrier diode. According to fundamental optical theory, the effect of the optical cavity depends on the thickness and refractive index of the dielectric films, and the wavelength. The conventional 1/4 wavelength design for the optical cavity thickness is a good first approximation for optimising the responsivity [115].

The main advantage of the Schottky-barrier detectors is that they can be fabricated as monolithic arrays in a standard silicon VLSI process. Typically, the silicon array is completed up to the Al metallizational step. A Schottky-contact mask is used to open SiO_2 surface to p-type (1 0 0) silicon (with resisitivity 30–50 Ωcm) at the Schottky-barrier detector location. In the case of PtSi detectors, a very thin layer of Pt (1–2 nm) is deposited and sintered (annealed at a temperature in the range of 300–600°C) to form PtSi and the unreacted Pt on the SiO_2 surfaces is removed by dipetching in hot aqua regia [116]. The Schottky-barrier structure is then completed by a deposition of a suitable dielectric (usually SiO_2) for forming the "resonant cavity," removing this dielectric outside the Schottky-barrier regions, and depositing

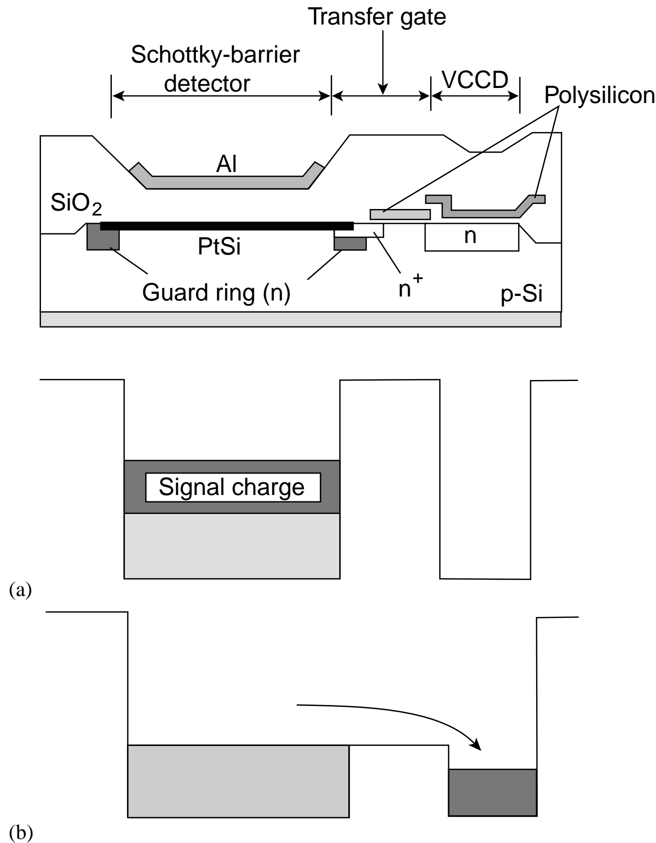

Fig. 41. Typical construction and operation of PtSi Schottky-barrier IR FPA designed with interline transfer CCD readout architecture. (a) and (b) show the potential diagrams in the integration and readout operations, respectively (after Ref. [110]).

and defining Al for the detector reflector and the interconnects of the Si readout multiplexer. In the case of the 10 μm IrSi Schottky-barrier detectors, the IrSi was formed by in situ vacuum annealing and the unreacted Ir was removed by reactive ion etching [117].

The progress of the Schottky-barrier FPA technology has been constant [118]. The first Schottky-barrier FPA was the 25×50 element IR-CCD developed at RCA laboratories under contract to the Rome Air Development Center [119]. At the present time Schottky-barrier FPAs represent the most advanced FPAs technology for medium wavelength applications (see Table 7). Scanning PtSi FPAs with up to 4×4096 elements [120] and 2048×16 TDI [121] elements were developed for space-borne remote sensing applications. Review of different configuration of staring Schottky-barrier FPAs is given e.g. by Kosonocky [108,109] Kimata and Tsubouchi, [110] and Kimata et al. [110,112,118].

Table 7
Specifications and performances of typical PtSi Schottky-barrier FPAs (after Ref. [112])

Array size	Readout	Pixel size (μm^2)	Fill factor (%)	Saturation (e^-)	NEDT/(*f*/#) (K)	Year	Company
512×512	CSD	26×20	39	1.3×10^6	0.07(1.2)	1987	Mitsubishi
512×488	IL-CCD	31.5×25	36	5.5×10^5	0.07(1.8)	1989	Fairchild
512×512	LACA	30×30	54	4.0×10^5	0.10(1.8)	1989	RADC
640×486	IL-CCD	25×25	54	5.5×10^5	0.10(2.8)	1990	Kodak
640×480	MOS	24×24	38	1.5×10^6	0.06(1.0)	1990	Sarnoff
640×488	IL-CCD	21×21	40	5.0×10^5	0.10(1.0)	1991	NEC
640×480	HB/MOS	20×20	80	7.5×10^5	0.10(2.0)	1991	Hughes
1040×1040	CSD	17×17	53	1.6×10^6	0.10(1.2)	1991	Mitsubishi
512×512	CSD	26×20	71	2.9×10^6	0.03(1.2)	1992	Mitsubishi
656×492	IL-CCD	26.5×26.5	46	8.0×10^5	0.06(1.8)	1993	Fairchild
811×508	IL-CCD	18×21	38	7.5×10^5	0.06(1.2)	1996	Nikon
801×512	CSD	17×20	61	2.1×10^6	0.04(1.2)	1997	Mitsubishi
1968×1968	IL-CCD	30×30	—	—	—	1998	Fairchild

The details of the geometry, and the method of charge transfer differ for different manufacturers. The design of a staring Schottky-barrier FPAs for given pixel size and design rules, involves a trade-off between the charge handling capacity and the fill factor. Most of the reported Schottky-barrier FPAs have the interline transfer CCD architecture. The typical cross section view of the pixel and its operation in interline transfer CCD architecture is shown in Fig. 41. The pixel consists of a Schottky-barrier detector with an optical cavity, a transfer gate, and a stage of vertical CCD. The n-type guard ring on the periphery of the Schottky-barrier diode reduces the edge electric field and suppresses dark current. The effective detector area is determined by the inner edge of the guard ring. The transfer gate is an enhancement MOS transistor. The connection between detector and the transfer gate is made by an n^+ diffusion. A buried-channel CCD is used for the vertical transfer. During the optical integration time the surface-channel transfer gate is biased into accumulation. The Schottky-barrier detector is isolated from the CCD register in this condition. The IR radiation generates hot holes in the PtSi film and some of the excited hot holes are emitted into the silicon substrate leaving excess electrons in the PtSi electrode. This lowers the electrical potential of the PtSi electrode. At the end of the integration time, the transfer gate is pulsed-on to read out the signal electrons from the detector to the CCD register. At the same time, the electrical potential of the PtSi electrode is reset to the channel level of the transfer gate.

A unique feature of the Schottky-barrier IR FPAs is the built-in blooming control (blooming is a form of crosstalk in which a well saturates and the electrons spill over into neighbouring pixels). A strong illumination forward biases the detector and no further electrons are accumulated at the detector. The small negative voltage developed at the detector is not sufficient to forward bias the guard ring to the extent that electrons are injected to the CCD register through the silicon region under the

transfer gate. Therefore, unless the vertical CCD has an insufficient charge handling capacity, blooming is suppressed perfectly in the Schottky-barrier IR FPA.

The responsivity of the FPAs is proportional to their fill factor, and improvement in the fill factor has been one of the most important issues in the development of imagers. For improving the fill factor a readout architecture called the charge sweep device (CSD) developed by Mitsubishi Corporation is also used. Kimata and co-workers have developed a series of IR image sensors with the CSD readout architecture with array sizes from 256×256 to 1040×1040 elements. Specifications and performance of these devices are summarised in Table 8. The effectiveness of this readout architecture is enhanced as the design rule becomes finer. Using a 1.2 μm CSD technology, a large fill factor of 71% was achieved with a $26 \times 20\,\mu m^2$ pixel in the 512×512 monolithic structure [122]. The NETD was estimated as 0.033 K with $f/1.2$ optics at 300 K. The 1040×1040 element CSD FPA has the smallest pixel size ($17 \times 17\,\mu m^2$) among two-dimensional IR FPAs. The pixel was constructed with 1.5 μm design rules and has 53% fill factor [123]. If the signal charges of 1040×1040 pixels are read out from one output port at the TV compatible frame rate, an unrealistic pixel rate of about 40 MHz is required. Therefore, a 4-output chip design was adopted [124]. The array of 1040×1040 pixels is divided into four blocks of 520×520 pixels. Each block has a horizontal CCD and a floating diffusion amplifier. 1-million pixel data at a 30 Hz frame rate can be readout by operating each horizontal CCD at a 10 MHz clock frequency. The NEDT of 1040×1040 element FPA at 300 K with an $f/1.2$ cold shield and a 30 Hz frame is 0.1 K. More recently, a high-performance 801×512-element PtSi Schottky-barrier infrared image sensor has

Table 8
Specifications and performance of 2-D PtSi Schottky-barrier FPAs with CSD readout (after Ref. [118])

Array size	256×256	512×512	512×512	512×512	801×512	1040×1040
Pixel size (μm^2)	26×26	26×20	26×20	26×20	17×20	17×17
Fill factor (%)	58	39	58	71	61	53
Chip size (mm^2)	9.9×8.3	16×12	16×12	16×12	16×12	20.6×19.4
Pixel capacitor	Normal	Normal	High-C	High-C	High-C	High-C
CSD	4-phase	4-phase	4-phase	4-phase	4-phase	4-phase
HCCD	4-phase	4-phase	4-phase	4-phase	4-phase	4-phase
Number of outputs	1	1	1	1	1	4
Interface	Non integration	Field integration	Frame/Field integration	Frame/Field integration	Flexible	Field integration
Number of I/O pins	30	30	30	30	25	40
Process technology	NMOS/ CCD 2 poly/2 Al	NMOS/ CCD 2 poly/2 Al	NMOS/ CCD 2 poly/2 Al	NMOS/ CCD 2 poly/2 Al	CMOS/ CCD 2 poly/2 Al	NMOS/ CCD 2 poly/2 Al
Design rule (μm)	1.5	2	1.5	1.2	1.2	1.5
Thermal response (ke/K)	—	13	—	32	22	9.6
Saturation (e)	0.7×10^6	1.2×10^6	—	2.9×10^6	2.1×10^6	1.6×10^6
NETD (K)	—	0.07	—	0.033	0.037	0.1

been developed with an enhanced CSD readout architecture [125,126]. The developed image sensor has a large fill factor of 61% in spite of a small pixel size of $17 \times 20\,\mu m^2$. The NEDT was 0.037 K with $f/1.2$ optics at 300 K. The total power consumption of the device was less than 50 mW.

Current PtSi Schottky barrier FPAs are mainly manufactured in 150 mm wafer process lines with around 1 μm lithography technologies; the most advanced Si technology offers 200 mm wafers process with 0.25 mm design rules. Furthermore, 300 mm Si wafer processes with 0.15 μm fine patterns will soon available. However, the performance of monolithic PtSi Schottky-barrier FPAs has reached a plateau, and a slow progress from now on is expected.

8.2.2. *Novel internal photoemissive detectors*

The recent development in the MBE technology made it possible to fabricate high quality Ge_xSi_{1-x} (GeSi) thin films onto silicon substrates, and several works concerning the realisation of the idea of utilising the internal photoemission of GeSi/Si heterojunction diodes for IR detection have been reported [127–136]. The band gap energy of the strained SiGe is smaller than that of Si, and can be tailored by changing the composition and doping concentration. The cutoff wavelength of the device can be varied from 2 to 25 μm [129,130]. Fig. 40 compares the quantum efficiencies of several technologies: a conventional PtSi/p-Si detector, IrSi/p-Si detector, PtSi/p-$Si_{0.85}Ge_{0.15}$/p-Si detector, PtSi/p-Si detector with a 1 nm doping spike of 2×10^{20} cm^{-3} boron, and p-$Si_{0.7}Ge_{0.3}$/p-Si heterojunction detector with a boron doping of 5×10^{20} cm^{-3} in the SiGe layer.

The first 400×400 element GeSi/Si heterojunction internal photoemission (HIP) array with a CCD readout has been developed by Tsaur et al. [131,132]. They demonstrated uncorrected thermal imagers operated at 53 K with cutoff wavelength at 9.3 μm and with minimum resolvable temperature difference of 0.2 K ($f/2.35$). The responsivity nonuniformity of this array was less than 1%. Next, they improved the performance of Ge_xSi_{1-x}/Si 320×244 and 400×400 element arrays with $\lambda_c = 10\,\mu m$ (pixel sizes 40×40 and $28 \times 28\,\mu m^2$ and fill factors 43 and 40%, respectively) incorporating monolithic Si microlens arrays [133]. Recently, Wada et al. [136] have developed a high-resolution 8–12-μm 512×512 element FPA with pixel size $34 \times 34\,\mu m^2$ and a fill factor of 59%. A NEDT of 0.08 K ($f/2.0$) was obtained at 43 K with 300 K background with a very small responsivity dispersion of 2.2% and high pixel yield of 99.998%.

The concept of homojunction internal photoemissive detector for IR was first realised in 1988 by Tohyama et al. [137] Recently, various detector approaches based on a high-low Si and GaAs homojunction interfacial workfunction internal photoemission (HIWIP) junctions have been discussed by Perera et al. [138–143] The operation of HIWIP detectors is based on the internal photoemission occurring at the interface between a heavily doped absorber/emitter layer and an intrinsic layer, with the cutoff wavelength mainly determined by the interfacial workfunction. The detection mechanism involves far infrared (FIR) absorption in the highly doped thin emitter layers by free carrier absorption followed by the internal photoemission of photoexcited carriers across the junction barrier and then collection.

Fig. 42 shows the basic structure and energy band diagram for a n^+–i HIWIP detector. The structure consists of the emitter, intrinsic, and collector layers, with the respective thickness represented by W_e, W_i, and W_c. The top contact layer is formed as a ring surrounding the active area to minimize absorption loss. The collector layer is moderately doped and has a relatively low resistance due to the impurity band conduction, while it is still transparent in the FIR range when the photon energy is smaller than the impurity ionisation energy. The interfacial work function is given by $\Delta = \Delta E_c - E_F - \Delta\phi$, where ΔE_c is the conduction band edge offset due to band gap narrowing in the heavily doped emitter layer, E_F is the Fermi energy, and $\Delta\phi$ is a lowering of interfacial barrier height due to image force effect. In order to get high internal quantum efficiency, the emitter layer thickness should be thin enough, in spite of the reduction of the photon absorption efficiency. Thus, the optimal thickness is a tradeoff of photon absorption and hot electron scattering.

Si HIWIP FIR detectors could have a performance comparable to that of conventional Ge FIR photoconductors [145] or Ge BIB detectors [146]. In addition to Si, significant bandgap shrinkage has been observed for heavily doped p-GaAs. Better carrier transport properties of GaAs may produce improved performance for this type of device. p-GaAs HIWIP FIR detectors show great potential to become a strong competitor in FIR applications: responsivity of $3.10 \pm 0.p5$ A/W, quantum efficiency of 12.5% and detectivity of 5.9×10^{10} cmHz$^{1/2}$/W at 4.2 K, for λ_c from 80 to 100 μm.

8.3. Extrinsic silicon and germanium detectors

Research and development of extrinsic IR photodetectors have been ongoing for more than 40 years. In the 1950s and 1960s, germanium could be made purer than silicon; doped Si then needed more compensation than doped Ge and was characterised by shorter carrier lifetimes than extrinsic germanium. Today, the problems with producing pure Si have been largely solved, with the exception of boron contamination. Si has several advantages over Ge; for example, three orders of magnitude higher impurity solubilities are attainable, hence thinner detectors with

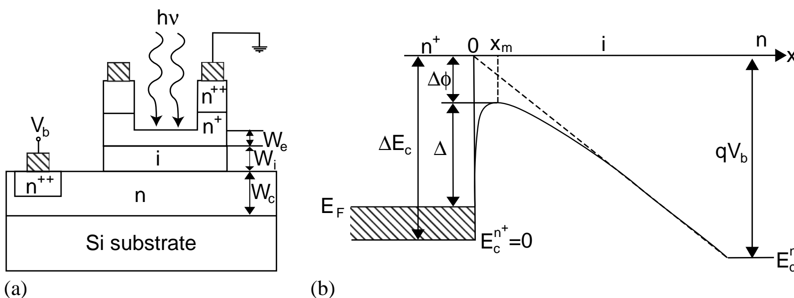

Fig. 42. Basic structure (a) and energy band diagram (b) of a frontside illuminated n^+–i HIWIP (after Ref. [144]).

better spatial resolution can be fabricated from silicon. Si has lower dielectric constant than Ge, and the related device technology of Si has now been more thoroughly developed, including contacting methods, surface passivation and mature MOS and CCD technologies. Moreover, Si detectors are characterised by superior hardness in nuclear radiation environments. The well-established technology also helps in the manufacturing of uniform detector arrays and the formation of low-noise contacts. Although the potential of large extrinsic silicon focal plane arrays for terrestrial applications has been examined, interest has declined in favour of HgCdTe and InSb with their more convenient operating temperatures. Strong interest in doped silicon continues for space applications, particularly in low background flux and for wavelengths from 13 to 20 μm, where compositional control is difficult for HgCdTe. The shallower impurity energies in germanium allow detectors with spectral response up to beyond 100 μm wavelength and major interest still exists in extrinsic germanium for wavelengths beyond about 20 μm.

The development and manufacture of extrinsic photodetectors are mainly concentrated in the USA and Russia. The programs on the use of off-atmospheric astronomy have spread especially intensively after the outstanding success of the Infrared Astronomical Satellite (IRAS) [147,148], which used 62 discrete photodetectors arranged in the focal plane. In the USA, a number of NASA-supported programs have been initiated by various research centres and universities.

8.3.1. Silicon and germanium photoconductive detectors

Table 9 presents a summary of the properties of some doped silicon and doped germanium devices for low-background space applications, while Fig. 43 illustrates the spectral response for several extrinsic detectors. Note that the exact long wavelength spectral cutoff is a function of the impurity doping density, with higher densities giving slightly longer spectral response. The longer spectral response of the blocked impurity band (BIB) Si:As device compared with the bulk Si:As device is due to the higher doping level in the former that reduces the binding energy of an electron. Typical quantum efficiencies are in the range of 10–50% at the response peak. Extrinsic detectors are frequently cooled with liquid He for applications such as ground- and space-based astronomy. Closed cycle two- and three-stage refrigerators are available for use with these detectors for cooling to 20–60 and 10–20 K, respectively.

For the 3–5-μm range, Si doped with the acceptor In (Si:In) offers an ideal choice. The In hole ground state lies at $E_v + 156\,\text{meV}$ (E_v is the energy at the valence band top) leading to a photoconductive onset at $\lambda \approx 8\,\mu\text{m}$, with peak response at 7.4 μm. For the longer wavelength detectors, Ga is chiefly used. However, low activation energy (0.074 eV) of Ga is not optimum for use in the 8–14 μm window and unnecessarily contributes to its low operational temperature. Nevertheless, a 128×192 Si:Ga FPA has been used in an IR camera for application in cryogenic windtunnel [151]. A number of other impurities have been investigated. The comprehensive reviews of Si and Ge detectors operated in various spectral ranges are presented in Bratt [152] and Sclar's papers [149,153–156].

Table 9
Status summary of some Si and Ge IR detectors for low-background applications (after Ref. [149])

Detector	$(\Delta E)_{opt}$ (meV)	λ_p (μm)	λ_c(T) μm(K)	$\eta(\lambda_p)$ (%)	Φ_B (ph cm^{-2} s^{-1})	NEP (WHz$^{-1/2}$)	λ(μm); T(K); f(Hz)
Si:As	53.76	23	24–24.5 (5)	50(T)	9×10^{6}	0.88×10^{-17}	(19;6;1.6)
				20(L)	6.4×10^{7}	4.0×10^{-17}	(23;5;5)
Si:P	45.59	24/26.5	28/29 (5)	~30(T)	2.5×10^{8}	7.5×10^{-17}	(28;4.2;10)
Si:Sb	42.74	28.8	31 (5)	58(T)	1.2×10^{8}	5.6×10^{-17}	(28.8;5;5)
				13(L)	1.2×10^{8}	5.5×10^{-17}	(28.8;5;5)
Si:Ga	74.05	15.0	18.4 (5)	47(T)	6.6×10^{8}	1.4×10^{-17}	(15;5;5)
Si:Bi	70.98	17.5	18.5 (27)	34(L)	$<1.7\times10^{8}$	3×10^{-17}	(13;11;–)[a]
Ge:Li	9.98		125 (calc)		8×10^{8}	1.2×10^{-16}	(120;2;13)
Ge:Cu	43.21	23	29.5 (4.2)	50	5×10^{10}	1.0×10^{-15}	(12;4.2;1)
Ge:Be[b]	24.81	39	50.5 (4.2)	100[b]	1.9×10^{10}	1.8×10^{-16}	(43;3.8;20)
Ge:Ga	11.32	94	114 (3)	34	6.1×10^{9}	5.0×10^{-17}	(94;3;150)
Ge:Ga[b]	11.32	94	114 (3)	~100[b]	5.1×10^{9}	2.4×10^{-17}	(94;3;150)
Ge:Ga[b](s)[c]	~6	150	193 (2)	73[b]	2.2×10^{10}	5.7×10^{-17}	(150;2;150)

T and L indicate transverse and longitudinal geometry detector.
[a] signal integrated for 1 s.
[b] results obtained with an integrating cavity.
[c] (s): stress = 6.6×10^{3} kg cm^{-2}.

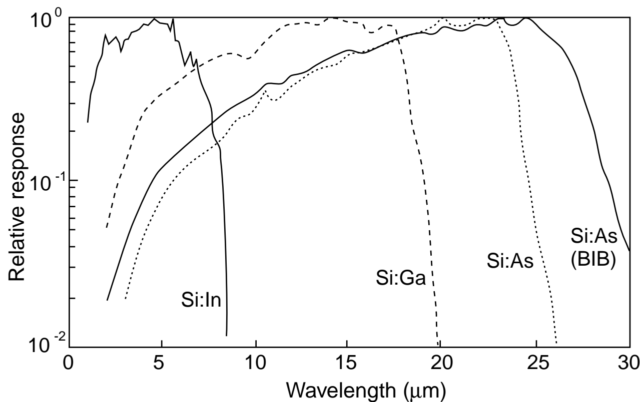

Fig. 43. Examples of extrinsic silicon detector spectral response. Shown are Si:In, Si:Ga, and Si:As bulk detectors and a Si:As BIB (after Ref. [150]).

Germanium extrinsic detectors are still of interest for very long wavelengths. Very shallow donors, such as Sb, and acceptors, such as B, In or Ga, provide cut-off wavelengths in the region of 100 μm. Ge:Be photoconductors cover the spectral range from ≈30 to 50 μm. Ge:Ga photoconductors are the best low background photon detectors for the wavelength range from 40 to 120 μm [157]. However, typical values of quantum efficiency range from 10 to 20%.

Application of uniaxial stress along the [100] axis of Ge:Ga crystals reduces the Ga acceptor binding energy, extending the cutoff wavelength to $\approx 240\,\mu m$ [158,159]. The stressed Ge:Ga photoconductor systems have found a wide range of astronomical and astrophysical applications [160,161].

8.3.2. Blocked impurity band devices

In order to maximise the quantum efficiency and detectivity of extrinsic photoconductors, the doping level should be as high as possible. This is particularly important when the devices are required to be radiation hard and are made as thin as possible to minimise the absorbing volume for ionising radiation. The limit to the useful doping which is possible in conventional extrinsic detectors is set by the onset of impurity banding. This occurs when the doping level is sufficiently high that the wavefunctions of neighbouring impurities overlap and their energy level is broadened to a band which can support hopping conduction. When this occurs it limits the detector resistance and photoconductive gain, and also increases the dark current and noise. In Si:As, for example, theses effects become important for doping levels above $7 \times 10^{16}\,cm^{-3}$. To overcome the impurity banding effect and in addition, to improve radiation hardness and reduce the optical cross-talk between adjacent elements of an array, the blocked impurity band (BIB) device was proposed. BIB detectors have demonstrated other significant advantages, such as freedom from the irregular behaviour typical of photoconductive detectors (spiking, anomalous transient response), increased frequency range for constant responsivity and superior uniformity of response over the detector area and from detector to detector.

BIB devices made from either doped silicon or doped germanium are sensitive to infrared wavelength range located between 2 and 220 μm. They were first conceived at Rockwell International Science Center in 1977 by Petroff and Stapelbroeck [162]. At the beginning, most of the BIB detector development has centred on arsenic-doped silicon, Si:As [163,164]. The Si:As detector is sensitive to IR radiation only in the 2–30 μm wavelength range. Extension of BIB performance to longer wavelengths, awaited the development of suitable materials. Data on antimony-doped silicon (Si:Sb) BIB detectors [165] for wavelengths between 2 and 50 μm, and gallium-doped germanium (Ge:Ga) BIB detectors [166–168] for wavelengths between 50 and 220 μm have been published.

A BIB detector structure based on epitaxially grown n-type material is displayed in Fig. 44. The active layer is sandwiched between a higher doped degenerate substrate electrode and an undoped blocking layer. Doping of active layer with a thickness value in the 10-μm range is high enough for the onset of an impurity band in order to display a high quantum efficiency for impurity ionization (in the case of Si:As BIB, the active layer is doped to $\approx 5 \times 10^{17}\,cm^{-3}$). The device exhibits a diode-like characteristics, except that photoexcitation of electrons takes place between the donor impurity and the conduction band. The heavily doped n-type IR-active layer has a small concentration of negatively charged compensating acceptor impurities ($N_a \approx 10^{13}\,cm^{-3}$). In the absence of an applied bias, charge neutrality requires an equal concentration of ionosed donors. Whereas the negative charges are fixed at acceptor sites, the positive charges associated with ionised donor sites (D^+ charges)

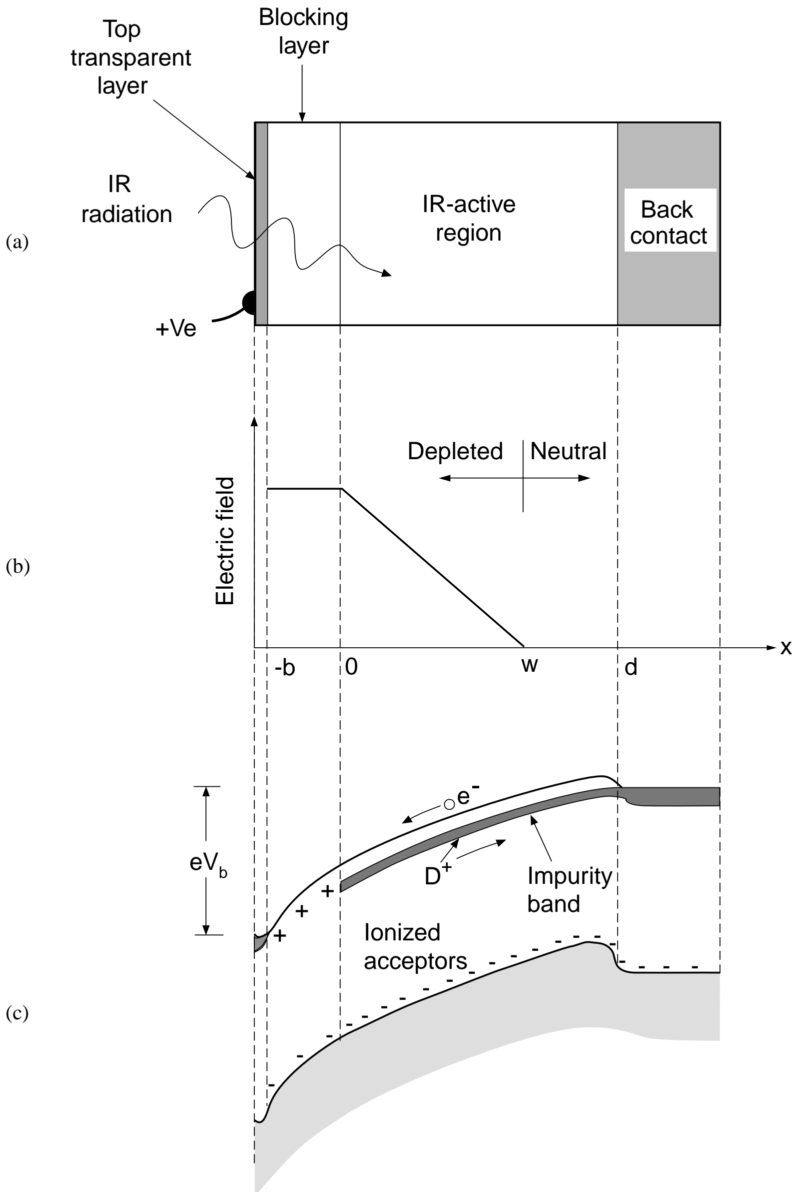

(a)

(b)

(c)

Fig. 44. Blocked impurity band detector: (a) cross section, (b) electric field, and (c) energy-band diagram of positively biased detector.

are mobile. The D^+ charges can propagate through the IR-active layer via the mechanism of hopping between occupied (D^0) and vacant (D^+) neighbouring sites. Applying a positive bias to the transparent contact creates a field that drives the pre-existing D^+ charges towards the substrate, while the undoped blocking layer

prevents the injection of new D^+ charges. A region depleted of D^+ charges is therefore created, with a width depending on the applied bias and on the compensating acceptor concentration. It should be stressed that the local electric field at the substrate injecting contact is near zero. Consequently spiking, anomalous transition pulse characteristics attributed to field effects at this contact are expected to vanish. For a detailed analysis of the BIB detector see Szmulowicz and Madarsz [169].

Impressive progress has been achieved in Si BIB array technology [170]. BIB devices, in large staring array formats are now becoming commercially available. They open the possibility for astronomers to efficiently observe in the VLWIR spectral range, where at high altitudes the atmosphere has reasonable transmission. The best results have been achieved to date for Si:As BIB hybrid FPAs (HFPAs) produced by Hughes Technology Center in Carlsbad [171,172] and Rockwell International Science Center in Anaheim [173].

HFPAs with Si:As BIB detectors have been optimised for low, moderate, and high IR backgrounds in 128×128-pixel formats, and a high-flux 256×256-pixel version. For high-flux applications, both the detector array and multiplexer are optimised to handle incident flux densities $>10^{16}$ photons $cm^{-2} s^{-1}$, providing high spatial uniformity, high pixel operability, and background limited performance down to low frequencies (<10 Hz). Table 10 summarises the specifications for low-cost, high performance Si:As BIB HFPAs. The effective fill-factor of the arrays is nearly 100% because the electric field established between a pixel's top contact and the common transparent contact tends to fringe outward. The 256×256 format with 30 μm pixels and 240×320 format with 50 μm pixels are available for low- and high background applications, respectively. Other formats available include 128×128 and 192×12, and 64×20 [44,174]. Antimony-doped silicon (Si:Sb) arrays and 128×128-pixel Si:Sb HFPAs having response to wavelengths >40 μm have been also demonstrated, primarily for use at low and moderate backgrounds [172]. Germanium BIB devices have been developed on an experimental basis, but have not yet been reported in large two dimensional array formats.

8.4. InSb photodiodes

InSb material is more mature than HgCdTe and good-quality larger than 7-cm diameter bulk substrates are commercially available [175]. InSb photodiodes have been available since the late fifties and they are generally fabricated by impurity diffusion (usually Cd) and ion implantation (usually Be^+ or B^+). Epitaxy is not used; instead, the standard manufacturing technique begins with bulk n-type single crystal wafers with donor concentration about 10^{15} cm^{-3}. A highly controlled diffusion process allows p-layer diffusion to occur with little surface damage, eliminating the need for deep diffusion and subsequent etch-back. The accuracy of the photolithography along with the controlled diffusion process provide excellent uniformity of response. The status of InSb photodiode technology for a wide variety of linear and FPAs have been presented by Wimmers et al. [176,177].

Table 10
Specifications for Si:As BIB FPAs (after Ref. [173])

Format	256×256	240×320
Pixel size	30 μm	50 μm
Spectral response	2–28 μm	2–28 μm
Fill factor	$>90\%$	$>95\%$
Peak quantum efficiency	$>40\%$	$>40\%$
Operability	$\geqslant 99\%$	$\geqslant 99\%$
Response nonuniformity (σ/mean)	$\leqslant 9\%$	$\leqslant 10\%$
Operating temperature	4–10 K	4–10 K
Electron rms noise	$<100\,e^-$	$<300\,e^-$ at 2 Hz
e/sec dark current	<100	<100
Pixel charge storage capacity	3×10^5	5×10^7
Number of outputs	4	16 and 32 option

Typical InSb photodiode RA product at 77 K is $2 \times 10^6\,\Omega\text{cm}^2$ at zero bias and $5 \times 10^6\,\Omega\text{cm}^2$ at a slight reverse bias of approximately 100 mV. This characteristic is beneficial when the detector is used in the capacitive discharge mode. As element size decreases below $10^{-4}\,\text{cm}^{-2}$ the ratio of the circumference to area is increased, and some slight degradation in resistance due to surface leakage occurs.

InSb photovoltaic detectors are widely used for ground-based infrared astronomy and for applications aboard the Space Infrared Telescope Facility (SIRTF). For applications in astrophysics, these devices are very often operated at 4–7 K with a resistive or capacitive transimpedance amplifier to achieve the lowest noise performance. The photodiodes, whose performance is optimised for 60–80 K operation, have been shown to lose long-wavelength quantum efficiency at lower temperatures, due to a decrease in the minority carrier lifetime in the n-region [178]. Thus, the process of device optimisation must be redone for low temperature applications with emphasis on reducing detector capacitance while simultaneously maximising the quantum efficiency [179]. A reduction in doping density in the n-type region to $\approx 10^{14}\,\text{cm}^{-3}$, along with other minor process modifications, minimises decrease in the carrier lifetime, providing an added benefit of reduced capacitance. This approach also reduces the RA product slightly, but the RA product still increases exponentially with decreasing temperature, until detector resistance once again is not a significant noise contribution.

InSb photodiodes can also be operated in the temperature range above 77 K. Of course, the RA products degrade in this region. At 120 K, RA products of $10^4\,\Omega\text{cm}^2$ are still achieved with slight reverse bias, making BLIP operation possible. The quantum efficiency in InSb photodiodes optimised for this temperature range remains unaffected up to 160 K [178].

InSb devices are usually made with both p–n junction as well as MIS capacitors. In p–n junctions, the base material is n-type with the minority diffusion length of about 30 μm. Staring arrays of backside illuminated, direct hybrid InSb detectors in different formats are available with readouts suitable for both high-background $f/2$

operation and for low-background astronomy applications [180–185]. An array size of 1024 × 1024 is possible because the InSb detector material is thinned to less than 10 μm (after surface passivation and hybridisation to a readout chip) which allows it to accommodate the InSb/silicon thermal mismatch [185]. Table 11 shows Santa Barbara Research Center (SBRC) InSb FPA characteristics. The 1024 × 1024 architecture consists of four independent 512 × 512 quadrants with eight outputs per quadrant. Linear array formats of 64, 128 and 256 elements are also produced with frontside-illuminated detectors for both high-background and astronomy applications [177,186,187]. Element sizes depend on device format and range from 20 × 20 to 200 × 200 μm.

The cryogenically cooled InSb and HgCdTe arrays have comparable array size and pixel yield at MWIR spectral band. However, wavelength tunability and high quantum efficiency have made HgCdTe the preferred material.

8.5. InGaAs photodiodes

The energy gap of the $In_{1-x}Ga_xAs$ ternary system spans from 0.35 eV (3.5 μm) for InAs to 1.43 eV (0.87 μm) for GaAs. $In_{0.53}Ga_{0.47}As$ alloy ($E_g = 0.73$ eV, $\lambda_c = 1.7$ μm) lattice matched to the InP substrate has already been shown to be a suitable detector material for near-IR (1.0–1.7-μm) spectral range. Having lower dark current and noise than indirect-bandgap germanium, the competing near-IR material, the material is addressing both entrenched applications including lightwave communication systems, low light level night vision, and new applications such as remote sensing, eye-safe range finding and process control [188–196]. The fundamental device parameters (energy band-gap, absorption coefficient, and background carrier concentration) distinguish InGaAs from germanium [197]. Low background doping level ($n = 1 \times 10^{14}$ cm^{-3}) and high mobilities (11500 cm^2/Vs) for InGaAs at room temperature were achieved [198]. By changing the alloy composition of the InGaAs

Table 11
InSb astronomy focal plane arrays characteristics (after Refs. [180,183])

	Configuration	
	256 × 256	1024 × 1024
Number of pixels	65 536	1 048 576
Architecture		4-fully independent 512 × 512 quadrants
Pixel size	30 μm square	27 μm square
Effective fill factor	100%	100%
Readout type	PMOS using a SPD	CMOS or PMOS using a SPD
Number of outputs	4	32 (8 per quadrant)
Operating temperature	50 K	35 K
Dark current	<400 e/s	<0.1 e/s
Noise	<100 e rms	<25 e rms
Quantum efficiency	>80%	>80%
Defective pixels	<3%	<0.5%

absorption layer, the photodetector responsivity can be maximised at the desired wavelength of the end user to enhance the signal to noise ratio.

InGaAs-detector processing technology is similar to that used with silicon, but the detector fabrication is different. The InGaAs detector's active material is deposited onto a substrate using chloride VPE or MOCVD [199] techniques adjusted for thickness, background doping, and other requirements. Planar technology evolved from the older mesa technology and at present is widely used due to its simple structure and processing as well as the high reliability and low cost. When the indium content of the alloy is increased, the long wavelength cut-off extends to cover the entire traditional near IR band [200,201]. However, due both to the smaller bandgap and to interface defects resulting from the lattice mismatch, longer wavelength InGaAs photodiodes have considerably higher dark currents than those fabricated from the lattice-matched alloy. Standard $In_{0.53}Ga_{0.47}As$ photodiodes have detector-limited room temperature detectivity of $\sim 10^{13}$ cmHz$^{1/2}$W^{-1}. With increasing cutoff wavelength, detectivity decreases, what is shown in Fig. 45. The highest quality InGaAs photodiodes have been grown by MOCVD [195]. Their performance agrees with the radiative limit and is comparable with HgCdTe photodiodes (see Fig. 34).

Due to similar band structure of InGaAs and HgCdTe ternary alloys, the ultimate fundamental performance of both type of photodiodes are similar in the wavelength range $1.5 < \lambda < 3.7$ μm [88]. Fig. 46 compares the ultimate performance of n-type base InGaAs with attainable experimental data. InGaAs photodiodes have shown high device performance close to theoretical limits for material whose composition is nearly matched to that of InP ($\cong$1.7 μm cut-off wavelength) and InAs ($\cong$3.6 μm cut-off wavelength).

Linear array formats of 256, 512 and 1024 elements [192] have been fabricated for environmental sensing from 0.8 to 2.6 μm. The size of pixels are different; from 30×30 μm^2 (with spacing of 50 μm), 25×500 to 13×500 μm^2 (with spacing of 25 μm). In the photodiode arrays with cutoff wavelength longer than 1.7 μm, several $InAs_yP_{1-y}$ layers between the InGaAs absorption layer and the InP substrate have been deposited to accommodate the lattice mismatch between substrate and photodiode active layer [199].

Sensors Unlimited offers $10 \times 10 \times 6$-cm line-scan cameras incorporating linear InGaAs FPAs of up to 512 elements on a 50-μm pitch [201]. Two versions of the units are available, optimised for wavelength bands of either 0.8–1.7 or 1.0–2.2 μm. Exposure times for line-scan cameras range from 25 μs to 1 s.

The first two-dimensional 128×128 $In_{0.53}Ga_{0.47}As$ hybrid FPA for the 1.0–1.7 μm spectral range was demonstrated by Olsen et al. [189] in 1990. Recently, the performance of InGaAs FPAs has been considerably improved. At 290 K the mean D^* is 1.35×10^{13} cmHz$^{1/2}$/W and pixel operability is 99.78% ($D^* > 5 \times 10^{12}$ cmHz$^{1/2}$/W). The highest mean D^* achieved to date is 1.09×10^{15} cmHz$^{1/2}$/W (84% BLIP) on a 128×128 FPA at 195 K [195]. This corresponds to a read noise of only 1.7 carriers. It was achieved using a CMOS readout with gate modulation input. Standard FPAs have pixel operability typically exceeding 99.5%.

Table 12 lists the measured characteristics of near-infrared cameras fabricated by Sensors Unlimited, Inc. The largest and finest pitched imager in $In_{0.53}Ga_{0.47}As$

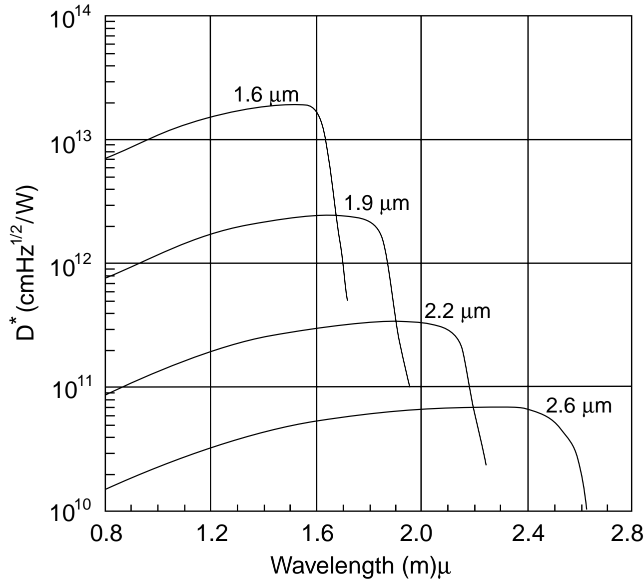

Fig. 45. Room temperature detectivity of InGaAs photodiodes with cutoff wavelength at 1.6, 1.9, 2.2, and 2.6 μm, respectively.

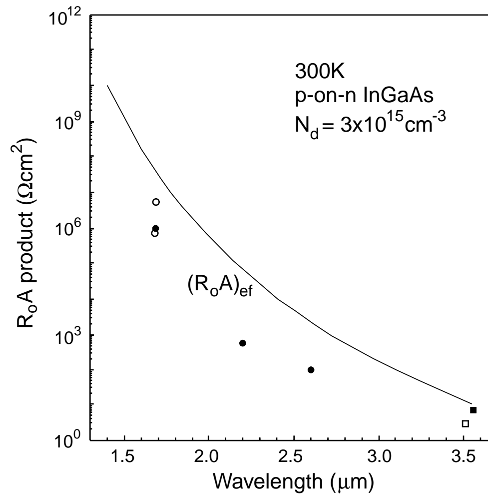

Fig. 46. The dependence of effective R_oA product on the long wavelength cutoff for SWIR InGaAs photodiodes at room temperature. The calculations are performed assuming that the performance of photodiodes is due to fundamental generation–recombination processes in the base p-type region of photodiodes with $t = 5\,\mu m$ and $N_a = 3 \times 10^{15}\,cm^{-3}$. The experimental values are taken from different papers (after Ref. [88]).

Table 12
Specification of the near-infrared cameras fabricated by Sensors Unlimited, Inc.

	Configuration	
	128×128	320×240
Pitch	60 μm	40 μm
Optical fill factor	100%	100%
Spectral response	0.9 to 1.7 μm	0.9 to 1.7 μm
Quantum efficiency	65% from 1.0 to 1.6 μm	>70% from 1.0 to 1.6 μm
Mean detectivity	$>10^{13}$ cmHz$^{1/2}$/W	$>10^{12}$ cmHz$^{1/2}$/W
Uniformity	>98%	>98%
Full well capacity	1×10^7 photoelectrons/pixel	>10 milion electrons
Digitization	10 bit	12 bit
Electronic readout noise	50 equivalent photoelectrons	⩽2 000 equivalent photoelectrons
FPA temperature	20°C	18°C
Length × width × height (cm)	$27 \times 10.3 \times 10.3$	$15.8 \times 10.3 \times 10.3$

material system has been demonstrated recently [196]. The 640×512 FPAs with 25-μm pixels is sensitive to the 0.9–1.7-μm and features a room temperature detectivity greater than 5×10^{12} cmHz$^{1/2}$/W with greater than 98% of the pixel operable.

8.6. InAsSb photodiodes

The InAsSb ternary alloy is more stable in comparison with HgCdTe and has a fairly weak dependence of the band edge on composition. The stability of this material is conditioned by the stronger chemical bonds available in the lower atomic number III–Vs family and the larger covalent bonding contribution compared to ionic bonding in HgCdTe. Some other physical properties of InAsSb material are better compared to those of HgCdTe. For instance, its dielectric constant is low (≈ 11.5) and the room temperature self-diffusion coefficient is low ($\approx 5.2 \times 10^{-16}$ cm^2/s).

The main effort in InAsSb detector technology has been shifted to the development of photodiodes as useful devices for the second-generation thermal imaging systems and the next generation very low loss fiber communication systems [91,202–204]. The best performance of conventional InAsSb photodiodes has been obtained when lattice-matched $InAs_{1-x}Sb_x$/GaSb ($0.09 \leqslant x \leqslant 0.15$) device structure was used [205]. The backside-illuminated $InAs_{0.86}Sb_{0.14}$/GaSb photodiodes fabricated by LPE technique, covered the spectral range 1.7–4.2 μm. The typical R_oA product was in excess of 10^9 Ωcm^2.

The InAsSb ternary alloy does not have a sufficiently small gap at 77 K for operation in the 8–14 μm wavelength range, but work began on strained-layer superlattices (SLSs). In particular, Osbourn [206] predicted that previously inaccessible InAsSb alloy could be grown as the SLS and used for long wavelength intrinsic infrared applications. Significant progress step in InAsSb SLSs development has been achieved by using MBE and MOCVD. Kurtz et al. [207] have fabricated the

first high-detectivity $InAs_{0.15}Sb_{0.85}$/InSb SLS photodiodes with detectivity $\geqslant 1 \times 10^{10}$ cmHz$^{1/2}$W^{-1} at wavelength $\leqslant 10\,\mu$m. To date, however, the growth of InAsSb/InSb SLSs on InSb substrates, which places the SLS under net tension, usually leads to cracking of the epitaxial material, precluding the fabrication of detector arrays. To mitigate this problem, the growth of similar structures on GaSb and InAs substrates has been proposed [208], however, without considerable success. Work on these SLS detectors has slowed due to emergence of more promising InAs/GaInSb SLSs (see Section 8.9.2).

Recently, considerable progress has been achieved in near room-temperature InSb-based ternary alloy IR detectors. It has been shown that the theoretical performance of high temperature $InAs_{1-x}Sb_x$ ($0 \leqslant x \leqslant 0.4$) photodiodes is comparable to that of HgCdTe photodiodes [209]. The first InAsSb-based long wavelength (8–14 m) photodiode operating at room temperature has been described by Kim et al. [210]. This p^+–InSb/π–$InAs_{0.15}Sb_{0.85}$/n^+–InSb heterojunction optimised for $\lambda = 10.6$ m was characterised by the voltage responsivity-area product of 3×10^{-5} Vcm^2/W and detectivity of $\approx 1.5 \times 10^8$ cmHz$^{1/2}$W^{-1}. A review of recent work on Sb-based materials for IR detector applications has been given by Michel and Razeghi [211]. p^+–P^+–π–n^+ InSb/$In_{1-x}Al_xSb$ unbiased heterostructure photodiodes give detectivity above 2×10^9 cmHz$^{1/2}$W^{-1}, with peak responsivity at 6 μm [212,213]. This value is an order of magnitude higher than that of typical, commercially available, single-element, thermal detectors.

Rapid development in epitaxial growth techniques has made it possible to explore the unprecedented alloys. Lee and Razeghi [214] reported on the growth and characterization of novel InSbBi alloy for uncooled infrared photodetector applications. The InSbBi epilayers were grown on GaAs substrates by low pressure MOCVD. The estimated Johnson noise limited detectivity of an $InSb_{0.96}Bi_{0.04}$ photoconductive detector at 7 μm was 4.7×10^8 cmHz$^{1/2}$/W at 77 K. $InSb_{0.95}Bi_{0.05}$ detector operating at room temperature showed a 12 μm cutoff wavelength. These results of InSbBi photodetectors showed the feasibility of using III–V ternary alloy for long-wavelength infrared photodetector applications as an alternative to HgCdTe.

8.7. Hg-based alternatives to HgCdTe

This section is devoted to the achievements of infrared detectors manufactured from alternative to HgCdTe, ternary alloy systems, such as $Hg_{1-x}Zn_xTe$ (HgZnTe) and $Hg_{1-x}Mn_xTe$ (HgMnTe). Only selected topics are reviewed. More information can be found in two comprehensive reviews [215,216] and three monographs [91,203,204].

Physical properties of these ternary alloys are determined by the energy gap structure near the Γ-point of the Brilloiun zone. The shape of the electron band and the light mass hole band can be determined using the $\mathbf{k} \cdot \mathbf{p}$ theory. Some physical properties of alternative alloys indicate a structural advantage in comparison with HgCdTe. Introducing ZnTe in HgTe decreases statistically the ionicity of the bond, improving the stability of the alloy. HgZnTe is a material that is more resistant to

dislocation formation and plastic deformation than HgCdTe. Interdiffusion studies between HgTe and ZnTe indicate that the interdiffusion coefficient is about 10 times lower in HgZnTe than in HgCdTe [217]. For HgMnTe, the above relations are not exactly known.

The HgMnTe alloy is a semimagnetic narrow-gap semiconductor. The exchange interaction between band electrons and Mn^{2+} d-electrons modifies their band structure, making it dependent on magnetic field at very low temperature. In the range of temperatures typical for intrinsic detectors operation ($\geqslant 77$ K), the spin-independent properties of HgMnTe are practically identical to the properties of HgCdTe, discussed exhaustively in the literature. Both HgZnTe and HgMnTe exhibit composition-dependent optical and transport properties like HgCdTe material with the same energy gap.

8.7.1. *HgZnTe detectors*

The technology for HgZnTe infrared detectors has benefited greatly from the HgCdTe device technology base. It is expected that HgZnTe devices should have greater thermal stability and therefore potentially greater operation time [218].

The research group at Santa Barbara Research Center [219] has developed very long wavelength HgZnTe photoconductive detectors with $\lambda_c = 17\,\mu m$ at temperatures $\geqslant 65$ K. These detectors were processed (from LPE epitaxial layers on lattice-matched CdZnTe substrates) into linear arrays with $50 \times 50\,\mu m^2$ active areas, CdTe passivation and ZnS antireflection coating. Peak responsivity for overlap devices average 2×10^6 V/W is comparable to the best HgCdTe photoconductive detectors. At the background of 10^{17} photons $cm^{-2} s^{-1}$ peak $D^* = 8 \times 10^{10}\,cmHz^{1/2}W^{-1}$ has been obtained for the best wafers.

Several different techniques have been used to obtain p–n HgZnTe junction, including Hg in-diffusion, Au diffusion, ion implantation, and ion etching [203,204,215]. To date, the ion implantation method gives the best quality n^+–p HgZnTe photodiodes. This technological process, elaborated at Societe Anonyme de Telecommunications (SAT), was identical to the one used for HgCdTe photodiodes in planar structures [218]. The HgZnTe photodiodes characteristics are similar to those of HgCdTe ones. Comparable values of R_oA for both types of photodiodes have been obtained (Fig. 47). For a staggered, 32-element linear array the following average values were measured at 77 K: $\lambda_c = (10.5 \pm 0.1)\,\mu m$, $\eta = 65\%$, and detectivity $1.1 \times 10^{11} < D^* < 1.2 \times 10^{11}\,cmHz^{1/2}W^{-1}$ at 30° FOV.

8.7.2. *HgMnTe detectors*

Technology of HgMnTe photodiodes has received sufficient level of maturity since they are produced by Brimrose Corporation of America [221].

Becla et al. [222–224] have produced good quality p–n HgMnTe and HgCdMnTe junctions by annealing as-grown, p-type samples in Hg-saturated atmospheres. These junctions were made in HgMnTe or HgCdMnTe epitaxial layers grown isothermally on CdMnTe substrate. The detectivities of the photodiodes with 60° FOV in the 3–5 μm and 8–12 μm spectral ranges were close to the background limit.

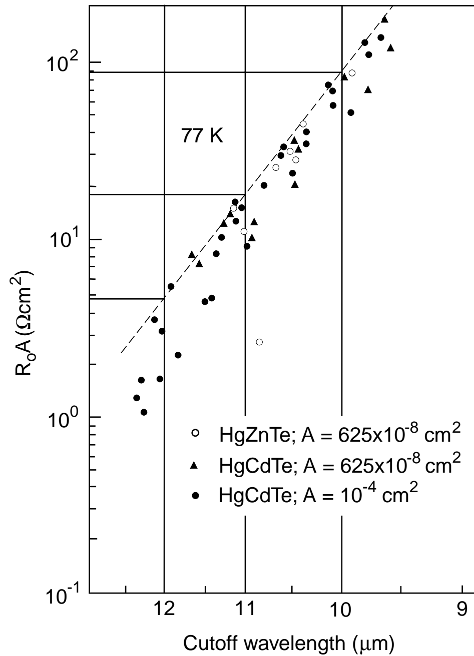

Fig. 47. R_oA comparison between HgZnTe and HgCdTe photodiodes. The broken line is the upper limit of experimental data (after Ref. [220]).

Typical quantum efficiencies were in the 20–40% range without using an antireflection coating.

Recently, high quality planar and mesa HgMnTe photodiodes have been fabricated by Kosyachenko et al. [225,226] using ion etching in a system generated an argon beam of 500–1000 eV energy and 0.5–1 mA/cm^2 current density. The hole concentration of annealed as-grown Bridgman wafers selected for photodiode preparation was $(2–5)\times10^{16}$ cm^{-3}. For $Hg_{1-x}Mn_xTe$ photodiodes operated at 80 K with cutoff wavelength of 10–11 μm the R_0A product is equal to 20–30 Ωcm^2, whereas for photodiodes with λ_c of 7–8 μm, $R_0A \approx 500$ Ωcm^2 has been obtained.

Also HgMnTe avalanche photodiodes (APDs) have been developed [223], which have increased speed and performance compared to the standard line of photodiodes. Avalanche gain in 7-μm devices is more than 40, and 10.6 μm detectors show gains better than 10. Preliminary results indicate that D^* values of the APDs are increased by a factor of 2 and that 10.6 μm devices should operate at speeds up to 1 GHz.

8.8. *Lead chalcogenide photodiodes*

For a period of decade from the late 1960s to the mid 1970s, because of production and storage problems, HgCdTe alloy detectors were in serious competition with IV–VI alloy devices (mainly PbSnTe) for developing photodiodes [15,16]. PbSnTe alloy

seemed easier to prepare and appeared more stable. Development of PbSnTe photodiodes was discontinued because the chalcogenides suffered from two significant drawbacks. The first was a high dielectric constant that resulted in high diode capacitance and therefore limited frequency response. For scanning systems under development at that time, this was a serious limitation. However, for staring imaging systems under development today using two-dimensional arrays, this would not be as significant of an issue. The second drawback to IV–VI compounds is their very high thermal coefficient of expansion [227]. This limited their applicability in hybrid configurations with silicon multiplexers. Today, with the ability to grow these materials on alternative substrates such as silicon, this would not be a fundamental limitation either. Moreover, as regards ease of manufacture, homogeneity and costs, photovoltaic IV–VI arrays on Si substrates offer substantial advantages compared to HgCdTe. The maximum available doping levels due to onset of tunnelling are more than an order of magnitude higher with IV–VIs than with HgCdTe photodiodes [228]. This is due to their high permittivities ε_s, because tunnelling contribution of the R_oA product contains a factor $\exp[\mathrm{const}(m^*\varepsilon_s/N)^{1/2}E_g]$ The maximum allowable concentrations above $10^{17}\,\mathrm{cm}^{-3}$ are easily controllable in IV–VIs grown by MBE. The research group at the Swiss Federal Institute of Technology continues to pursue this technology and has made significant progress [229–238].

To overcome thermal mismatch problems between silicon readout substrate and lead chalcogenide detector for large arrays, Zogg et al. have used an epitaxial stacked CaF_2–BaF_2 buffer layer of ≈ 200 nm thickness. However, due to the limited stability of BaF_2 (BaF_2 is soluble in water), standard processing techniques for detector delineation prooved to be cumbersome. Therefore, only growth at about 750°C, a technique where the MBE-growth is performed on a very thin, 5 nm CaF_2 intermediate epitaxial buffer layer, has been developed.

The fabrication process of PbSnSe photodiodes starts with a layer deposition in the second growth chamber at 350–400°C onto a CaF_2 buffer on a 3″ Si(1 1 1)-wafer. Typical carrier concentration in p-type layers is $(2–5)\times10^{17}\,\mathrm{cm}^{-3}$; thickness of the layers is 2–3 μm (i.e. a thickness just below the critical thickness for creation of misfit dislocations). Growth with (1 1 1) orientation is preferred, since thermal mismatch strain relaxation occurs by dislocation glide in the main $\{100\}\langle 110\rangle$ glide system with the glide planes inclined to the surface. When grown on (1 0 0) oriented substrates, thermal mismatch strain relaxation has to occur via higher glide systems, which normally leads to cracking of the layers as soon as their thickness exceeds about 0.5 μm [235]. Dislocation densities down to $10^6\,\mathrm{cm}^{-2}$ have been obtained in unprocessed layers of a few μm thickness, while for layers used to fabricate detectors, dislocation densities range from the low 10^7 to low $10^8\,\mathrm{cm}^{-2}$ range.

Fig. 48 shows a schematic cross section of a device. Photodiodes are fabricated in the layers with metal/semiconductor contacts or p–n junctions. For metal/semiconductor sensors, Pb has proven to be a good blocking material. In the case of p–n junction detectors, the p-base layer is overgrown with a Bi doped n^+ cap, and mesas are etched [236]. The p–n junction works well with tellurides, while selenides exhibit a too high diffusion in order to obtain reliable devices. For both types of junctions, the performance is limited by the dislocation densities in the layers. The

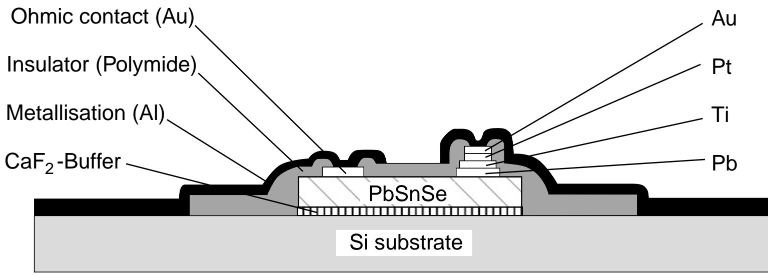

Fig. 48. Cross section of PbSnSe photovoltaic infrared detector (after Ref. [234]).

low temperature R_oA products scale linearly with the inverse dislocation denisity. The optimal carrier concentration is in the low $10^{17}\,\mathrm{cm}^{-3}$ range. No surface passivation was needed, since surface effects were negligible as deduced from the R_oA-values for diodes with different sizes. The active areas are 30–70 μm in diameter. Illumination is from the backside through the infrared transparent Si-substrate.

Fig. 49 shows the R_oA product at 77 K as a function of cutoff wavelength for different lead salt photodiodes on Si with stacked BaF_2/CaF_2 and CaF_2 buffer layers. Although these values are considerably above the BLIP limit (for 300 K, 2π FOV and $\eta = 50\%$), they are still significantly below theoretical limit given by Auger recombination [240]. The performance of IV–VI photodiodes is inferior to HgCdTe photodiodes; their R_oA products are two orders of magnitude below values for p^+–n HgCdTe photodiodes. R_oA products of PbSnSe photodiodes with the cutoff wavelength of 10.5 μm were about $1\,\Omega\mathrm{cm}^2$ at 77 K. The temperature dependence of R_oA is diffusion limited down to 100 K, while depletion-limited noise dominates below this temperature.

A new insight into theory of Schottky barrier lead salt photodiodes has been presented by Paglino et al. [241]. By using the Schottky barrier fluctuation model introduced by Werner and Güttler [242], it is assumed that the Schottky barrier height ϕ_b has the continuous Gaussian distribution σ around the mean value ϕ. Due to exponential dependence of saturation current on ϕ_b, it follows that the effective barrier responsible for current is given by

$$\phi_b = \phi - \frac{q\sigma^2}{2kT}. \tag{35}$$

This barrier ϕ_b is smaller than the mean value ϕ which is derived from capacitance–voltage characteristics. Therefore, since ϕ_b depends on temperature, no straight line is obtained in the Richardson plot.

A plot of the R_oA product versus temperature for Pb–PbSe Schottky barrier photodiode on Si substrate is shown in Fig. 50. A near perfect fit is obtained over the whole temperature range. The fluctuation σ leads to the saturation of the R_oA product at low temperature. For Pb–PbSnSe Schottky barriers, these fluctuations with an assumed Gaussian distribution have a width σ of up to 35 meV. The values

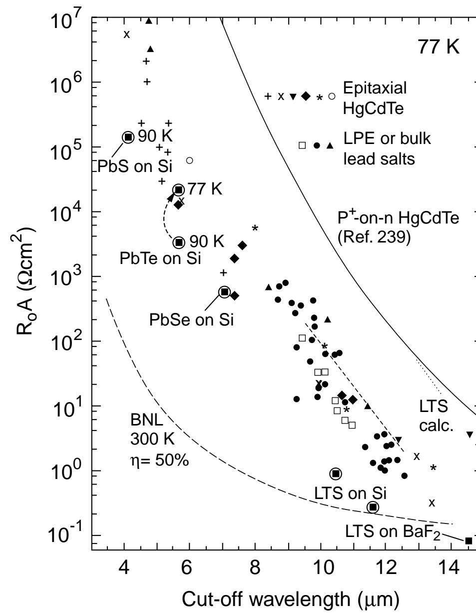

Fig. 49. Experimental R_oA products at 77 K versus cut-off wavelength for different lead salt photodiodes in comparison with HgCdTe photodiodes. The 300 K background noise limit (BNL) for 180° FOV and 50% quantum efficiency is included. The dotted line labelled LTS is the calculated ultimate value for PbSnSe (after Ref. [17]); the broken line is the upper limit of numerous experimental HgCdTe data points (after Ref. [220]); solid line represents calculated data for p-on-n HgCdTe photodiodes according to Ref. [239] (after Ref. [233]).

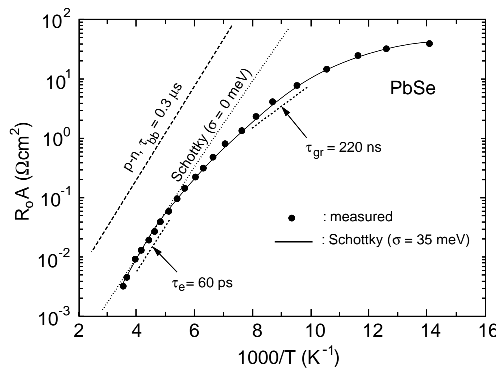

Fig. 50. Resistance area product R_oA versus inverse temperature for Pb–PbSe Schottky barrier photodiodes on Si substrates. The values are fitted with the barrier fluctuation model (solid line). For comparison, the values calculated for the ideal Schottky barrier photodiode are plotted, as well as the values from the p–n theory in the diffusion case for band-to-band recombination limited lifetime $\tau_{bb} = 0.3\,\mu s$ as well as for a recombination lifetime $\tau_e = 60$ ps and a depletion layer limited lifetime $\tau_{gr} = 220$ ns (after Ref. [241]).

depend on the structural quality; higher quality devices show lower σ. The ideality factors β are correctly described with the model even if $\beta > 2$. The barrier fluctuations can be caused by threading dislocations; lower densities of these dislocations lead to lower σ and higher saturation R_oA values at lower temperatures. The dislocation densities for PbSe were in the 2×10^7 to $5 \times 10^8\,cm^{-2}$ range for the 3–4 μm thick as grown layers. Higher R_oA products are obtainable by lowering these densities by thermal annealing [243], which sweeps the threading ends of the misfit dislocations over appreciable distances (in the cm range) to the edges of the sample [244].

The research group at the Swiss Federal Institute of Technology fabricated linear lead chalcogenide photodiode sensor monolithic arrays with 2×128 pixels and with cutoff wavelength ranging from 3 to 12 μm, which have been used in one-direction mechanically scanned thermal imaging camera [233,245]. Also the first realization of monolithic 2-D PbTe FPA (96×128) on a Si-substrate containing the active addressing electronics has been recently demonstrated [237,238]. Much improvement is still possible by improving the material quality and device fabrication technique.

8.9. *Quantum wells and superlattice detectors*

Since the initial proposal by Esaki and Tsu [246] and the advent of MBE, the interest in semiconductor superlattices (SLs) and quantum well structures has increased continuously over the years, driven by technological challenges, new physical concepts and phenomena as well as promising applications. A new class of materials and heterojunctions with unique electronic and optical properties has been developed. Here we focus on devices which involve infrared excitation of carriers in quantum wells. A distinguishing feature of these infrared detectors is that they can be implemented in chemically stable wide bandgap materials, as a result of the use of intraband processes. On account of this, it is possible to use such material systems as $GaAs/Al_xGa_{1-x}As$ (GaAs/AlGaAs), $In_xGa_{1-x}As/In_xAl_{1-x}As$ (InGaAs/InAlAs), $InSb/InAs_{1-x}Sb_x$ (InSb/InAsSb), $InAs/Ga_{1-x}In_xSb$ (InAs/GaInSb), and $Si_{1-x}Ge_x/Si$ (SiGe/Si), as well as other systems, although most of the experimental work has been carried out with AlGaAs. Some of devices are sufficiently advanced that there exists the possibility of their incorporation in high-performance integrated circuits. High uniformity of epitaxial growth over large areas shows promise for the production of large area 2-D quantum well infrared photodetector (QWIP) arrays. In addition, flexibility associated with control over composition during epitaxial growth can be used to tailor the response of quantum well infrared detectors to particular infrared bands or multiple bands.

At present QWIP FPAs are into a mainstream IR technology. The QWIP 2000 workshop on 27–29 July 2000 in Dana Point, CA, USA (see *Infrared Physics and Technology*, 42 (3–5) (2001)) covered many team efforts in bringing the technology into the commercial market.

8.9.1. GaAs/AlGaAs QWIPs

Among the different types of QWIPs, technology of the GaAs/AlGaAs multiple quantum well detectors is the most mature. Rapid progress has recently been made in the performance of these detectors [32,247–266]. Detectivities have improved dramatically and they are now high enough so that large 640×480 FPAs with LWIR imaging performance comparable or even better to state of the art of HgCdTe are fabricated.

Despite large research and development efforts, large photovoltaic HgCdTe FPAs remain expensive, primarily because of the low yield of operable arrays. The low yield is due to sensitivity of LWIR HgCdTe devices to defects and surface leakage, which is a consequence of basic material properties. With respect to HgCdTe detectors, GaAs/AlGaAs quantum well devices have a number of potential advantages, including the use of standard manufacturing techniques based on mature GaAs growth and processing technologies, highly uniform and well-controlled MBE growth on greater than 6 in. GaAs wafers, high yield and thus low cost, more thermal stability, and extrinsic radiation hardness. These detectors are extrinsic devices in which the dopant concentrations are limited by the epitaxial growth processes. As a result, the optical cross-sections for absorption are also limited. In addition, the intersubband lifetimes in MQW detectors are inherently short (about 10^{-11} s) which results in low quantum efficiency and relatively poor performance at temperatures >40 K. At these higher temperatures, thermally stimulated carriers dominate optically produced carriers, resulting in a low signal-to-noise ratio. However, the signal to noise ratio is usually sufficient for the most common imaging applications.

All QWIPs are based on "bandgap engineering" of layered structure of wide bandgap (relative to thermal IR energies) materials. The structure is designed such that the energy separation between two of the states in the structure match the energy of the infrared photons to be detected. Several QWIP configurations have been reported based on transitions from bound-to-extended states, bound-to-quasicontinuum states, bound-to-quasibound states, and bound-to-miniband states.

Fig. 51 shows two detector configurations used in fabrication of QWIP FPAs. The major advantage of the bound-to-continuum QWIP is that the photoelectron can escape from the quantum well to the continuum transport states without being required to tunnel through the barrier. As a result the voltage bias required to efficiently collect the photoelectrons can be reduced dramatically, thereby lowering the dark current. Furthermore, since the photoelectrons do not have to tunnel through them, the AlGaAs barriers can be made thicker without reducing the photoelectron collection efficiency. Multilayer structure consist of a periodic array of Si-doped ($N_d \approx 10^{18}$ cm^{-3}) GaAs quantum wells of thickness L_w separated by undoped $Al_xGa_{1-x}As$ barriers of thickness L_b. The heavy n-type doping in the wells assured that freezeout would not occur at low temperatures and that a sufficient number of electrons would be available to absorb the infrared radiation. For operation at $\lambda = 7-11$ μm typically $L_w = 40$ Å, $L_b = 500$ Å, $x = 0.25-0.30$ and 50 periods are growth. In order to shift the intersubband absorption to longer

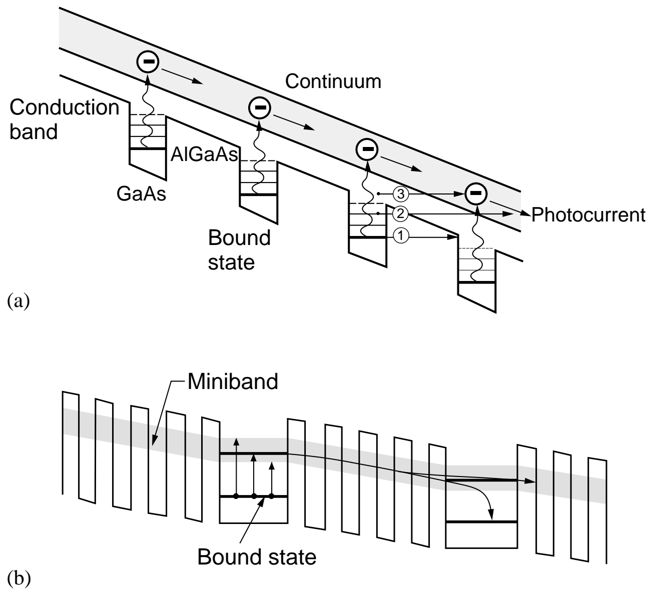

Fig. 51. Band diagram of demonstrated QWIP structures: (a) bound-to-extended and (b) bound-to-miniband. Three mechanisms creating dark current are also shown in Fig. (a): ground-state sequential tunneling (1), intermediate thermally assisted tunneling (2), and thermionic emission (3). The grey indicates extended states through which current flows.

wavelength the x value is decreased to $x = 0.15$ and in addition, in order to maintain the strong optical absorption and reasonably sharp cutoff λ_c line shape, the quantum-well width is increased to 50–60 Å. This optimization allows the same bound state to excited continuum state optical absorption and efficient hot-electron transport and collection. It appears that the dark current decreases significantly when the first excited state is dropped from the continuum to the well top, bound-to-quasibound QWIP (see Fig. 52), without sacrificing the responsivity [256,257]. The active structures are sandwiched between about 1-μm-thick heavily doped (also $N_d \approx 10^{18}\,cm^{-3}$) GaAs contact layers. The photoconductive detectors are then fabricated by etching mesas through the superlattice. Ohmic contacts are made to the n^+-doped GaAs contact layers.

A key factor in QWIP FPA performance is the light-coupling scheme. Different light-coupling mechanisms used in QWIPs are shown in Fig. 53. A distinct feature of n-type QWIPs is that the optical absorption strength is proportional to an incident photon's electric-field polarization component normal to the quantum wells. This implies that a photon propagating normal to the quantum wells, whose polarization is entirely in the plane of the quantum wells, is not absorbed. Therefore, these detectors have to be illuminated through a 45° polished facet. For imaging, it is necessary to be able to couple light uniformly to 2-D arrays of these detectors, so a diffraction grating or other similar structure is typically fabricated on one side of the detectors to redirect a normally incident photon into propagation angles more

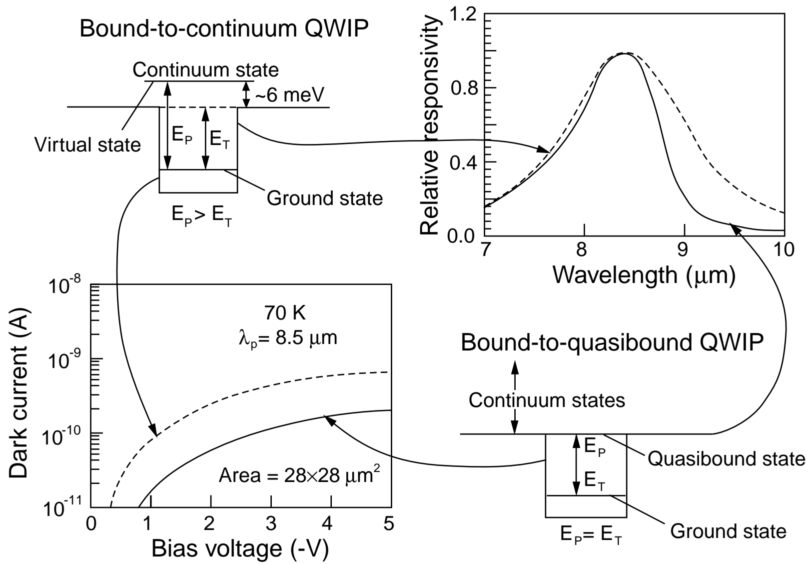

Fig. 52. In typical photoresponse curves of bound-to-quasibound and bound-to-continuum 8.5 μm QWIPs at a temperature of 77 K the dark current (lower left) decreases significantly when the first excited state is dropped from the continuum to the well top, bound-to-quasibound QWIP, without sacrificing the responsivity (upper right). The first excited state now resonating with barrier top produces sharper absorption and photoresponse (after Ref. [257]).

favourable for absorption. The pixels of 2-D arrays are thinned to about 5 μm in thickness. The thinning traps diffracted light inside the illuminated pixels, increasing responsivity and eliminating crosstalk. The thinning also allows the detector array to stretch and accommodate the thermal expansion mismatch with the Si readout integrated circuit (ROIC).

The light coupling, such as diffraction gratings and random gratings, achieves high quantum efficiency only when the detector size is large. In addition, because of its wavelength dependence, each grating design is only suitable for a specific wavelength. A size and wavelength independent coupling scheme is much needed. In order to simplify array production, a new detector structure for normal incidence light coupling, which is referred to as the corrugated QWIP (C-QWIP) has been proposed [267,268]. The device structure is shown in Fig. 53(d). This structure utilises total internal reflection at the sidewalls of triangular wires to create favourable optical polarization for infrared absorption. These wires are created by chemically etching an array of V grooves through the detector active region along a specific crystallographic direction.

Fig. 54 shows the dependence of detectivity on the long wavelength cutoff for GaAs/AlGaAs QWIPs at different temperatures. The satisfactory agreement with experimental data in wide range of cutoff wavelength $8 \leqslant \lambda_c \leqslant 19$ μm and temperature $35 \leqslant T \leqslant 77$ K has been obtained, considering the samples have different doping,

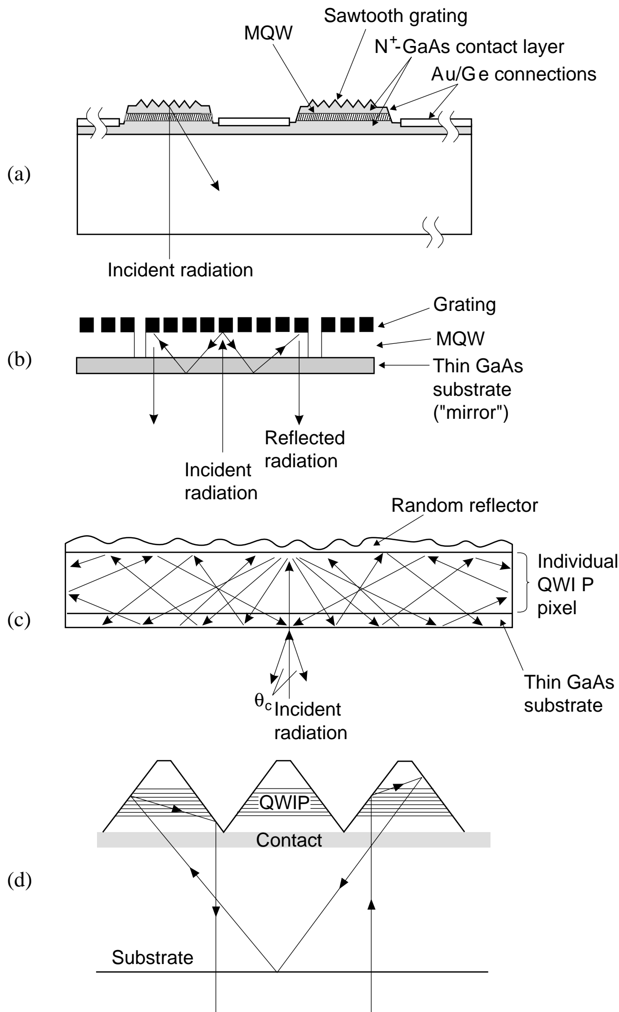

Fig. 53. Grating light-coupling mechanisms used in QWIPs: (a) linear or two-dimensional gratings on each detector, (b) gratings with optical cavity, (c) random scatterer reflector and (d) corrugated quantum wells.

different methods of crystal growth (MBE, MOCVD, and gas source MBE), different spectral widths, different excited states (continuum, bound, and quasi-continuum), and even in one case a different materials system (InGaAs). All the QWIP data with cutoff wavelength about 9 μm is clustered between 10^{10} and 10^{11} cmHz$^{1/2}$/W at about 77 K operating temperature. Investigations of the fundamental physical limitations of HgCdTe photodiodes indicate better performance of this type of detector in comparison with QWIPs operated in the range 40–77 K [269,270].

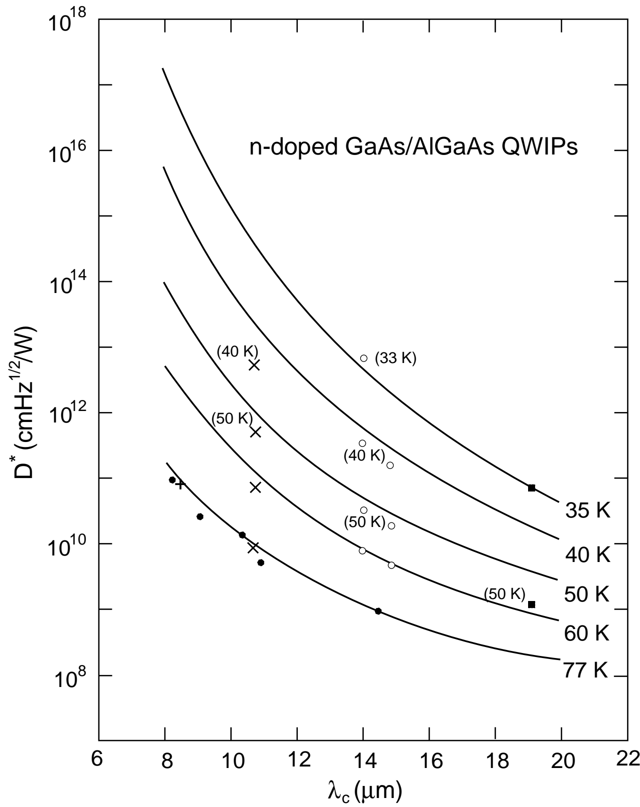

Fig. 54. Detectivity versus cutoff wavelength for n-doped GaAs/AlGaAs QWIPs at temperatures ⩽77 K. The solid lines are theoretically calculated. The experimental data are taken from different papers (after Ref. [37]).

Gunapala and co-workers at Jet Propulsion Laboratory (JPL) demonstrated several types of LWIR and VLWIR QWIP FPAs. Table 13 presents some important parameters of JPL FPAs with cutoff wavelengths 9 μm and 15 μm.

The current state of the art for QWIP FPA size is 640×480 (640×512) demonstrated by Lockheed Martin [255], Jet Propulsion Laboratory [260], and Fraunhofer-Institut für Angewandte Festkörperphysik [264]. Beck et al. [252,255] adopted the bound-to-miniband approach and demonstrated excellent IR imagers. This FPA employs an advanced silicon ROIC. Distinguishing features of the ROIC include: 0.8-μm CMOS at 24-μm pixel pitch, RS-170 format direct readout at 30 frames per second, non-interlaced 640×480 readout at 60 frames per second, adjustable transfer impedance charge well, switched capacitor low pass filtering in the unit cell, and sub-frame windowing of any portion of the 640×480 image with four pixel resolution. Preliminary imaging on early samples has demonstrated operability of greater than 99.98%, power dissipation for an imaging is <150 mW.

Table 13
Properties of JPL 9-μm and 15-μm GaAs/AlGaAs QWIP FPAs

Parameter	$\lambda_c = 9\,\mu m$	$\lambda_c = 15\,\mu m$		
Array size	256×256 (Ref. [262])	320×256 (Ref. [266])	640×486 (Ref. [261])	128×128 (Ref. [258])
Pixel pitch (μm)	38×38	30×30	25×25	50×50
Pixel size (μm)	28×28	28×28	18×18	38×38
Optical coupling	2-D periodic grating	2-D periodic grating	2-D periodic grating	2-D periodic grating
Peak wavelength (μm)	8.5	8.5	8.3	14.2
Cutoff wavelength, 50% (μm)	8.9	8.9	8.8	14.9
Operability (%)	99.98	99.98	99.9	> 99.9
Uncorrected nonuniformity (%)	5.4		5.6	2.4
Corrected uniformity, 17–27°C (%)	0.03		0.04	0.05
Quantum efficiency (%)	6.4	6.9	2.3	3
D^* ($cmHz^{1/2}W^{-1}$)	2.0×10^{11} (70 K)		2.0×10^{11} (70 K)	1.6×10^{10} (55 K)
NEDT with $f/2$ optics (mK)	23 (70 K)	33 (70 K)	36 (70 K)	30 (45 K)

Recently, Gunapala et al. [260] have fabricated 640×486 FPA with pitch size 25 μm and pixel size 18×18 μm. The array was back-illuminated through the flat thinned substrate membrane (thickness ≈ 1300 Å) which has completely eliminated the thermal mismatch between the silicon CMOS readout multiplexer and the GaAs based QWIP FPA and the pixel-to-pixel optical cross-talk. The measured mean NEDT of the QWIP camera was 36 mK at an operating temperature of $T = 70$ K and bias voltage equal to –2 V at 300 K background. The uncorreected NEDT nonuniformity was about 5.6% and after two-point correction improves to an impressive 0.1%.

Schneider and co-workers have developed the other QWIP structures where the capture of the photoexcited carriers is controlled by the incorporation of additional epitaxial layers [271]. The process technology for the fabrication of QWIP arrays is described in detail elsewhere [272]. In these low-noise QWIPs, the photoconductive gain, g, is drastically reduced while maintaining a high detectivity since the recombination-noise can be suppressed [273]. Moreover, a small g is useful to improve the NEDT (see Section 8.10.4). For this reason the cameras containing these QWIPs are operated at a bias voltage below 0.3 V in order to reduce the gain and optimised temperature resolution. Several camera systems with NEDT < 10 mK and NEDT < 20 mK for FPAs with 256×256 and 640×512 pixels have been demonstrated [274–276].

The GaAs/AlGaAs QWIPs are well situated to multi-colour IR sensors. This topic is considered in Section 8.12.2.

8.9.2. InAs/InGaSb strained layer superlattice detectors

Unlike GaAs/AlGaAs QWPIs, InAs/$In_xGa_{1-x}Sb$ (InAs/InGaSb) strained layer superlattice (SLS) detectors employ transitions across a fundamental gap [249,277,278]. Thus, carrier lifetime is limited by radiative and Auger recombination processes rather than the much faster hot-electron processes in QWIPs. SLSs are based on a type II interface where the conduction band edge of one material (e.g. InAs) is lower than the valence band edge of the second material (e.g. InGaSb). Because of this unusual band lineup, the superlattice can have a band gap smaller than that of either constituent material. However, also because of this band lineup, the electrons and holes tend to be localized in different material layers, the electrons in InAs and the holes in InGaSb. As a result, the electron-hole wave function overlap, i.e. the optical matrix element for IR absorption decreases rapidly with increasing superlattice period. However, a small lattice mismatch ($<5\%$) between the InGaSb and InAs layers causes the tetragonal distortions which shift the bulk energy levels and split the valence band degeneracies of the light and heavy hole energy levels. The presence of coherent strain shifts the band edges such that the SL energy gap is reduced. In the SLS, the band gap forms between electron states split upward from the InAs conduction band and heavy hole states split downward from the InGaSb valence band. This reduced band gap is advantageous because longer cut-off wavelengths can be obtained with reduced layer thickness in the strained SL, leading to even higher optical absorption coefficient.

Absorption of IR radiation occurs between the valence band of the first material and the conduction band of the second one. The resultant effective bandgap is dependent upon the composition, well width, and strain within the SL, and is smaller than the bandgap of either layer material. It should be noted that SLSs are intrinsic devices because optical absorption occurs via interband transitions. Carrier recombination occurs primarily by the relatively slow Auger process, and subsequently carrier lifetimes are longer than those in extrinsic MQW detectors. Therefore, SLS detectors should offer better performance at higher temperatures.

The InAs/InGaSb type II superlattice is the most likely candidate to replace the conventional narrow gap semiconductor. Electronic properties of InAs/GaInSb SLSs may be superior [278] to those of the HgCdTe alloy as the electron effective mass of InAs/GaInSb SLS is larger ($m^*/m_o = 0.031$ [279], compared to $m^*/m_o = 0.009$ in HgCdTe alloy with the same band-gap of $E_g \approx 0.1$ eV). Thus, diode tunnelling currents in the SL can be reduced compared to the HgCdTe alloy. Although in-plane mobilities drop precipitously for thin wells, electron mobilities approaching 10^4 cm^2/V s have been observed in InAs/GaInSb superlattices with layers less than 40 Å thick. While mobilities in these SLs are found to be limited by the same interface roughness scattering mechanism, detailed band structure calculations reveal a much weaker dependence on layer thickness, in reasonable agreement with experiment [280].

The calculations [281,282] of band-to-band Auger and radiative recombination lifetimes for InAs/GaInSb SLSs showed that in these structures the p-type Auger recombination rates are suppressed by several orders, compared to those of bulk HgCdTe with similar band-gap, due to the flatness of the light and heavy hole bands

whose large splitting exceeds the energy gap, thus limiting phase space for recombination transitions. The suppression is large enough that these materials are excellent candidates in the LWIR range (> 11 μm). By contrast, n-type materials are less advantageous because the Auger suppression achieved by increasing the $Ga_{1-x}In_xSb$ layer widths, thereby flattening the lowest conduction band, is far less effective than the band structure adjustments possible in the valence band [282–284]. Comparison of theoretically calculated and experimentally observed lifetimes at 77 K for 10 μm 39 Å InAs/25 Å $Ga_{0.75}In_{0.25}Sb$ SL and 10 μm HgCdTe indicates on good agreement in the range of densities above 2×10^{17} cm^{-3}. The discrepancy for lower carrier densities is due to Shockley–Read recombination processes having a $\tau \approx 6 \times 10^{-9}$ s which has been not taken into account in the calculations. For higher carrier densities, the SL carrier lifetime is two orders of magnitude longer than in HgCdTe, however, in low doping region (below 10^{15} cm^{-3}, necessary for fabrication of high performance p-on-n HgCdTe photodiodes) experimentally measured carrier lifetime in HgCdTe is more that two orders of magnitude longer than in SL.

Fig. 55 compares the temperature dependence of detectivity of three types of HgCdTe photodiodes and InAs/InGaSb SL photovoltaic detectors operating at 11 μm. The curves calculated for two InAs/InGaSb SLs (39.8 Å InAs/15 Å $In_{0.4}Ga_{0.6}Sb$ and 41 Å InAs/25 Å $In_{0.25}Ga_{0.75}Sb$) are taken from Ref. [285]. As Fig. 55 shows, the ultimate detectivity of HgCdTe photodiodes with optimally doped base region is comparable with that of InAs/InGaSb SLs in the temperature region between 300 and 77 K. High performance of InAs/InGaSb SLSs detectors (also at higher operating temperatures) is a result of longer carrier lifetimes caused by the splitting of the light-hole and heavy-hole bands. Recombination in SLSs occurs by relatively slow Auger recombination process.

The first InAs/InGaSb SLS photodiodes with photoresponse out to 10.6 μm at 78 K, have been presented by Johnson et al. [286]. The detectors consist of double heterojunctions (DH) of the 0.75-μm thick SLS with n-type and p-type GaSb grown on n-GaSb susbstrates. An analysis of the reverse-bias quantum efficiency suggests that a diffusion barrier at the isotype heterojunction impedes the zero-bias photocurrent. The overall device performance is adversely affected by low R_oA product (4 Ωcm^2) accompanied by large reverse-bias leakage currents. The leakage currents may be attributed in part to the high native concentration (2×10^{16} cm^{-3}) of the SLS and in part to surface recombination mechanisms.

Considerable progress in InAs/GaInSb SL photodiodes has been recently achieved by Fuchs et al. [272,287,288]. Fig. 56 shows the calculated band alignment of the photodiode together with the electric filed in the depletion layer of the diode (in lower part). The growth direction is from right to left. A p-type background of the SL is in the mid 10^{15} cm^{-3}. A 500 nm thick Be-doped GaSb layer establishes the bottom p-contact. The first 90 periods of the diode are doped with a low Be-level to compensate for the residual n-type background. The upper 20 periods of the diode are highly n-doped with Si (1.8×10^{17} cm^{-3}), inserted in the InAs layers. Finally 20 nm of InAs is deposited to 5×10^{17} cm^{-3} to reduce the tunneling barrier at the top of the diode to a size which provides ohmic transport. Superlattices consisting of 12 monolayers (MLs) of InAs alternated with 10 MLs of $Ga_{0.8}In_{0.2}Sb$ were grown by

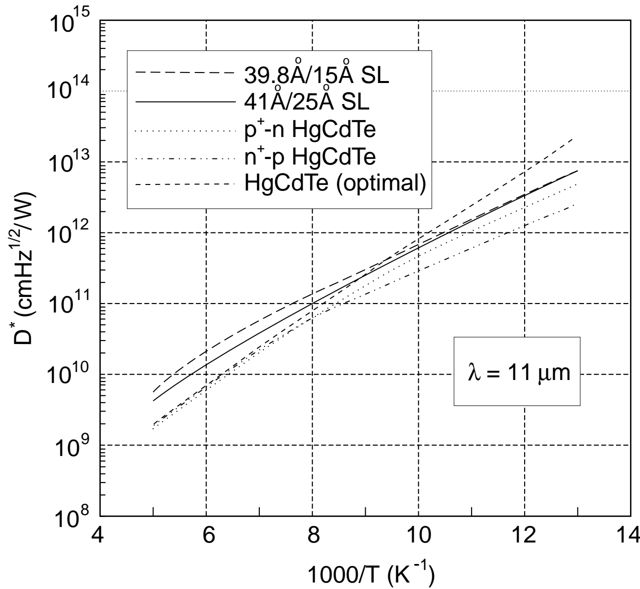

Fig. 55. Calculated detectivity of three types of HgCdTe photodiodes and InAs/InGaSb SL photovoltaic detectors operated at 11 μm as a function of temperature. The base-region limited detectivities are calculated for HgCdTe photodiodes assuming: $\eta = 1, t = 10\,\mu m$, $N_a = 5 \times 10^{15}\,cm^{-3}$ for n^+-p structures; $\eta = 1, t = 10\,\mu m$, $N_d = 3 \times 10^{14}\,cm^{-3}$ for p^+–n structures; and $\eta = 1$, $t = 10\,\mu m$ for photodiode with optimal doping in the base region. The curves calculated for two InAs/InGaSb SLs (39.8 Å InAs/15 Å $In_{0.4}Ga_{0.6}Sb$ and 41 Å InAs/25 Å $In_{0.25}Ga_{0.75}Sb$) are taken from Ref. [285] (after Refs. [37,60]).

MBE at substrate temperatures of 410°C on undoped (1 0 0) GaSb substrates. Ohmic contact metalization was performed by conventional lift-off technique using Ti/Au for n-type InAs and Ti/Pt/Au for p-type GaSb.

The heterooffstes between the active SL layer and the GaSb p-contact (see Fig. 56) are ideally suited for detector applications: the photogenerated electrons cannot diffuse outside the mesa structure because of the high conduction band offset of the common GaSb p-contact, the type II offset of the effective valence band leads to perfect hole transport between p-contact and SL. However, care has to be taken, that the p–n junction does not shift to the heterointerface between SL and GaSb p-contact.

The diodes operated at 77 K with a cut-off wavelength around 8 μm show a current responsivity of 2 A/W. Fig. 57 shows the dependence of the R_oA product on temperature for four samples with cutoff wavelengths at 8 and 12 μm. The maximum of the dynamic resistance (not shown) found at small reverse bias voltages around 20 mV, exceeds the value plotted in Fig. 57 by a factor of 2–3. Both sets of diodes show diffusion-limited behaviour down to temperatures close to 77 K with activation energies about 20 mV lower than the optical bandgap. At lower temperatures, other mechanisms limit the performance of the devices. It is more emphasized for photodiodes with higher effective doping level $N_{ef} = (1/N_a + 1/N_d)^{-1}$. R_oA values

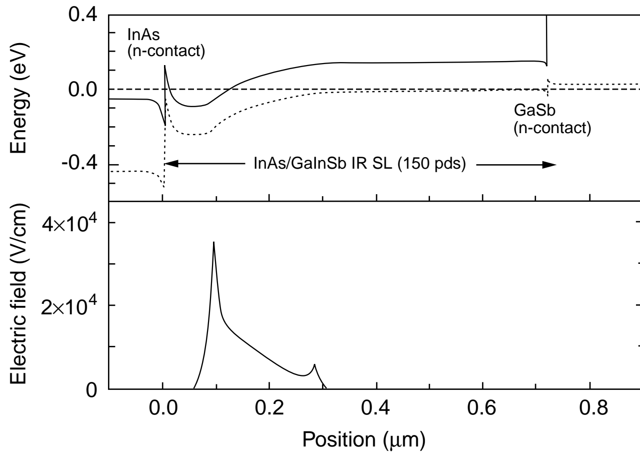

Fig. 56. Effective band alignment of a InAs/GaInSb SLS photodiode with 10 μm cutoff wavelength. In the lower panel the electric field in the depleted part of the diode is shown (after Ref. [288]).

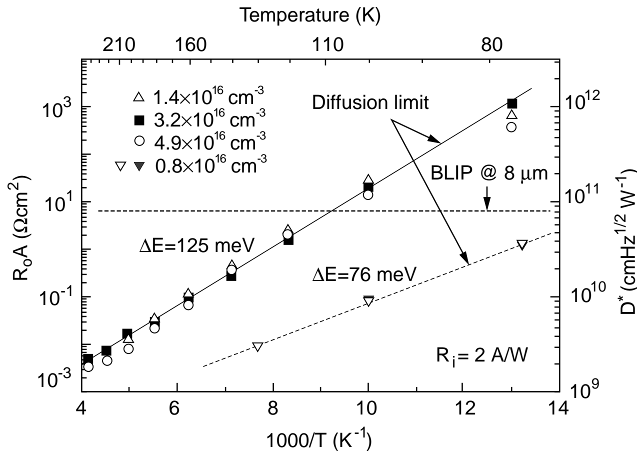

Fig. 57. Temperature dependence of the R_oA product and detectivity for photodiodes based on InGa/GaInSb superlattices. The effective doping concentration N_{ef} is indicated. Samples with cutoff 8 μm are plotted as full line, samples with cutoff 12 μm are plotted as dashed line. The Johnson-noise limited peak-detectivity for responsivity of 2 A/W is shown as the scale on the right hand side (after Ref. [272]).

above 1 kΩ lead to a Johnson-noise-limited detectivity at 77 K in excess of 1×10^{12} cmHz$^{1/2}$W^{-1} for photodiodes with 8 μm cutoff wavelength. Status of the processing technology demonstrates feasibility for the fabrication of 256 × 256 FPAs operating in the 8–12 μm region [288]. Fig. 58 compares the R_oA values of InAs/GaInSb SLS and HgCdTe photodiodes in the long wavelength spectral range. The upper line denotes the theoretical diffusion limited performance corresponding to

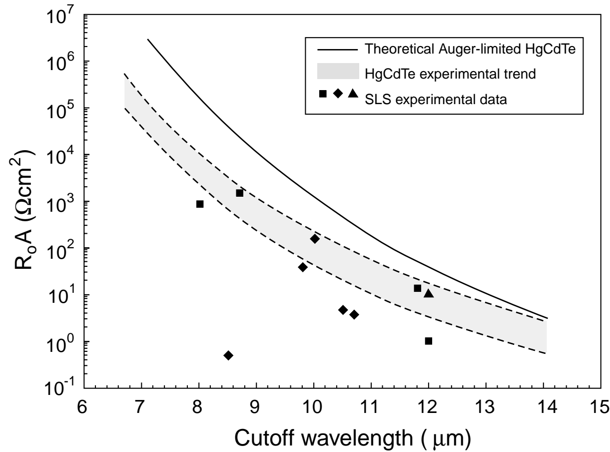

Fig. 58. Dependence of the R_oA product of InAs/GaInSb SLS photodiodes on cut-off wavelength compared to theoretical and experimental trendlines for comparable HgCdTe photodiodes at 78 K (courtesy J.L. Johnson).

Auger 7 limitation in p-type HgCdTe material. As can be seen in the figure, the most recent photodiode results for SLS devices rival that of practical HgCdTe devices, indicating substantial improvement has been achieved in SLS detector development. However, significant obstacles in material growth and device fabrication need to be addressed before its full potential can be realised.

InAs/GaSb photodiodes have been also demonstrated in the VLWIR range [289]. Devices with $\lambda_c = 16\,\mu$m showed a quantum efficiency of about 35% and Johnson noise limited detectivity of about $1.5 \times 10^{10}\,$cmHz$^{1/2}$/W at 80 K.

8.10. QWIP versus HgCdTe in LWIR spectral region

Table 14 compares the essential properties of HgCdTe and QWIP devices at 77 K.

8.10.1. Quantum efficiency

HgCdTe has large optical absorption and wide absorption band irrespective of the light polarization what greatly simplifies the detector array design. Quantum efficiency is routinely produced around 70% without antireflection (AR) coating and in excess of 90% with AR coating and is spectrally constant from less than 1 μm out to near the cutoff of the detector. The wide-band spectral sensitivity with near perfect η enables greater system collection efficiency (smaller aperture) making the FPA useful for imaging, spectral radiometry, and long-range target acquisition. It should be noticed however, that the current LWIR staring array performance is mostly limited by the charge handling capacity on the ROIC and the background (warm optics).

Due to intersubband transitions in the conduction band, the n-type QWIP detection mechanism requires photons with non-normal angle of incidence to

Table 14
Essential properties of LWIR HgCdTe photodiodes and m-type QWIPs at $T = 77\,K$

Parameter	HgCdTe	QWIP (n-type)
IR absorption	Normal incidence	$E_{optical} \perp$ plane of well required Normal incidence: no absorption
Quantum efficiency	$\geqslant 70\%$	$\leqslant 10\%$
Spectral sensitivity	Wide-band	Narrow-band (FWHM $\approx 1 \div 2\,\mu m$)
Optical gain	1	0.4 (30–50 wells)
Thermal generation lifetime	≈ 1 ìs	≈ 10 ps
R_oA product ($\lambda_c = 10$ ìm)	$300\,\Omega cm^2$	$10^4\,\Omega cm^2$
Detectivity ($\lambda_c = 10$ ìm, FOV = 0)	$2 \times 10^{12}\,cmHz^{1/2}W^{-1}$	$2 \times 10^{10}\,cmHz^{1/2}W^{-1}$

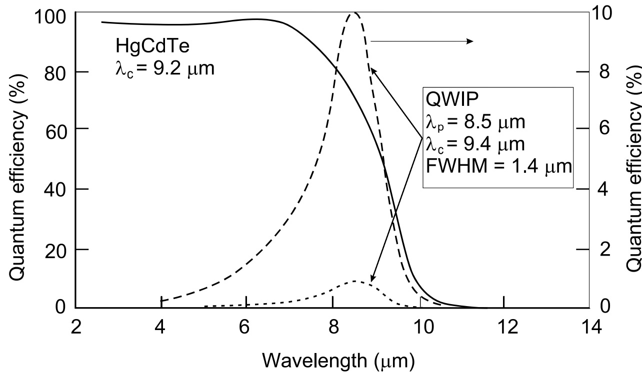

Fig. 59. Quantum efficiency versus wavelength for a HgCdTe photodiode and GaAs/AlGaAs QWIP detector with similar cutoff.

provide proper polarization for photon absorption. The absorption quantum efficiency is relatively small, about 20% using 2-D grating. Since QWIP is a photoconductive detector, the responsivity is proportional to the conversion efficiency, which is the product of the absorption quantum efficiency times the optical gain. The optical gain of QWIP structures is typically 0.4. It results from above consideration that the η is typically below 10% at the maximum response, rapidly rolling off both the short and long wavelength sides off the peak. Fig. 59 compares the spectral η of HgCdTe photodiode to a QWIP.

8.10.2. Dark current and R_oA product

Fig. 60 shows typical current–voltage characteristics of HgCdTe photodiode at temperatures between 40 and 90 K for a 12 μm cutoff detector at 40 K. Leakage current is less than $10^{-5}\,A/cm^2$ at 77 K. The biases-independent leakage current aids in achieving FPA uniformity as well as reducing detector bias-control requirements during changes in photocurrent.

Usually for $Hg_{1-x}Cd_xTe$ photodiodes with $x \approx 0.22$, in the zero-bias and low-bias region, diffusion current is the dominant current down to 60 K [91]. For medium

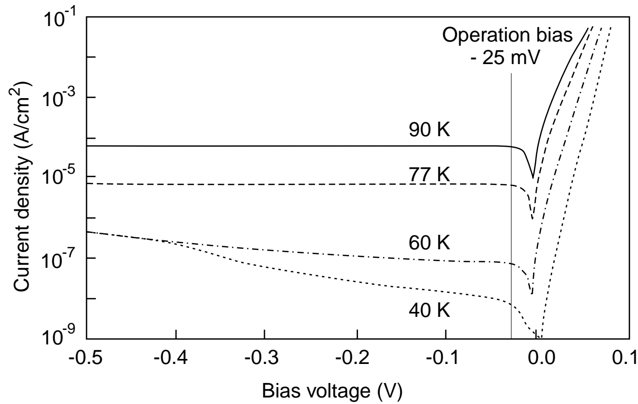

Fig. 60. Current–voltage characteristics at various temperatures for a 12 μm cutoff HgCdTe photodiode (after Ref. [44]).

reverse bias, trap-assisted tunnelling produces the dark current, and also dominates the dark current at zero bias below 50 K. For a high reverse bias, bulk band-to-band tunnelling dominates. At low temperature, such as 40 K, large spreads in R_oA product distributions are typically observed due to onset of tunnelling currents associated with localized defects. Moreover, the HgCdTe photodiodes often have additional dark current, particularly at low temperature, which is related to the surface.

The average value of R_oA product at 77 K for a 10-μm cutoff HgCdTe photodiodes at 77 K is around 300 Ωcm^2 and drops to 30 Ωcm^2 at 12 μm. At 40 K, the R_oA product varies between 10^5 and 10^8 Ωcm^2 with 90% above the 10^5 Ωcm^2 at 11.2 μm [61,74,290].

In comparison with HgCdTe photodiodes, the behaviour of the dark current of QWIPs is better understood. At low temperatures ($T<40$ K for $\lambda_c = 10$ μm), the dark current is mostly caused by defect related direct tunnelling. In the medium operating range between 40 and 70 K (for $\lambda_c = 10$ μm), the thermally assisted tunnelling dominates. In this case, electrons are thermally excited and tunnel through the barriers with assistance from the defects and the triangle part of the barrier at high bias. At high temperature (>70 K for $\lambda_c = 10$ μm), thermally excited electrons are thermionically emitted and transport above the barriers. It is difficult to block this dark current without sacrificing the photoelectrons (transport mechanisms of thermionically emitted current and photocurrent are similar). Minimizing thermionically emitted current is critical to the commercial success of the QWIP, as it allows the highly desirable high-temperature camera operation. Dropping the first excited state to the top theoretically causes the dark current to drop by a factor of ≈ 6 at a temperature of 70 K. This compares well with the fourfold drop experimentally observed for 9-μm cutoff QWIPs [259].

The value of the QWIP dark current could be adjusted using different device structures, doping densities, and bias conditions. Fig. 61 shows the I–V

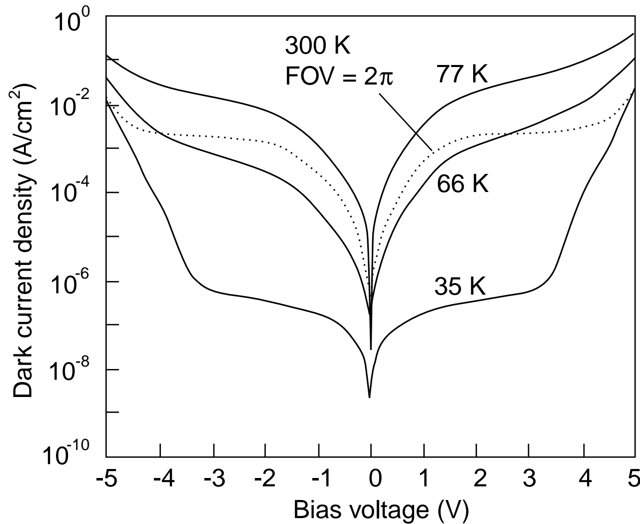

Fig. 61. Current–voltage characteristics of a QWIP detector having a peak response of 9.6 μm at various temperatures, along with the 300 K background window current measured at 30 K with a 180° FOV (after Ref. [291]).

characteristics for a range of temperature between 35 and 77 K measured on a device with 9.6 μm spectral peak. Typical operation at 2 V applied bias in the slowly-varying region of current with bias between the initial rise in current at low voltage and the later rise at high bias. Typical LWIR QWIP dark current at 77 K is about 10^{-4} A/cm^2, which is in the nanoamper range for $24 \times 24\,\mu m^2$ pixel [292]. Comparing Figs. 22 and 23 we can see that a 9.6-μm QWIP must be cooled to 60 K to achieve leakage current comparable to a 12 μm HgCdTe photodiode operating 25° warmer.

QWIP operates at a bias voltage from 1 to 3 V depending on the structure and periods of the devices. Using the voltage divided by the dark current density, the R_oA products are usually larger than 10^7 and $10^4\,\Omega$cm^2 when operated at 40 and 77 K, respectively [292]. These values indicate very high impedance.

8.10.3. Detectivity

We can distinguish two types of detector noise: radiation noise and intrinsic noise. Radiation noise includes signal fluctuation noise and background fluctuation noise. For infrared detectors, background fluctuation noise is higher compared to the signal fluctuation noise. Usually for photodiodes, shot noise is the major noise.

In the case of QWIPs, the major source of noise is the dark current. Due to high dark current, Johnson noise is neglected in most cases, especially at high temperature operation. But at lower temperature and when the array pixel size is smaller, Johnson noise becomes comparable to dark noise. Owing to stable surface properties, there is very little $1/f$ noise observed in QWIPs.

At FPA level, the pattern noise (which results from local variation of the dark current, photoresponse, and cutoff wavelength) is the major limitation to the array

performance, especially at low temperature. This type of noise is a nonuniformity appearing across the array, which does not vary with time and reflects the intrinsic properties of a FPA. The fixed pattern noise is smaller for QWIP arrays than that of HgCdTe arrays due to their material quality and better-controlled cutoff wavelength.

Fig. 62 compares the detectivities of p-on-n HgCdTe photodiodes with GaAs/AlGaAs QWIPs. The theoretical curves for HgCdTe photodiodes are calculated assuming constant cutoff wavelengths 10 and 11 μm. The VLWIR results for HgCdTe (14.8 μm at 80 K and 16.2 μm at 40 K) and the QWIP at 16 μm show the intrinsic superiority of the HgCdTe photodiodes. HgCdTe has roughly an order of magnitude higher detectivity, though the advantage decreases as the temperature is reduced. The best example of where the QWIP could have a performance advantage is at low temperature. As we can see from Fig. 62, the QWIP at 7.7 μm peak wavelength offers superior performance relative to a ≈10.6 μm HgCdTe at temperature ⩽45 K.

The above performance comparison of QWIPs with HgCdTe in the low temperature range is less profitable for photodiodes in the case of n^+–p structures due to same non-fundamental limitations (contacts, surface, Schockley-Read processes). Including the influence of tunnelling, the comparison of detectivity is more advantageous for GaAs/AlGaAs QWIPs in spectral region below 14 μm and at temperature below 50 K [37].

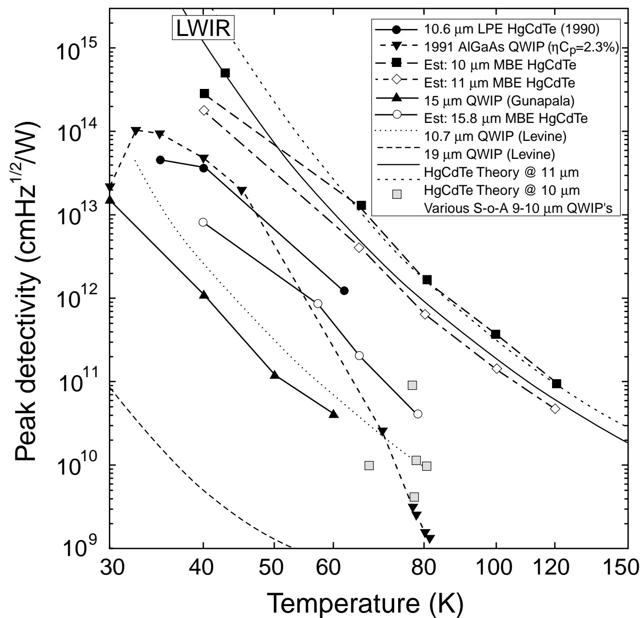

Fig. 62. LWIR detector detectivity versus temperature for GaAs/AlGaAs QWIPs and p-on-n HgCdTe photodiodes (after Refs. [32,293]).

8.10.4. Noise equivalent difference temperature

The noise in HgCdTe photodiodes at 77 K is due to two sources; the shot noise from the photocurrent and the Johnson noise from the detector resistance. It can be expressed as

$$I_n = \sqrt{\left(2qI_{ph} + \frac{4kT_d}{R}\right)\Delta f}, \tag{36}$$

where k is the Boltzmann's constant and R is the dynamic resistance of photodiode. Assuming that the integration time, τ_{int}, is such that readout node capacity kept half full, we have

$$\Delta f = \frac{1}{2\tau_{int}}, \tag{37}$$

and then

$$I_n = \sqrt{\left(2qI_{ph} + \frac{4kT_d}{R}\right)\frac{1}{2\tau_{int}}}. \tag{38}$$

At tactical background levels, the Johnson is much smaller than the shot noise from the photocurrent. In the case where the number of electrons collected in a frame is limited by the capacity of the ROIC charge well, what is often true, the signal to noise ratio is given by

$$\frac{S}{N} = \frac{qN_w/2\tau}{\sqrt{2q\left(\frac{qN_w}{2\tau}\right)\frac{1}{2\tau}}} = \sqrt{\frac{N_w}{2}}. \tag{39}$$

Assuming that the temperature derivative of the background flux can be written to a good approximation as

$$\frac{\partial Q}{\partial T} = \frac{hc}{\bar{\lambda}kT_B^2}Q, \tag{40}$$

and using Eq. (26), the NEDT under these conditions is equal

$$\mathrm{NEDT} = \frac{2kT_B^2\bar{\lambda}}{hc\sqrt{2N_w}}. \tag{41}$$

In last two equations $\bar{\lambda} = (\lambda_1 + \lambda_2)/2$ is the average wavelength of the spectral band between λ_1 and λ_2.

For typical storage capacity of 2×10^7 electrons, $\bar{\lambda} = 10\,\mu m$, and $T_B = 300$ K, from Eq. (41) appears an NEDT of 19.8 mK.

The same estimations can be made for QWIP. In this case the Johnson noise is negligible compared to the generation-recombination noise, and then

$$I_n = \sqrt{4qg(I_{ph} + I_d)\frac{1}{2\tau}}, \tag{42}$$

where dark current can be approximated by

$$I_d = I_0 \exp\left(-\frac{E_a}{kT}\right). \tag{43}$$

In the above expressions g is the photoconductive gain, I_d is the dark current, I_0 is the constant that depends on the transport properties and the doping level, and E_a is the thermal activation energy, which is usually slightly less than the energy corresponding to the cutoff wavelength of the spectral response. It should be also stressed that g, I_{ph}, and I_0 are bias-dependent parameters.

The signal to noise ratio for a storage capacity-limited QWIP is given by

$$\frac{S}{N} = \frac{qN_w/2\tau}{\sqrt{4qg\left(\frac{qN_w}{2\tau}\right)\frac{1}{2\tau}}} = \frac{1}{2}\sqrt{\frac{N_w}{g}}, \tag{44}$$

and the NEDT is

$$\mathrm{NEDT} = \frac{2kT_B^2\bar{\lambda}}{hc}\sqrt{\frac{g}{N_w}}, \tag{45}$$

Comparing Eqs. (41) and (45) we can notice that NEDT value for charge-limited QWIP detectors is better than for HgCdTe photodiodes by factor $(2g)^{1/2}$ since reasonable value of g is 0.4. Assuming the same operation conditions as for HgCdTe photodiodes, the NEDT is 17.7 mK. So, a low photoconductive gain actually increases the S/N ratio and a QWIP FPA can have a better NEDT than an HgCdTe FPA with similar storage capacity. This deduction was experimentally confirmed by Schneider et al. [294]. Using a photovoltaic "low-noise" QWIP structure in which g is only 0.05, the group achieved a NEDT of 7.4 mK with 20 ms integration time and 5.2 mK with 40 ms.

For a system operating in the LWIR band, the scene contrast is about 2%/K of change in scene temperature. Therefore, to obtain a pixel to pixel variation in apparent temperature to less than, e.g., 20 mK, the nonuniformity in response must be less than 0.04%. This is nearly impossible to obtain in the uncorrected response of the FPA, so a two-point correction is typically used.

The nonuniformity can be different depending on the specification of operability; e.g., a higher requirement on the operability usually leads to a lower uniformity and vice verse. Typical uncorrected response nonuniformity in QWIP FPAs is 1–3% with an operability (the fraction of good pixels) greater than 99.9%. For the 128×128 15-μm array fabricated by Jet Propulsion Laboratory (see Table 13), the uncorrected standard deviation is 2.4% and the corrected nonuniformity 0.05%. For recently described large 640×486 9-μm FPA, the uncorrected noise nonuniformity is about 6%, and after two-point correction improves to an impressive 0.04%. For the same format FPA, demonstrated by Lockheed Martin, the operability of greater than 99.98% was described [255].

It is very hard for HgCdTe to compete with QWIP for high uniformity and operability with large array format, especially at low temperature and VLWIR. The

variation of x across the $Hg_{1-x}Cd_xTe$ wafer causes a much larger spectral nonuniformity (e.g., at 77 K, a variation of $\Delta x = 0.2\%$ gives a $\Delta\lambda_c = 0.064\,\mu m$ at $\lambda_c = 5\,\mu m$, but $\Delta\lambda_c = 0.51\,\mu m$ at $14\,\mu m$), which cannot be fully corrected by the two or three point corrections. Therefore, the required composition control is much more stringent for VLWIR than for MWIR.

High uniformity and high operability, as shown in the above examples, demonstrate the mature GaAs growth and processing technology. In this context, the nonuniformity and operability have been an issue for HgCdTe, although recently published values for Sofradir and SBRC arrays are as high as 99%. As we compare the performance of both types of FPAs (see Tables 13 and 15), the array operability is higher for QWIPs, above 99.9%.

In the case of QWIPs, extending cut-off wavelength to VLWIR is relatively easier since there is little change in material properties, growth and processing. However, a serious requirement for maintaining the device performance is to lower the operating temperature. Due to lower quantum well barriers, the dark current of thermionic emission dominates at a lower temperature. In order to achieve equivalent performance of a 10-μm cutoff QWIP at 77 K, the temperature needs to be cooled down to 55 K for a 15-μm cutoff and 35 K for a 19-μm cutoff (see Table 13 and Fig. 62).

Fig. 63 compares the performance of two Sofradir's HgCdTe staring arrays sensitive between 7.7 and 9 μm, and 7.7 and 9.5 μm. Higher performance with improved technology has been obtained using, on the one hand, a reduced dark current detector technology and, on the other hand, new readout circuit architecture which maximises both charge handling capacity and responsivity [295]. For a constant temperature, the performance is higher for $\lambda_c = 9\,\mu m$ due to the fact that dark current is lower and integration time can be increased. In consequence, focal

Table 15
Performance specifications for LWIR HgCdTe FPAs (after SOFRADIR and SBRC data sheets)

Parameter	SOFRADIR		SBRC
Format	128×128	320×256	256×256
Cut on–Cut off (μm)	7.7–10.3	7.7–9.0	8.5–11.0
FPA temperature (K)	< 85	< 90	77 (up to 100)
Detector pitch (μm)	50	30	30
Fill factor (%)	> 70		
Charge handling capacity	$> 118\ 10^6 e^-$	12 or 36	$8 \times 10^6\ e^-$ (min)
Frame rate (Hz)	to 300	to 400	to 120
D^* peak RMS/T_{int}/pitch (average) ($cmHz^{1/2}W^{-1}$)	1.1×10^{11}		
Pixel NETD (average)	10 mK for 275 Hz	18	
NEI ($photons/cm^2s$) (max)			1.52×10^{12}
Typical FOV	$f/2$	$f/2$	
Fixed pattern noise	7% RMS		
Crosstalk (optical and electrical) (%)	2		
Array operability (%)	99		99

plane operating temperature of improved arrays with $\lambda_c = 9\,\mu m$ can be increased up to 105 and to 102 K for array with $\lambda_c = 9.5\,\mu m$ (for NEDT <18 mK, for the given example).

Fig. 64 shows the measured and estimated NEDT as a function temperature for 8.9- μm QWIP FPA. In comparison with representative HgCdTe FPA (Fig. 63), this parameter exhibits strong temperature dependence. At temperatures <70 K, the signal-to-noise (SNR) ratio of the system is limited by multiplexer readout noise, and shot noise of the photocurrent. At temperatures >70 K, temporal noise due to the QWIP's higher dark current becomes the limitation. As mentioned earlier, this higher dark current is due to thermionic emission and thus causes the charge storage capacitors of the readout circuitry to saturate.

Comparing the values of NEDT parameters for both types of FPAs (see also Tables 13 and 15), we can see that the performance of LWIR HgCdTe arrays is better.

The well charge capacity is the maximum amount of charge that can be stored on the storage capacitor of each cell. The size of the unit cell is limited to the dimensions

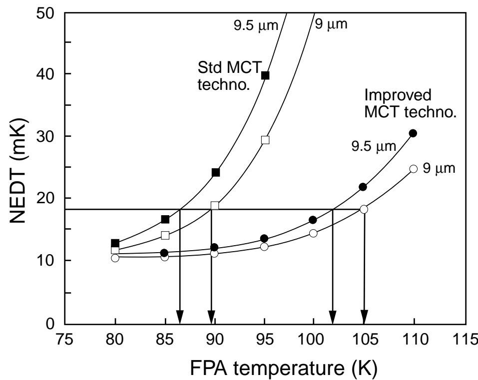

Fig. 63. NEDT of 128 × 128 HgCdTe FPA ($f/2$ optics, 50% well fill, pitch 50 μm) as a function of operating temperatures (after Ref. [295]).

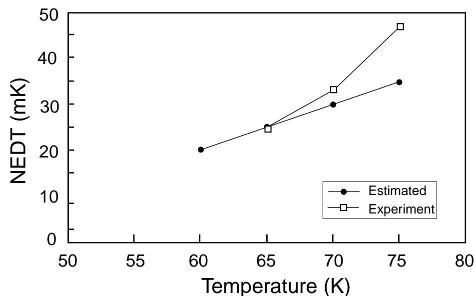

Fig. 64. NEDT of 320 × 256 QWIP FPA ($\lambda_c = 8.9\,\mu m$, $f/2$ optics, 50% well fill, pitch 30 μm) as a function of operating temperature (after Ref. [266]).

of the detector element in the array (of large LWIR HgCdTe hybrid array, a mismatch in the coefficient of thermal expansion between detector array and the readout can force the cell pitch to 20 μm or less to minimise lateral displacement). However, the development of heteroepitaxial growth techniques for HgCdTe on Si has opened up the possibility of cost-effectively producing significant quantities of large-area arrays through utilisation of large-diameter Si substrates.

For a $30 \times 30\,\mu m^2$ pixel size, the storage capacities are limited to 1 to 5×10^7 electrons. For example, for a 5×10^7 electron storage capacity, the total current density of a detector with a $30 \times 30\,\mu m^2$ pixel size has to be smaller than $27\,\mu A/cm^2$ with a 33 ms integration time [292]. If the total current density is in 1 mA/cm^2 range, the integration time has to be reduced to 1 ms. For the LWIR HgCdTe FPAs the integration time is usually below 100 μs. Since the noise power bandwidth $\Delta f = 1/2t_{int}$, a small integration time causes extra noise in integration.

Usually, LWIR QWIP FPAs using conventional ROIC typically operated at 60–65 K. Due to a smaller quantum efficiency of QWIP, filling the charge capacitor is not a problem at high background application. QWIP allows a longer integration time, which gives a relatively lower NEDT. However, at higher temperatures the dark current of QWIP is high and fills the charge capacitor very quickly. The current subtraction and switched capacitor noise filtering capabilities of ROICs permit low NEDT at higher operating temperatures. In this case, however, the readout circuit is complicated what limits the size of array.

A goal of third-generation imagers is to achieve sensitivity improvement corresponding to NEDT of about 1 mK. It results from Eq. (27) that in a 300 K scene in LWIR region with thermal contrast of 0.04, the required charge storage capacity is above 10^9 electrons. This high charge-storage density within the small pixel dimensions cannot be probably done with standard CMOS capacitors. Norton et al. [296] have suggested using of stacked hybrid structures as at least an interim solution to incorporate the desired charge storage density in detector–readout–capacitor structures.

8.10.5. Cost

The cost of a FPA depends strongly on the maturity of the technology and varies with production quantity in different companies. So far, large size LWIR FPAs are developed in R&D laboratories without mass production experience. According to Sofradir HgCdTe experience, by a continuous effort in the domain of industrialization decreased the cost of HgCdTe detectors by a factor of 5–10 [297]. The cost of making high performance cooled components can be broken down into three parts of about equal weight: the chip (detector and ROIC), the dewar, integration and tests [298]. In addition, the user must add the cryogenic machine cost that is not negligible compared to the component one's. Even if the detection circuit is free of charge, the total cost would only be reduced by about 15–20%. This explains why the cost of PtSi and QWIP detectors is not markedly less than that of photon detectors of the same complexity, even though the raw materials (Si or GaAs) is much less than for HgCdTe. Moreover, since PtSi requires a very wide optical

aperture to obtain acceptable performance, and since QWIP requires lower operating temperatures than other photon detectors, a possible reduction in the purchase price is counterbalance by a significant increase in operating cost.

HgCdTe detectors have been the centre of a major industry by the last three decades. The technology is relatively mature at MWIR but it does not fold over to LWIR. To make components with more pixels requires reducing the pitch or mastering the thinning operation needed to withstand the thermal cycling (differential thermal expansion between CdZnTe and silicon). In the future, more advantage approach seems to be using of Si substrates, which offer many well-known advantages relative to bulk CdZnTe substrates (much larger available size at lower cost, a thermal expansion match to Si readout chips, higher purity, and compatibility with automated wafer processing/handling methodology due to their superior mechanical strength and flatness). Promising results have been achieved in the SWIR and MWIR spectral region. During the last four years the defect density for MWIR layers of HgCdTe grown by MBE on silicon substrates has decreased from $2000\,\mathrm{cm}^{-2}$ to below $500\,\mathrm{cm}^{-2}$ [296]. Currently MWIR arrays with pixel operability of 98% can be produced from this material. For comparison, CdZnTe material operability is typically 99% or better. Defect densities for LWIR material grown on silicon substrates continue to limit performance, but they have been reduced by an order of magnitude in the past decade [296,299].

In comparison with HgCdTe FPAs, the industrial experience in QWIP FPAs is lower and improvements can be expected because this technology is at a lower step of development. The major challenge is at the device and grating designs to improve the device performance. Because of the maturity of the GaAs growth technology and stability of the material system, no investment is needed for developing QWIP substrates, MBE growth, and processing technology [292]. Development of LWIR and multicolour HgCdTe detectors are extremely difficult, especially for low background applications. It means a lower cost in QWIP technology developing and production compared with HgCdTe.

8.10.6. *Reliability*

In our discussion the reliability issue has been omitted due to the fact that statistical data on this subject is not available. In several applications, especially military systems demand high reliability to ensure both the success of the mission and minimal risk to the user. Two reliability challenges affect both FPAs; survival in high temperature system storage environments and withstanding repetitive thermal cycles between ambient and cryogenic temperatures. In HgCdTe as well as in QWIP FPAs, the indium bumps are used to hybridise both type of detectors with silicon multiplexer. However, certain problems can be expected in the case of QWIP arrays, since the indium bumps have many known alloys with III–V compounds.

Very large FPAs may exceed the limits of hybrid reliability engineered into current cooled structures. Hybrids currently use mechanical constraints to force the contraction of the two components to closely match each other. This approach

may have limits, when the stress reaches a point where the chip fractures. Three approaches offer an opportunity to resolve this issue:

- to eliminate the thick substrate which limits the detector active region from deforming at the slower rate of the silicon readout,
- to subdivide the array into a plurality of regions,
- to use silicon as the substrate for growth of the detector material.

  A technology for making HgCdTe photodiodes and QWIPs on silicon substrate would be the ultimate simply because of the vast existing silicon technology. However, major issue with this approach are: [296]
- less area would be available for readout circuitry,
- microlens arrays would be required to regain fill factor,
- material quality may not be adequate for low-leakage detectors, particularly for LWIR HgCdTe photodiodes,
- silicon integrated circuits are processed on $\langle 100 \rangle$ oriented silicon, but e.g., the preferred orientation for HgCdTe growth on silicon is near the $\langle 211 \rangle$ orientation.

Less demanding approaches to the elimination of the thick detector substrate is the loophole or high density vertically integrated photodetector device structures already practiced by GEC Marconi and DRS, respectively. In this approach, HgCdTe material is glued to the readout and contacts made through thin layer (10–20-μm) after the substrate is removed [see Fig. 14(b)]. Another approach is to remove the substrate after hybridisation with indium bumps. Substrate removal is standard practice with very large hybrid InSb arrays (1024×1024 pixels). This approach has been recently adopted for QWIP arrays [262,263,266]. After epoxy backfilling of the gaps between array and the readout multiplexer, the substrate is thinned to a very thin membrane (≈ 1000 Å). This allows not only elimination of the thermal mismatch problem between the silicon readout and the GaAs based detector array, but also completely eliminates pixel-to-pixel crosstalk, and finally, significantly enhances an optical coupling of IR radiation into QWIP pixels.

8.10.7. Summary

LWIR QWIP cannot compete with HgCdTe photodiode as the single device, especially at temperature above 70 K due to fundamental limitations associated with intersubband transitions. However, the advantage of HgCdTe is less distinct in temperature range below 50 K.

Comparing photovoltaic HgCdTe and QWIP technologies, we arrive at the following conclusions:

- two major issues that impede the performance of QWIPs should be overcome: optical conversion efficiency and dark current,
- for HgCdTe, the improvment of the array uniformity is necessary,
- QWIP seems more potential to realize VLWIR FPA operation (also with multicolour detection).

The main drawbacks of LWIR QWIP FPA technology are the performance limitation for low integration time applications and low operating temperature. Their main advantages are linked to performance uniformity and to availability of large size arrays. Next, the main drawback of LWIR HgCdTe FPA technology is the unavailability of large size arrays necessary for TV format and larger ones.

Several properties of QWIP such as high impedance, fast response time, long integration time, and low power consumption, well comply requirements of fabrication large FPAs. Due to the high material quality at low temperature, QWIP has potential advantages over HgCdTe for VLWIR FPA applications in terms of the array size, uniformity, yield and cost of the systems. Three-band and four-band FPAs will be demonstrated in the near future.

State of the art QWIP and HgCdTe FPAs provide similar performance figure of merit, because they are predominantly limited by the readout circuits. The performance is, however, achieved with very different integration times. The very short integration time of LWIR HgCdTe devices of typically below 300 μs is very useful to freeze a scene with rapidly moving objects. QWIP devices achieve, due to excellent homogeneity, an even better NEDT, however, the integration time must be 10–100 times longer for that, and typically is 5–20 ms. Decision of the best technology is therefore driven by the specific needs of a system. Observation of the global market through past several years has indicated that even HgCdTe photodiodes intrinsically exhibit higher performance that the QWIP detectors, the market tendencies for the future are:

- HgCdTe for small formats (e.g., 128×128), small pitch, high frame rates and low integration times,
- QWIP for large formats (e.g., 640×480 and larger), low frame rates and large integration time.

Despite serious competition from alternative technologies and slower progress than expected, HgCdTe is unlikely to be seriously challenged for high-performance applications, applications requiring multispectral capability and fast response.

8.11. Quantum dot infrared photodetectors

The 2-D confinement of carriers in quantum wells, with the resultant discretization of the energy structure, is not the only approach to infrared photodetection. Carrier confinement in all three dimensions can also be used. This can be realized via semiconductor nanostructures known as quantum dots. The beginning of the interest in quantum dot research can be traced back to a sugestion by Arakawa and Sakaki in 1982 [300] that the performance of semiconductor lasers could be improved by reducing the dimensionality of the active regions of these devices. Initial efforts at reducing the dimensionality of the active regions focused on using ultrafine lithography coupled with wet or dry chemical etching to form 3-D structures. It was soon realized, however, that this approach introduced defects that greatly limited the performance of such quantum dots. Initial efforts were mainly focused on

the growth of InGaAs nanometer-sized islands on GaAs substrates. In 1993, the first epitaxial growth of defect-free quantum-dot nanostructures was achieved by using MBE [301]. Most of the practical quantum-dot structures today are synthesized by either MBE and MOCVD.

Under certain growth conditions, when the thickness of the film with the larger lattice constant exceeds a certain critical thickness, the compressive strain within the film is relieved by the formation of coherent island. These islands may be quantum dots. Coherent quantum-dot islands are generally formed only when the growth proceeds in what is known as Stranski–Krastanow growth model [302]. The onset of the transformation of the growth process from a 2-D layer-by-layer growth mode to a 3-D island growth mode results in a spotty RHEED pattern. This is in contrast to the conventional streaky pattern generally observed for the layer-by-layer growth mode. The transition typically occurs after the deposition of a certain number of monolayers. For InAs on GaAs, this transition occurs after about 1.7 monolayers of InAs have been grown; this is the onset of islanding and, hence, quantum-dot formation. There have been extensive studies of island growth on other material systems, such as: InGaAlAs on InP, InSb on GaSb and GaAs, InGaAs on Si, Ge on Si, and InGaAs on InGaP.

Recent studies have shown the potential advantages in using quantum dot infrared photodetectors (QDIPs) between three major of quantum dots over quantum wells are as follows:

- Intersubband absorption may be allowed at normal incidence (for n-type material). In QWIPs only transitions polarized perpendicular to the growth direction are allowed, due to absorption selection rules. The selection rules in QDIPs are inherently different, and normal incidence absorption is observed.
- Thermal generation of electrons is significantly reduced due to the energy quantization in all three dimensions. Generation by LO phonons is prohibited unless the gap between the discrete energy levels equals exactly to that of the phonon. This prohibition does not apply to quantum wells, since the levels are quantized only in the growth direction and a continuum exists in the other two (hence generation-recombination by LO phonons with capture time of few picoseconds). Thus, it is expected that S/N ratio in QDIPs will be significantly larger than that of QWIPs.
- It is expected lower dark current of QDIPs than HgCdTe detectors and QWIPs due to 3-D quantum confinement of the electron wavefunction.

The main disadvantage of the QDIP is the large inhomogeneous linewidth of the quantum-dot ensemble variation of dot size in the Stranski–Krastanow growth mode [303,304]. As a result, the absorption coefficient is reduced, since it is inversely proportional to the ensemble linewidth. Vertical coupling of quantum-dot layers also reduces the inhomogeneous linewidth of the quantum-dot ensemble; however, it may also increase the dark current of the device, since carriers can tunnel through adjacent dot layers more easily. As in other type of detectors, also nonuniform dopant incorporation adversely affects the performance of the QDIP.

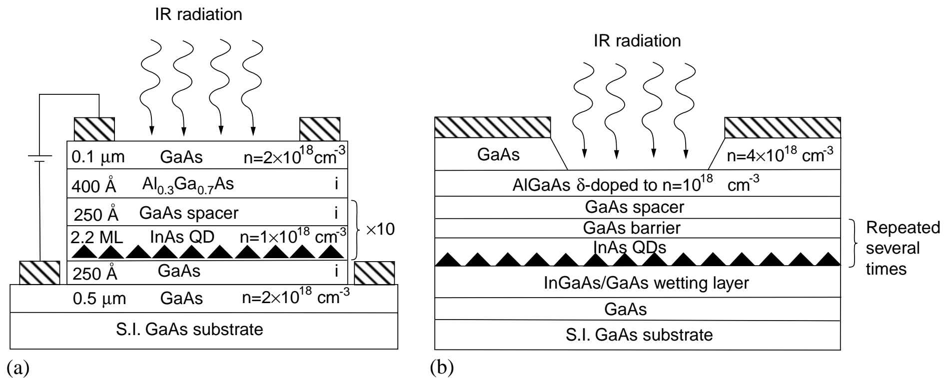

Fig. 65. Schematic diagrams of the two basic quantum-dot detector structures. Structure (a) is identical to the conventional QWIP structure (the photoexcited carriers use vertical transport through the stack of self-assembled quantum-dot layers to reach the external circuit conduction). In structure (b) the carrier use lateral transport similar to that in a channel of a field-effect transistor.

There are two possible kinds of device structures for a QDIP shown in Fig. 65: conventional photodetector structure (vertical structure) and lateral structure [303]. The vertical QDIP is so called because it collects the photocurrent through vertical transport of carriers between a top and bottom contact. The quantum dots are directly doped (usually with silicon) in order to provide free carriers during photoexcitation, and an AlGaAs barrier can be included in the vertical device heterostructure in order to block dark current created by thermionic emission [305,306].

The lateral QDIP collects photocurrent through transport of carriers across a high-mobility channel between two top contacts, operating much like a field-effect transistor. As previously, again AlGaAs barriers are present, but instead of blocking the dark current, these barriers are used to both modulation-dope the quantum dots and to provide the high-mobility channel. Lateral QDIPs have demonstrated lower dark currents and higher operating temperatures than vertical QDIPs since the major components of the dark current arise from interdot tunneling and hopping conduction [307]. However, these devices will be difficult to incorporate into a FPA hybrid-bump bonded to a silicon read-out circuit. Because of this, more efforts is directed to improve the performance of vertical QDIPs which are more compatible with commercially available read-out circuits.

Fig. 65(a), for example, shows vertical structure of InAs–GaAs QDIP. First, a 0.5 μm silicon-doped ($n = 2 \times 10^{18}\,\text{cm}^{-3}$) GaAs contact layer was deposited on a semi-insulating (1 0 0) GaAs substrate. Next, a 250 Å intrinsic GaAs buffer was grown. To form InAs quantum dots, after the completion of growth of the initial "wetting layer", the silicon doped ($n = 2 \times 10^{18}\,\text{cm}^{-3}$) InAs quantum dots were grown. A 250 Å intrinsic cap layer was grown on top of the InAs in order to complete the quantum-dot barrier. This sequence of growth was then repeated nine times for a ten-layer InAs–GaAs quantum-dot active region. After the final GaAs layer was grown, a 400 Å intrinsic $Al_{0.3}Ga_{0.7}As$ was deposited in order to form a

current-blocking barrier. Finally, a 0.1-μm silicon-doped ($n = 2 \times 10^{18}\,\mathrm{cm}^{-3}$) GaAs top contact layer was grown.

To fabricate the vertical InAs–GaAs QDIPs, a standard, three-step photolithography and wet-etching process was used:

- Ni–Ge–Au–Ti-Au mesa evaporation for the top ring contact,
- a mesa etch ($\approx 1\,\mu\mathrm{m}$) was performed around the top contact to define the active region,
- the metal evaporation was repeated for the bottom contact.

To make ohmic contacts, the device was finally annealed at 400°C for 1 minute.

At present stage of their development, the performance of QDIPs is clearly inferior to the related QWIPs [304,308–310]. For example, the above described MWIR InAs–GaAs QDIPs are characterized by peak responsivity of 2 mA/W at 4 μm and peak detectivity of $3 \times 10^9\,\mathrm{cmHz}^{1/2}/\mathrm{W}$ at $T = 100\,\mathrm{K}$; a photoconductive gain of $g = 18$ for bias voltage of 0.3 V was measured in these detectors [308]. However, because of their potential theoretical promise, quantum-dot detectors are likely to emerge as an alternative to QWIPs.

For the most part of the active photosensitive region of conventional quantum well photodetectors the electronic structure is symmetric about a plane of symmetry at the midpoint of the region. Most of the device characteristics for quantum well detectors are therefore symmetric. The common techniques for incorporating asymmetries in quantum well structures include grading the barriers unequally on either side of the well, sandwiching the well between barriers of unequal gaps, or nonuniformily doping the barriers. As a result, quantum well devices with built-in electric fields can operate as photovoltaic detectors; no applied external bias is necessary for the device operation.

QDIPs are intrinsically photovoltaic what originates from the geometric shape of the dots. Because the wetting layers introduce a shallower potential than do the dots, and overall asymmetrical band structure is naturally formed [see Fig. 66(a)]. In addition to the asymmetric effect of the wetting layer, the dots are also asymmetric with respect to the growth plane because of their shape (which can be pyramidal or planoconvex lens-shaped, depending on the growth conditions). The shape of the dots, therefore, further increases the degree of asymmetry of the band structure of the detector layers, what is schematically shown in Fig. 66(b). Electrons in the excited state of such a structure are swept across by the built-in field, thus contributing to the photocurrent. The intrinsic photovoltaic capability also belongs to key advantages of QDIPs.

8.12. Dual-band detectors

Multicolour capabilities are highly desirable for advance IR systems. Systems that gather data in separate IR spectral bands can discriminate both absolute temperature and unique signatures of objects in the scene. By providing this new dimension of contrast, multiband detection also enables advanced colour processing algorithms to further improve sensitivity above that of single-colour devices.

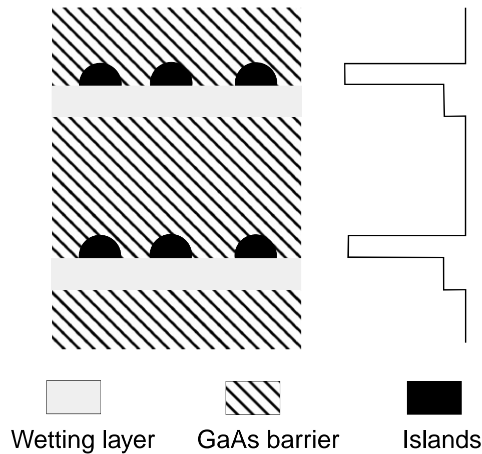

Fig. 66. Schematic diagram of stacked layers of (a) InGaAs-on-GaAs quantum dot islands; (b) the electronic structure of the conduction band of such layers (after Ref. [303]).

Multispectral detection permits rapid and efficient understanding of the scene in a variety of ways. In particular, two-colour IR FPAs can be especially beneficial for threat-warning applications. By using two IR wavebands, spurious information, such as background clutter and sunglint, may be subtracted from an IR image, leaving only the objects of interest. Multispectral IR FPAs can also play many important roles in Earth and planetary remote sensing, astronomy, etc. Thus, the effective signal-to-noise ratio of two-colour IR FPAs greatly exceeds that of single-colour IR FPAs for specific applications.

Currently, multispectral systems rely on cumbersome imaging techniques that either disperse the optical signal across multiple IR FPAs or use a filter wheel to spectrally discriminate the image focused on single FPA. These systems contain beam-splitters, lenses, and bandpass filters into the optical path to focus the images onto separate FPAs responding to different IR bands. Also complex alignment is required to map the multispectral image pixel for pixel. Consequently, these approaches are expensive in terms of size, complexity, and cooling requirements.

At present, considerable efforts are directed to fabricate a single FPA with multicolour capability to eliminate the spatial alignment and temporal registration problems that exist whenever separate arrays are used, to simplify optical design, and reduce size, weight, and power consumption. Considerable progress has been recently demonstrated by research groups at Hughes Research Laboratory (Raytheon) [311,312], Lockheed Martin (BAE Systems) [313], DRS Infrared Technology [314], AIM [275], Rockwell [315], and Leti [316] in multispectral HgCdTe detectors employing mainly MBE (although LPE and MOCVD are also used) for the growth of variety devices. Also QWIP's technology demonstrates considerably progress in fabrication of multicolour FPAs [255,263,266,317–322]. It is, perhaps, the niche in which QWIPs have an intrinsic advantage due to relative ease of growing multi-band structures by MBE with very low defect density. Devices

for the sequential and simultaneous detection of two closely spaced sub-bands in the MWIR and LWIR radiation have been demonstrated.

8.12.1. Dual-band HgCdTe

In the back-illuminated dual-band detectors, the photodiode with longer cutoff wavelength is grown epitaxially on top of the photodiode with the short cutoff wavelength. The shorter-cutoff photodiode acts as a long-wavelength-pass filter for the longer-cutoff photodiode.

Both sequential mode and simultaneous mode detectors are fabricated from the multi-layer materials. The simplest two-colour HgCdTe detector, and the first to be demonstrated, is the bias-selectable n–p–n back-to-back photodiode shown in Fig. 67(a). The n-type base absorbing regions are deliberately doped with indium at a level of about $(1–3) \times 10^{15}\,\mathrm{cm}^{-3}$. Critical step in device formation is connected with in situ doped p-type As-doped layer with good structural and electrical properties to prevent internal gain from generating spectral crosstalk. The band-gap engineering effort consists of increasing the CdTe mole fraction and the effective thickness of the p-type layer to suppress out-off-band carriers from being collected at the terminal. The sequential-mode detector has a single indium bump per unit cell that permits sequential bias-selectivity of the spectral bands associated with operating tandem photodiodes. When the polarity of the bias voltage applied to the bump contact is positive, the top (LW) photodiode is reverse biased and the bottom (SW) photodiode is forward biased. The SW photocurrent is shunted by the low impedance of the forward-biased SW photodiode, and the only photocurrent to emerge in the external circuit is the LW photocurrent. When the bias voltage polarity is reversed, the situation reverses; only SW photocurrent is available. Switching times within the detector can be relatively short, in the order of microseconds, so detection of slowly changing targets or imagers can be done by switching rapidly between the MW and LW modes.

One bump contact per unit cell, as for single-colour hybrid FPAs, is the big advantage of the bias-selectable detector. It is compatible with existing silicon readout chips. The problems with the bias selectable device are the following: its construction does not allow independent selection of the optimum bias voltage for each photodiode, and there can be substantial MW crosstalk in the LW detector. An implementation of the simultaneous mode using a second indium bump in the unit cell is shown in Fig. 68.

Many applications require true simultaneity of detection in the two spectral bands. This has been achieved in a number of ingenious architecture described by Reine [323]. All these simultaneous dual-band detector architectures require an additional electrical contact to an underlying layer in the multijunction structure to both the SW and LW photodiode. The most important distinction is the requirement of a second readout circuit in each unit cell.

Integrated two-colour HgCdTe technology has been developed for nearly a decade with a steady progression having a wide variety of pixel size (30 to 61 μm), array formats (64×64 up to 320×240) and spectral-band sensitivity (MWIR/MWIR, MWIR/LWIR and LWIR/LWIR). Fig. 69 shows examples of spectral response from different two-colour devices. Note that there is a minimal crosstalk between the

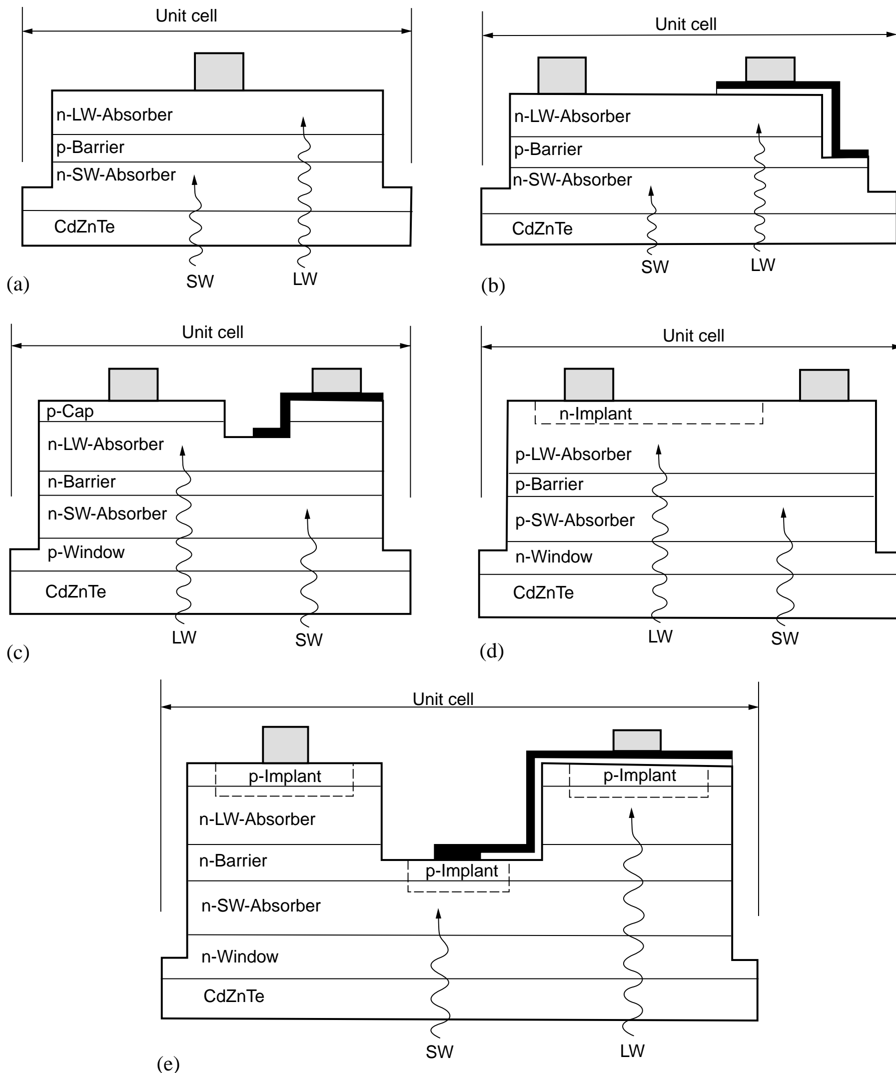

Fig. 67. Cross section views of unit cells for various back-illuminated dual-band HgCdTe detector approaches: (a) bias-selectable n–p–n structure reported by Raytheon [311], (b) simultaneous n–p–n design reported by Raytheon [312], (c) simultaneous p–n–n–p reported by BAE Systems [313], (d) simultaneous n–p–p–p–n design reported by Leti [316] and (e) simultaneous structure based on p-on-n junctions reported by Rockwell [315] (after Ref. [323]).

bands, since the short wavelength band absorbs nearly 100% of the shorter wavelengths. Test structure indicates that the separate photodiodes in a two-colour detector perform exactly as single-colour detectors in terms of achievable R_oA product variation with wavelength at a given temperature.

Fill factors of 128×128 MWIR/MWIR FPAs as high as 80% were achieved by using a single mesa structure to accommodate the two indium bump contacts

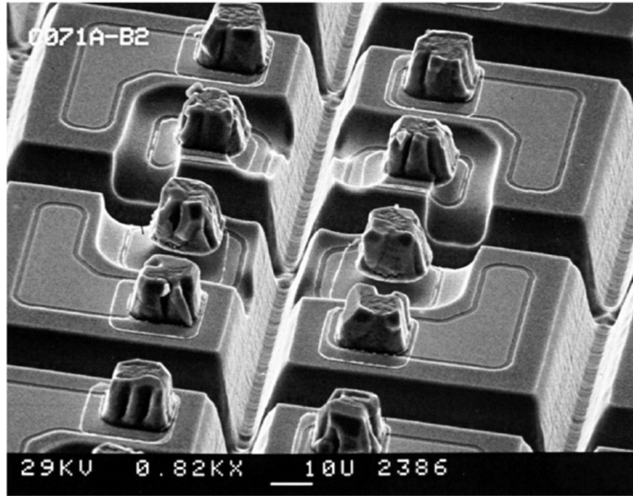

Fig. 68. SEM photo of a 64 × 64 two-colour HgCdTe detector array with 75 × 75 μm^2 unit cells (after Ref. [313]).

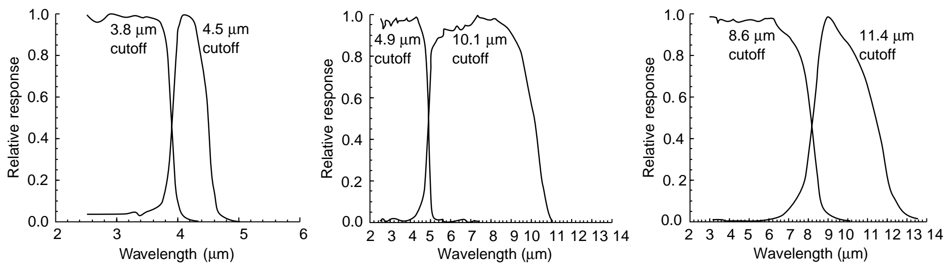

Fig. 69. Spectral response curves for two-color HgCdTe detectors in various dual-band combinations of MWIR and LWIR spectral bands (after Ref. [44]).

required for each unit cell with 50-μm size [9]. The NEDT for both bands was below 25 mK and imagery was acquired at temperatures as high as 180 K with no visible degradation in image quality. The camera used for these measurements had a 50 mm, $f/2.3$ lens.

Recently, Rockwell and Boeing have extended a single-colour DLHJ planar technology (see Section 8.1.2) to two-colour architecture [see Fig. 67(e)] [315]. Two-colour 128 × 128 FPAs of 40-μm pitch have been fabricated; low-10^{13} cm^{-2}s^{-1} background limited detectivity performance have been obtained for MWIR (3–5 μm) devices at $T < 130$ K and for LWIR (8–10 μm) devices at $T \approx 80$ K.

8.12.2. Dual-band QWIPs

Sanders was first to fabricate two-colour, 256 × 256 bound-to-miniband QWIP FPAs in each of four important combinations: LWIR/LWIR, MWIR/LWIR, near IR (NIR)/LWIR and MWIR/MWIR—with simultaneous integration [255,318].

Device capable of simultaneously detecting two separate wavelengths can be fabricated by vertical stacking of the different QWIP layers during epitaxial growth. Separate bias voltages can be applied to each QWIP simultaneously via the doped contact layers that separate the MQW detector heterostructures. Fig. 70 shows schematically the structure of a two-colour stacked QWIP with contacts to all three ohmic-contact layers. The device epilayers were grown by MBE on 3-in semi-insulating GaAs substrate. An undoped GaAs layer, called an isolator, was grown between two AlGaAs each stop layers, followed by Au/Ge ohmic contact of 0.5 μm thick doped GaAs layer. Next, the two QWIP heterostructures were grown, separated by another ohmic contact. The long wavelength sensitive stack (red QWIP, $\lambda_c = 11.2\,\mu m$) is grown above the shorter wavelength sensitive stack (blue QWIP, $\lambda_c = 8.6\,\mu m$). Each QWIP is a 20-period GaAs/$Al_xGa_{1-x}As$ MQW stack in which the thickness of the Si-doped GaAs QWs (with typical electron concentration $5 \times 10^{17}\,cm^{-3}$) and the Al composition of the undoped $Al_xGa_{1-x}As$ barriers ($\approx$550–600 Å) is adjusted to yield the desired peak position and spectral width. The gaps between FPA detectors and the readout multiplexer were backfilled with epoxy. The epoxy backfilling provides the necessary mechanical strength to the detector array and readout hybrid prior to array's thinning process.

Most QWIP arrays use 2-D grating, which is very wavelength dependent, and efficiency gets lower when the pixel size gets smaller. Lockheed Martin has used rectangular and rotated rectangular 2-D gratings for their two-colour LW/LW FPAs. Although random reflectors have achieved relatively high quantum efficiencies with large test device structure, it is not possible to achieve the similar high quantum efficiencies with random reflectors on small FPA pixels due to the reduced width-to-height aspect rations [266]. In addition, it is difficult to fabricate random reflectors for shorter wavelength detectors relative to long wavelength detectors due to the fact that feature sizes of random reflectors are linearly proportional to the peak wavelength of the detectors. The quantum efficiency becomes a more difficult issue for QWIP multicolour FPA than for single colour.

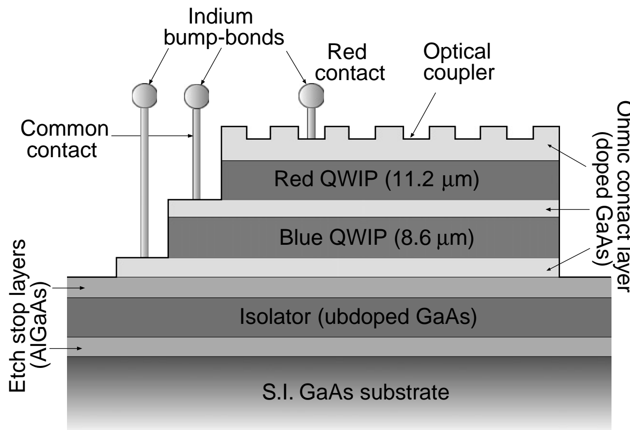

Fig. 70. Structure of two-color stacked QWIP (after Ref. [318]).

Typical operating temperature for QWIP detectors is in the region of 40–80 K. The bias across each QWIP can be adjusted separately, although it is desirable to apply the same bias to both colours. As shown in Fig. 71, the responsivity of both QWIPs is around 300–350 mA/W. It appears that the complex two-colour processing has not compromised the electrical and optical quality of either colour in the two-colour device since the peak quantum efficiency for each of the 20-period QWIPs was estimated to be $\approx$ 10% in comparison with a normal single-colour QWIP with twice the number of periods has a quantum efficiency of around 20%. A pixel operability for each colour is $>97\%$ in comparison to the value of $>99.9\%$ routinely achieved for single-colour QWIPs. The NEDT value was 24 mK for the blue QWIP and 35 mK for the red QWIP. The difference was assigned to the poor transmission properties of the optics in the 11.2 μm band. An accurate methodology is needed to design the detector structure properly to meet different requirements. In the production process, the fabrication of gratings is still quite involved, and its efficiency is rather uncertain in small pixels and in pixels with thick material layers.

To cover MWIR range a strained layer InGaAs/AlGaAs material system is used. InGaAs in MWIR stack produces high in-plane compressive stain which enhances the responsivity [266,324]. The MWIR/LWIR FPAs fabricated by Sanders consist of an 8.6 μm GaAs/AlGaAs QWIP on top of 4.7 μm strained InGaAs/GaAs/AlGaAs heterostructure.

Recently, Gunapala et al. [319,320] have demonstrated the first 8–9 and 14–15 μm two-colour imaging camera based on a 640 × 486 dual-band QWIP FPA, which can be processed with dual or triple contacts to access the CMOS readout multiplexer. Single indium bump per pixel is usable only in the case of interlace readout scheme (i.e., odd rows for one colour and the even rows for the other colour) which uses an existing single colour CMOS readout multiplexer. However, the disadvantage is that it does not provide a full fill factor for both wavelength bands.

The 640 × 486 GaAs/AlGaAs gave excellent images with 99.7% of the LWIR pixels and 98% of VLWIR pixels working, demonstrating the high yield of GaAs

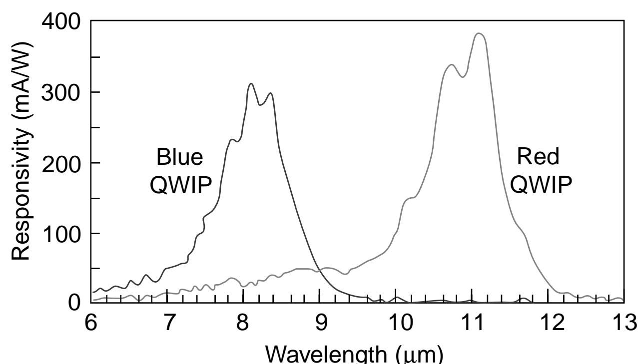

Fig. 71. Typical responsivity spectra at 40 K and a common bias of 1.5 V, recorded simultaneously for two QWIPs in the same pixel (after Ref. [318]).

technology. The estimated NEDT of LWIR and VLWIR detectors at 40 K are 36 and 44 mK, respectively. Due to BLIP, the estimated and experimentally obtained NEDT values of the LWIR detectors do not change significantly at temperatures below 65 K. The experimentally measured values of LWIR NEDT equal to 29 mK are lower than the estimated ones. This improvement is attributed to the 2-D periodic grating light coupling efficiency. However, the experimental VLWIR NEDT value is higher than the estimated value. It is probably a result of the inefficient light coupling at 14–15 μm region, readout multiplexer noise, and noise of the proximity electronics. At 40 K the performance of both bands detector pixels are limited by photocurrent noise and readout noise.

9. Thermal detectors

The use of thermal detectors for IR imaging has been the subject of research and development for many decades. Thermal detectors are not useful for high-speed scanning thermal imagers. Only pyroelectric vidicons have found more widespread use. These devices achieved their fundamental limits of performance by about 1970. However, the speed of thermal detectors is quite adequate for non-scanned imagers with 2-D detectors. Fig. 72 shows the dependence of NEDT on noise bandwith for typical detectivities of thermal detectors. The calculations have been carried out assuming $100 \times 100\,\mu m^2$ pixel size, 8–14-μm spectral range, $f/1$ optics and $t_{op} = 1$ of IR system. With large arrays of thermal detectors the best values of NEDT below 0.1 K could be reached because effective noise bandwidths less than 100 Hz can be achieved. This compares with a bandwidth of several hundred kilohertz for a conventional cooled thermal imagers with a small photon detector array and scanner. Realization of this fact caused a new revolution in thermal imaging, which is underway now [23,326]. This is due to the development of 2-D electronically scanned arrays, in which moderate sensitivity can be compensated by a large number of elements. Large scale integration combined with micromachining has been used for manufacturing of large 2-D arrays of uncooled IR sensors. This will enable low cost and high-quality thermal imagers in near future.

Typical costs of cryogenically cooled imagers of around $50000 restrict their installation to critical military applications allowing conducting of operations in complete darkness. Very encouraging results have been obtained with micro-machined silicon bolometer arrays [23,24,26,27,29] and pyroelectric detector arrays [25,28,29,327]. Several countries have demonstrated imagers with NEDT below 100 mK, and the cost of simple systems is sometimes below $10000. It is expected that high-performance imager system costs will be reduced to less than $1000 [328], and above IR cameras will become widely available in the near future. Although developed for military applications, low-cost IR imagers are used in nonmilitary applications such as: drivers aid, aircraft aid, industrial process monitoring, community services, firefighting, portable mine detection, night vision, border surveillance, law enforcement, search and rescue, etc.

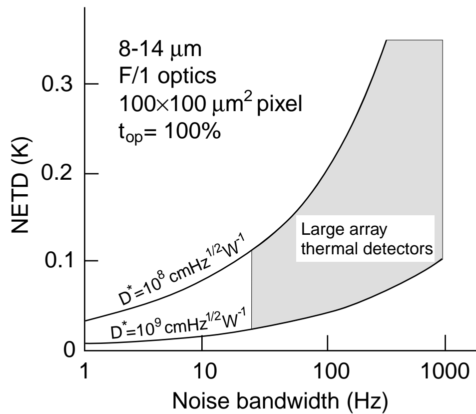

Fig. 72. The NETD versus equivalent noise bandwidth for typical detectivities of thermal detectors (after Ref. [325]).

9.1. Micromachined silicon bolometers

A new generation of monolithic Si bolometers has been introduced by Downey et al. [329]. They presented a bolometer concept in which a thin Si substrate supported by narrow Si legs is micromachined from a Si wafer using the techniques of optical lithography. A conventional Bi film absorber was used on the back of the substrate, but the thermometer was created directly in the Si substrate by implanting P and B ions to achieve a suitable donor density and compensation ratio. However, the performance of the bolometer was not good. Further progress in monolithic Si bolometer technology is fascinating. Honeywell Sensor and System Development Center in Minneapolis began developing silicon micromachined IR sensors in the early 1980s. The goal of the work sponsored by DARPA and US Army Night Vision and Electronic Sensors Directorate was aimed at producing low-cost night-vision systems amenable to wide use throughout the military with NETD of 0.1°C using $f/1$ optics. Both Si bolometer arrays and pyroelectric arrays of Texas Instruments have exceeded that goal [330]. The microbolometer will have the lowest unit cost, as it uses a monolithic fabrication process that is compatible with standard silicon process on 8″ or greater wafers. Chopperless operation can be obtained using the microbolometer, thereby eliminating all mechanical parts from the sensor. This not only decreases the ultimate unit cost, but improves both the reliability and operating range. Greater dynamic range and a more linear response makes the microbolometer technology more highly suited for applications like mine detection, target signature, radiometric measurement, process control, and facilities/equipment maintenance.

In practice, two options for the detector structure are used: microbridge and pellicle-supported designs. The former comprises detector elements which are supported on legs above the plane of the microcircuit. The legs are designed to have a high thermal resistance, and carry electrical conductors from the detector to microcircuit. This approach is applied in the Honeywell microbolometer design

[23,24,27]. The second concept consists of detector elements deposited onto a thin dielectric pellicle which is coplanar with the surface of the wafer, and is the basis of Australian monolithic detector technology [331,332].

The most popular thermistor material used in fabrication of the micromachined silicon bolometers is vanadium dioxide, VO_2 [333,334]. Vanadium is a metal with a variable valence forming a large number of oxides. Preparation of these materials in both bulk and thin film forms is very difficult given the narrowness of the stability range of any oxide. Some of the vanadium oxides, among them the best known being V_2O_3 and VO_2, show a temperature-induced crystallographic transformation that is accomplished by reversible semiconductor (low-temperature phase) to metal (high-temperature phase) phase transition with a significant change in electrical and optical properties (Fig. 73). Vanadium dioxide undergoes its transition in the temperature range from about 50 to 70°C. The resistivity change and optical properties of VO_2 films strongly depend on the fabrication conditions and the resulting crystallographic structure and stoichiometry. There are two reasons for not using VO_x ($x > 2$) with substantially higher temperature coefficient: first, reproducibility of properties suffers in the higher x-value films, second, heating becomes a problem with high resisitivity films.

The basic fabrication process used to fabricate Honeywell silicon microbolometers together with a brief explanation of the micromachinning process steps is shown in Fig. 74. Fabrication begins with implantation of the required read-out electronics and conducting metallizations in the Si wafer. The wafer is then planarized with a material, such as spun-on polyimide, which can be photolithographically patterned to form sacrificial mesas. Silicon nitride layers are sputtered over the sacrificial mesas, together with TCR material and connecting metallizations. As a final step, the sacrificial mesas are removed by a material-selective etch, for example, oxygen plasma etching to leave a self-supporting two-level structure.

The final microbolometer pixel structure is shown in Fig. 75. The microbolometer consists of a 0.5 μm thick bridge of Si_3N_4 suspended about 2 μm above the underlying silicon substrate. The use of a vacuum gap of approximately 2.5 μm,

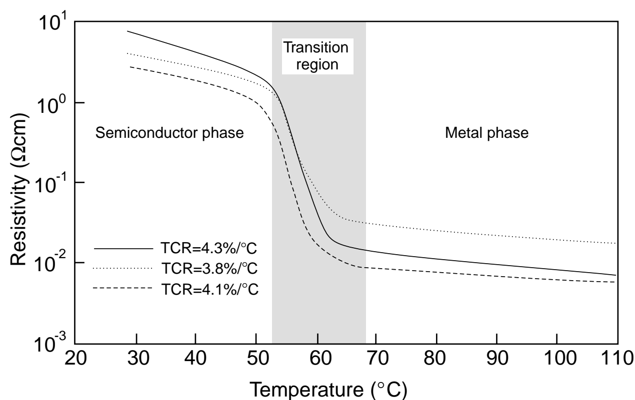

Fig. 73. Resistivity versus temperature characteristics of three VO_2 films (after Ref. [334]).

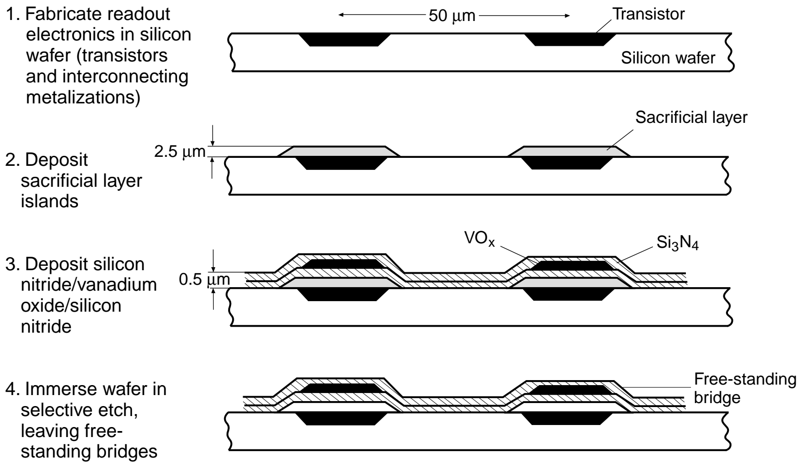

Fig. 74. Simplified process of two-level Honeywell microbolometer fabrication (after Ref. [24]).

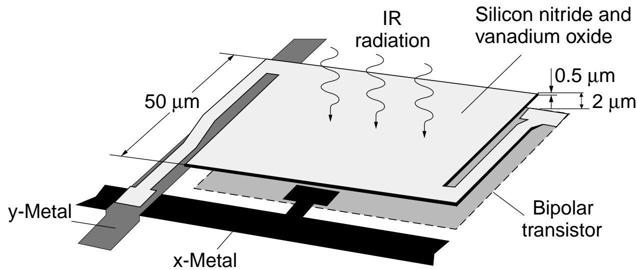

Fig. 75. Bridge structure of Honeywell microbolometer (after Ref. [335]).

together with a quarter wave resonant cavity between the bolometer and the underlying substrate, can produce a reflector for wavelengths near 10 μm [24]. The bridge is supported by two narrow legs of Si_3N_4. The Si_3N_4 legs provide the thermal isolation between the microbolometer and the heat-sink readout substrate. The Si_3N_4 supporting legs with 500-Å Ni–Cr conductive films give a thermal conductance $G_{th} = 2 \times 10^{-7}$ W/K and a thermal time constant $\tau_{th} = 20$ ms. A bipolar input amplifier is normally required, and this can be obtained with biCMOS processing technology. Si_3N_4 is used because of its excellent processing characteristics. This allowed microbolometers to be fabricated with thermal isolation close to the attainable physical limit which is about 1×10^8 K/W for a 50-μm-square detector. It was demonstrated that, with a microbolometer having a thermal isolation of 1×10^7 K/W, a typical incident IR signal of 10 nW was sufficient to change the microbolometer temperature by 0.1 K [23]. The measured thermal capacity was about 10^{-9} J/K which corresponds to a thermal time constant of 10 ms. Honeywell has determined that the microbridges are robust structures that can tolerate shocks

of several thousand g-forces. Encapsulated in the centre of the Si_3N_4 bridge is a thin layer (500 Å) of polycrystalline VO_x. Vanadium oxide based materials exhibit a high TCR (typical for pixel array about –2%/K). Moreover, VO_x assures good combination of high TCR, electrical resistivity, and fabrication capability, which has resulted in pixels with responsivity of 250 000 V/W in response to 300 K blackbody radiation [336]. To obtain the high thermal isolation of the microbolometer, the ambient gas pressure must be less than about 75 mtorr (at these conditions the mean free path becomes limited by the physical gap distance of about 2 μm). The bolometers in principle do not need to be thermally stabilized. A bipolar input amplifier is normally required, and this can be obtained with biCMOS technology. In order to achieve bandwidth limitation at pixel level, and to avoid aliasing if filtering takes place after multiplexing, a large value of capacitance must be provided. This presents significant challenges in CMOS processing technology. The dominant noise was Johnson noise in the sensitive resistor (typically 10–20 kΩ), with some additional contribution from $1/f$ noise and transistor readout noise. A monolithic multiplexer on the Honeywell's array periphery allows random access addressing of any pixel in the array. In operation, an array consumed about 40 mW [336]. An average NEΔT of better than 0.05 K was demonstrated with uncooled imager fitted with an $f/1$ optic (Fig. 76).

Honeywell has licensed this technology to several companies for the development and production of uncooled FPAs for commercial and military systems. At present, the compact 320 × 240 microbolometer cameras are produced by Raytheon, Boeing, and Lockheed-Martin in the United States. The U.S. government allowed these manufactures to sell their devices to foreign countries, but not to divulge manufacturing technologies. In recent years, several countries, including the United Kingdom, Japan, Korea, and France have picked up the ball, determined to develop

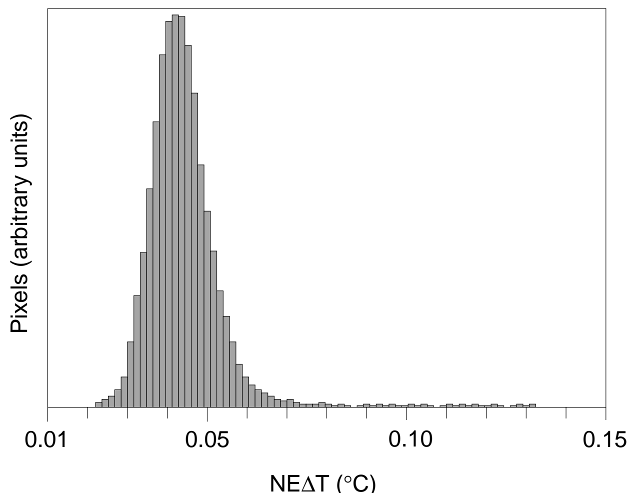

Fig. 76. Measured pixel NEDT histogram of Honeywell uncooled imager with $f/1$ optics (after Ref. [336]).

their own uncooled imaging systems. As a result, although the U.S. has a significant lead, some of the most exciting and promising developments for low-cost uncooled IR systems may come from non-U.S. companies, e.g., microbolometer FPAs with series p–n junction elaborated by Mitsubishi Electric [337]. This approach is unique, based on an all-silicon version of microbolometer.

The 240×320 arrays of 50-μm microbolometers are fabricated on industry-standard wafer (4-in diameter) complete with monolithic readout circuits integrated into underlying silicon. Radford et al. [338] have reported a 240×320 pixel array with 50-μm square vanadium oxide pixels and thermal time constant of about 40 ms, for which the average NETD ($f/1$ optics) was 8.6 mK.

However, there is a strong system need to reduce the pixel size to achieve several potential benefits. The detection range of many uncooled IR imaging systems is limited by pixel resolution rather than sensitivity. Because the cost of the optics made of Ge, the standard material, depends approximately upon the square of the diameter, so reducing of the pixel size causes reducing cost of the optics. These reductions in optics size would have a major benefit in reducing the overall size, weight and cost of manportable IR systems. In addition the reduction in pixel size allows a significantly larger number of FPAs to be fabricated on each wafer what allows a significantly larger of FPAs to be fabricated on each wafer. However, the NEDT is inversely proportional to the pixel area, thus, if the pixel size is reducing from 50×50-μm to 25×25-μm, and everything else remained the same, the NEDT would increase by the factor of four. Improvements in the readout electronics are needed to compensate for this. For future arrays, the $f/1$ NEDT performance of 25-μm pitch microbolometer FPAs is projected to be below 20 mK (see Fig. 77) [338–340]. The development of highly sensitive 25-μm microbolometer pixels, however, presents significant challenges in both fabrication process improvements and in pixel design. Microbolometr pixels fabricated with conventional single-level micromachining processes suffer severe performance degradation as the unit cell is reduced below 40 μm. This problem can be mitigated to some degree if the microbolometer process capability (design rules) is improved dramatically. Table 16 summarises the design and performance parameters for Raytheon's VO_x microbolometers. Similar performance has been described by Altman and colleagues at BAE Systems (Lockheed Martin) [341,342]; they reported a 640×480 FPA with $28 \times 28\ \mu m^2$ pixels with NETD ($f/1$ optics) of below 55 mK.

At present, several research programmes are focused towards enhancement of performance level in excess of $10^9\ cmHz^{1/2}W^{-1}$. It is anticipated that new materials will form the basis of the next generation of semiconductor film bolometers.

The most promising material appears to be amorphous silicon (a-Si). Temperature coefficient of resistance (TCR) values for a-Si range from $-0.025°C^{-1}$ for doped, low resistivity films at room temperature to $-0.08°C^{-1}$ for high resistivity materials [29]. So, although high TCR values are attainable, they are accompanied by high level of $1/f$ noise [343]. Properties of the films depend upon the method of preparation and the type of dopant. Amorphous hydrogenated silicon (a-Si:H) has a metastable state caused by defects arising from prolonged illumination (Staebler and Wronski effect). This is an undesirable feature that requires a specific annealing cycle during

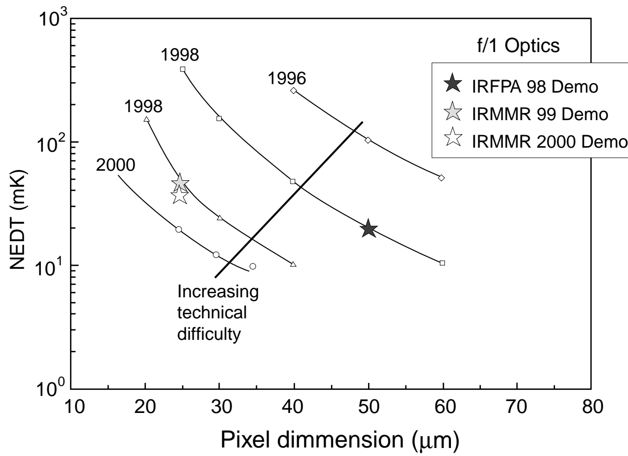

Fig. 77. VO_x FPA development (after Ref. [339]).

Table 16
Performance characteristics of Raytheon's VO_x microbolometers (after Refs. [338,340])

Performance parameter	Capability (*f*/1 and 300 K scene)		
Array configuration	320 × 240	320 × 240	640 × 480
Pixel size (μm^2)	50 × 50	25 × 25	25 × 25
Spectral response (μm)	8–14	8–14	8–14
Signal responsivity (V/W)	$>2.5\times10^7$ V/W or 50 mK/K_{scene}	$>2.5\times10^7$ V/W or 20 mK/K_{scene}	$>2.5\times10^7$ V/W or 25 mK/K_{scene}
NEDT @ $f/1$ (mK)	<20	<50	
Offset nonuniformity (mV)	<150 p–p	<150 p–p	<150 p–p
Output noise (mV)	1.0 rms	1.0 rms	0.6 rms
Intrascene dynamic range @ $f/1$ (K)	>40	>100	>100
Pixel operability (%)	>98	>98	>98
Power dissipation (mW)	200	150	390
Nominal operating temperature (°C)	25	25	25

preparation (methodology for reliability enhancement is described in Ref. [344]). If not removed, it adversely affects long-term reliability. Nevertheless, progress in the development of a-Si:H uncooled FPAs has been reported. 320 × 240 arrays with 45-μm pitch have been developed with an average NETD of 70 mK (for $f/1$ aperture and 50 Hz imagery frequency) [344]. Using an improved technological stack, fully compatible with industrial process, good quality 320 × 240 FPA with 35-μm pitch and $f/1$ optics has been presented with NEDT close to 35 mK [345]. Because the typical resisitivity of amorphous silicon films is several orders of magnitude higher than that of VO_x, a-Si finds application in uncooled arrays in which bias is continuous rather than pulsed without excessive Joulean heating of the FPA [29].

Very encouraging results have also been obtained using semiconducting $YBa_2Cu_3O_{6+x}$ ($0.5 \leqslant x \leqslant 1$) thin films on silicon [346–352]. The room temperature resistivity of this material has a high and relatively constant TCR $\geqslant 3\%$/K. Amorphous YBaCuO thin films deposited on silicon wafers with a MgO buffer layer have exhibited TCRs as high as 4%/K. The responsivity of 3.8×10^5 V/W and detectivity of 1.6×10^9 cmHz$^{1/2}$W^{-1} are possible if these thin films are integrated into typical air-gap microbolometer structures [347,348]. To ensure compatibility and potential integration with CMOS-based processing circuitry, silicon micromachining and ambient temperature processing were employed [349].

Recently, Wada et al. [352] have developed 320×240 YBaCuO microbolometer FPA with a pixel pitch of 40 μm, NEDT of 0.08 K with a prototype camera and $f/1.0$ optics. To decrease to resistance of bolometers (which is 10 Ωcm—two orders of magnitude higher than that of a conventional VO_x bolometer films) the RF magnetron sputtered films were deposited on silicon with previously prepared SiO_2 isolation layer and platinum comb-shaped electrodes.

9.2. Pyroelectric detectors

Whenever a pyroelectric crystal undergoes a change of temperature, surface charge is produced in a particular direction as a result of the change in its spontaneous polarization with temperature. This effect has been known as a physically observable phenomenon for many centuries, being described by Theophrastus in 315 BC [353].

A typical circuit for implementation of a pyroelectric detector is shown in Fig. 78. It can be shown that the responsivity of a pyroelectric detector is given by [25]

$$R = \frac{\varepsilon}{C_{th}} \frac{pA}{C_d + C_L} \frac{\omega\tau_e}{(1+\omega^2\tau_e^2)^{1/2}} \frac{\tau_{th}}{(1+\omega^2\tau_{th}^2)^{1/2}}, \tag{46}$$

where ε is the emissivity of detector, p is the pyroelectric coefficient of the detector material, C_d is the capacitance of the detector, R_d is the detector resistance, C_L is the load resistor capacitance, R_L is the load resistance, C_{th} is the thermal capacitance, τ_{th} is the thermal time constant, τ_e= RC is the electrical time constant. It should be noted that $C = C_d + C_L$ and $R = R_d R_L/(R_d + R_L)$.

The choice of pyroelectric materials is not an obvious one as it will depend on many factors including the size of the detector required, the operating temperature and the frequency of operation. It is possible to formulate a number of figures-of-merit, which describe the contribution of the physical properties of a material to the performance of a device. For example, the current responsivity [which can be obtained from Eq. (36) assuming $C_d \ll C_L$] is proportional to [354–356]

$$F_i = \frac{p}{c_{th}}, \tag{47}$$

where c_{th} is the volume specific heat.

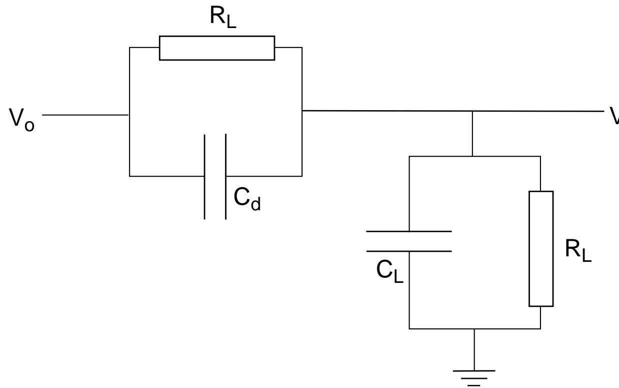

Fig. 78. Equivalent electrical circuit for a pyroelectric detector. C_d—capacitance of the detector, R_d—detector resistance, C_L—load resistor capacitance, R_L—load resistance, and V_o—applied constant bias voltage.

The voltage responsivity [which can be obtained from Eq. (46) assuming $C_d \gg C_L$] is proportional to [354–356]

$$F_v = \frac{p}{\varepsilon_o \varepsilon_r c_{th}}, \tag{48}$$

where ε_r is the relative permittivity of the pyroelectric material.

The conventional sensitivity figure of merit, detectivity D^*, is of little practical use because of frequency dependencies and filter factors. However, its analytical expression is useful for examining the relative importance of various parameters. In the case of a detector dominated by the AC Johnson noise, the detectivity is proportional to [354–356]

$$F_d = \frac{p}{c_{th}(\varepsilon_o \varepsilon_r \, tan \, \delta)^{1/2}}, \tag{49}$$

where $\tan \delta$ is the loss tangent of the detector material. F_d also forms the figure of merit for pyroelectric detectors.

More useful figure of merit, which includes the effect of input capacitance of the circuit with which the detector is used, is

$$F = \frac{1}{C_d + C_L} \frac{p}{c_{th}}. \tag{50}$$

This equation reduces to F_i or F_v when C_L is comparatively small or large, respectively.

A responsivity figure of merit is valuable in selecting material with responsivity sufficiently high that preamplifier noise is small compared to temperature fluctuation noise. A Johnson noise sensitivity figure of merit is valuable in selecting a material whose Johnson noise is small compared with the temperature fluctuation noise. Thus, both figures of merit must be large to ensure temperature fluctuation noise-limited performance.

An ideal material should have large pyroelectric coefficient, low dielectric constant, low dielectric loss and low volume specific heat. The possibility of satisfying these requirements in a single material is not promising. While it is generally true that a large pyroelectric coefficient and a small dielectric constant are desirable, it is also true that these two parameters are not independently adjustable. Thus, we find that materials having a high pyroelectric coefficient also have a high dielectric constant, and materials having a low dielectric constant also have a low pyroelectric coefficient. This means that different detector-preamplifier sizes and configurations will be optimized with different materials [354]. Thus, Eq. (50) is a better responsivity figure of merit, assuming one knows the pixel geometry and the circuit with which the detector material will be used. Table 17 shows the parameter values and traditional figures of merit for typical materials. The traditional figures of merit indicate, for example, that TGS (triglycine sulfate) and $LiTaO_3$ (lithium tantalate) should be much better than BST (barium strontium titanate) and PST (lead scandium tantalate); however, sensor system results indicate the contrary.

The imaging systems based on pyroelectric arrays, usually need to be operated with optical modulators, which chop or defocus the incoming radiation. This may be an important limitation for many applications in which chopperless operation is highly desirable (e.g., guided munitions).

Most of the pyroelectric materials considered for thermal detector arrays are the lead-based ‘‘perovskite’’ oxides such as lead titanate [$PbTiO_3$ –PT]. These materials have structural similarities with the mineral perovskite ($CaTiO_3$). The basic formula is ABO_3; where A is lead, O is oxygen and B may be one, or a mixture, of cations e.g., lead zirconate titanate [$Pb(ZrTi)O_3$—PZT], barium strontium titanate [$BaSrTiO_3$—BST], lead scandium tantalate [$Pb(Sc_{0.5}Ta_{0.5})O_3$—PST] and lead magnesium niobate [$Pb(Mg_{1/3}Nb_{2/3})O_3$—PMN]. Often dopants are added to these basic formulations to enhance or tune the material properties. Above Curie temperature, T_C, these materials form a symmetric non-polar, cubic structure. On cooling they undergo a structural phase transition to form a polar, ferroelectric phase.

The above materials can be further sub-divided into two groups. The ‘‘conventional’’ pyroelectric materials, such as PT and PZT, operate at room temperature well below their Curie temperature without the need for an applied field. Requirements for detector temperature stabilization is minimal or can be eliminated

Table 17
Typical properties of ferroelectric materials (after Ref. [25])

Material	p (nC/cm^{2}K)	ε	tan δ	c_{th} (J/cm^3 K)	F_v (m^2/C)	F_d (Pa$^{-1/2}$)	NEDT[a] (K)
TGS	35	30	0.01	2.30	0.573	9.34×10^{-5}	0.123
$LiTaO_3$	20	60	0.003	3.30	0.114	4.80×10^{-5}	0.258
BST [$Ba_{0.67}Sr_{0.33}TiO_3$]	350	5000	0.01	2.55	0.031	6.52×10^{-5}	0.066
PST [$Pb(Sc_xTa_{1-x})_2O_6$]	500	8000	0.01	2.70	0.026	6.96×10^{-5}	0.061

[a] Calculated using typical device and system parameters with $f/1$ optics and 50-μm square pixels.

since there is little variation in detector performance over quite a large temperature range.

It is, however, possible to operate ferroelectrics at or above T_C, with an applied bias field, in the mode of a "dielectric bolometer". This second group of materials (including BST, PST and PMN) has T_C slightly below the detector operating temperature, resulting in minimal pyroelectricity. In this case a constant dc field is applied during operation to induce a polarisation and hence regain pyroelectric properties.

Barium strontium titanate (BST) ceramic is a relatively well behaved material with a very high permittivity. Texas Instruments (Raython) has improved the performance of pyroelectric FPAs using a bias voltage applied to maintain and optimise the pyroelectric effect near the phase transition [357]. Fig. 79 shows details of the completed pyroelectric detector device structure. The 320×240 hybrid arrays with pixels 48.5-μm are characterized by NEDT as low as 40 mK (array average) and the production average is between 70 and 80 mK. A demonstrated sustained production rate in excess of 500 units per month is a small fraction of factory capacity.

For the United Kingdom array programme lead scandium tantalate (PST) material has been chosen [359].

Hybrid pyroelectric/ferroelectric bolometer detector was the first to enter production, and is the most widely used type of thermal detector (in the U.S., the Cadillac Division of General Motors has pioneered this application, selling thermal imagers to the customer for just under $2000) [29]. Although many applications for this hybrid array technology have been identified, and imagers employing these arrays are in mass production, no hybrid technology advances are foreseen. The reason is that the thermal conductance of the bump bonds is so high that the array NETD ($f/1$ optics) is limited to about 50 mK. The best NEDT achieved with a hybrid array is about 38 mK, which is consistent with thermal conductance of

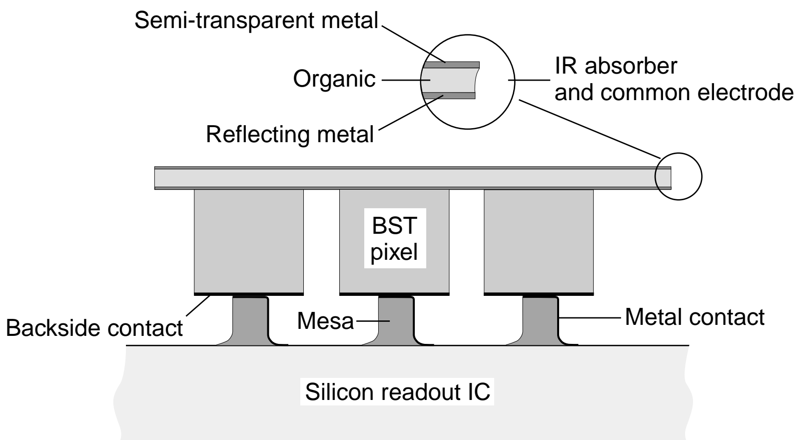

Fig. 79. BST dielectric bolometer pixel (after Ref. [358]).

approximately 4 μW/K. Pyroelectric array technology therefore is moving toward monolithic silicon microstructure technology. The monolithic process should have fewer steps and shorter cycle time. Most ferroelectrics tend to lose their interesting properties as the thickness is reduced. However, some ferroelectric materials seem to maintain their properties better than others. This seems particularly true for PT and related materials, whereas BST, the material does not hold its properties well in thin-film form.

Thin-film ferroelectric (TFFE) detectors have the performance potential of microbolometers with minimum NEDT of about 1 mK [360]. Fig. 80 shows NEDT calculated as a function of pixel pitch assuming a constant 30 Hz signal and a thermal time constant of about 15 ms. Reducing the pixel pitch from 50 to 25 μm requires a concomitant increase in thermal isolation by about a factor of four. This seriously impacts the possibility of high performance arrays with small pixels.

TFFE device approach appears remarkably similar to the VO_x microbolometer structure developed by Honeywell. However, there are several key features that distinguish it from that technology [359–361]. Since, the device is a capacitor rather than a resistor as in a bolometer, the electrodes are located above and below the face of the pixel; are transparent and do not obscure the active optical area. Usually, the electrical resistance of the leads can be quite large without degrading signal to noise ratio, since the detector capacitance is approximately 3 pF. This enables the use of thin, poorly conducting electrode materials to minimize thermal conductance. A key feature of the design is that the ferroelectric film is self-supporting; there is no underlying membrane necessary to provide mechanical support. In such a way, with the use of transparent oxide electrodes, the ferroelectric material can dominate thermal conductance.

It is well known, that absorption of IR radiation is accomplished by means of a resonant optical cavity. In monolithic bridge structure, the cavity is located within

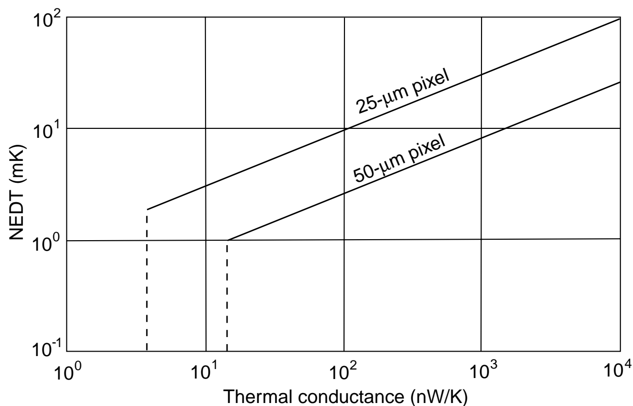

Fig. 80. The relationship between thermal isolation and performance of uncooled IR detectors in the thermal fluctuation noise limit (after Ref. [360]).

the ferroelectric itself or in the space between ferroelectric and the ROIC. This can be realized in two ways [360]:

- the bottom electrode must be highly reflective, the top electrode must be semi-transparent, and the ferrolectric must be approximately 1 μm thick for optimal tuning of the cavity for 10–12 μm radiation,
- both electrodes must be semi-transparent, a reflective mirror must be present on the ROIC under each pixel, and the pixel must be located approximately 2 μm above the ROIC.

A key factor to performance of the ceramic thin films is the high temperature processing required achieving the correct ferroelectric crystal phase. The TFFE's of interest are refractory, and require annealing at elevated temperatures to crystallize and develop good pyroelectric properties. Thermal treatments at temperatures that exceed about 450°C may lead to adverse interaction between the silicon and aluminium interconnects. Various techniques for the deposition of thin ferroelectric films have been investigated including spin-on metal-organic decomposition, radio frequency magnetron sputtering, dual ion beam sputtering, sol–gel processing, and laser ablation. Also a number of surface rapid thermal annealing techniques have been investigated to obtain optimum material response whilst leaving the underlying silicon substrate undamaged [361].

Monolithic arrays produced to date have demonstrated poor sensitivity. Raytheon's group has demonstrated 320 × 240 array with NEDT of about 400 mK with operability in excess of 95%.

Research group from DERA (UK) has developed "integrated" and "composite" detector technology [359,361]. In the first technology, the detector material was deposited as a thin film onto free standing micro-bridge structure defined on the surface of the silicon ROIC. The "composite" technology combines elements of hybrid and integrated technologies (see Fig. 81). Microbridge pixels are fabricated in a similar fashion to the integrated technology and next are formed onto a high density interconnect silicon wafer. The interconnect wafer uses materials that can withstand the intermediate high temperature processing stage during fabrication of thin ferroelectric films and contains a narrow conducting channel via for every pixel, permitting electrical connection to the underside. Finally, the detector wafer is solder bump bonded to the ROIC as per the established hybrid array process. It is predicted that using PST films an NEDT of 20-mK (50 Hz image rate and $f/1$ optics) is possible to achieve.

9.3. Thermoelectric arrays

Thermopile detectors [362], while only limited use for imaging applications, have a combination of characteristics that make them well suited for some low-power applications. They are highly linear, require no optical chopper, and have D^* values comparable to resistive bolometers and pyroelectric detectors. They operate over a broad temperature range with little or no temperature stabilization. They have no electrical bias, leading to negligible $1/f$ noise and no voltage pedestal in their output

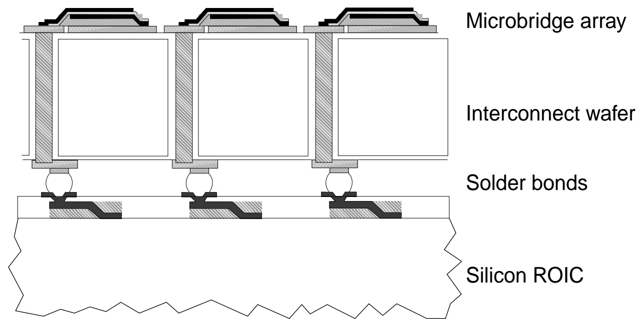

Fig. 81. Schematic cross-section of the "composite" detector array design (after Ref. [361]).

signal. However, much less effort has been made in their development. The reason is that their responsivity and noise are orders of magnitude less and thus their applications in thermal imaging systems require very low-noise electronics to realize their potential performance. Thermoelectric detectors found almost no use as matrix arrays in TV frame rate imagers. Instead, they are employed as linear arrays that are mechanically scanned to form an image of stationary or nearly stationary objects. The wide operating-temperature range, lack of temperature stabilization, and radiometric accuracy make thermopiles well situated for same space-based scientific imaging applications.

Two-dimensional thermopile arrays have been reported only by two groups [363,364]. In both cases, a desire for low cost and manufacturability led to the use of polysilicon thermoelectric material, which have relatively low thermoelectric figures of merit. Fote and co-workers [365,366] have improved the performance of thermopile linear arrays by combining Bi-Te and Bi-Sb-Te thermoelectric materials. Compared with most other thermoelelectic arrays, their D^* values are highest, what is shown in Fig. 82. This technology has been developed to improve the performance of 2-D arrays using a three-level structure with two sacrificial layers. In such a way, it is possible to improve fill factor and incorporate a large number of thermocouple per pixel. Fig. 83 shows the thermopile detector structure. The structure allows almost 100% fill factor and model suggests that optimised detectors will have D^* values over $10^9\,\mathrm{cmHz}^{1/2}/\mathrm{W}$. Further efforts are continued to fabricate high performance 128×128 FPAs [367].

9.4. Novel sensors

Recent advances in micro-mechanical systems (MEMS) have lead to the development of uncooled IR detectors operating as micromechanical thermal detectors as well as micromechanical photon detectors.

A new type of thermal detector was developed with a reported detectivity of $10^8\,\mathrm{cmHz}^{1/2}/\mathrm{W}$ [368,369]. Using a micro-optomechanical receiver, Norton et al. [370] have demonstrated uncooled IR detector having an optical readout. In this case one

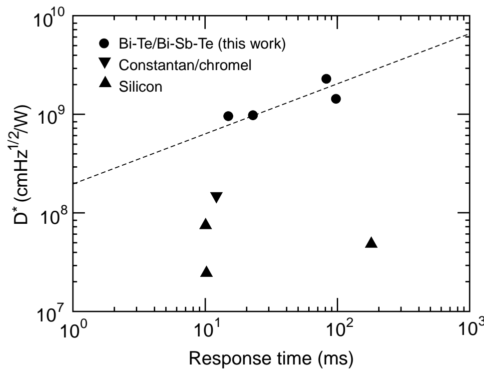

Fig. 82. Representative data from literature showing reported D^* values as a function of response time for thin film thermopile linear arrays. The dashed line represents the Fote and Jones results. Its slope indicates D^* proportional to the square root of response time, which is typical for thermopiles or bolometers with different geometries and the same material system (after Ref. [366]).

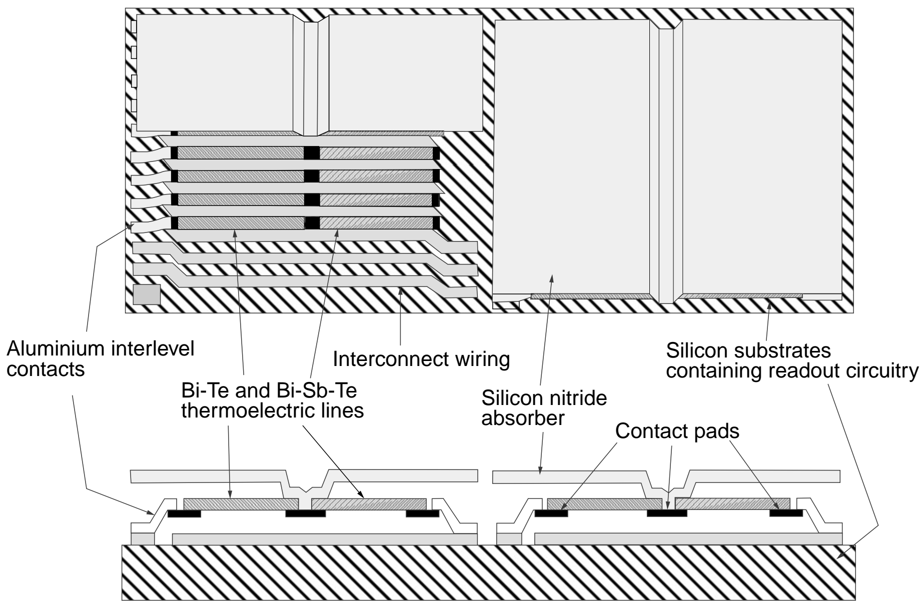

Fig. 83. Schematic diagram of thermopile detector structure. The top diagram shows two pixels viewed from the top, with part of the left pixel cut away to show the underlying structure. The lower diagram shows a cross-section side view of two pixels (after Ref. [367]).

side of the bimaterial cantilever is an optical reflector. Visible light reflecting off the bent cantilever is detected with a CCD camera to provide the sensor output. The system sensitivity about 1–2 K has been received.

To improve detector performance a novel micromechanical IR sensor has been developed using commercially available microcantilevers [371–374]. This new type of semiconductor micromechanical detector operates as a photon detector. Recently, Datskos [374] has discussed both thermal and photonic microstructures.

When a silicon microcantilever is exposed to photons, the excess charge carriers generated induce an electronic stress which causes the silicon microcantilever to deflect (see Fig. 84). The surface stresses S_1 and S_2 are balanced at equilibrium, generating the radial force F_r along the medial plane of the microcantilevers. These stresses become unequal upon exposure to photons, producing the bending force, F_z, that displaces the tip of the microcantilever. If these microcantilevers are coated with a material exhibiting dissimilar thermal expansion properties than silicon, the bimaterial effect causes the silicon microcantilever to bend even more in response to electronic stress. The extent of bending is proportional to the radiation intensity. The devices are typically 50–200 μm long, 10–30 μm wide and 0.4 to 4 μm thick, and can detect temperature difference as small as 10^{-6} K [371].

There are three methods for detecting the degree of bending: piezoelectric resistance, a laser and position-sensitive photodetector, and capacitance. The capacitance measurement detects changes in capacitance between the cantilever and the substrate. It occupies the middle ground in the trade-off between sensitivity and simplicity, and it would be useful in measuring cantilever arrays. It is expected that 2-D cantilever arrays could become very attractive for a number of applications due to their inherent simplicity, high sensitivity, and rapid response to radiation.

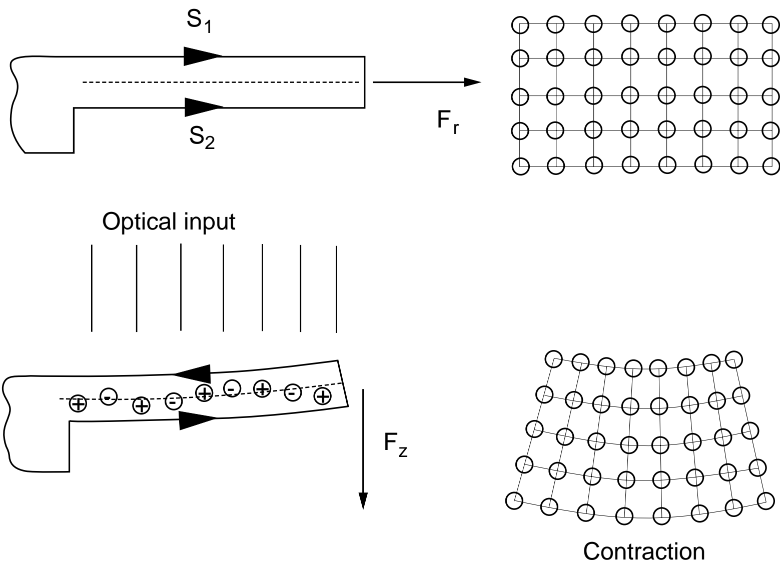

Fig. 84. Schematic diagram showing the bending process of a silicon microcantilever exposed to radiation. Surface stresses S_1 and S_2 are balanced at equilibrium. Also depicted is the accompanied contraction of the silicon lattice following the generation of electron-hole pairs (after Ref. [372]).

9.5. Status and trends of uncooled arrays

The information gathered here follows Kruse [29]. Table 18 illustrates the status and trends of uncooled arrays for military and commercial applications. As it was previously mentioned, under development are microbolometer arrays containing 640×480 pixels. The pixel size is being reduced to $25 \times 25\,\mu m$ (in order to reduce the optics cost); $35 \times 35\,\mu m$ is an intermediate objective. The NEDT goal is 10 mK for high performance applications, instead low cost performance applications (e.g., security sensors) use 160×120 pixels, $50 \times 50\,\mu m$, and NEDT of 100 mK.

The commercial systems (microbolometer imagers and radiometers and ferroelectric imagers) derive from military systems that are too costly for widespread use. Imaging radiometers employ linear thermoelelctric arrays operating in the snapshot mode; they are less costly than the TV-rate imaging radiometers employing microbolometer arrays [375,376]. In the large volume production, the cost of commercial systems will inevitably decrease (see Table 18).

It seems likely that microbolometer FPAs will become dominant uncooled detector technology in the near future. It does not require a radiation chopper and it has very low thermal conductance what influence a high responsivity and a low NEDT. Moreover, changes in the shape of the lags of the monolithic construction allow trade-off between speed of response and NEDT. It is predicted that the performance of monolithic ferroelectric bolometers can be considerably improved unlike hybrid pyroelectric detectors where is little development effort under way. The hybrid pyroelelctric FPAs are not commercially available.

Table 18
Status and trends of commercial uncooled arrays (after Ref. [29])

Feature	Cost ($)
Status	
Commercial marketing of military thermal imagers	
Overspecified for commercial applications	
320×240 pixel, $50 \times 50\,\mu m$ bolometer arrays for thermal imagers	15 000–20 000
320×240 pixel, $50 \times 50\,\mu m$ bolometer arrays for imaging radiometers	20 000–50 000
120×1 pixel, $50 \times 50\,\mu m$ thermoelectric arrays for imaging radiometers	15 000
320×240 pixel, $50 \times 50\,\mu m$ hybrid ferroelectric bolometer array imagers for drivers' vision enhancement	2 000–4 000
Trends	
Developed of new, low-cost thermal imagers and imaging radiometers	
Designed for specific commercial applications and meeting commercial requirements	
160×120 pixel, $50 \times 50\,\mu m$ bolometer arrays for thermal imagers	$<3\,000$
160×120 pixel, $50 \times 50\,\mu m$ bolometer arrays for imaging radiometers	$<5\,000$
160×120 pixel, $50 \times 50\,\mu m$ bolometer arrays for driver's vision enhancement systems	$<2\,000$
160×120 pixel, $50 \times 50\,\mu m$ bolometer arrays for driver's vision enhancement systems in extremely large volumes	1 000

10. Conclusions

The intention of this paper has been to present state-of-the-art both photon and thermal detectors, with emphasis on the material properties, device structure, and their impact on FPA performance, especially in LWIR and VLWIR spectral regions.

At present, HgCdTe is widely used variable gap semiconductor and has a privilege position both in LWIR as well as VLWIR spectral ranges. Fig. 85 shows a plot of the thermal detectivity (300 K, 0° FOV) versus operating temperature for the most prominent detector technologies. The thermal detectivity is used here to compare the various technologies for equivalent NETD irrespective of wavelength. The thermal D^* figure of merit for photon detectors was obtained by equating the NETD of an ideal thermal detector for a given D^* to the NETD of an ideal photon detector with a given $D^*_{\lambda_p}$. The various regions show the appropriate applications including "low cost" uncooled thermal detectors, "high performance uncooled" for night vision enhancement and earth reconnaissance, "tactical" for most imaging uses, and "strategic" for various military-type instruments. Strategic sensors generally detect point targets, so the D^* must be as high as possible within the constraint that the cooler must not pose overriding size, weight, reliability and cost issue. High performance near infrared has similar performance requirements, but can only provide a minimum of cooling because cost and weight minimisation is critical. The extrinsic silicon detectors offer very high sensitivity but at the very low operating temperature which is prohibitive in the most applications. The cryogenically cooled

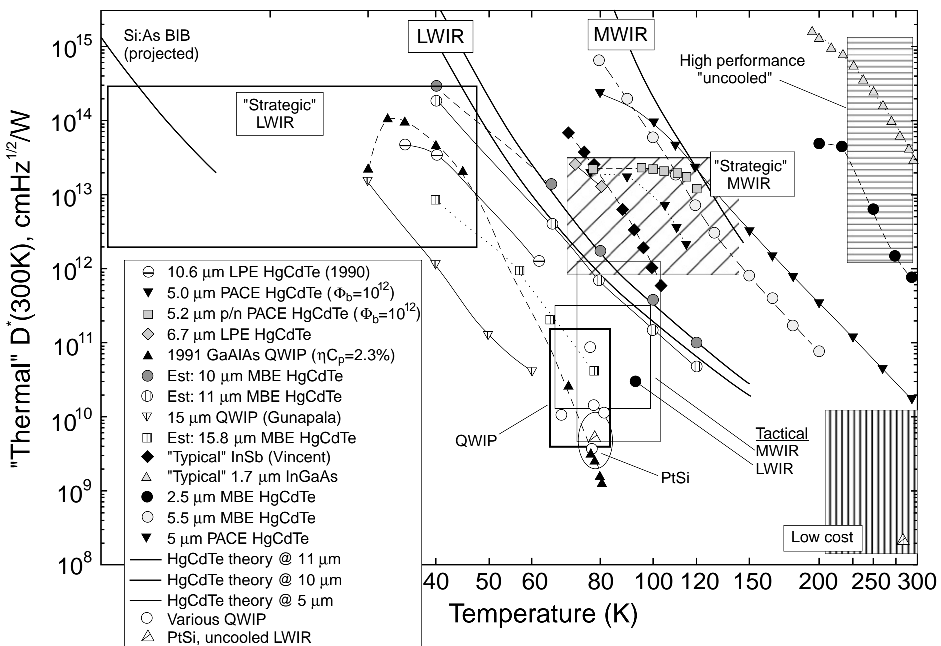

Fig. 85. Thermal D^* versus operating temperature for different FPA technologies (after Ref. [195]).

InSb and HgCdTe arrays have comparable array size and pixel yield at MWIR spectral band. However, wavelength tunability and high quantum efficiency have made HgCdTe the preferred material. Thus, the associated cooling and system power requirements can thus be optimally distributed. The monolithic PtSi Schottky barrier FPAs lead all other technologies with respect to array size (more than 10^6 pixels). It can insist, however, that the thermal mismatch barrier in hybrid FPAs has been overcome by developers fabricating InSb and HgCdTe arrays.

Detector maturity is a function of the accumulated experience and development effort, the complexity of the device required, and the inherent difficulty presented by the material technology. At present, HgCdTe photodiodes and BIB extrinsic silicon detectors are not fully mature. PtSi technology is mature and has received a plateau. Other two detector technologies such as InSb and silicon bolometers are still evolving significantly as applications for larger array configurations and smaller pixel sizes continue to push the technology.

The recent successes of competing to HgCdTe cryogenically cooled detectors are due to technological, not fundamental issues. The steady progress in epitaxial technology would make HgCdTe devices much more affordable in the near future. The much higher operation temperature of HgCdTe, compared to Schottky barrier devices and low-dimensional solid devices, may become a decisive argument in this case.

The fundamental performance limits of HgCdTe photodiodes have not been reached yet. Continued development of the in situ vapour phase epitaxy methods (MBE and MOCVD) will allow bandgap engineering heterojunction devices of increasing quality and complexity. Also continued development of epitaxial growth on alternative substrates such as silicon will reduce the cost of 2-D arrays. Development of dual-band array will continue and three-band detectors will soon be demonstrated. To provide high resolution spectroscopic imaging larger HgCdTe FPAs will be used in Fourier-transform interferometers. Photodiodes will replace photoresistors for detection out to 15 μm since they characterised by more linear response.

State of the art QWIP and HgCdTe FPAs provide similar performance figure of merit, since they are predominantly limited by the readout circuits. A low photoconductive gain actually causes a better NEDT of QWIP FPA than that of HgCdTe FPA with similar storage capacity. The performance is, however, achieved with very different integration times. The integration time of QWIP devices is 10–100 times longer than that of HgCdTe arrays, and is typically 5–20 ms. Powerful possibilities of QWIP technology are connected with large LWIR and VLWIR FPA applications and with multicolour detection. Three-band and four-band FPAs will be soon demonstrated in thr near future.

Thermal detector arrays will increase in size and improve in thermal sensitivity to a level satisfying high performance applications at ambient temperature. It is supposed that the silicon microbolometers arrays and the monolithic ferroelectric arrays will capture the low-cost markets. Current uncooled bolometer FPAs have achieved NEDT less than 10 mK (with 50-μm pixels and $f/1$ optics), what open the door to the use of less expensive slower optical systems.

It is supposed that sales of IR thermal imaging equipment to the automobile market will begin to rapidly change the relative ratio between military/government and commercial IR markets. Today, only about 10% of the market is commercial. After a decade the commercial market can grow to over 70% in volume and 40% in value, largely connected with volume production of uncooled imagers for automobile driving [44]. In large volume production for automobiles drivers the cost of uncooled imaging systems will decrease to below $1000. Of course, these systems will cover other segments of the transportation industry: trucks, trains, ships, barges, buses, and airplanes.

For some applications requiring uncooled detectors, the slow response speed is unacceptable. Recently, a number of concepts (e.g., non-equilibrium device [377], multi-junction HgCdTe photodiodes [378], optical immersion) and new materials (InAsSb, InAs/GaSb-based type II superlattices) [58] have been proposed to improve performance of photon detectors operating at near room temperature. The measurements show the possibility to achieve detectivity of $\approx 1 \times 10^9\,\mathrm{cmHz^{1/2}/W}$ at the 8–9-μm range and potentially, the devices can be assembled in large FPAs.

A new IR detector concept is micro electromechanical structures (MEMSs). This technology is a marriage of photolithography and mechanics. FPAs based on MEMS technology and a visible optical readout system may offer lower-cost LWIR imaging systems.

Finally, considerable development of signal processing function into FPAs can be anticipated.

References

[1] W. Herschel, Experiments on the refrangibility of the invisible rays of the Sun, Philosophical Transaction on Royal Society of London 90 (1800) 284.
[2] R.A. Smith, F.E. Jones, R.P. Chasmar, The Detection and Measurement of Infrared Radiation, Clarendon, Oxford, 1958.
[3] P.W. Kruse, L.D. McGlauchlin, R.B. McQuistan, Elements of Infrared Technology, Wiley, New York, 1962.
[4] E.S. Barr, Historical survey of the early development of the infrared spectral region, American Journal of Physics 28 (1960) 42–54.
[5] E.S. Barr, The infrared pioneers—II. Macedonio Melloni, Infrared Physics 2 (1962) 67–73.
[6] E.S. Barr, The Infrared Pioneers—III. Samuel Pierpont Langley, Infrared Physics 3 (1963) 195–206.
[7] T.W. Case, Notes on the change of resistance of certain substrates in light, Physics Reviews 9 (1917) 305–310.
[8] R.J. Cushman, Film-type infrared photoconductors, Proceedings of IRE 47 (1959) 1471–1475.
[9] P.R. Norton, Infrared detectors in the next millennium, Proceedings of SPIE 3698 (1999) 652–665.
[10] A. Rogalski, Infrared Detectors, Gordon and Breach Science Publishers, Amsterdam, 2000.
[11] W.S. Boyle, G.E. Smith, Charge-coupled semiconductor devices, Bell Syst. Tech. J. 49 (1970) 587–593.
[12] F. Shepherd, A. Yang, Silicon Schottky retinas for infrared imaging, IEDM Technology Digist (1973) 310–313.
[13] W.D. Lawson, S. Nielson, E.H. Putley, A.S. Young, Preparation and properties of HgTe and mixed crystals of HgTe-CdTe, Journal of Physics and Chemistry of Solids 9 (1959) 325–329.

[14] P.W. Kruse, M.D. Blue, J.H. Garfunkel, W.D. Saur, Long wavelength photoeffects in mercury selenide, mercury telluride and mercury telluride-cadmium telluride, Infrared Physics 2 (1962) 53–60.
[15] J. Melngailis, T.C. Harman, Single-crystal lead-tin chalcogenides, in: R.K. Willardson, A.C. Beer (Eds.), Semiconductors and Semimetals, Vol. 5, Academic Press, New York, 1970, pp. 111–174.
[16] T.C. Harman, J. Melngailis, Narrow gap semiconductors, in: R. Wolfe (Ed.), Applied Solid State Science, Vol. 4, Academic Press, New York, 1974, pp. 1–94.
[17] A. Rogalski, J. Piotrowski, Intrinsic infrared detectors, Progress in Quantum Electronics 12 (1988) 87–289.
[18] M.J.E. Golay, A pneumatic infrared detector, Review of Scientific Instruments 18 (1947) 357–362.
[19] E.M. Wormser, Properties of thermistor infrared detectors, Journal of Optics Society of America 43 (1953) 15–21.
[20] G.W. McDaniel, D.Z. Robinson, Thermal imaging by means of the evaporograph, Applied Optics 1 (1962) 311–324.
[21] C. Hilsum, W.R. Harding, The theory of thermal imaging, and its application to the absorption-edge image tube, Infrared Physics 1 (1961) 67–93.
[22] A.J. Goss, The pyroelectric vidicon—A review, Proceedings of SPIE 807 (1987) 25–32.
[23] R.A. Wood,N.A. Foss, Micromachined bolometer arrays achieve low-cost imaging, Laser Focus World, June, 1993, pp. 101–106.
[24] R.A. Wood, Monolithic silicon microbolometer arrays, in: P.W. Kruse, D.D. Skatrud (Eds.), Semiconductors and Semimetals, Vol. 47, Academic Press, San Diego, 1997, pp. 45–121.
[25] C.M. Hanson, Hybrid pyroelectric–ferroelectric bolometer arrays, in: P.W. Kruse, D.D. Skatrud (Eds.), Semiconductors and Semimetals, Vol. 47, Academic Press, San Diego, 1997, pp. 123–174.
[26] P.W. Kruse, Uncooled IR focal plane arrays, Opto-Electronics Review 7 (1999) 253–258.
[27] R.A. Wood, Uncooled microbolometer infrared sensor arrays, in: P. Capper, C.T. Elliott (Eds.), Infrared Detectors and Emitters: Materials and Devices, Kluwer Academic Publishers, Boston, 2000, pp. 149–174.
[28] R.W. Whatmore, R. Watton, Pyroelectric materials and devices, in: P. Capper, C.T. Elliott (Eds.), Infrared Detectors and Emitters: Materials and Devices, Kluwer Academic Publishers, Boston, 2000, pp. 99–147.
[29] P.W. Kruse, Uncooled Thermal Imaging. Arrays, Systems, and Applications, SPIE Press, Bellingham, 2001.
[30] A. Rose, Concepts in Photoconductivity and Allied Problems, Interscience, New York, 1963.
[31] J. Piotrowski, W. Gawron, Ultimate performance of infrared photodetectors and figure of merit of detector material, Infrared Physics Technology 38 (1997) 63–68.
[32] B.F. Levine, Quantum-well infrared photodetectors, Journal of Applied Physics 74 (1993) R1–R81.
[33] J. Piotrowski, A. Rogalski, New generation of infrared photodetectors, Sensors and Actuators A 67 (1998) 146–152.
[34] R.G. Humpreys, Radiative lifetime in semiconductors for infrared detection, Infrared Physics 26 (1986) 337–342.
[35] P.W. Kruse, L.D. McGlauchlin, R.B. McQuistan, Elements of Infrared Technology, Wiley, New York, 1962.
[36] P.W. Kruse, The photon detection process, in: R.J. Keyes (Ed.), Optical and Infrared Detectors, Springer-Verlag, Berlin, 1977, pp. 5–69.
[37] A. Rogalski, Comparison of the performance of quantum well and conventional bulk infrared photodetectors, Infrared Physics Technology 38 (1997) 295–310.
[38] A. Smith, F.E. Jones, R.P. Chasmar, The Detection and Measurement of Infrared Radiation, Clarendon, Oxford, 1968.
[39] R. Ciupa, A. Rogalski, Performance limitations of photon and thermal infrared detectors, Opto-Electronics Review 5 (1997) 257–266.
[40] D.A. Scribner, M.R. Kruer, J.M. Killiany, Infrared focal plane array technology, Proceedings of IEEE 79 (1991) 66–85.

[41] L.J. Kozlowski, J.M. Arias, G.M. Williams, K. Vural, D.E. Cooper, S.A. Cabelli, C. Bruce, Recent advances in staring hybrid focal plane arrays: comparison of HgCdTe, InGaAs, and GaAs/AlGaAs detector technologies, Proceedings of SPIE 2274 (1994) 93–116.
[42] I.M. Baker, R.A. Ballinga, Photovoltaic CdHgTe-silicon hybrid focal planes, Proceedings of SPIE 510 (1984) 121–129.
[43] N. Yutani, H. Yagi, M. Kimata, J. Nakanishi, S. Nagayoshi,N. Tsubouchi, 1040×1040 element PtSi Schottky-barrier IR image sensor, IEDM Technical Digest (1991) 175–178.
[44] P.R. Norton, Status of infrared detectors, Proceedings of SPIE 3379 (1998) 102–114.
[45] K. Vural, L.J. Kozlowski, D.E. Cooper, C.A. Chen, G. Bostrup, C. Cabelli, J.M. Arias, J. Bajaj, K.W. Hodapp, D.N.B. Hall, W.E. Kleinhans, G.G. Price, J.A. Pinter, 2048×2048 HgCdTe focal plane arrays for astronomy applications, Proceedings of SPIE 3698 (1999) 24–35.
[46] L.J. Kozlowski, J. Montroy, K. Vural, W.E. Kleinhans, Ultra-low noise infrared focal plane array status, Proceedings of SPIE 3436 (1998) 162–171.
[47] L.J. Kozlowski, K. Vural, J. Luo, A. Tomasini, T. Liu, W.E. Kleinhans, Low-noise infrared and visible focal plane arrays, Opto-Electronics Review 7 (1999) 259–269.
[48] E.R. Fossum, Active pixel sensors: are CCD'S dinosaurs?, Proceedings of SPIE 1900 (1993) 2–14.
[49] E.R. Fossum, B. Pain, Infrared readout electronics for space science sensors: state of the art and future directions, Proceedings of SPIE 2020 (1993) 262–285.
[50] M.J. Hewitt, J.L. Vampola, S.H. Black, C.J. Nielsen, Infrared readout electronics: a historical perspective, Proceedings of SPIE 2226 (1994) 108–119.
[51] L.J. Kozlowski, S.A. Cabelli, D.E. Cooper, K. Vural, Low background infrared hybrid focal plane array characterization, Proceedings of SPIE 1946 (1993) 199–213.
[52] J.L. Vampola, Readout electronics for infrared sensors, in: J.S. Accetta, D.L. Shumaker (Eds.), The Infrared and Electro-Optical Systems Handbook, Vol. 3, Infrared Information Analysis Center, Ann Arbor, and SPIE Optical Engineering Press, Bellingham, 1993, pp. 285–342.
[53] L.J. Kozlowski, W.F. Kosonocky, Infrared detector arrays, in: M. Bass, E.W. Van Stryland, D.R. Williams, W.L. Wolfe (Eds.), Handbook of Optics, McGraw-Hill Inc., New York, 1995 (Chapter 23).
[54] M. Kimata, N. Tubouchi, Charge transfer devices, in: A. Rogalski (Ed.), Infrared Photon Detectors, SPIE Optical Engineering Press, Bellingham, 1995, pp. 99–144.
[55] J. Bajaj, State-of-the-art HgCdTe materials and devices for infrared imaging, in: V. Kumar, S.K. Agarwal (Eds.), Physics of Semiconductor Devices, Narosa Publishing House, New Delhi, 1998, pp. 1297–1309.
[56] M.A. Kinch, Fundamental physics of infrared detector materials, Journal of Electronic Materials 29 (2000) 809–817.
[57] T. Ashley, C.T. Elliott, Non-equilibrium devices for infrared detection, Electronic Letters 21 (1985) 451–452.
[58] M. Razeghi, Current status and future trends of infrared detectors, Opto-Electronics Review 6 (1998) 155–194.
[59] F. Fuchs, L. Bürkle, R. Hamid, N. Herres, W. Pletschen, R.E. Sah, R. Kiefer, J. Schmitz, Optoelectronic properties of photodiodes for mid- and far-infrared based on the InAs/GaSb/AlSb materials family, Proceedings of SPIE 4288 (2001) 171–182.
[60] J. Piotrowski,A. Rogalski, Comment on Temperature limits on infrared detectivities of InAs/ $In_xGa_{1-x}Sb$ superlattices and bulk $Hg_xCd_{1-x}Te$, [Journal of Applied Physics 74 (1993) 4774]. Journal of Applied Physics 80 (1996) 2542–2544.
[61] M.B. Reine, Photovoltaic detectors in HgCdTe, in: P. Capper, C.T. Elliott (Eds.), Infrared Detectors and Emitters, : Materials and Devices, Chapman & Hall, London, 2000.
[62] M. Rodot, C. Verie, Y. Marfaing, J. Besson, H. Lebloch, Semiconductor lasers and fast detectors in the infrared (3 to 15 microns), IEEE J. Quant. Electr. 2 (1966) 586–593.
[63] I. Melngailis, W.E. Keicher, C. Freed, S. Marcus, B.E. Edwards, A. Sanchez, T. Yee, D.L. Spears, Laser radar component technology, Proceedings of IEEE 84 (1996) 227–267.
[64] G.D. Cohen-Solal, A.G. Lussereau, U.S. Patent 3 (1976) 988.
[65] Infra-red Detectors—Product Profile, GEC-Marconi Infra-Red Limited, 1997.

[66] A. Turner, T. Teherani, J. Ehmke, C. Pettitt, P. Conlon, J. Beck, K. McCormack, L. Colombo, T. Lahutsky, T. Murphy, B. Williams, Producibility of VIP^{TM} scanning focal plane arrays, Proceedings of SPIE 2228 (1994) 237–248.

[67] L.O. Bubulac, W.E. Tennant, Role of Hg in junction formation in ion-implanted HgCdTe, Applied Physics Letters 51 (1987) 355–357.

[68] G. Destefanis, J.P. Chamonal, Large improvement in HgCdTe photovoltaic detector performances at LETI, Journal of Electronic Materials 22 (1993) 1027–1032.

[69] A. Rogalski, R. Ciupa, Theoretical modeling of long wavelength n^+-on-p HgCdTe photodiodes, Journal of Applied Physics 80 (1996) 2483–2489.

[70] T. Ashley, T.C. Elliott, A.M. White, Non-equilibrium devices for infrared detection, Proceedings of SPIE 572 (1985) 123–132.

[71] T. Elliott, New infrared and other applications of narrow gap semiconductors, Proceedings of SPIE 3436 (1998) 763–775.

[72] S.P. Tobin, M.H. Weiler, M.A. Hutchins, T. Parodos, P.W. Norton, Advances in composition control for 16 μm LPE p-on-n HgCdTe heterojunction photodiodes for remote sensing applications at 60 K, Journal of Electronic Materials 28 (1999) 596–602.

[73] J.M. Arias, J.G. Pasko, M. Zandian, L.J. Kozlowski, R.E. DeWames, Molecular beam epitaxy HgCdTe infrared photovoltaic detectors, Optical Engineering 33 (1994) 1422–1428.

[74] W.E. Tennant, C.A. Cockrum, J.B. Gilpin, M.A. Kinch, M.B. Reine, R.P. Ruth, Key issues in HgCdTe-based focal plane arrays: a industry perspective, Journal of Vaccum Science and Technology B10 (1992) 1359–1369.

[75] T. Tung, L.V. DeArmond, R.F. Herald, P.E. Herning, M.H. Kalisher, D.A. Olson, R.F. Risser, A.P. Stevens, S.J. Tighe, State of the art of Hg-melt LPE HgCdTe at Santa Barbara Research Center, Proceedings of SPIE 1735 (1992) 109–134.

[76] T.J. de Lyon, R.D. Rajavel, J.E. Jensen, O.K. Wu, S.M. Johnson, C.A. Cockrum, G.M. Venzor, Heteroepitaxy of HgCdTe(1 1 2) infrared detector structures on Si(1 1 2) substrates by molecular-beam epitaxy, Journal of Electronic Materials 25 (1996) 1341–1346.

[77] P.S. Wijewarnasuriya, M. Zandian, D.D. Edwall, M.V. McLevige, C.A. Chen, J.G. Pasko, H. Hildebrandt, A.C. Chen, J.M. Arias, A.I. D'Souza, S. Rujirawat, S. Sivananthan, MBE p-on-n $Hg_{1-x}Cd_xTe$ heterostructure detectors on silicon substrates, Journal of Electronic Materials 27 (1998) 546–549.

[78] A. Rogalski, Heterostructure infrared photovoltaic detectors, Infared Phys. Technol. 41 (2000) 213–238.

[79] J. Piotrowski, W. Galus, M. Grudzień, Near room-temperature IR photodetectors, Infrared Physics 31 (1991) 1–48.

[80] S.M. Johnson, T.J. deLyon, C.A. Cockrum, W.J. Hamilton, T. Tung, F.I. Gesswein, B.A. Baumgratz, L.M. Ruzicka, O.K. Wu, J.A. Torh, Direct growth of CdZnTe/Si substrates for large-area HgCdTe infrared focal plane arrays, Journal of Electronic Materials 24 (1995) 467–473.

[81] K. Vural, Mercury cadmium telluride short- and medium-wavelength infrared staring focal plane arrays, Optical Engineering 26 (1987) 201–208.

[82] L.J. Kozlowski, R.B. Bailey, S.A. Cabelli, D.E. Cooper, I.S. Gergis, A.C. Chen, W.V. McLevige, G.L. Bostrup, K. Vural, W.E. Tennant, P.H. Howard, High-performance 5-μm 640 × 480 HgCdTe-on-sapphire focal plane arrays, Optical Engineering 33 (1994) 54–63.

[83] L.J. Kozlowski, HgCdTe focal plane arrays for high performance infrared cameras, Proceedings of SPIE 3179 (1997) 200–211.

[84] T.J. de Lyon, R.D. Rajavel, J.A. Vigil, J.E. Jensen, O.K. Wu, C.A. Cockrum, S.M. Johnson, G.M. Venzor, S.L. Bailey, I. Kasai, W.L. Ahlgren, M.S. Smith, Molecular-beam epitaxial growth of HgCdTe infrared focal-plane arrays on silicon substrates for midwave infrared applications, Journal of Electronic Materials 27 (1998) 550–555.

[85] L.J. Kozlowski, K. Vural, D.Q. Bui, R.B. Bailey, D.E. Cooper, D.M. Stephenson, Status and direction of PACE-1 HgCdTe FPAs for astronomy, Proceedings of SPIE 1946 (1993) 148–160.

[86] L.J. Kozlowski, K. Vural, S.C. Cabelli, C.Y. Chen, D.E. Cooper, G.L. Bostrup, D.M. Stephenson, W.L. McLevige, R.B. Bailey, K. Hodapp, D. Hall, W.E. Kleinhans, 2.5 μm PACE-1 HgCdTe 1024×1024 FPA for infrared astronomy, Proceedings of SPIE 2268 (1994) 353–364.
[87] L.O. Bubulac, W.E. Tennant, J.G. Pasko, L.J. Kozlowski, M. Zandian, M.E. Motamedi, R.E. DeWames, J. Bajaj, N. Nayar, W.V. McLevige, N.S. Gluck, R. Melendes, D.E. Cooper, D.D. Edwall, J.M. Arias, R. Hall, High performance SWIR HgCdTe detector arrays, Journal of Electronic Materials 26 (1997) 649–655.
[88] A. Rogalski, R. Ciupa, Performance limitation of short wavelength infrared InGaAs and HgCdTe photodiodes, Journal of Electronic Materials 28 (1999) 630–636.
[89] R.G. Humpreys, Radiative lifetime in semiconductors for infrared detection, Infrared Physics 23 (1983) 171–175.
[90] R.G. Humpreys, Radiative lifetime in semiconductors for infrared detection, Infrared Physics 26 (1986) 337–342.
[91] A. Rogalski, K. Adamiec, J. Rutkowski, Narrow-Gap Semiconductor Photodiodes, SPIE Press, Bellingham, 2000.
[92] Y. Nemirovsky, D. Rosenfeld, R. Adar, A. Kornfeld, Tunneling and dark currents in HgCdTe photodiodes, Journal of Vaccum Science and Technology A 7 (1989) 528–535.
[93] R.E. DeWames, G.M. Williams, J.G. Pasko, A.H.B. Vanderwyck, Current generation mechanisms in small band gap HgCdTe p–n junctions fabricated by ion implantation, Journal of Crystal Growth 86 (1988) 849–858.
[94] Y. Nemirovsky, R. Fastow, M. Meyassed, A. Unikovsky, Trapping effects in HgCdTe, Journal of Vaccum Science and Technology B9 (1991) 1829–1839.
[95] S.M. Johnson, D.R. Rhiger, J.P. Rosbeck, J.M. Peterson, S.M. Taylor, M.E. Boyd, Effect of dislocations on the electrical and optical properties of long-wavelength infrared HgCdTe photovoltaic detectors, Journal of Vaccums Science and Technology B10 (1992) 1499–1506.
[96] M.C. Chen, R.S. List, D. Chandra, M.J. Bevan, L. Colombo, H.F. Schaake, Key performance-limiting defects in p-on-n HgCdTe heterojunction infrared photodiodes, Journal of Electronic Materials 25 (1996) 1375–1382.
[97] R.S. List, J.H. Tregilgas, A.M. Turner, J.D. Beck, J.C. Ehmke, Electrical effects of subgrain boundaries, twins, dislocations and Te precipitation on LWIR HgCdTe photodiode arrays, Proceedings of SPIE 2228 (1994) 274–282.
[98] C. Verie, F. Raymond, J. Besson, T. Nquyen Duy, Bandgap spin-orbit splitting resonance effects in $Hg_{1-x}Cd_xTe$ alloys, Journal of Crystal Growth 59 (1982) 342–346.
[99] P. Norton, HgCdTe infrared detectors, Opto-Electronics Review 10 (2002) 159–174.
[100] O.K. Wu, R.D. Rajavel, T.J. deLyon, J.E. Jensen, M.D. Jack, K. Kosai, G.R. Chapman, S. Sen, B.A. Baumgratz, MBE-grown HgCdTe multi-layer heterojunction structures for high speed low-noise 1.3–1.6 μm avalanche photodetectors, Journal of Electronic Materials 26 (1997) 488–492.
[101] T.J. deLyon, B.A. Baumgratz, G.R. Chapman, E. Gordon, M.D. Gorwitz, A.T. Hunter, M.D. Jack, J.E. Jensen, W. Johnson, K. Kosai, W. Larsen, G.L. Olson, M. Sen, B. Walker, Epitaxial growth of HgCdTe 1.55 μm avalanche photodiodes by MBE, Proceedings of SPIE 3629 (1999) 256.
[102] C.T. Elliott, N.T. Gordon, R.S. Hall, T.J. Phillips, A.M. White, C.L. Jones, C.D. Maxey, N.E. Metcalfe, Recent results on metalorganic vapor phase epitaxially grown HgCdTe heterostructure devices, Journal of Electronic Materials 25 (1996) 1139–1145.
[103] C.T. Elliott, N.T. Gordon, T.J. Phillips, H. Steen, A.M. White, C.L. Jones, C.D. Maxey, N.E. Metcalfe, Minimally cooled heterojunction laser heterodyne detectors in metalorganic vapor phase epitaxially grown $Hg_{1-x}Cd_xTe$, Journal of Electronic Materials (1996) 1146–1150.
[104] K. Jóźwikowski, A. Rogalski, A. Jóźwikowska, Numerical modeling of fluctuation phenomena in semiconductors and detailed noise study of MWIR HgCdTe heterostructure devices, Journal of Electronic Materials 31 (2002) 1139–1145.
[105] F.D. Shepherd, A.C. Yang, Silicon Schottky retinas for infrared imaging, Technical Digest of IEDM 310–313 (1973).
[106] F.D. Shepherd, Schottky diode based infrared sensors, Proceedings of SPIE 443 (1984) 42–49.
[107] F.D. Shepherd, Silicide infrared staring sensors, Proceedings of SPIE 930 (1988) 2–10.

[108] W.F. Kosonocky, Review of infrared image sensors with Schottky–barrier detectors, Optoelectronics-Devices and Technologies 6 (1991) 173–203.

[109] W.F. Kosonocky, State-of-the-art in Schottky-barrier IR image sensors, Proceedings of SPIE 1682 (1992) 2–19.

[110] M. Kimata, N. Tsubouchi, Schottky barrier photoemissive detectors, in: A. Rogalski (Ed.), Infrared Photon Detectors, SPIE Optical Engineering Press, Bellingham, 1995, pp. 299–349.

[111] F.D. Shepherd, Platinum silicide internal emission infrared imaging arrays, in: M.H. Francombe, J.L. Vossen (Eds.), Thin Films, Vol. 23, Academic Press, New York, 1998, pp. 83–114.

[112] M. Kimata, Metal silicide Schottky infrared detector arrays, in: P. Capper, C.T. Elliott (Eds.), Infrared Detectors and Emitters: Materials and Devices, Kluwer Academic Publishers, Boston, 2000, pp. 77–98.

[113] S.M. Sze, Physics of Semiconductor Devices, John Wiley & Sons Inc., New York, 1982.

[114] F.D. Shepherd, Silicide infrared staring sensors, Proceedings of SPIE 930 (1988) 2–10.

[115] J.M. Kurianski, S.T. Shanahan, U. Theden, M.A. Green, J.W.V. Storey, Optimization of the cavity for silicide Schottky infrared detectors, Solid-State Electronics 32 (1989) 97–101.

[116] W.F. Kosonocky, F.V. Shallcross, T.S. Villani, J.V. Groppe, 160×244 element PtSi Schottky-barrier IR-CCD image sensor, IEEE Transactions on Electron Devices ED-32 (1995) 1564–1572.

[117] B.Y. Tsaur, M.M. Weeks, R. Trubiano, P.W. Pellegrini, T.R. Yew, IrSi Schottky-barrier infrared detectors with 10-μm cutoff wavelength, IEEE Transaction on Electron Device Letters 9 (1988) 650–653.

[118] M. Kimata, M. Ueno, H. Yagi, T. Shiraishi, M. Kawai, K. Endo, Y. Kosasayama, T. Sone, T. Ozeki, N. Tsubouchi, PtSi Schottky-barrier infrared focal plane arrays, Opto-Electronics Review 6 (1998) 1–10.

[119] E.S. Kohn, W.F. Kosonocky,F.V. Shallcross, Charge-coupled scanned IR imaging sensors, Final Report RADC-TR-308, Rome Air Developemnt Center, 1977.

[120] M. Denda, M. Kimata, S. Iwade, N. Yutani, T. Kondo, N. Tsubouchi, Schottky-barrier infrared linear image sensor with 4-band $\times$ 4096-element, IEEE Transactions on Electron Devices 38 (1991) 1145–1151.

[121] M.T. Daigle, D. Colvin, E.T. Nelson, S. Brickman, K. Wong, S. Yoshizumi, M. Elzinga, P. Sorlie, D. Rockafellow, T. Travers, R. Avel, High resolution 2048×16 TDI PtSi IR imaging CCD, Proceedings of SPIE 1308 (1990) 88–98.

[122] H. Yagi, N. Yutani, J. Nakanishi, M. Kimata, M. Nunoshita, A monolithic Schottky-barrier infrared image sensor with 71% fill factor, Optical Engineering 33 (1994) 1454–1460.

[123] M. Kimata, N. Yutani, N. Tsubouchi, T. Seto, High performance 1040×1040 element PtSi Schottky-barrier image sensor, Proceedings of SPIE 1762 (1992) 350–360.

[124] T. Shiraishi, H. Yagi, K. Endo, M. Kimata, T. Ozeki, K. Kama, T. Seto, PtSi FPA with improved CSD operation, Proceedings of SPIE 2744 (1996) 33–43.

[125] M. Inoue, T. Seto, S. Takahashi, S. Itoh, H. Yagi, T. Siraishi, K. Endo, M. Kimata, Portable high performance camera with 801×512 PtSi-SB IRCSD, Proceedings of SPIE 3061 (1997) 150–158.

[126] M. Kimata, T. Ozeki, M. Nunoshita, S. Ito, PtSi Schottky-barrier infrared FPAs with CSD readout, Proceedings of SPIE 3179 (1997) 212–223.

[127] T.L. Lin, A. Ksendzov, S.M. Dajewski, E.W. Jones, R.W. Fathauer, T.N. Krabach, J. Maserjian, A novel Si-based LWIR detector: The SiGe/Si heterojunction internal photoemission detector, IEDM Technical Digest (1990) 641–644.

[128] T.L. Lin, J. Maserjian, Novel $Si_{1-x}Ge_x$/Si heterojunction internal photoemission long-wavelength infrared detectors, Applied Physics Letters 57 (1990) 1422–1424.

[129] T.L. Lin, A. Ksendzov, S.M. Dejewski, E.W. Jones, R.W. Fathauer, T.N. Krabach, J. Maserjian, SiGe/Si heterojunction internal photoemission long-wavelength infrared detectors fabricated by molecular beam epitaxy, IEEE Transactions on Electron Devices 38 (1991) 1141–1144.

[130] T.L. Lin, E.W. Jones, T. George, A. Ksendzov, M.L. Huberman, Advanced Si IR detectors using molecular beam epitaxy, Proceedings of SPIE 1540 (1991) 135–139.

[131] B.Y. Tsaur, C.K. Chen, S.A. Marino, Long-wavelength GeSi/Si heterojunction infrared detectors and 400×400-element imager arrays, IEEE Electronic Device Letters 12 (1991) 293–296.

[132] B.Y. Tsaur, C.K. Chen, S.A. Marino, Long-wavelength $Ge_{1-x}Si_x$/Si heterojunction infrared detectors and focal plane arrays, Proceedings of SPIE 1540 (1991) 580–595.
[133] B.Y. Tsaur, C.K. Chen, S.A. Marino, Heterojunction $Ge_{1-x}Si_x$/Si infrared detectors and focal plane arrays, Optical Engineering 33 (1994) 72–78.
[134] T.L. Lin, J.S. Park, S.D. Gunapal, E.W. Jones, H.M. Del Castillo, Photoresponse model for $Si_{1-x}Ge_x$/Si heterojunction internal photoemission infrared detector, IEEE Electron Device Letters 15 (1994) 103–105.
[135] T.L. Lin, J.S. Park, S.D. Gunapala, E.W. Jones, H.M. Del Castilo, $Si_{1-x}Ge_x$/Si heterojunction internal photoemission long wavelength infrared detector, Proceedings of SPIE 2474 (1994) 17–23.
[136] H. Wada, M. Nagashima, K. Hayashi, J. Nakanishi, M. Kimata, N. Kumada, S. Ito, 512×512 element GeSi/Si heterojunction infrared focal plane array, Opto-Electronics Review 7 (1999) 305–311.
[137] S. Tohyama, N. Teranishi, K. Kunoma, M. Nishimura, K. Arai, E. Oda, A new concept silicon homojunction infrared sensor, IEDM Technical Digest 82–85 (1988).
[138] A.G.U. Perera, H.X. Yuan, M.H. Francombe, Homojunction internal photoemission far-infrared detectors: photoresponse performance analysis, Journal of Applied Physics 77 (1995) 915–924.
[139] A.G.U. Perera, Physics and novel device applications of semiconductor homojunctions, in: M.H. Francombe, J.L. Vossen (Eds.), Thin Solid Films, Vol. 21, Academic Press, New York, 1995, pp. 1–75.
[140] A.G.U. Perera, H.X. Yuan, J.W. Choe, M.H. Francombe, Novel homojunction interfacial workfunction internal photoemission (HIWIP) tunable far-infrared detectors for astronomy, Proceedings of SPIE 2475 (1995) 76–87.
[141] W. Shen, A.G.U. Perera, M.H. Francombe, H.C. Liu, M. Buchanan, W.J. Schaff, Effect of emitter layer concentration on the performance of GaAs p^+-i homojunction far-infrared detectors: A comparison of theory and experiment, IEEE Transactions on Electron Devices 45 (1988) 1671–1677.
[142] A.G.U. Perera, W.Z. Shen, GaAs homojunction interfacial workfunction internal photoemission (HIWIP) far-infrared detectors, Opto-Electronics Review 7 (1999) 153–180.
[143] A.G.H. Perera, Semiconductor photoemissive structures for far infrared detection, in: M.H. Francombe (Ed.), Handbook of Thin Devices, Vol. 2, Academic Press, San Diego, 2000, pp. 135–170.
[144] H.X. Yuan, A.G.H. Perera, Dark current analysis of Si homojunction interfacial work function internal photoemission far-infrared detectors, Applied Physics Letters 66 (1995) 2262–2264.
[145] E.E. Haller, Advanced far-infrared detectors, Infrared Physics 35 (1994) 127.
[146] D.W. Watson, M.T. Guptill, J.E. Huffman, T.N. Krabach, S.N. Raines, S. Satyapal, Germanium blocked-impurity-band detector arrays: unpassivated devices with bulk substrates, Journal of Applied Physics 74 (1993) 4199.
[147] F.J. Low, C.A. Beichman, F.C. Gillett, J.R. Houck, G. Neugebauer, D.E. Langford, R.G. Walker, R.H. White, Cryogenic telescope on the Infrared Astronomical Satellite (IRAS), Proceedings of SPIE 430 (1983) 288–296.
[148] N.W. Boggess, NASA space programs in infrared astronomy, Laser Focus/Electro-Optics 116-127 (June 1984).
[149] N. Sclar, Properties of doped silicon and germanium infrared detectors, Progress in Quantum Electronics 9 (1984) 149–257.
[150] P.R. Norton, Infrared image sensors, Optical Engineering 30 (1991) 1649–1663.
[151] S. Suffis, M. Caes, P. Deliot, J. Deschamps, M. Tauvy, Characterisation of 128×192 Si:Ga focal plane array: study of nonuniformity, stability, of its correction, and application for CRYSTAL camera, Proceedings of SPIE 3379 (1998) 235–248.
[152] P.R. Bratt, Impurity germanium and silicon infrared detectors, in: R.K. Willardson, A.C. Beer (Eds.), Semiconductors and Semimetals, Vol. 12, Academic Press, New York, 1977, pp. 39–141.
[153] N. Sclar, Extrinsic silicon detectors for 3–5 and 8–14 μm, Infrared Physics 16 (1976) 435–448.

[154] N. Sclar, Survey of dopants in silicon for 2–2.7 and 3–5 μm infrared detector application, Infrared Physics 17 (1977) 71–82.
[155] N. Sclar, Development status of silicon extrinsic IR detectors, Proceedings of SPIE 409 (1983) 53–61.
[156] N. Sclar, Development status of silicon extrinsic IR detectors, Proceedings of SPIE 443 (1984) 11–41.
[157] M. Fujiwara, N. Hiromoto, H. Shibai, T. Hirao, T. Nakagawa, Development of far-infrared Ge: Ga photoconductor 2D array for 3 THz imaging, Proceedings of SPIE 4130 (2000) 842–849.
[158] A.G. Kazanskii, P.L. Richards, E.E. Haller, Far-infrared photoconductivity of uniaxially stressed germanium, Applied Physics Letters 31 (1977) 496–497.
[159] E.E. Haller, M.R. Hueschen, P.L. Richards, Ge:Ga photoconductors in low infrared backgrounds, Applied Physics Letters 34 (1979) 495–497.
[160] J. Wolf, C. Gabriel, U. Grözinger, I. Heinrichsen, G. Hirth, S. Kirches, D. Lemke, J. Schubert, B. Schulz, C. Tilgner, M. Boison, A. Frey, I. Rasmussen, R. Wagner, K. Proetel, Calibration facility and preflight characterization of the photometer in the Infrared Space Observatory, Optical Engineering 33 (1994) 26–36.
[161] J. Wolf, H. Driescher, J. Schubert, D. Rabanus, E. Paul, K. Rösner, Photoconductor arrays for a spectral-photometric far-infrared camera on SOFIA, Proceedings of SPIE 3287 (1998) 272–279.
[162] M.D. Petroff, M.G. Stapelbroeck, Blocked impurity band detectors, U.S. Patent, No. 4 568 960, filed 23 October 1980, granted 4 February 1986.
[163] S.B. Stetson, D.B. Reynolds, M.G. Stapelbroeck, R.L. Stermer, Design and performance of blocked-impurity-band detector focal plane arrays, Proceedings of SPIE 686 (1986) 48–65.
[164] D.B. Reynolds, D.H. Seib, S.B. Stetson, T.L. Herter, N. Rowlands, J. Schoenwald, Blocked impurity band hybrid infrared focal plane arrays for astronomy, IEEE Transactions on Nuclear Science 36 (1989) 857–862.
[165] J.E. Huffman, A.G. Crouse, B.L. Halleck, T.V. Downes, T.L. Herter, Si:Sb blocked impurity band detectors for infrared astronomy, Journal of Applied Physics 72 (1992) 273–275.
[166] D.M. Watson, J.E. Huffman, Germanium blocked impurity band far infrared detectors, Applied Physics Letters 52 (1988) 1602–1604.
[167] D.M. Watson, M.T. Guptill, J.E. Huffman, T.N. Krabach, S.N. Raines, S. Satyapal, Germanium blocked impurity band detector arrays: unpassiviated devices with bulk substrates, Journal of Applied Physics 74 (1993) 4199–4206.
[168] I.C. Wu, J.W. Beeman, P.N. Luke, W.L. Hansen, E.E. Haller, Ion-implanted extrinsic Ge photodetectors with extended cutoff wavelength, Applied Physics Letters 58 (1991) 1431–1433.
[169] F. Szmulowicz, F.L. Madarsz, Blocked impurity band detectors—an analytical model: figures of merit, Journal of Applied Physics 62 (1987) 2533–2540.
[170] G.G. Fazio, Infrared array detectors in astrophysics, Infrared Physics Technology 35 (1994) 107–117.
[171] J. Venzon, N. Lum, S. Freeman, G. Domingo, High-background, longwave IR focal plane array development using Si:As IBC detectors, Proceedings of SPIE 2475 (1995) 34–40.
[172] S. Solomon, A. Tribble, N. Lum, J. Venzon, G. Domingo, A. Hofman, M. Smith, High-background, longwave Si:As IBC 320×240 IR focal plane array, Proceedings of SPIE 2816 (1996) 161–168.
[173] M.G. Stapelbroeck, D.H. Seib, J.E. Huffman, R.A. Florence, Large-format blocked-impurity-band focal plane arrays for long wavelength infrared astronomy, Proceedings of SPIE 2476 (1995) 41–48.
[174] P.R. Norton, Infrared image sensor status, Proceedings of SPIE 2274 (1994) 82–92.
[175] W.F.M. Micklethwaite, A.J. Johnson, InSb: Materials and devices, in: P. Capper, C.T. Elliott (Eds.), Infrared Detectors and Emitters: Materials and Devices, Kluwer Academic Publishers, Boston, 2000, pp. 177–204.
[176] J.T. Wimmers, D.S. Smith, Characteristics of InSb photovoltaic detectors at 77 K and below, Proceedings of SPIE 364 (1983) 123–131.
[177] J.T. Wimmers, R.M. Davis, C.A. Niblack, D.S. Smith, Indium antimonide detector technology at Cincinnati Electronics Corporation, Proceedings of SPIE 930 (1988) 125–138.

[178] R. Schoolar, E. Tenescu, Analysis of InSb photodiode low temperature characteristics, Proceedings of SPIE 686 (1986) 2–11.
[179] J.T. Wimmers, D.S. Smith, Optimization of InSb detectors for use at liquid helium temperatures, Proceedings of SPIE 510 (1984) 21.
[180] W.J. Parrish, J.D. Blackwell, G.T. Kincaid, R.C. Paulson, Low-cost high performance InSb 256×256 infrared camera, Proceedings of SPIE 1540 (1991) 274–284.
[181] A.M. Fowler, J.B. Heynssens, Evaluation of the SBRC 256×256 InSb focal plane array and preliminary specifications for the 1024×1024 InSb focal plane array, Proceedings of SPIE 1946 (1993) 25–32.
[182] A.M. Fowler, D. Bass, J. Heynssens, I. Gatley, F.J. Vrba, H.D. Ables, A. Hoffman, M. Smith, J. Woolaway, Next generation in InSb arrays: ALADDIN, the 1024×1024 InSb focal plane array readout evaluation results, Proceedings of SPIE 2268 (1994) 340–345.
[183] A.M. Fowler, J.B. Heynssens, I. Gatley, F.J. Vrba, H.D. Ables, A. Hoffman, J. Woolaway, ALADDIN, the 1024×1024 InSb array: Test results, Proceedings of SPIE 2475 (1995) 27–33.
[184] A.M. Fowler, I. Gatley, P. McIntyre, F.J. Vrba, A. Hoffman, ALADDIN, the 1024×1024 InSb array: design, description, and results, Proceedings of SPIE 2816 (1996) 150–160.
[185] M. Davis, M. Greiner, J. Sanders, J. Wimmers, Resolution issues in InSb focal plane array system design, Proceedings of SPIE 3379 (1998) 288–299.
[186] H. Fujisada, N. Nakayama, A. Tanaka, Compact 128 InSb focal plane assembly for thermal imaging, Proceedings of SPIE 1341 (1990) 80–91.
[187] C. Niblack, M. Blessinger, J. Forsthoefel, C. Staller, H. Sobel, InSb linear miltiplexed FPAs for the CRAF/Cassini visible and infrared mapping spectrometer, Proceedings of SPIE 1494 (1991) 403–418.
[188] G.H. Olsen, A.M. Joshi, S.M. Mason, K.M. Woodruff, E. Mykietyn, V.S. Ban, M.J. Lange, J. Hladky, G.C. Erickson, G.A. Gasparian, Room-temperature InGaAs detector arrays for 2.5 μm, Proceedings of SPIE 1157 (1989) 276–282.
[189] G. Olsen, A. Joshi, M. Lange, K. Woodruff, E. Mykietyn, D. Gay, G. Erickson, D. Ackley, V. Ban, C. Staller, A128×128 InGaAs detector array for 1.0–1.7 microns, Proceedings of SPIE 1341 (1990) 432–437.
[190] G.H. Olsen, InGaAs fills the near-IR detector-array vacuum, Laser Focus World, 1991, A21–A30.
[191] G.H. Olsen, A.M. Joshi, V.S. Ban, Current status of InGaAs detector arrays for 1–3 μm, Proceedings of SPIE 1540 (1991) 596–605.
[192] A.M. Joshi, V.S. Ban, S. Mason, M.J. Lange, W.F. Kosonocky, 512 and 1024 element linear InGaAs detector arrays for near-infrared (1–3 μm) environmental sensing, Proceedings of SPIE 1735 (1992) 287–295.
[193] M.J. Cohen, G.H. Olsen, Room temperature InGaAs camera for NIR imaging, Proceedings of SPIE 1946 (1993) 436–443.
[194] L.J. Kozlowski, W.E. Tennant, M. Zandian, J.M. Arias, J.G. Pasko, SWIR staring FPA performance at room temperature, Proceedings of SPIE 2746 (1996) 93–100.
[195] L.J. Kozlowski, K. Vural, J.M. Arias, W.E. Tennant, R.E. DeWames, Performance of HgCdTe, InGaAs and quantum well GaAs/AlGaAs staring infrared focal plane arrays, Proceedings of SPIE 3182 (1997) 2–13.
[196] M.H. Ettenberg, M.J. Lange, M.T. O'Grady, J.S. Vermaak, M.J. Cohen, G.H. Olsen, A room temperature 640×512 pixel near-infrared InGaAs focal plane array, Proceedings of SPIE 4028 (2000) 201–207.
[197] G.H. Olsen, V.S. Ban, InGaAsP: The next generation in photonics materials, Solid State Technology, 1987, pp. 99–105.
[198] I. Gyuro, MOVPE for InP-based optoelectronic device application, in: Compound Semiconductor Industry Directory, Elsevier Science Ltd, 1996, pp. 58–68.
[199] A.M. Joshi, G.H. Olsen, S. Mason, M.J. Lange, V.S. Ban, Near-infrared (1–3 μm) InGaAs detectors and arrays: crystal growth, leakage current and reliability, Proceedings of SPIE 1715 (1992) 585–593.
[200] G.H. Olsen, M.J. Lange, M.J. Cohen, D.S. Kim, S.R. Forrest, Three-band 1.0–2.5 μm near-infrared InGaAs detector array, Proceedings of SPIE 2235 (1994) 151–159.

[201] G.H. Olsen, M.J. Cohen, Applications of near-infrared imaging, Proceedings of SPIE 3379 (1998) 300–306.

[202] A. Rogalski, $InAs_{1-x}Sb_x$ infrared detectors, Progress in Quantum Electronics 13 (1989) 191–231.

[203] A. Rogalski, New Ternary Alloy Systems for Infrared Detectors, Optical Engineering Press, Bellingham, 1994.

[204] Infrared Photon Detectors, In: A. Rogalski (Ed.), SPIE Optical Engineering Press, Bellingham, 1995.

[205] L.O. Bubulac, A.M. Andrews, E.R. Gertner, D.T. Cheung, Backside-illuminated InAsSb/GaSb broadband detectors, Applied Physics Letters 36 (1980) 734–736.

[206] G.C. Osbourn, InAsSb strained-layer superlattice for long wavelength detector applications, Journal of Vaccum Science and Technology B2 (1984) 176–178.

[207] S.R. Kurtz, L.R. Dawson, T.E. Zipperian, R.D. Whaley, High-detectivity ($>1\times10^{10}$ $cmHz^{1/2}W^{-1}$), InAsSb strained-layer superlattice, photovoltaic infrared detector, IEEE Electron Device Letters 11 (1990) 54–56.

[208] L.R. Dawson, Applications of narrow gap strained layer supperlattices, presented at International Conference on Narrow Gap Semiconductors, 19–23 July 1992, University of Southampton.

[209] A. Rogalski, R. Ciupa, W. Larkowski, Near room-temperature InAsSb photodiodes: theoretical predictions and experimental data, Solid-State Electronics 39 (1996) 1593–1600.

[210] J.D. Kim, S. Kim, D. Wu, J. Wojkowski, J. Xu, J. Piotrowski, E. Bigan, M. Razeghi, 8–13 μm InAsSb heterojunction photodiode operating at near room temperature, Applied Physics Letters 67 (1995) 2645–2647.

[211] E. Michel, M. Razeghi, Recent advances in Sb-based materials for uncooled infrared photodetectors, Opto-Electronics Review 6 (1998) 11–23.

[212] C.T. Elliott, Advanced heterostructures for $In_{1-x}Al_xSb$ and $Hg_{1-x}Cd_xTe$ detectors and emiters, Proceedings of SPIE 2744 (1996) 452–462.

[213] T. Ashley, A.B. Dean, C.T. Elliott, A.D. Johnson, G.J. Pryce, A.M. White, C.R. Whitehouse, A heterojunction minority carrier barrier for InSb devices, Semiconductor Science and Technology 8 (1993) S386–S389.

[214] J.J. Lee, M. Razeghi, Exploration of InSbBi for uncooled long-wavelength infrared photodetectors, Opto-Electronics Review 6 (1998) 25–36.

[215] A. Rogalski, $Hg_{1-x}Zn_xTe$ as a potential infrared detector material, Progress in Quantum Electronics 13 (1989) 299–353.

[216] A. Rogalski, $Hg_{1-x}Mn_xTe$ as a new infrared detector material, Infrared Physics 31 (1991) 117–166.

[217] R. Triboulet, (Hg,Zn)Te: a new material for IR detection, Journal of Crystal Growth 86 (1988) 79–86.

[218] R. Triboulet, M. Bourdillot, A. Durand, T. Nguyen-Duy, (Hg,Zn)Te among the other materials for IR detectors, Proceedings of SPIE 1106 (1989) 40–47.

[219] E.A. Patten, M.H. Kalisher, G.R. Chapman, J.M. Fulton, C.Y. Huang, P.R. Norton, M. Ray, S. Sen, HgZnTe for very long wavelength infrared applications, Journal of Vaccum Science and Technology B9 (1991) 1746–1751.

[220] J. Ameurlaine, A. Rousseau, T. Nguyen-Duy, R. Triboulet, (HgZn)Te infrared photovoltaic detectors, Proceedings of SPIE 929 (1988) 14–20.

[221] Detector Mini-Magazine, Photonics Spectra, 94, July 1988.

[222] P. Becla, Infrared photovoltaic detectors utilizing $Hg_{1-x}Mn_xTe$ and $Hg_{1-x-y}Cd_xMn_yTe$ alloys, Journal of Vaccum Science and Technology A4 (1986) 2014–2018.

[223] P. Becla, S. Motakef, T. Koehler, Long wavelength HgMnTe avalanche photodiodes, Journal of Vaccum Science and Technology B10 (1992) 159–601.

[224] P. Becla, Advanced infrared photonic devices based on HgMnTe, Proceedings of SPIE 2021 (1993) 22–33.

[225] L.A. Kosyachenko, I.M. Rarenko, Sun Weiguo, L. Zheng Xiong, Charge transport mechanisms in HgMnTe photodiodes with ion etched p–n junctions, Solid-State Electronics 44 (2000) 1197–1202.

[226] L.A. Kosyachenko, I.M. Rarenko, Sun Weiguo, L. Zheng Xiong, G. Qibing, Photoelectric properties of HgMnTe photodiodes with ion etched p–n junctions, Opto-Electronics Review 8 (2000) 251–262.
[227] J.T. Longo, D.T. Cheung, A.M. Andrews, C.C. Wang, J.M. Tracy, Infrared focal planes in intrinsic semiconductors, IEEE Transactions on Electron Devices ED-25 (1978) 213–232.
[228] A. Rogalski, W. Larkowski, Comparison of photodiodes for the 3–5.5 μm and 8–14 μm spectral regions, Electron Technology 18 (3/4) (1985) 55–69.
[229] H. Zogg, S. Blunier, T. Hoshino, C. Maissen, J. Masek, A.N. Tiwari, Infrared sensor arrays with 3–12 μm cutoff wavelengths in heteroepitaxial narrow-gap semiconductors on silicon substrates, IEEE Transactions on Electronic Devices 38 (1991) 1110–1117.
[230] T. Hoshino, C. Maissen, H. Zogg, J. Masek, S. Blunier, A.N. Tiwari, S. Teodoropol, W.J. Bober, Monolithic PbSnSe infrared sensor arrays on Si prepared by low-temperature process, Infrared Physics 32 (1991) 169–175.
[231] J. Masek, T. Hoshino, C. Maissen, H. Zogg, S. Blunier, J. Vermeiren, C. Claeys, Monolithic lead-chalcogenide IR-arrays on silicon: fabrication and use in thermal imaging applications, Proceedings of SPIE 1735 (1993) 54–61.
[232] H. Zogg, A. Fach, C. Maissen, J. Masek, S. Blunier, Photovoltaic lead-chalcogenide on silicon infrared sensor arrays, Optical Engineering 33 (1994) 1440–1449.
[233] H. Zogg, A. Fach, J. John, J. Masek, P. Müller, C. Paglino, S. Blunier, Photovoltaic IV–VI on Si infrared sensor arrays for thermal imaging, Optical Engineering 34 (1995) 1964.
[234] H. Zogg, A. Fach, J. John, J. Masek, P. Müller, C. Paglino, $Pb_{1-x}Sn_xSe$-on-Si LWIR thermal imaging system, Proceedings of SPIE 2552 (1995) 404–410.
[235] H. Zogg, A. Fach, J. John, P. Müller, C. Paglino, A.N. Tiwari, PbSnSe-on-Si: material and IR-device properties, Proceedings of SPIE 3182 (1997) 26–29.
[236] J. John, H. Zogg, Infrared p–n-junction diodes in epitaxial narrow gap PbTe layers on Si substrates, Applied Physics Letters 85 (1999) 3364–3366.
[237] K. Alchalabi, D. Zimin, H. Zogg, W. Buttler, Monolithic heteroepiraxial PbTe-on-Si infrared focal plane array with 96×128 pixels, IEEE Electron Device Letters 22 (2001) 110–112.
[238] K. Alchalabi, D. Zimin, H. Zogg, W. Buttler, Heteroepitaxial 96×128 lead chalcogenide on silicon infrared focal plane array for thermal imaging, Proceedings of SPIE 4369 (2001) 405–411.
[239] A. Rogalski, R. Ciupa, Long wavelength HgCdTe photodiodes: n^+-on-p versus p-on-n structures, Journal of Applied Physics 77 (1995) 3505–3512.
[240] A. Rogalski, R. Ciupa, H. Zogg, Computer modeling of carrier transport in PbSnSe photodiodes, Infrared Physics Technology 37 (1994) 837–845.
[241] C. Paglino, A. Fach, J. John, P. Müller, H. Zogg, D. Pescia, Schottky-barrier fluctuations in $Pb_{1-x}Sn_xSe$ infrared sensors, Journal of Applied Physics 80 (1996) 7138–7143.
[242] J.H. Werner, H.H. Güttler, Barrier inhomogeneities at Schottky contacts, Journal of Applied Physics 69 (1991) 1522–1533.
[243] A. Fach, J. John, P. Müller, C. Paglino, H. Zogg, Material properties of $Pb_{1-x}Sn_xSe$ epilayers on Si and their correlation with the performance of infrared photodiodes, Journal of Electronic Materials 26 (1997) 873–877.
[244] P. Müller, H. Zogg, A. Fach, J. John, C. Paglino, A.N. Tiwari, M. Krejci, G. Kostorz, Reduction of threading dislocation densities in heavily lattice mismatched PbSe on Si(1 1 1) by glide, Physics Review Letters 78 (1997) 3007–3010.
[245] H. Zogg, Lead chalcogenide on silicon infrared sensor arrays, Opto-Electronics Review 6 (1998) 37–46.
[246] L. Esaki, R. Tsu, Superlattice and negative conductivity in semiconductors, IBM Journal of Research and Development 14 (1970) 61–65.
[247] L.J. Kozlowski, G.M. Williams, G.J. Sullivan, C.W. Farley, R.J. Anderson, J. Chen, D.T. Cheung, W.E. Tennant, R.E. DeWames, LWIR 128×128 GaAs/AlGaAs multiple quantum well hybrid focal plane array, IEEE Transactions on Electron Devices 38 (1991) 1124–1130.
[248] B.F. Levine, C.G. Bethea, K.G. Glogovsky, J.W. Stay, R.E. Leibenguth, Long wavelength 128×128 GaAs quantum well infrared photodetector arrays, Semiconductor Science and Technology 6 (1991) C114–C119.

[249] M.O. Manasreh (Ed.), Semiconductor Quantum Wells and Superlattices for Long-Wavelength Infrared Detectors, Artech House, Norwood, MA, 1993.
[250] C.G. Bethea, B.F. Levine, M.T. Asom, R.E. Leibenguth, J.W. Stayt, K.G. Glogovsky, R.A. Morgan, J.D. Blackwell, W.J. Parrish, Long wavelength infrared 128×128 $Al_xGa_{1-x}As/GaAs$ quantum well infrared camera and imaging system, IEEE Transactions on Electron Devices 40 (1993) 1957–1963.
[251] F.F. Sizov, A. Rogalski, Semiconductor superlattices and quantum wells for infrared optoelectronics, Progress in Quantum Electronics 17 (1993) 93–164.
[252] W.A. Beck, J.W. Little, A.C. Goldberg, T.S. Faska, Imaging performance of LWIR miniband transport multiple quantum well infrared focal plane arrays, in: H.C. Liu, B.F. Levine, J.Y. Anderson (Eds.), Quantum Well Intersubband Transition Physics and Devices, Kluwer Academic Publishers, Dordrecht, 1994, pp. 55–68.
[253] L.J. Kozlowski, Background limited 128×128 GaAs/AlGaAs multiple quantum well infrared focal plane arrays, in: H.C. Liu, B.F. Levine, J.Y. Anderson (Eds.), Quantum Well Intersubband Transition Physics and Devices, Kluwer Academic Publishers, Dordrecht, 1994, pp. 43–54.
[254] S.D. Gunapala, K.M.S.V. Bandara, Recent development in quantum-well infrared photodetectors, Thin Films, Vol. 21, Academic Press, New York, 1995, pp. 113–237.
[255] W.A. Beck, T.S. Faska, Current status of quantum well focal plane arrays, Proceedings of SPIE 2744 (1996) 193–206.
[256] S.D. Gunapala, J.K. Liu, M. Sundaram, S.V. Bandara, C.A. Shott, T. Hoelter, P.D. Maker, R.E. Muller, Long-wavelength 256×256 QWIP hand-held camera, Proceedings of SPIE 2746 (1996) 124–133.
[257] S. Gunapala, M. Sundaram, S. Bandara, Quantum wells stare at long-wave IR scenes, Laser Focus World 233–240 (June 1996).
[258] S.D. Gunapala, J.S. Park, G. Sarusi, T.L. Lin, J.K. Liu, P.D. Maker, R.E. Muller, C.A. Shott, T. Hoelter, 15-μm 128×128 $GaAs/Al_xGa_{1-x}As$ quantum well infrared photodetector focal plane array camera, IEEE Transactions on Electron Devices 44 (1997) 45–50.
[259] S.D. Gunapala, J.K. Liu, J.S. Park, M. Sundaram, C.A. Shott, T. Hoelter, T.L. Lin, S.T. Massie, P.D. Maker, R.E. Muller, G. Sarusi, 9-μm cutoff 256×256 $GaAs/Al_xGa_{1-x}As$ quantum well infrared photodetector hand-held camera, IEEE Trans. Electron Devices 44 (1997) 51–57.
[260] S.D. Gunapala, S.V. Bandara, J.K. Liu, W. Hong, E.M. Luong, J.M. Mumolo, M.J. McKelvey, D.K. Sengupta, A. Singh, C.A. Shott, R. Carralejo, P.D. Maker, J.J. Bock, M.E. Ressler, M.W. Werner, T.N. Krabach, Quantum well infrared photodetector research and development at Jet Propulsion Laboratory, Proceedings of SPIE 3379 (1998) 382–395.
[261] S.D. Gunapala, S.V. Bandara, J.K. Liu, W. Hong, M. Sundaram, P.D. Maker, R.E. Muller, C.A. Shott, R. Carralejo, Long-wavelength 640×486 GaAs/AlGaAs quantum well infrared photodetector snap-shot camera, IEEE Transactions on Electron Devices 45 (1998) 1890–1895.
[262] S.D. Gunapala, S.V. Bandara, J.K. Liu, E.M. Luong, N. Stetson, C.A. Shott, J.J. Bock, S.B. Rafol, J.M. Mumolo, M.J. McKelvey, Long-wavelength 256×256 GaAs/AlGaAs quantum well infrared photodetector (QWIP) palm-size camera, IEEE Transactions on Electron Devices 47 (2000) 326–332.
[263] S.D. Gunapala, S.V. Bandara, Quantum well infrared photodetectors, in: M.H. Francombe (Ed.), Handbook of Thin Devices, Vol. 2, Academic Press, San Diego, 2000, pp. 63–99.
[264] H. Schneider, M. Walther, C. Schönbein, R. Rehm, J. Fleissner, W. Pletschen, J. Braunstein, P. Koidl, G. Weimann, J. Ziegler, W. Cabanski, QWIP FPAs for high-performance thermal imaging, Physica E 7 (2000) 101–107.
[265] H.C. Liu, An introduction to the physics of quantum well infrared photodetectors and other related new devices, in: M.H. Francombe (Ed.), Handbook of Thin Devices, Vol. 2, Academic Press, San Diego, 2000, pp. 101–134.
[266] S.D. Gunapala, S.V. Bandara, J.K. Liu, E.M. Luong, S.B. Rafol, J.M. Mumolo, D.Z. Ting, J.J. Bock, M.E. Ressler, M.W. Werner, P.D. LeVan, R. Chehayeb, C.A. Kukkonen, M. Ley, P. LeVan, M.A. Fauci, Recent developments and applications of quantum well infrared photodetector focal plane arrays, Opto-Electronics Review 8 (2001) 150–163.

[267] C.J. Chen, K.K. Choi, M.Z. Tidrow, D.C. Tsui, Corrugated quantum well infrared photodetectors for normal incident light coupling, Applied Physics Letters 68 (1996) 1446–1448.
[268] C.J. Chen, K.K. Choi, W.H. Chang, D.C. Tsui, Performance of corrugated quantum well infrared photodetectors, Applied Physics Letters 71 (1997) 3045–3047.
[269] A. Singh, M.O. Manasreh, Quantum well and superlattice heterostructures for space-based long wavelength infrared photodetectors, Proceedings of SPIE 2397 (1995) 193–209.
[270] A. Rogalski, Assessment of HgCdTe photodiodes and quantum well infrared photoconductors for long wavelength focal plane arrays, Infrared Physics and Technology 40 (1999) 279–294.
[271] H. Schneider, C. Schönbein, M. Walther, K. Schwarz, J. Fleißner, P. Koidl, Photovoltaic quantum well infrared photodetectors: the four zone scheme, Applied Physics Letters 71 (1997) 246–248.
[272] M. Walther, F. Fuchs, H. Schneider, J. Fleißner, J. Schmitz, W. Pletschen, J. Braunstein, J. Ziegler, W. Cabanski, P. Koidl, G. Weimann, III–V semiconductor quantum well and superlattice detectors, Proceedings of SPIE 3436 (1998) 348–358.
[273] C. Schönbein, H. Schneider, R. Rehm, M. Walther, Noise gain and detectivity of n-type GaAs/AlGaAs quantum well infrared photodetectors, Applied Physics Letters 73 (1998) 1251–1253.
[274] R. Breiter, W. Cabanski, R. Koch, W. Rode, J. Ziegler, K. Eberhardt, O. Oelmaier, M. Walther, High resolution QWIP and MCT FPA modules at AIM, Proceedings of SPIE 3698 (1999) 397–406.
[275] W. Cabanski, R. Breiter, R. Koch, K-H. Mauk, W. Rode, J. Ziegler, H. Schneider, M. Walther, O. Oelmaier, 3rd gen focal plane array IR detection modules at AIM, Proceedings of SPIE 4369 (2001) 547–558.
[276] H. Schneider, P. Koidl, M. Walther, J. Fleissner, R. Rehm, E. Diwo, K. Schwarz, G. Weimann, Ten years of QWIP development at Fraunhofer, Infrared Physics and Technology 42 (2001) 283–289.
[277] D.L. Smith, C. Mailhiot, Proposal for strained type II superlattice infrared detectors, Journal of Applied Physics 62 (1987) 2545–2548.
[278] C. Mailhiot, D.L. Smith, Long-wavelength infrared detectors based on strained InAs/$Ga_{1-x}In_xSb$ type-II superlattices, Journal of Vaccum Science and Technology A7 (1989) 445–449.
[279] J.P. Omaggio, J.R. Meyer, R.J. Wagner, C.A. Hoffman, M.J. Yang, D.H. Chow, R.H. Miles, Determination of band gap and effective masses in InAs/$Ga_{1-x}In_xSb$ superlattices, Applied Physics Letters 61 (1992) 207–209.
[280] C.A. Hoffman, J.R. Meyer, E.R. Youngdale, F.J. Bartoli, R.H. Miles, L.R. Ram-Mohan, Electron transport in InAs/$Ga_{1-x}In_xSb$ superlattices, Solid State Electronics 37 (1994) 1203–1206.
[281] C.H. Grein, P.M. Young, H. Ehrenreich, Minority carrier lifetimes in ideal InGaSb/InAs superlattice, Applied Physics Letters 61 (1992) 2905–2907.
[282] C.H. Grein, P.M. Young, M.E. Flatté, H. Ehrenreich, Long wavelength InAs/InGaSb infrared detectors: optimization of carrier lifetimes, Journal of Applied Physics 78 (1995) 7143–7152.
[283] E.R. Youngdale, J.R. Meyer, C.A. Hoffman, F.J. Bartoli, C.H. Grein, P.M. Young, H. Ehrenreich, R.H. Miles, D.H. Chow, Auger lifetime enhancement in InAs-$Ga_{1-x}In_xSb$ superlattices, Applied Physics Letters 64 (1994) 3160–3162.
[284] E.R. Youngdale, J.R. Meyer, C.A. Hoffman, F.J. Bartoli, R.H. Miles, D.H. Chow, Recombination lifetime in InAs-$Ga_{1-x}In_xSb$ superlattices, Journal of Vaccum Science and Technology B12 (1994) 1129–1132.
[285] H. Ehrenreich, C.H. Grein, R.H. Miles, M.E. Flatte, Reply to Comment on Temperature limits on infrared detectivities of InAs/$In_xGa_{1-x}Sb$ superlattices and bulk $Hg_xCd_{1-x}Te$, [Journal of Applied Physics 80 (1996) 2542]; Journal of Applied Physics 80 (1996) 2545–2546.
[286] J.L. Johnson, L.A. Samoska, A.C. Gossard, J.L. Merz, M.D. Jack, G.H. Chapman, B.A. Baumgratz, K. Kosai, S.M. Johnson, Electrical and optical properties of infrared photodiodes using the InAs/$Ga_{1-x}In_xSb$ superlattice in heterojunctions with GaSb, Journal of Applied Physics 80 (1996) 1116–1127.
[287] F. Fuchs, U. Weimer, W. Pletschen, J. Schmitz, E. Ahlswede, M. Walther, J. Wagner, P. Koidl, High performance InAs/$Ga_{1-x}In_xSb$ superlattice infrared photodiodes, Applied Physics Letters 71 (1997) 3251–3253.

[288] F. Fuchs, L. Bürkle, R. Hamid, N. Herres, W. Pletschen, R.E. Sah, R. Kiefer, J. Schmitz, Optoelectronic properties of photodiodes for the mid- and far-infrared based on the InAs/GaSb/AlSb materials family, Proceedings of SPIE 4288 (2001) 171–182.
[289] H. Mohseni, M. Razeghi, G.J. Brown, T.S. Park, High-performance InAs/GaSb superlattice photodiodes for the very long wavelength infrared range, Applied Physics Letters 78 (2001) 2107–2109.
[290] J. Bajaj, J.M. Arias, M. Zandian, J.G. Pasko, L.J. Kozlowski, R.E. De Wames, W.E. Tennant, Molecular beam epitaxial HgCdTe material characteristics and device performance: reproducibility status, Journal of Electronic Materials 24 (1995) 1067–1076.
[291] M.Z. Tidrow, J.C. Chiang, S.S. Li, K. Bacher, A high strain two-stack two-color quantum well infrared photodetector, Applied Physics Letters 70 (1997) 859–861.
[292] M.Z. Tidrow, W.A. Beck, W.W. Clark, H.K. Pollehn, J.W. Little, N.K. Dhar, P.R. Leavitt, S.W. Kennerly, D.W. Beekman, A.C. Goldberg, W.R. Dyer, Device physics and focal plane applications of QWIP and MCT, Opto-Electronics Review 7 (1999) 283–296.
[293] L.J. Kozlowski, K. Vural, J.M. Arias, W.E. Tennant, R.E. DeWames, Performance of HgCdTe InGaAs and quantum well GaAs/AlGaAs staring infrared focal plane arrays, Proceedings of SPIE 3182 (1997) 2–13.
[294] H. Schneider, M. Walther, J. Fleissner, R. Rehm, E. Diwo, K. Schwarz, P. Koidl, G. Weimann, J. Ziegler, R. Breiter, W. Cabanski, Low-noise QWIPs for FPA sensors with high thermal resolution, Proceedings of SPIE 4130 (2000) 353–362.
[295] A. Manissadjian, P. Costa, P. Tribolet, G. Destefanis, HgCdTe performance for high operating temperatures, Proceedings of SPIE 3436 (1998) 150–161.
[296] P. Norton, J. Campbell, S. Horn, D. Reago, Third-generation infrared imagers, Proceedings of SPIE 4130 (2000) 226–236.
[297] J.P. Chatard, LW MCT IRFPA cost optimization, Proceedings of SPIE 3698 (1999) 407–419.
[298] F. Bertrand, J.T. Tissot, G. Destefanis, Second generation cooled infrared detectors. State of the art. prospects, in: V. Kumar, S.K. Agarwal (Eds.), Physics of Semiconductor Devices, Vol. 2, Narosa Publishing House, New Delhi, 1998, pp. 713–720.
[299] T.J. DeLyon, J.E. Jensen, M.D. Gorwitz, C.A. Cockrum, S.M. Johnson, G.M. Venzor, MBE growth of HgCdTe on silicon substrates for large-area infrared focal plane arrays: a review of recent progress, Journal of Electronic Materials 28 (1999) 705–711.
[300] Y. Arakawa, H. Sakaki, Multidimensional quantum well laser and temperature dependence of its threshold current, Applied Physics Letters 40 (1982) 939–941.
[301] D. Leonard, M. Krishnamurthy, C.M. Reaves, S.P. Denbaars, P.M. Petroff, Direct formation of quantum-sized dots from uniform coherent islands of InGaAs on GaAs surface, Applied Physics Letters 63 (1993) 3203–3205.
[302] I.N. Stranski, L. Krastanow, Zur theorie der orientierten ausscheidung von lonenkristallen aufeinander, Sitzungsberichte d. Akad. d. Wissenschaften in Wein. Abt. IIb 146 (1937) 797–810.
[303] E. Towe, D. Pan, Semiconductor quantum-dot nanostructures: their application in a new class of infrared photodetectors, IEEE Journal of Selected Topics in Quantum Electronics 6 (2000) 408–421.
[304] A.D. Stiff, S. Krishna, P. Bhattacharya, S.W. Kennerly, Normal-incidence, high-temperature, mid-infrared, InAs-GaAs vertical quantum-dot infrared photodetector, IEEE Journal of Quantum Electronics 37 (2001) 1412–1419.
[305] S.Y. Wang, S.D. Lin, W. Wu, C.P. Lee, Low dark current quantum-dot infrared photodetectors with an AlGaAs current blocking layer, Applied Physics Letters 78 (2001) 1023–1025.
[306] V. Ryzhii, Physical model and analysis of quantum dot infrared photodetectors with blocking layer, Journal of Applied Physics 89 (2001) 5117–5124.
[307] S.W. Lee, K. Hirakawa, Y. Shimada, Bound-to-continuum intersubband photoconductivity of self-assembled InAs quantum dots in modulation-doped heterostructures, Applied Physics Letters 75 (1999) 1428–1430.
[308] A.D. Stiff, S. Krishna, P. Bhattacharya, S.W. Kennerly, High-detectivity, normal-incidence, mid-infrared ($\lambda \sim 4$ m) InAs/GaAs quantum-dot detector operating at 150 K, Applied Physics Letters 79 (2001) 421–423.

[309] J. Phillips, P. Bhattacharya, S.W. Kennerly, D.W. Beekman, M. Dutta, Self-assembled InAs-GaAs quantum-dot intersubband detectors, IEEE Journal of Quantum Electronics 35 (1999) 936–943.
[310] A.I. Yakimov, A.V. Dvurechenskii, A.I. Nikiforov, Yu.Yu. Proskuryakov, Interlevel Ge/Si quantum dot infrared photodetector, Journal of Applied Physics 89 (2001) 5676–5681.
[311] R.D. Rajavel, D.M. Jamba, J.E. Jensen, O.K. Wu, P.D. Brewer, J.A. Wilson, J.L. Johnson, E.A. Patten, K. Kasai, J.T. Caulfield, P.M. Goetz, Molecular beam epitaxial growth and performance of integrated multispectral HgCdTe photodiodes for the detection of mid-wave infrared radiation, Journal of Crystal Growth 184 (1998) 1272–1278.
[312] R.D. Rajavel, D.M. Jamba, J.E. Jensen, O.K. Wu, J.A. Wilson, J.L. Johnson, E.A. Patten, K. Kasai, P.M. Goetz, S.M. Johnson, Molecular beam epitaxial growth and performance of HgCdTe-based simultaneous-mode two-color detectors, Journal of Electronic Materials 27 (1998) 747–751.
[313] M.B. Reine, A. Hairston, P. O'Dette, S.P. Tobin, F.T.J. Smith, B.L. Musicant, P. Mitra, F.C. Case, Simultaneous MW/LW dual-band MOCVD HgCdTe 64×64 FPAs, Proceedings of SPIE 3379 (1998) 200–212.
[314] M.A. Kinch, HDVIP^{TM} FPA technology at DRS, Proceedings of SPIE 4369 (2001) 547–558.
[315] W.E. Tennant, M. Thomas, L.J. Kozlowski, W.V. McLevige, D.D. Edwall, M. Zandian, K. Spariosu, G. Hildebrandt, V. Gil, P. Ely, M. Muzilla, A. Stoltz, J.H. Dinan, A novel simultaneous unipolar multispectral integrated technology approach for HgCdTe IR detectors and focal plane arrays, Journal of Electronic Materials 30 (2001) 590–594.
[316] J.P. Zanatta, P. Ferret, R. Loyer, G. Petroz, S. Cremer, J.P. Chamonal, P. Bouchut, A. Million, G. Destefanis, Single and two colour infrared focal plane arrays made by MBE in HgCdTe, Proceedings of SPIE 4130 (2000) 441–451.
[317] H.K. Pollehn, J. Ahearn, Multi-domain smart sensors, Proceedings of SPIE 3698 (1999) 420–426.
[318] T. Whitaker, Sanders' QWIPs detect two color at once, Compound Semiconductors 5 (7) (1999) 48–51.
[319] S.D. Gunapala, S.V. Bandara, A. Sigh, J.K. Liu, S.B. Rafol, E.M. Luong, J.M. Mumolo, N.Q. Tran, J.D. Vincent, C.A. Shott, J. Long, P.D. LeVan, 8–9 and 14–15 μm two-color 640×486 quantum well infrared photodetector (QWIP) focal plane array camera, Proceedings of SPIE 3698 (1999) 687–697.
[320] S.D. Gunapala, S.V. Bandara, A. Singh, J.K. Liu, B. Rafol, E.M. Luong, J.M. Mumolo, N.Q. Tran, D.Z. Ting, J.D. Vincent, C.A. Shott, J. Long, P.D. LeVan, 640×486 long-wavelength two-color GaAs/AlGaAs quantum well infrared photodetector (QWIP) focal plane array camera, IEEE Transactions on Electron Devices 47 (2000) 963–971.
[321] A. Rogalski, Dual-band infrared detectors, Journal of Infrared and Millimeter Waves 19 (2000) 241–258.
[322] A.C. Goldberg, S.W. Kennerly, J.W. Little, H.K. Pollehn, T.A. Shafer, C.L. Mears, H.F. Schaake, M. Winn, M. Taylor, P.N. Uppal, Comparison of HgCdTe and QWIP dual-band focal plane arrays, Proceedings of SPIE 4369 (2001) 532–546.
[323] M.B. Reine, HgCdTe photodiodes for IR detection: a review, Proceedings of SPIE 4288 (2001) 266–277.
[324] Ph. Bois, E. Costard, J.Y. Duboz, J. Nagle, Technology of multiquantum well infrared detectors, Proceedings of SPIE 3061 (1997) 764–771.
[325] R. Watton, M.V. Mansi, Performance of a thermal imager employing a hybrid pyroelectric detector array with MOSFET readout, Proceedings of SPIE 865 (1987) 78–85.
[326] P.W. Kruse, D.D. Skatrud, in: Semiconductors and Semimetals, Vol. 47, Academic Press, San Diego, 1997.
[327] D.L. Polla, J.R. Choi, Monolithic pyroelectric bolometer arrays, in: P.W. Kruse, D.D. Skatrud (Eds.), Semiconductors and Semimetals, Vol. 47, Academic Press, San Diego, 1997, pp. 175–1201.
[328] P.W. Kruse, Principles of uncooled infrared focal plane arrays, in: P.W. Kruse, D.D. Skatrud (Eds.), Semiconductors and Semimetals, Vol. 47, Academic Press, San Diego, 1997, pp. 17–42.
[329] P.M. Downey, A.D. Jeffries, S.S. Meyer, R. Weiss, F.J. Bachner, J.P. Donnelly, W.T. Lindley, R.W. Mountain, D.J.S. Silversmith, Monolithic silicon bolometers, Applied Optics 23 (1984) 910–914.

[330] R.E. Flannery, J.E. Miller, Status of uncooled infrared imagers, Proceedings of SPIE 1689 (1992) 379–395.
[331] K.C. Liddiard, Thin film monolithic arrays for uncooled thermal imaging, Proceedings of SPIE 1969 (1993) 206–216.
[332] M.H. Unewisse, S.J. Passmore, K.C. Liddiard, R.J. Watson, Performance of uncooled semiconductor film bolometer infrared detectors, Proceedings of SPIE 2269 (1994) 43–52.
[333] H. Jerominek, F. Picard, D. Vincent, Vanadium oxide films for optical switching and detection, Optical Engineering 32 (1993) 2092–2099.
[334] H. Jerominek, T.D. Pope, M. Renaud, N.R. Swart, F. Picard, M. Lehoux, S. Savard, G. Bilodeau, D. Audet, L.N. Phong, C.N. Qiu, 64×64, 128×128 and 240×320 pixel uncooled IR bolometric detector arrays, Proceedings of SPIE 3061 (1997) 236–247.
[335] R.A. Wood, C.J. Han, P.W. Kruse, Integrated uncooled IR detector imaging arrays, Proceedings of IEEE Solid State Sensor and Actuator Workshop, 132–135, Hilton Head Island, S.C., (June, 1992).
[336] R.A. Wood, Uncooled thermal imaging with monolithic silicon focal planes, Proceedings of SPIE 2020 (1993) 322–329.
[337] T. Ishikawa, M. Ueno, K. Endo, Y. Nakaki, H. Hata, T. Sone, M. Kimata, Low-cost 320×240 uncooled IRFPA using conventional silicon IC process, Opto-Electronics Review 7 (1999) 297–303.
[338] W. Radford, D. Murphy, A. Finch, K. Hay, A. Kennedy, M. Ray, A. Sayed, J. Wyles, R. Wyles, J. Varesi, E. Moody, F. Cheung, Sensitivity improvements in uncooled microbolometer FPAs, Proceedings of SPIE 3698 (1999) 119–130.
[339] J. Anderson, D. Bradley, D.C. Chen, R. Chin, K. Jurgelewicz, W. Radford, A. Kennedy, D. Murphy, M. Ray, R. Wyles, J. Brown, G. Newsome, Low cost microsensors program, Proceedings of SPIE 4369 (2001) 559–565.
[340] D. Murphy, M. Ray, R. Wyles, J. Asbrock, N. Lum, A. Kennedy, J. Wyles, C. Hewitt, G. Graham, W. Radford, J. Anderson, D. Bradley, R. Chin, T. Kostrzewa, High sensitivity (25 μm pitch) microbolometer FPAs and application development, Proceedings of SPIE 4369 (2001) 222–234.
[341] M. Altman, B. Backer, M. Kohin, R. Blackwell, N. Butler, J. Cullen, Lockheed Martin 640×480 uncooled microbolometer camera, Proceedings of SPIE 3698 (1999) 137–143.
[342] M.N. Gurnee, M. Kohin, R. Blackwell, N. Butler, J. Whitwan, B. Backer, A. Leary, T. Nielson, Developments in uncooled IR technology at BAE Systems, Proceedings of SPIE 4369 (2001) 287–296.
[343] B.I. Craig, R.J. Watson, M.H. Unewisse, Anisotropic excess noise within a-Si:H, Solid-State Electronics 39 (1996) 807–812.
[344] J.L. Tissot, J.L. Martin, E. Mottin, M. Vilain, J.J. Yon, J.P. Chatard, 320×240 microbolometer uncooled IRFPA development, Proceedings of SPIE 4130 (2000) 473–479.
[345] E. Mottin, J.L. Martin, J.L. Ouvrier-Buffet, M. Vilain, A. Bain, J.J. Yon, J.L. Tissot, J.P. Chatard, Enhanced amorphous silicon technology for 320×240 microbolometer arrays with a pitch of 35 μm, Proceedings of SPIE 4369 (2001) 250–256.
[346] P.C. Shan, Z. Celik-Butler, D.P. Butler, A. Jahanzeb, Semiconducting YBaCuO thin films for uncooled infrared bolometers, Journal of Applied Physics 78 (1995) 7334–7339.
[347] P.C. Shan, Z. Celik-Butler, D.P. Butler, A. Jahanzeb, C.M. Travers, W. Kula, R. Sobolewski, Investigation of semiconducting YBaCuO thin films: a new room temperature bolometer, Journal of Applied Physics 80 (1996) 7118–7123.
[348] A. Jahanzeb, C.M. Travers, Z. Celik-Butler, D.P. Butler, S.G. Tan, A semiconductor YBaCuO microbolometer for room temperature IR imaging, IEEE Transactions on Electron Devices 44 (1997) 1795–1801.
[349] L. Mechin, J.C. Villegier, D. Bloyet, Suspended epitaxial YBaCuO microbolometers fabricated by silicon micromachining: modeling and measurements, Journal of Applied Physics 81 (1997) 7039–7047.
[350] J. Gray, Z. Celik-Butler, D.P. Butler, M. Almasri, Semiconducting YBaCuO as infrared detecting bolometers, Proceedings of SPIE 3436 (1998) 555–565.
[351] M. Almasri, Z. Celik-Butler, D.P. Butler, A. Yaradanakul, A. Yildiz, Semiconducting YBaCuO microbolometers for uncooled broad-band IR sensing, Proceedings of SPIE 4369 (2001) 264–273.

[352] H. Wada, T. Sone, H. Hata, Y. Nakaki, O. Kaneda, Y. Ohta, M. Ueno, M. Kimata, YBaCuO uncooled microbolometer IRFPA, Proceedings of SPIE 4369 (2001) 297–304.
[353] S.B. Lang, Ferroelectrics 7 (1974) 231–234.
[354] W. Whatmore, Pyroelectric devices and materials, Report on Progress in Physics 49 (1986) 1335–1386.
[355] R.R.W. Whatmore, Pyroelectric ceramics and devices for thermal infra-red detection and imaging, Ferroelectrics 118 (1991) 241–259.
[356] A. Mansingh, A.K. Arora, Pyroelectric films for infrared applications, Indian Journal of Pure and Applied Physics 29 (1991) 657–664.
[357] C.M. Hanson, Uncooled thermal imaging at Texas Instruments, Proceedings of SPIE 2020 (1993) 330–339.
[358] H. Beratan, C. Hanson, E.G. Meissner, Low cost uncooled ferroelectric detector, Proceedings of SPIE 2274 (1994) 147–156.
[359] R.K. McEwen, P.A. Manning, European uncooled thermal imaging sensors, Proceedings of SPIE 3698 (1999) 322–337.
[360] J.F. Belcher, C.M. Hanson, H.R. Beratan, K.R. Udayakumar, K.L. Soch, Uncooled monolithic ferroelectric IRFPA technology, Proceedings of SPIE 3436 (1998) 611–622.
[361] M.A. Todd, P.A. Manning, O.D. Donohue, A.G. Brown, R. Watton, Thin film ferroelectric materials for microbolometer arrays, Proceedings of SPIE 4130 (2000) 128–139.
[362] N. Teranishi, Thermoelelctric uncooled infrared focal plane arrays, in: P.W. Kruse, D.D. Skatrud (Eds.), Semiconductors and Semimetals, Vol. 47, Academic Press, San Diego, 1997, pp. 203–218.
[363] T. Kanno, M. Saga, S. Matsumoto, M. Uchida, N. Tsukamoto, A. Tanaka, S. Itoh, A. Nakazato, T. Endoh, S. Tohyama, Y. Yamamoto, S. Murashima, N. Fujimoto, N. Teranishi, Uncooled infrared focal plane array having 128×128 thermopile detector elements, Proceedings of SPIE 2269 (1994) 450–459.
[364] A.D. Oliver, W.G. Baer, K.D. Wise, A bulk-micromachined 1024-element uncooled infrared imager, Proceedings of 8th International Conference on Solid-State Sensors and Actuators (Transducers '95), and Eurosensors vol. IX, 1995, pp. 636–639.
[365] M.C. Fote, E.W. Jones, T. Caillat, Uncooled thermopile infrared detector linear arrays with detectivity greater than 10^9 cmHz$^{1/2}$/W, IEEE Transactions on Electron Devices 45 (1998) 1896–1902.
[366] M.C. Fote, E.W. Jones, High performance micromachined thermopile linear arrays, Proceedings of SPIE 3379 (1998) 192–197.
[367] M.C. Fote, S. Gaalema, Progress towards high-performance thermopile imaging arrays, Proceedings of SPIE 4369 (2001) 350–354.
[368] E.A. Wachter, T. Thundat, P.I. Oden, R.J. Warmack, P.D. Datskos, S.L. Sharp, Remote optical detection using microcantilevers, Review on Science and Instruments 67 (1996) 3434–3439.
[369] R. Amantea, L.A. Goodman, F. Pantuso, D.J. Sauer, M. Varghese, T.S. Villani, L.K. White, Progress towards an uncooled IR imager with 5 mK NEDT, Proceedings of SPIE 3436 (1998) 647–659.
[370] P. Norton, M. Mao, T. Perazzo, Y. Zhao, O. Kwon, A. Majumdar, J. Varesi, Micro-optomechanical infrared receiver with optical readout—MIRROR, Proceedings of SPIE 4028 (2000) 72–78.
[371] P.D. Datskos, P.I. Oden, T. Thundat, E.A. Wachter, R.J. Warmack, S.R. Hunter, Remote infrared radiation detection using piezoresistance microcantilevers, Applied Physics Letters 69 (1996) 2986–2988.
[372] P.D. Datskos, S. Rajic, I. Datskos, C.M. Eger, Novel photon detection based electronically induced stress in silicon, Proceedings of SPIE 3379 (1998) 173–181.
[373] K. Robinson, Cantilever thermal detector challenge microbolometer, Photonics Spectra, 50 (March 1998).
[374] P.D. Datskos, Micromechanical uncooled photon detectors, Proceedings of SPIE 3948 (2000) 80–93.
[375] P.W. Kruse, Application of uncooled monolithic thermoelectric linear arrays to imaging radiometers, in: P.W. Kruse, D.D. Skatrud (Eds.), Semiconductors and Semimetals, Vol. 47, Academic Press, San Diego, 1997, pp. 297–318.

[376] T. McManus, S. Mickelson, Imaging radiometers employing linear thermolelectric arrays, Proceedings of SPIE 3698 (1999) 352–360.
[377] C.T. Elliott, Photoconductive and non-equilibrium devices in HgCdTe and related alloys, in: P. Capper, C.T. Elliott (Eds.), Infrared Detectors and Emitters: Materials and Devices, Kluwer Academic Publishers, Boston, 2000, pp. 279–312.
[378] J. Piotrowski, M. Grudzień, Z. Nowak, Z. Orman, J. Pawluczyk, M. Romanis, W. Gawron, Uncooled photovoltaic $Hg_{1-x}Cd_xTe$ LWIR detectors, Proceedings of SPIE 4130 (2000) 175–184.